The Sodium Metal Electrode and its Interface with Inorganic Solid Electrolytes for Solid-State Batteries

Die Natriummetallelektrode und ihre Grenzfläche
mit Festelektrolyten für Feststoffbatterien

Dissertation

Zur Erlangung des akademischen Grades
Doktor der Naturwissenschaften
– Dr. rer. nat. –

vorgelegt dem
Fachbereich 08 - Biologie und Chemie
der Justus-Liebig-Universität Gießen

von

Till Ortmann

Oktober 2024

Dekan / Dean	Prof. Dr. Holger Zorn
1. Gutachter / 1st Reviewer	Prof. Dr. Dr. h.c. Jürgen Janek (Justus-Liebig-Universität Gießen)
2. Gutachter / 2nd Reviewer	Prof. Dr. Bernd Smarsly (Justus-Liebig-Universität Gießen)
Eingereicht / Submitted	28.10.2024
Disputation / Disputation	12.12.2024

Eidesstattliche Erklärung

Die vorliegende Arbeit wurde im Zeitraum vom 01.10.19 bis 28.10.24 am Physikalisch-Chemischen Institut der Justus-Liebig-Universität Gießen unter Betreuung von Prof. Dr. Dr. h.c. Jürgen Janek angefertigt.

Ich erkläre: Ich habe die vorgelegte Dissertation selbstständig und ohne unerlaubte fremde Hilfe und nur mit den Hilfen angefertigt, die ich in der Dissertation angegeben habe. Alle Textstellen, die wörtlich oder sinngemäß aus veröffentlichten Schriften entnommen sind, und alle Angaben, die auf mündlichen Auskünften beruhen, sind als solche kenntlich gemacht. Ich stimme einer evtl. Überprüfung meiner Dissertation durch eine Antiplagiat-Software zu. Bei den von mir durchgeführten und in der Dissertation erwähnten Untersuchungen habe ich die Grundsätze guter wissenschaftlicher Praxis, wie sie in der „Satzung der Justus-Liebig-Universität Gießen zur Sicherung guter wissenschaftlicher Praxis“ niedergelegt sind, eingehalten.

Gießen, 28.10.24

Till Ortmann

Für meine Familie

Mit dem Kopf in der Zukunft,
mit dem Herzen in der Vergangenheit.
- Benjamin Griffey

Zusammenfassung

Im Zuge der Dekarbonisierung moderner Gesellschaften steigt der Bedarf an Energiespeichern wie Batterien rapide. Während Lithiumionen-Batterien (LIB) bald ihre physikalisch-chemischen Grenzen erreichen, gelten Festkörperbatterien (FKB) als vielversprechende Weiterentwicklung. Der Einsatz eines Festelektrolyten (FE) statt eines flüssigen Elektrolyten ermöglicht die Verwendung von Metallelektroden, die eine höhere Energie- und Leistungsdichte bieten als kohlenstoffbasierte Anoden. Zugleich gewinnen Nachhaltigkeit und Ressourcenverfügbarkeit an Bedeutung, wodurch natriumbasierte Batterien zunehmend in den Fokus der Forschung rücken. Vor diesem Hintergrund stellt sich die Frage, ob natriumbasierte FKBs, insbesondere Reservoir-freie Zellen (RFZ), geeignete Alternativen zur LIB sein können. Die Implementierung von Metallelektroden aus Lithium oder Natrium in FKB wird jedoch durch Herausforderungen wie chemische Degradation und morphologische Veränderungen an der Metallelektrode|FE-Grenzfläche (Me|FE) erschwert. Um diese Probleme zu bewältigen und eine reversible Natriummetallelektrode (NME) in FKBs zu realisieren, ist ein fundiertes Verständnis der zugrundeliegenden Prozesse an der Na|FE-Grenzfläche erforderlich.

Diese Doktorarbeit konzentriert sich auf die Charakterisierung der Grenzflächenkinetik und die Entwicklung der Grenzflächenmorphologie während der anodischen Auflösung und kathodischen Abscheidung einer Natriummetallelektrode (NME) in Kontakt mit einem $Na_{3.4}Zr_2Si_{2.4}P_{0.6}O_{12}$ (NZSP) Festelektrolyten. Die Untersuchungen zeigen, dass der Ladungstransfer an der Na|NZSP-Grenzfläche von Natur aus schnell ist und chemische Degradation eine untergeordnete Rolle spielt. Als geschwindigkeitsbestimmender Prozess wurde das Phänomen der Stromeinschnürung festgestellt. Untersuchungen mittels Impedanzspektroskopie und Elektronenmikroskopie identifizieren die Porenbildung als Hauptursache für Kontaktverlust an der Na|NZSP-Grenzfläche und deren Polarisation bei der anodischen Auflösung. Im Hinblick auf Reservoir-freie Zellkonzepte wurde die Formierung einer NME an einer Stromableiter|FE-Grenzfläche mittels kathodischer Abscheidung charakterisiert. Unabhängig von den Abscheidungsparametern wurden dichte Natriumschichten im Mikrometerbereich beobachtet, wobei keine Anzeichen von Dendritenbildung im Impedanzspektrum beobachtet wurden. Eine höhere Abscheidestromdichte führte zu einer gleichmäßigeren Natriumverteilung auf dem Stromableiter, während höhere Stapeldrücke nur eine geringfügige Verbesserung nach sich zog. Diese Ergebnisse zeigen, dass RFZ mit Natrium aus physikalisch-chemischer Sicht realisierbar sind.

In einer weiteren Studie wurde der Einfluss der Mikrostruktur von Alkalimetallen auf deren elektrochemischen Eigenschaften betrachtet. Zunächst wurde die Elektronenrückstreubeugung (EBSD) als Methode zur Visualisierung der Mikrostruktur von Alkalimetallen etabliert. Korngrößen im Bereich mehrere hundert Mikrometer wurden für verschiedene Natriummetallfolien ermittelt, wobei kein signifikantes Kornwachstum bei der Lagerung bei Raumtemperatur beobachtet wurde. Verglichen dazu weist elektrochemisch abgeschiedenes Natrium an einer Fest|Fest-Grenzfläche eine säulenartige Kornstruktur mit einer kleineren Korngröße auf. Basierend auf In situ EBSD-Experimenten wurde ein laterales Kornwachstum während der elektrochemischen Abscheidung durch die Verschiebung von Korngrenzen beobachtet. Eine Bildung von Poren bei der anodischen Auflösung der NME wurde bevorzugt an der Na|NZSP-Grenzfläche im Inneren der Körner beobachtet.

Die Ergebnisse dieser Dissertation erweitern das Verständnis der Grenzflächenkinetik und morphologischen Entwicklung von NME|FE-Grenzflächen. Die vorstellte systematische Analyse der Na|NZSP-Grenzfläche bietet einen fundierten Ausgangspunkt für die Charakterisierung anderer FE in Kontakt mit NME. Das etablierte EBSD-Arbeitsprotokoll ermöglicht die Charakterisierung der elektrochemischen Eigenschaften von Metallelektroden unter Einbeziehung von deren Mikrostruktur. Die gewonnenen Erkenntnisse können einen Beitrag zur Entwicklung geeigneter Lösungsansätze zur Optimierung von ME-Grenzflächen für die Implementierung von NMEs in FKB leisten.

Abstract

In the pursuit of the decarbonization of modern societies, the demand for energy storage solutions such as rechargeable batteries is rapidly increasing. Although conventional lithium-ion batteries are approaching their physicochemical limits, solid-state batteries (SSBs) are emerging as a promising alternative. Using a solid electrolyte (SE) instead of a liquid electrolyte, SSBs may enable the use of metal electrodes, which offer higher energy and power densities than traditional carbon-based anode materials. Concurrently, the importance of sustainability and the availability of resources is increasing, which is why sodium-based batteries are becoming the focus of research. These considerations raise the question of whether sodium-based SSBs, particularly reservoir-free battery designs, could be viable alternatives compared to LIBs. However, the implementation of metal electrodes (MEs) such as lithium or sodium in SSBs is complicated by challenges such as chemical degradation and morphological changes at the Me|SE interface. To overcome these challenges requires a fundamental understanding of the underlying processes that occur at the Me|SE interface during electrochemical reactions to enable the use of a sodium metal electrode (SME) in sodium-based SSBs.

This doctoral thesis focuses on characterizing the interfacial kinetics and morphological changes upon anodic dissolution and cathodic deposition of a SME in contact with a $Na_{3.4}Zr_2Si_{2.4}P_{0.6}O_{12}$ (NZSP) SE. The results indicate that the fundamental charge transfer process is inherently fast and chemical degradation has a minimal effect on the interfacial kinetics. Instead, the current constriction phenomenon was identified as the rate-determining process at the Na|NZSP interface. Based on this result, the evolution of interfacial morphology was investigated by impedance spectroscopy and electron microscopy. During anodic dissolution, pore formation was found to be the primary cause of contact loss and interfacial polarization. In view of reservoir-free cells (RFCs), the formation of an SME by cathodic deposition of sodium at a current collector|SE interface was examined. Independent of deposition parameters (current density and stack pressure), a dense sodium layer of micrometer thickness was observed, with impedance analysis showing no evidence of dendrite formation. Furthermore, increasing the current density during deposition improved sodium coverage across the electrode area, while increased the stack pressure only had a minor effect. These findings suggest that reservoir-free sodium SSBs are feasible from a physicochemical perspective.

In addition, the effect of metal microstructure on the electrochemical performance of SMEs was investigated. A reliable workflow was developed to visualize the microstructure of alkali metals using electron backscatter diffraction (EBSD). Sodium metal foils exhibit grain sizes on the order of several hundred micrometers, while no significant grain growth was observed during storage at room temperature. Electrochemically deposited sodium exhibits a columnar structure with a smaller grain size compared to mechanically prepared foils. In situ EBSD experiments revealed lateral grain growth during electrodeposition, attributed to the movement of grain boundaries. During anodic dissolution, pore formation was preferentially observed at the Na|NZSP interface within the interior of grains.

In summary, the findings presented in this doctoral thesis improve the understanding of interfacial kinetics and morphological evolution of SMEs in contact with SEs upon cycling. Furthermore, the systematic analysis of the Na|NZSP interface provides a fundamental framework for evaluating impedance data and offers guidance for the characterization of other SME|SE combinations. Additionally, EBSD has been established as a technique to visualize the microstructure of electrode materials, allowing the assessment of electrochemical properties from a microstructural perspective. This approach may facilitate the development of tailored solutions to optimize the Na|SE interface for the development of reservoir-free sodium SSBs.

List of Abbreviations

BASE	β´´- alumina solid electrolyte
CAM	Cathode active material
CC	Current collector
CCD	Critical current density
CBM	Conduction band minimum
DFT	Density functional theory
EIS	Electrochemical impedance spectroscopy
EBSD	Electron backscatter diffraction
ESW	Electrochemical stability window
FIB-SEM	Focused ion beam – scanning electron microscopy
GB	Grain boundary
LE	Liquid electrolyte
LIB	Lithium-ion battery
LiPON	Lithium phosphorus oxynitride
LLZO	$Li_{6+x}La_3Zr_{2-x}M_xO$ (with M = Al, Ta)
MCI	Mixed-conducting interphase
Me	Metal
NaSICON	Na Super Ion Conductor
NZSP	$Na_{3.4}Zr_2Si_{2.4}P_{0.6}O_{12}$
PEIS	Potentiostatic electrochemical impedance spectroscopy
RFC	Reservoir-free cell
SE	Solid electrolyte
SEI	Solid-electrolyte interphase
SEM	Scanning electron microscopy
SIB	Sodium-ion battery
SME	Sodium metal electrode
SSB	Solid-state battery
TEM	Transmission electron microscopy
XPS	X-ray photoelectron spectroscopy

Tabel of Contents

1 Introduction

In accordance with the Kyoto Protocol and the Paris Climate Agreement, 196 countries have collectively pledged to limit the global average temperature increase to 1.5 °C above the pre-industrial levels. To mitigate the potential consequences of global warming, it is essential to significantly reduce greenhouse gas emissions worldwide over the next decades.[1] In the context of the imminent replacement of fossil fuels by renewable energy sources in the coming decades, it is anticipated that electricity will become the dominating secondary energy form by 2050, with wind and solar power playing a pivotal role in this transition.[2] Shifting towards renewable energy will require efficient energy storage, e.g. to compensate for intermittent solar and wind power. In addition, electrical energy storage is necessary for mobile applications such as electric vehicles, laptops, or power tools.[3,4]

Rechargeable batteries represent the most prevalent technology for energy storage for mobile applications and gaining increased interest for stationary systems.[5,6] In recent years, lithium-ion batteries (LIBs) have emerged as the dominant technology in this field due to their high energy and power densities, reliability, and excellent cyclability.[7–9] However, the forecasted increase in the number of LIBs in the near future carries the risk of a shortage of resources and particularly lithium production bottlenecks increasing costs of LIBs.[10,11] In addition, the requirements for batteries regarding the energy density, safety and high power density (fast charge and discharge performance) increases, while commercial LIBs are anticipated to reach their physicochemical limits soon.[12] On the one hand, this motivates the development of batteries based on abundant and non-critical elements, while maintaining comparable properties to those of commercial LIBs.[13] On the other hand, it stimulates the development of new battery concepts aiming to enhance the performance.[14]

In this turn, sodium-ion batteries (SIBs) have re-experienced great interest in research and industry.[15–18] Although SIBs generally exhibit a lower energy density compared to LIBs (exact value depends on cell chemistry), the high abundance and availability of raw materials reduce the risk of resources shortages and production costs.[19,20] Furthermore, existing production technologies for manufacturing LIBs can be transferred to SIBs, which is favorable for large-scale production.[21,22] This makes SIBs an attractive alternative to LIBs for stationary energy storage, home grids, or electric vehicles.[22,23]

The energy and power density of batteries can in principle be enhanced by using metal electrodes such as sodium. Sodium metal exhibits a high theoretical gravimetric capacity q_{theo} (1165 mAhg^{-1}) and a low standard redox potential E_{H} of −2.71 V vs standard hydrogen electrode.[24] In addition, the use of a sodium metal electrode (SME) may improve cycling performance compared to current carbon-based anodes.[25–27] This is crucial for fast charging of batteries, which is required especially for automotive applications.

However, the high reactivity of sodium complicates the implementation of SMEs in batteries.[28] From a practical point of view, the processing of sodium metal requires an inert atmosphere, which complicates cell manufacturing on large scale and increases production costs. In principle, this issue could be mitigated by developing "anode-free" concepts.[29] Here the SME is formed after cell assembly by electrodeposition of enclosed sodium ions from the cathode active material on a current collector (CC). Hence, a direct processing of sodium could be avoided and the total amount of sodium metal is minimized economically. Nevertheless, independent of the cell configuration, the formation of dendrites upon cycling of the SME in conjunction with flammable organic electrolytes has thus far precluded the implementation of the SME in SIBs in general.[30]

Sodium solid-state batteries (SSBs) have emerged as a promising option to overcome these problems.[31,32] The benefits when the liquid electrolyte is replaced by a solid electrolyte (SE) can be summarized as follows:[33–35] First, the mechanical integrity of SEs prevents crosstalk between the electrodes and is less susceptible to penetration by metal dendrites than liquid electrolytes. Second, a transference number close to unity of SEs and sufficient ionic conductivity at room temperature serves to prevent the electrolyte from undergoing strong polarization during fast charging. Third, the replacement of flammable organic liquid electrolytes by SEs may enhance the safety of batteries.

Despite the advantages of SEs, issues associated with a high interface-related resistance between the SME and the SE as well as morphological instabilities upon cycling have to be solved to enable a reversible operation of an SME in SSBs.[36] In view of large-scale production, "anode-free", or more fittingly, reservoir-free cell concepts are desirable to simplify cell processing and develop sodium-based SSBs that are competitive with current LIBs in terms of cost and performance.[37,38] To overcome these issues and facilitate the development of reservoir-free cell configurations, a fundamental understanding of the electrochemical dissolution and deposition of sodium at the Na|SE interface is essential.

In this doctoral thesis, the interface between sodium and the inorganic SE $Na_{3.4}Zr_2Si_{2.4}P_{0.6}O_{12}$ (NZSP) under equilibrium and non-equilibrium conditions is investigated by means of electrochemical impedance spectroscopy (EIS) and electron microscopy. The overall aim is to gain a fundamental understanding of microscopic processes at the interface and their impact on the morphological evolution upon electrochemical dissolution and deposition. In addition, electron backscatter diffraction (EBSD) is employed as a characterization method for visualizing the microstructure of sodium metal, aiming to assess the influence of microstructure on the performance of SME and develop innovative concepts for their application in SSBs.

In the first publication, entitled: "*Kinetics and Pore Formation of the Sodium Metal Anode on NASICON-Type* $Na_{3.4}Zr_2Si_{2.4}P_{0.6}O_{12}$ *for Sodium Solid-State Batteries*", the interface between sodium and NZSP is comprehensively explored and the dominating process leading to large interface-related resistance is identified.[39] By a combined approach of EIS, photoelectron spectroscopy (XPS) and transmission electron microscopy (TEM), the formation of a kinetically stabilized interphase is revealed when contacting NZSP with sodium. Despite the interfacial degradation and the charge transfer process, EIS analysis demonstrated that insufficient physical contact between SME and SE is the underlying cause of the interface-related contribution observed in the impedance spectra. During electrochemical dissolution of the SME, the formation of pores at the interface is visualized by focused ion beam scanning electron microscopy (FIB-SEM) resulting in contact loss. Depending on the applied stack pressure, different geometric shapes of the formed pores are observed emphasizing the importance of the external load for operation of the SME. Importantly, time dependent EIS analysis during anodic dissolution verified the correlation between the interfacial morphology and the interface-related contribution in the impedance spectra. Consequently, changes at the interfacial morphology can be monitored by analyzing the evolution of the interface-related contribution in the impedance spectra. Based on this correlation, an equilibration of the interfacial morphology is observed in a subsequent resting phase after anodic dissolution, even at low stack pressures. This emphasizes a highly dynamic behavior of the interfacial morphology and reveals the strong dependence of the total stripping capacity on the used dissolution protocol, which is crucial for real-world battery applications. Moreover, this publication provides a guideline to systematically characterize metal|SE interfaces and determine the dominating interfacial process.

In the second publication, entitled: "*Deposition of Sodium Metal at the Copper-NaSICON Interface for Reservoir-Free Solid-State Sodium Batteries*", the cathodic deposition of sodium at the Cu|NZSP interface is explored at various current densities and stack pressures.[40] Based on the results from the first publication, the electrode morphology is monitored by means of EIS and the tomography of the CC after sodium deposition is visualized by 3D confocal microscopy. At higher current densities, a more uniform sodium layer over the entire copper electrode can be achieved. In contrast, only a minor effect on the coverage is found when the stack pressure was increased. Independent of the deposition parameters, a dense sodium layer with a proper contact to NZSP is proven by FIB-SEM cross-sectioning. Although slight spallation of the NZSP is observed by FIB-SEM cross-sections, no detrimental dendrites or filaments are identified by EIS. The nucleation and growth of sodium at the Cu|NZSP interface only occurs at contact spots, as shown by in situ TEM experiments. Overall, the presented results demonstrate the feasibility of electrodeposition of sodium between copper and NZSP, which is essential for the realization of reservoir-free sodium SSBs. Furthermore, the screened parameter window serves as an appropriate basis for subsequent optimization and enhancement of the sodium coverage.

In the third publication, entitled: "*Imaging the Microstructure of Lithium and Sodium Metal in "Anode-Free" Solid-State Batteries using EBSD*", the microstructure of highly reactive alkali metal foils and electrodeposited metal layers are characterized by a combined approach of FIB-SEM and EBSD.[41] Grain sizes in the range of several hundreds of micrometers are revealed for sodium and lithium metal foils. On the opposite, a smaller grain size is observed when the metals are electrochemically deposited at a CC|SE interface, where the metal grain boundaries are orientated mainly vertically to the interface. In view of reservoir-free SSBs, the evolution of the microstructure during electrodeposition and its impact on interfacial morphology during dissolution is further explored by an in situ EBSD experiment. During electrodeposition, the growth of grains in the vertical direction is observed, accompanied by lateral grain growth by the movement of grain boundaries. In contrast, during the dissolution of the metal electrode, the formation of pores is preferentially observed at the metal|SE interface within the grain, rather than at metal grain boundaries. This highlights the importance of the metal microstructure and its impact on the electrochemical performance. Overall, the established EBSD workflow is a promising approach for investigating microscopic processes in metal electrodes. It allows for the acquisition of additional information, including grain boundary structures, orientation dependencies, and mechanical deformation, which can be correlated with the electrochemical performance. Furthermore, the experimental results provide a fundamental basis for optimization strategies to enhance the electrochemical performance of metal electrodes in general.

In summary, the results of this doctoral thesis expand the knowledge on the SME and its interface with NZSP SE, which can help to develop reservoir-free sodium SSBs operating at room temperature. The fundamental characterization of the Na|NZSP interface provides a reliable guideline to characterize metal|SE interfaces and avoid misinterpretation of impedance data in general. Furthermore, this study demonstrates the feasibility of electrochemical deposition of sodium at the CC|SE interface. Additionally, this work introduces EBSD as a valuable characterization technique for metal and alloy electrodes enabling new possibilities to understand and analyze microscopic processes, which can help developing new concepts for boosting the electrochemical performance of Na|SE interfaces.

2 Fundamentals

The following section provides an overview on the metal electrode (Me)|SE interface with the focus on sodium and ceramic SEs to support the understanding of this doctoral thesis. Besides the interfacial stability, the fundamentals of anodic dissolution and cathodic deposition as well as reservoir-free cell concepts are briefly summarized. Furthermore, the role of microstructure and self-diffusion of metals in relation to the electrochemical performance of SMEs are shortly elucidated. This includes also the embedding of the obtained results and findings of this doctoral thesis into the scientific context.

It should be noted that the key focus of this doctoral thesis lies on room temperature applications of the SME. Although SMEs have already been successfully introduced in high temperature battery types operating above the melting point of sodium, the interfacial properties, processes and challenges at a liquid|solid interface differ strongly from a solid|solid interface. Therefore, these battery types will not be discussed in the following section. For the current status, progress and challenges of high- and intermediate-temperature sodium-sulfur and sodium-metal chloride batteries, the interested reader is referred to review articles by Armand and Rojo.[42–44]

2.1 The Interface between a Metal Electrode and a Solid Electrolyte

The primary SE material employed in this doctoral thesis belongs to the NaSICON compound family. The acronym NaSICON originates from *Na Super Ion Conductor* and describes a solid solution with the general formula $Na_{1+x}Zr_2Si_xP_{3-x}O_{12}$ ($0 < x < 3$).[45–47] NaSICONs are known for several decades and are intensively studied with respect to different synthesis methods, possibilities of doping and structure-property-relationship.[48–50] The combination of high ionic conductivity and thermal stability make NaSICONs a promising candidate as a separator in sodium SSBs.[51] Despite extensive research on the interface of NaSICONs in contact with an SME, the interfacial kinetics is still a topic of ongoing debate.[52–54] The following chapter provides an overview on the interfacial stability and kinetics, with a focus on Na|NaSICON interfaces.

2.1.1 Classification of Interfacial Stability – Interfaces and Interphases

The interfacial stability between a metal and SE plays a central role for the properties of the interface and thus its feasibility for battery applications.[55] In order to classify the interfacial stability of a specific Me|SE interface, it is necessary to evaluate the electrochemical stability window (ESW) of the SE. Previously, an estimate of the ESW under reducing conditions at the anode side was given based on the position of the conduction band minimum (CBM), which can be considered as lowest unoccupied molecular orbital.[56] Accordingly, the interface is thermodynamically stable when the CBM is above the Fermi level of the metal $\varepsilon_{F,Me}$. In contrast, the interface is unstable when $\varepsilon_{F,Me}$ is below the CBM, as electrons will be transferred from the metal to the SE resulting in the formation of an interphase. However, this approach often results in an overestimation of the ESW, as the redox potentials of the electrolyte are not taken into account. Consequently, the approach provides only an upper limit for the ESW.[57]

An accurate determination of the ESW given to a reference potential can be achieved by first-principle density functional theory (DFT) calculations.[58] The results of these DFT calculations indicate that the majority of binary compounds, such as Na_2S or NaCl, are thermodynamically stable in contact with sodium.[59,60] In contrast, common SEs exhibit a much smaller ESW and are mostly unstable in contact with sodium.[59,61]

Me|SE interfaces in general can be classified as either thermodynamically stable or unstable, as illustrated schematically in **Figure 1**.[62] In the case of a thermodynamically stable interface, no interfacial degradation takes place, as shown in **Figure 1a**. This type of interface would be suitable to enable stable operation as no parasitic side reactions and additional resistance occurs on the long term. For example, β´´-alumina SE (BASE) is thermodynamically stable in contact with sodium as shown by theoretical calculations and experimental results.[59,63] This property makes BASE a common separator for high-temperature battery applications.[64]

If the SE is thermodynamically unstable, an interphase will form by decomposition of the SE upon contacting with the respective parent metal. Depending on the ionic and electronic transport properties of the formed interphase, two types can be distinguished according to Wenzel et al.[62] When the formed interphase exhibit both a sufficient electronic and ionic conductivity, the interphase is classified as mixed-conducting interphase (MCI). The mixed-conducting property facilitates a transport of electrons and ions across the interphase, resulting in a continuous growth of the interphase, as visualized in **Figure 1b** on the left side. The growth of an interphase results in the continuous consumption of the metal and the SE, which ultimately leads to the failure of the battery. This occurs either as a result of a complete loss of capacity at the anode side or as a consequence of a short circuit caused by the complete degradation of the SE.

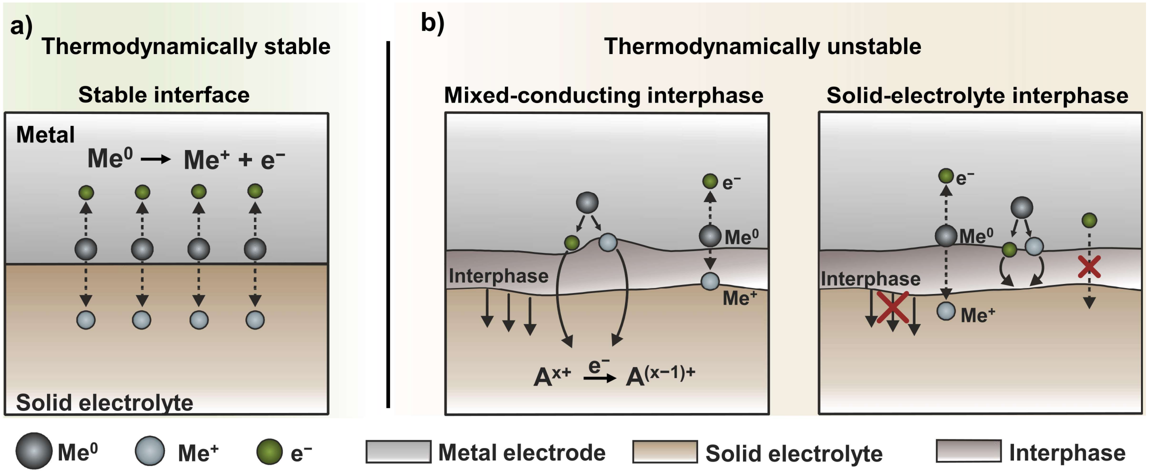

Figure 1: *Classification of Me|SE interfaces and interphases. A thermodynamically stable interface is schematically visualized in (a), while thermodynamically unstable interphases namely, mixed-conducting interphase (MCI)) and solid-electrolyte interphase (SEI), are depicted in b). The transport of Me$^+$ ions across the interface is indicated by dashed arrow lines. The growth of the interphase is indicated by solid lines. Figure modified from S. Wenzel et al., Solid State Ionics 2015, 278, 98–105.*[62]

In contrast, when the electronic conductivity of the formed degradation products is negligibly small, the sluggish electron transport trough the interphase reduces the growth rate with increasing thickness of the interphase (see **Figure 1b** on the right side).[65] Consequently, the interfacial degradation upon contacting is self-limiting with progressing growth of the interphase and a kinetically stabilized interphase, also named solid-electrolyte interphase (SEI), is formed.[65] Despite an interfacial degradation, an SEI could enable a stable operation of the Me|SE interface in SSBs as demonstrated for lithium and a lithium phosphorus oxynitride (LiPON) SE.[66,67]

Theoretically, a third case could occur when the partial electronic conductivity surpasses the partial ionic conductivity. Similar to an SEI, the growth of the interphase would be self-limiting. However, due to its ion blocking behavior this kind of interphase would not be suitable for battery applications.

Although the stability of NaSICONs in contact with sodium has been addressed in several reports, the interfacial kinetics and properties are not well understood.[54,68–71] Despite the consent that NaSICONs are thermodynamically unstable versus sodium, discrepancies emerge with respect to the formed degradation products and the growth of the interphase.[68,69] Furthermore, the reported resistances, as a result of the interphase formation, exhibit a considerable degree of variation over several orders of magnitue.[54,69–71] Considering other compounds from the NaSICON solid solution series, the interfacial stability in contact with sodium may alter, as theoretical calculations reveal different ESWs depending on the composition.[70] However, a clear classification of the interphase as well as the quantification of the interphase-related resistance for the respective NaSICON compound is of high relevance for the development of the SME in SSBs.

In view of the incomplete picture and discrepancies in the existing literature, the interfacial stability between sodium and $Na_{3.4}Zr_2Si_{2.4}P_{0.6}O_{12}$ (hereafter referred to as NZSP) has been subjected to a comprehensive characterization in the first publication of this doctoral thesis (see section 3.1). A kinetically stabilized interphase with a negligible resistance was found.[39] The findings were supported by an independent report from Quérel et al., which was published shortly after the first publication of this doctoral thesis.[72] In addition to the interphase formation, the following section will examine further processes that influence the interfacial kinetics.

2.1.2 The Interfacial Kinetics at the Na|NaSICON Interface

A fundamental process occurring at an electrode|electrolyte interface is the charge transfer. While considerable research has been conducted on the charge transfer reactions at Me|liquid electrolyte (LE) interfaces, the understanding of the underlying mechanisms of fundamental charge transfer reactions at Me|SE interfaces remains limited.[56] Experimentally, the interfacial kinetics at Me|SE interfaces is mainly characterized by potentiostatic electrochemical impedance spectroscopy (PEIS). The frequency-dependent technique enables the separation of microscopic transport processes based on their characteristic time constant. Typically, the ion transport process in the SE (bulk and across a grain boundary) has a small time constant (high frequency range), while interfacial processes are observed at higher time constants (low frequency range).[73] Accordingly, an identified process in the low frequency region of an impedance spectrum is often directly assigned to a "charge transfer process", without considering additional processes.[74,75]

For example, contaminations of the surface of the SE, like hydroxide or carbonate species, could impede the transfer of charge, which results in an increased resistance.[76] Depending on the degree of surface contamination, the assigned charge transfer resistance determined by PEIS varies strongly, as shown for NaSICON and BASE.[52,77] Accordingly, the given values reflect a charge transfer through a blocking layer rather than the fundamental charge transfer process. Contamination layers at the interface could not only originate from the SE, but also from the metal electrode. Otto et al. demonstrated that lithium forms a native passivation layer on the surface even it is stored and handled under an inert atmosphere.[78,79] Given its higher reactivity, the formation of a native passivation layer is also reasonable for sodium, although a detailed analysis of possible surface passivation on sodium is still lacking.[80]

For instance, a passivation-free Me|SE interface can be achieved through electrodeposition at microelectrodes on an SE cross-section. Such microelectrode experiments demonstrated that the resistance for the charge transfer at the Li|$Li_{6+x}La_3Zr_{2-x}M_xO$ (with M = Al, Ta) (LLZO) interface is in the order of 0.1 Ω cm^2.[81] Similar results were obtained in pellet-type cells, where no interface-related resistance (and thus no charge transfer) could be resolved by PEIS, when lithium and LLZO are contacted at high pressures.[82] A comparably low interface-related resistance of around 2 Ω cm^2 has been reported for pellet-type symmetrical Na|NZSP|Na cells.[39,71,83] For both material systems, the activation energy of the interface-related contribution obtained from PEIS is similar to that of the ion transport process in the SE.[39,82] This observation leads to the conclusion that the fundamental charge transfer process is not the rate-determining step at the Me|SE interface.

Apart from the charge transfer process and interfacial degradation another explanation for the occurrence of an interface-related contribution in PEIS is often assigned to an inadequate "wettability" (or more accurately, adhesion) between the metal anode and the SE.[84] Typically, this issue is addressed phenomenologically by introducing a "sodiophilic" interlayer to improve the "wettability" (adhesion) and thus the interfacial physical contact.[85,86] Although the electrochemical performance is mostly improved by such interlayers, a deeper understanding of the interfacial contact on the interfacial kinetics is lacking. A phenomenon which is mostly overlooked at Me|SE is the geometric current constriction phenomenon.

The current constriction phenomenon results from insufficient contact at the Me|SE interface which could be caused for example by a pore.[87,88] Although the phenomenon is a non-microscopic transport process, its impedance signature is similar to that of a true migration process, such as the transport of ions across a grain boundary.[87–89] Hence, a semicircle in a Nyquist diagram can also result from the current constriction phenomenon. As illustrated in **Figure 2a**, the conduction behavior of a pore depends on the excitation frequencies *f*. At high excitation frequencies, pores are actively involved in charge transport through the system via a displacement current, while at lower frequencies the pore becomes insulating. Therefore, depending on the excitation frequency *f*, the potential distribution in the SE near the interface becomes non-uniform. The region needed to equilibrate the potential distribution in the SE material increases as the excitation frequency *f* decrease, as indicated by the red arrow in **Figure 2a**.[88,89] In other words, the SE volume actively involved in the transport reduces with lowering the excitation frequency. Hence, the resistance of the systems increases which is reflected by an additional semicircle in the impedance spectrum.

The current constriction phenomenon is a purely geometric effect and occurs as soon as local microcontacts are present at the Me|SE interface. Microcontacts can be caused, for example, by a partial coverage of pores (or voids) as well as by the presence of insulating contamination or passivation layers or non-uniform metal deposition.[56] In principle, the current constriction phenomenon can also arise from a low concentration of active sites.[90] The metal surface and the SE exhibit distinct sites where electrodissolution (deposition) might be energetically favored. For instance, an adsorbed atom on the surface could be preferably dissolved (deposited) compared to a terrace atom which would also result in a current focusing.[56]

The occurrence of the geometric current constriction phenomenon has been observed for several parent metal|SE interfaces.[77,90] In particular, for the Li|LLZO and Na|NZSP interface it has been demonstrated that the interfacial kinetics is dominated by this geometric phenomenon (compare section 3.1).[39,82] Thus, variations of the interface-related contribution in the impedance can directly be assigned to changes of the interfacial morphology. For instance, it has been shown that the polarization occurring during electrodissolution has its origin in the current constriction phenomenon, as a consequence of alternations in the interface morphology due to pore formation.[39,82] Motivated by the observed correlation, Eckhardt et al. systematically investigated the influence of different interfacial morphologies on the resulting constriction contribution in the impedance using a microstructure-resolved electric network model.[87,91–93] Based on this network model, the evolution of the constriction resistance R_{Cstr}, constriction capacity C_{Cstr}, and the corresponding time constant τ_{Cstr} when altering the contact area, electrode position, contact area distribution, and pore height is summarized in **Figure 2b**.[87] It should be noted that the trends presented in **Figure 2b** are valid under the condition that the time constant for the SE bulk and grain boundary transport process is smaller than that of the constriction signal. Additionally, the charge transfer and the interphase formation processes are assumed to be negligible, as is the case for the Na|NZSP interface.[87]

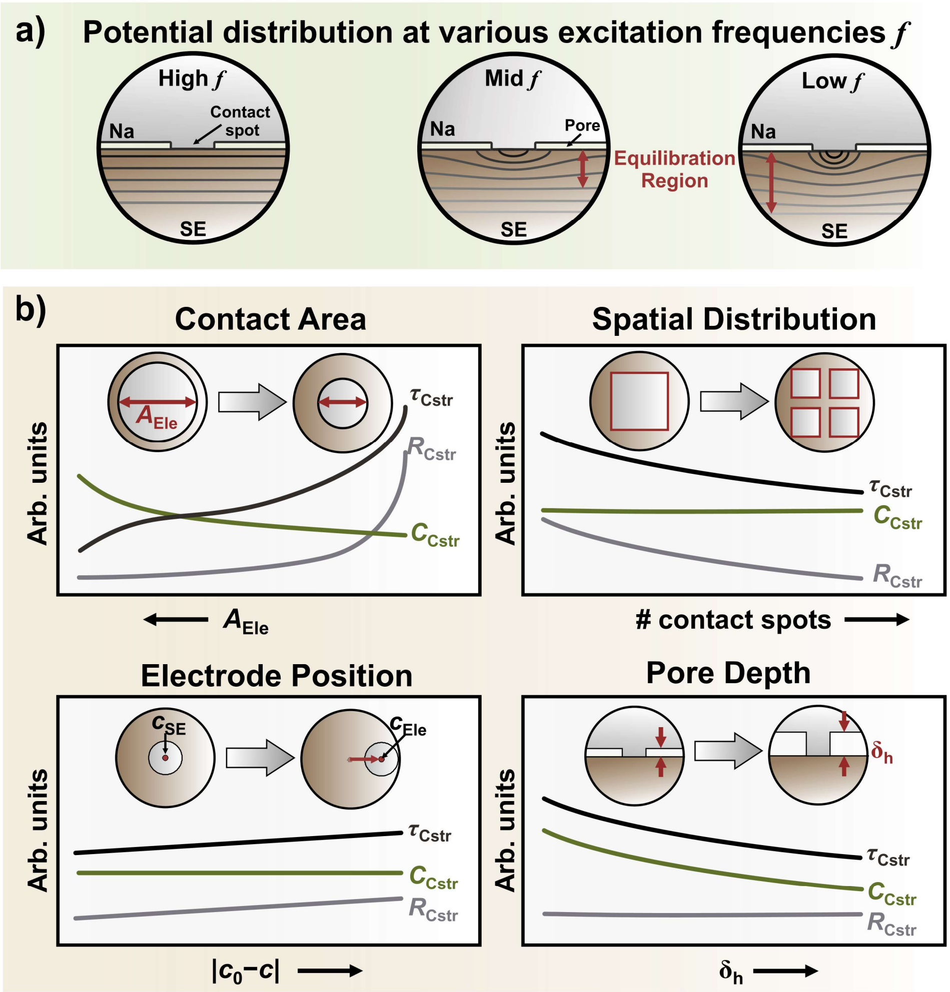

Figure 2: *a) Schematic illustration of the potential distribution equipotential line distribution (black lines) in an SE at various excitation frequencies. Equipotential lines are indicated by black lines. At high excitation frequencies, the potential distribution in the SE is homogeneous, as indicated by the equipotential lines. With decreasing excitation frequencies, the potential distribution becomes inhomogeneous, as shown by the bended equipotential lines in the scheme. Accordingly, the SE volume required for equilibration increases at lower frequencies, as indicated by the red arrow. The larger the volume necessary to balance the potential distribution, the larger the measured constriction contribution in the Nyquist representation of the EIS spectrum. The scheme is based on the results of reference [87-89]. b) Summary of the trends for constriction resistance* R_{Cstr}*, constriction capacity* C_{Cstr} *and the corresponding time constant* τ_{Cstr} *when the interfacial morphology is systematically altered. The evolution of the respective constriction parameters when the electrode area* A_{Ele} *decreases is visualized in the upper left graph, while an increase in the number of contact spots at constant contact area is shown in the upper right graph. The graph on the bottom left shows the evolution of the parameters when the center of the electrode (*c_{Ele}*) shifts away from the center of the SE (*c_{SE}*). The effect of an increasing pore depth* δ_{h} *on the constriction parameters is illustrated in the graph on the bottom right. The trends are schematically illustrated based on the results presented in reference [87].*

The fundamental understanding and correlation between the interfacial geometry and the constriction contribution in EIS enables a monitoring of the evolution of the interfacial morphology. Hence, EIS is a powerful tool to characterize the interfacial morphology “in situ” of otherwise buried Me|SE interfaces, such as Na|NZSP. For example, the morphological evolution during electrodeposition or electrodissolution has been analyzed by EIS as part of this doctoral thesis (c.f. section 3.1 and 3.2).[39,40] Similar studies have been conducted to analyze the pore formation or equilibration of stripped lithium metal anodes at the Li|LLZO interface.[82,94] Despite the valuable three-dimensional information provided by the constriction contribution, the interfacial morphology cannot be unambiguously extracted from the EIS data. Different interfacial morphologies can result in identical constriction signatures in the impedance spectrum, as variations in different geometric parameters exhibit opposing trends (c.f. **Figure 2b**). Therefore, to characterize the evolution of the interfacial morphology in real systems using EIS, an additional analytical technique is necessary to validate the interpretation.[40]

2.2 The Me|SE Interface during Anodic Dissolution

The dissolution of a metal anode alters the interfacial morphology and thus strongly affects the cell operation. To guarantee optimal cell functionality, it is essential to maintain a stable and predictable interface morphology. This is of particular significance for Me|SE interfaces, as the rigidity of SE precludes the possibility of compensating for morphological alterations at the interface. In the following, the interfacial kinetics at planar Me|SE interfaces is elaborated, and different concepts are transferred to the Na|SE interfaces. This includes also processes that affect the evolution of the interface morphology, which are briefly summarized. Finally, different possibilities to maintain a stable interface morphology during cell operation are discussed.

2.2.1 The Anodic Dissolution in View of the Vacancy Relaxation Model

The oxidation of a parent metal at a solid|solid interface has been studied intensively in the past decades, especially for Ag|AgX interface (X = Cl, Br).[95,96] In addition to the experimental characterization, Schmalzried and Janek developed a model to describe the kinetics of silver dissolution at the phase boundary.[97] Krauskopf et al. subsequently employed this model, with certain limitations, to describe lithium metal oxidation at a Li|SE interface.[56,82] The similar chemical nature of alkali metals makes the concept also relevant for the kinetics of Na|SE interfaces.

In general, the oxidation reaction at a metal anode at a Me|SE interface can be denoted in the Kröger-Vink notation as follows:

$$\mathrm{Me_{Me}(Me)} \rightleftharpoons \left[\mathrm{Me^{\times}_{Me^{+}}(SE)} - \mathrm{V'_{Me^{+}}(SE)}\right] + \mathrm{e'(Me)} + \mathrm{V^{\times}_{Me}\ (Me)} \qquad (1)$$

A metal atom is oxidized and passes through the Me|SE interface, subsequently occupying either a vacant lattice site $\mathrm{V'_{Me^{+}}(SE)}$ or an interstitial site within the SE. The specific site occupied by the metal ion depends on the ion conduction mechanism of the specific SE. The oxidized metal atom leaves an electron $\mathrm{e'(Me)}$ and vacant site $\mathrm{V^{\times}_{Me}(Me)}$ in the metal close to the surface. The metal vacancy $\mathrm{V^{\times}_{Me}(Me)}$ can either diffuse into the bulk of the metal electrode or annihilate at a grain boundary or dislocation (site of repeatable growth).

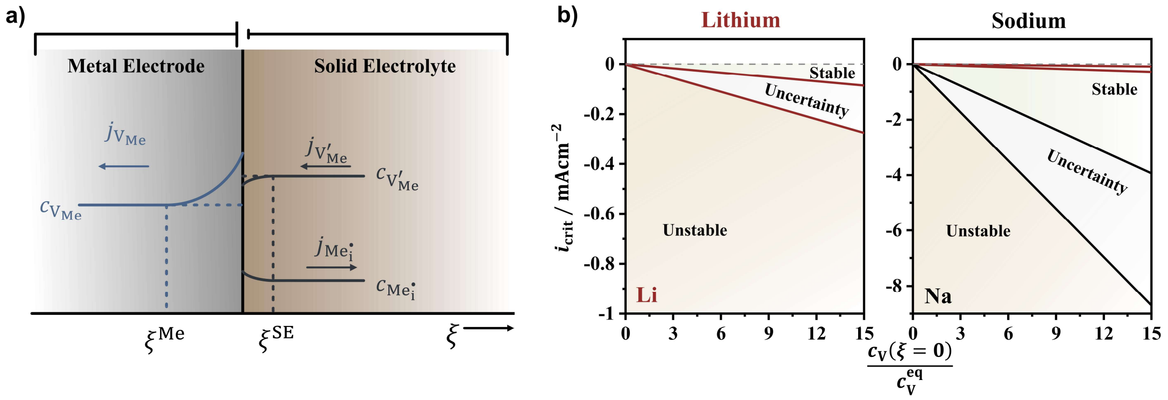

Figure 3: a) Schematic illustration of the vacancy relaxation model under steady state condition with a stable interfacial morphology developed by Schmalzried and Janek.[97] The relaxation zone of vacancy in the metal is marked by ξ^{Me}. The supersaturation of vacancies at the interface generates a vacancy concentration gradient $\nabla c_{V_{Me}}$ which results in a vacancy flux j_V into the bulk of the metal electrode. ξ^{SE} marks the relaxation zone of defects in the SE. Due to the high ionic conductivity, the concentration gradient of injected metal interstitials or depleted metal vacancies within the SE is significantly smaller. Therefore, the relaxation process in the SE

has no significant effect on the interfacial morphology. b) Critical current density i_{crit} as function of the supersaturation ratio for lithium (red lines) on the left side and sodium (black lines) on the right side. Representation for lithium bases on the data provided in reference [82]. The green highlighted area represents a parameter region where the interface remains morphologically unchanged (stable) during anodic dissolution, while in the brown highlighted region the morphology alternations would take place (unstable). The grey area indicates the uncertainty due to the vacancy relaxation time, degree of supersaturation and the determination of the equilibrium vacancy concentration. Figure modified from T. Krauskopf et al., ACS Appl. Mater. Interfaces 2019, 11, 15, 14463–14477.[82]

The interfacial kinetics can theoretically be determined by two different processes, which is either the relaxation of the point defects in the SE or the vacancy diffusion in the metal. Given the high ionic conductivity of SEs and assuming that the annihilation of vacancies is negligible, the interfacial kinetics will be mainly controlled by the vacancy diffusion in the metal. If the vacancy diffusion in the metal is in a local equilibrium with the vacancy injection rate, the interface will be morphologically stable during anodic dissolution. Based on the kinetic model by Schmalzried and Janek shown in **Figure 3a**, the flux of metal vacancies j_V across the interface that is exclusively driven by the vacancy concentration gradient $\nabla c_{\mathrm{V_{Me}}}$ can be estimated by

$$j_\mathrm{V} = \left(1 - \frac{c_\mathrm{V}(\xi = 0)}{c_\mathrm{V}^\mathrm{eq}}\right) c_\mathrm{V}^\mathrm{eq} \sqrt{\frac{D_\mathrm{V}}{\tau_\mathrm{V}}} \tag{2}$$

with D_V is the diffusion coefficient of vacancies in the metal, τ_V is the relaxation time for the vacancy equilibrium concentration, c_V^eq is the equilibrium bulk concentration of vacancies and $c_\mathrm{V}(\xi = 0)$ is the vacancy concentration at the interface. D_V can derived from the self-diffusion coefficient of the metal D_SD according to the following relation:

$$D_\mathrm{SD} = D_\mathrm{V} \cdot x_\mathrm{V}^\mathrm{eq} \tag{3}$$

Here x_V^eq is the molar equilibrium fraction of vacancies in the metal. The self-diffusion (of a metal atom) in a metal is mediated by vacancies. On the opposite, given the high molar fraction of metal atoms in a metal, the diffusion of a vacancy is not constrained by its mediation partner (metal atoms). Thus, D_V is much faster compared to D_SD, which is expressed in equation (3).

The equilibrium bulk concentration of vacancies c_V^eq can be obtained from the molar equilibrium vacancy fraction x_V^eq, which is given in equation (4) with G_V^F is the Gibbs energy of vacancy formation, k_B the Boltzmann constant and T the absolute temperature:[98]

$$x_\mathrm{V}^\mathrm{eq} = \exp\left(-\frac{G_\mathrm{V}^\mathrm{F}}{k_\mathrm{B}T}\right) \tag{4}$$

The critical current density i_crit for the anodic dissolution, at which a stable interfacial morphology is maintained, can be calculated according to equation (5), where $j_\mathrm{V,max}$ is the maximum vacancy flux originating from the vacancy concentration gradient $\nabla c_{\mathrm{V_{Me}}}$, z is the charge number of the ion and F is the Faraday constant:

$$i_{\mathrm{crit}} = z \cdot F \cdot j_{\mathrm{V,max}} \tag{5}$$

Based on this model, Krauskopf et al. estimated the critical current density i_{crit} for lithium as function of the supersaturation to be in the range of 10 – 100 µA·cm^{-2}.[82] A similar estimation for i_{crit} can also be stated for sodium, using the assumption of similar supersaturation ratio factors and the same τ_{V} of 5 s, as for lithium. By using the self-diffusion coefficient $D_{\mathrm{SD,Na}}$ and the Gibbs free energy for the vacancy formation $G_{\mathrm{V,Na}}^{\mathrm{F}}$, derived from first-principle calculations, the critical current density for sodium $i_{\mathrm{crit,Na}}$ lies in the range of 1 – 8 mA·cm^{-2}.[99,100] Consequently, the critical current density for sodium at room temperature is approximately two orders of magnitude higher than that of lithium at similar supersaturation ratios when no stack pressure is applied. This is attributed to the higher concentration and mobility of vacancies in sodium compared to lithium. However, it should be noted that due to the higher equilibrium bulk concentration of vacancies in the sodium, the supersaturation ratio for sodium is probably smaller compared lithium, and thus $i_{\mathrm{crit,Na}}$ might be overestimated.

In both cases, the high uncertainty of i_{crit} in **Figure 3b** is due to the unknown relaxation time of vacancies and the degree of supersaturation at the interface. In addition, the determination of the equilibrium bulk concentration of vacancies is also difficult. Moreover, the model does not consider the microstructure of the metal and therefore neglects different diffusion mechanisms, as will be elaborated in more detail in section 2.4. Also the model does not take into account interfacial effects and accumulation of vacancies at the interface, as a direct vacancy injection into the bulk metal is assumed.[56]

Seymour et. al. described the injection of a vacancy at a Me|SE interface from an energetically point of view by using a simplified bond-breaking model.[101] For a coherent Me|SE interface, the authors found a simple relation between the work of adhesion W_{ad} and the metal surface energy σ_{Me} on the tendency of a vacancy to be detached from a Me|SE interface, which are in line with first-principle calculations. Given the condition, $W_{\mathrm{ad}} \geq 2\sigma_{\mathrm{Me}}$, a vacancy at the Me|SE interface will migrate into the metal electrode, while it will remain at the interface when $W_{\mathrm{ad}} < 2\sigma_{\mathrm{Me}}$.[101] According to this relation, the lower surface energy of sodium ($\sigma_{\mathrm{Na}} = 0.230$ J m^{-2}) compared to lithium ($\sigma_{\mathrm{Li}} = 0.368$ J m^{-2}) suggests that less adhesion is required to energetically favor the migration of a vacancy from the interface into the bulk for sodium.[20]

When experimentally determined critical current densities (CCDs) are compared for sodium and lithium, a higher CCD is observed for sodium on average.[102,103] This is in line with the presented estimation based on the model from Schmalzried and Janek and the simplified model by Seymour et. al.. However, it should be noted that experimentally reported CCDs show a large variance, as the CCD strongly depends on the experimental parameters such as temperature, pressure, or the electrochemical test protocol.[104] Also the most reported CCDs are determine based on cell failure (short circuiting) and thus does not probe exclusively the anodic dissolution.

In contrast, morphological instabilities during anodic dissolution of lithium and sodium electrodes were observed already at lower current densities as estimated according to the vacancy relaxation model.[39,105] The occurrence and evolution of a morphological unstable Me|SE interface during anodic dissolution will be elaborated in the following section 2.2.2.

2.2.2 Formation of Pores and Evolution of the Interfacial Morphology

The following section elucidates the interfacial morphology between a parent metal and a SE as well as its evolution under an anodic current load. As described in the previous section 2.2.1, each oxidized metal atom at the Me|SE interface injects a vacancy in the near surface region, which can either migrate into the bulk metal or be annihilated at a place of repeatable growth. Especially for the migration of vacancies, calculations have shown that the detachment from the Me|SE interface has a considerable larger activation energy compared to vacancy migration in the bulk.[101] Thus, the adhesion at the Me|SE interface and the surface energy of the metal drastically influence the migration of vacancies. Nevertheless, if the applied external current i_{App} exceeds the vacancy flux, as indicated in equation (6),

$$i_{\mathrm{App}} > z \cdot F \cdot j_{\mathrm{V}} \tag{6}$$

vacancies will accumulate, which result in the formation of pores at the Me|SE interface. The formation of pores was experimentally confirmed for Li|SE and Na|SE interfaces and identified as the root cause for the interfacial deterioration.[39,82,106] With pores (which is, in essence, an "empty space") being present at the interface, the number of active sites is reduced and the current density locally increases at the remaining contact spots. The current focusing at these contact spots results in complete contact loss with the progression of dissolution. In principle, a proportional relation between the number of contact spots and the resulting potential response during a galvanostatic experiment is expected. Typically, an anodic dissolution experiment starts with a modest potential increase, which subsequently transitions into a plateau. The potential plateau is maintained for the major part of the dissolution time. Shortly before a state of complete contact loss is reached, a steep increase in the potential is observed.[82,107]

The course of the potential profile can be explained by the following process. As pores are formed at the Me|SE interface, they facilitate the diffusion of adsorbed metal atoms (further denoted as ad-atoms) along the surface of the pore walls. Hence, metal atoms can also be transported to the remaining contact area by ad-atom diffusion, which is much faster compared to the self-diffusion process (c.f. section 2.4.2). The ad-atom diffusion counteracts the contact loss at the interface leading to a potential plateau. However, if the transport of metal atoms is not fast enough, the contact area will further decrease until full contact loss.[56]

The resulting size, distribution and geometric shape of the pores cannot be predicted based on vacancy migration and surface diffusion processes. For instance, dissolution experiments at single crystalline copper electrodes indicated a relation between the pore structure and the dislocation density in the electrode.[95] Furthermore, a recent report characterized the pore structure at different current density and dissolved amount of lithium. The authors of this study have demonstrated that anodic dissolution at low current density results in the formation of a limited number of small pores during the initial dissolution stage, which subsequently evolve into a few larger pores. In contrast, at higher current density, the initial number of pores was significantly higher, while a porous interfacial morphology was observed following the attainment of full contact loss.[108] The resulting pore structure is of high relevance as it determines and affects the cycling behavior of the metal electrodes and thus the battery performance.

Although the interface between two solids seems to be rigid, different equilibration processes can result in an alternation of the interfacial morphology, which in turn affects the overall interfacial kinetics. For instance, the pore geometry can be smoothened due to the previously described ad-atom diffusion driven by the equilibration of the surface energies.[56] Also effects like electrochemical "Oswald ripening" can lead to a rearrangement of the pore structure at the interface.[109] The formation of pores is accomplished with a mechanical "weakening" of the interfacial structure. Hence, the local mechanical stress of the remaining "pillars" increases until a critical limit is reached at which plastic deformation may occur. Thus, the contact area is enlarged and the electrode can further be dissolved. Such phenomena lead to an oscillation in the potential profile and have been reported for Ag|AgX systems.[96,110] Despite the rarity of investigations of such phenomena in the field of battery research, oscillations have been observed at Na|SE interfaces within a pressure range of 0.1 to approximately 1 MPa.[111] Also time-resolved EIS revealed a dynamic behavior of the interface morphology of a dissolved SME pointing towards an equilibration phenomenon.[39] A reliable prediction of pore formation, its geometry as well as its evolution is thus of paramount importance to ensure a stable cell operation. While this section addresses the processes occurring at the Me|SE interface that alter its morphological structure, the following section (2.2.3) focuses on possibilities to reduce or suppress pore formation.

2.2.3 Strategies to Mitigate the Pore Formation during Anodic Dissolution

In this section, possibilities to reduce or suppress the formation of pores at a Me|SE interface are described. As elaborated in section 2.2.2, pores are formed by the aggregation of vacancies. In principle, the aggregation of vacancies can be avoided by increasing the transport rate of vacancies towards the bulk of the electrode (or the transport of matter towards the interface). According to equations (2) and (3), an increase of the vacancy flux can be achieved by tuning the diffusion rate in the electrode material. As the diffusion in matter is typically an activated process, the diffusion rate can be increased by elevating the temperature. However, higher operation temperatures are not always possible for battery applications, especially for small and mobile devices.

Another prominent possibility to enhance the diffusivity in the metal electrode can be achieved through alloying. For instance, a higher diffusion rate of lithium in lithium-magnesium alloys has been reported.[105] A comparable relation has been observed in the case sodium-tin alloys, which shows an improved dissolution performance.[112] The enhanced diffusivity originates from different lattice parameters and binding energies in the alloy which lowers the migration barrier.[113] However, the exact explanation why alloys shows an improved diffusivity is not yet investigated in detail. An aspect which is often not considered is the influence of the microstructure on the diffusion process.[114] As will be discussed in section 2.4.2, different diffusion processes determine the overall diffusion rate in a metal.

In addition to modify the diffusion rate, the formation of pores can be prevented by promoting mass transport to the interface. The high homologous temperature of sodium ($T_{\mathrm{H,Na}} \approx 0.8$) facilitates the climb of dislocations.[115] Hence sodium shows a pronounced creep behavior at room temperature, where the strain rate $\dot{\varepsilon}$ is predominantly given by the power-law creep relation by:[116]

$$\dot{\varepsilon} = A_c \sigma^m \exp\left(-\frac{Q_c}{RT}\right) \tag{7}$$

with A_c is a material specific creep parameter, σ is the external stress (applied stack pressure), m is the power-law creep exponent, Q_c is the activation energy for dislocation climb, and R is the molar gas constant. Accordingly, an increase of the stack pressure elevates the strain rate and hence the mass transport to the interface.[117] The positive effect of stack pressure on maintaining interfacial contact was also confirmed experimentally. By increasing stack pressure, higher current densities at the Me|SE interface were achieved, as pore formation was suppressed through the mechanical deformation of the metal electrode.[107,118] However, the influence of the applied stack pressure on the interfacial contact is complex. For instance, surface roughness leads to changes in pressure distribution at the interface, which subsequently gives rise to localized discrepancies in mechanical deformation. Consequently, modifications in the local contact area influence the mechanical deformation and is thus time-dependent.[119] Moreover, the mechanical properties depends on the aspect ratio, as adhesive forces (hydrostatic stress) at the CC|Me and Me|SE interfaces increase the yield strength of the metal.[115,120] While stack pressure represents an effective strategy for maintaining interfacial contact, it is not without limitations. For example, at exceedingly high stack pressures (in the range of several tens of MPa), the malleable nature of alkali metals can cause them to penetrate the SE, resulting in short-circuiting.[121]

2.3 Reservoir-free Sodium Solid-State Batteries

In the following chapter, the concept of reservoir-free solid-state batteries is elaborated. Besides their working principle, their advantages and current challenges of the cell concept are discussed. While the dissolution process at the Me|SE interface is described in the previous chapter, the electrodeposition of an alkali metal at a solid|solid interface is set into focus in this chapter, as it is central for the reservoir-free cell concepts. Since the knowledge about the electrodeposition at solid|solid interfaces is scarce for sodium, the results and concepts for lithium electrodeposition are summarized and discussed with respect to their applicability to sodium.

2.3.1 The Working Principle of Reservoir-free Solid-State Batteries

The implementation of a sodium metal electrode in solid-state batteries requires the preparation of a sodium electrode.[29] Different techniques are conceivable in order to process a sodium metal electrode that interfaces an SE or a separator. Besides the processing of a sodium foil by mechanical extrusion of an ingot, a sodium electrode could also prepared by vapor deposition or by melt processing e.g. dip coating.[122] However, these processing techniques requires the handling of the highly reactive sodium metal during cell manufacturing. Another possibility to generate a SME in SSBs is by electrodeposition.[123,124] Instead of assembling the SME during cell production, only a CC is attached to the SE on the negative electrode side, as shown on the left side in **Figure 4**. During the first charge, the SME is formed in situ by extracting enclosed sodium ions from the positive electrode (cathode active material) and electrodepositing them at the CC|SE interface (see **Figure 4** right side).[124] This approach works for most cathode active materials (CAM) such as layered oxides, polyanion compounds or Prussian white analogs, as they are synthesized in a discharged, meaning sodiated, state.[125] This concept is often referred to as “anode-free” in literature, as the cell is assembled without an “anode active material”.[126] However, the term "reservoir-free cells" (RFCs) is more accurate, as it highlights the absence of a sodium reservoir and prevents the misinterpretation of the absence of an "anode" in a battery. The feasibility of this cell concept was first demonstrated in a thin film battery based on a Cu|Li|LiPON|Li_xCoO_2 stack by Neudecker and co-workers.[127] The first electrodeposition of sodium metal at a CC|SE interface has been shown in the second publication of this doctoral thesis, while the first reservoir-free sodium SSB has been recently reported, demonstrating the feasibility of the cell concept.[40,128] The advantages and challenges of RFCs are shortly summarized in the following section 2.3.2.

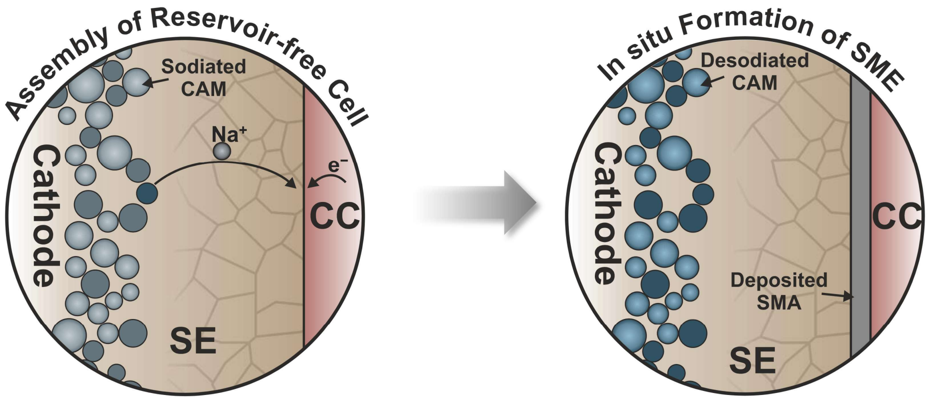

Figure 4: Schematic illustration of the reservoir-free cell concept. Instead of introducing an SME during cell assembly, the SME is formed in situ through electrodeposition of sodium ions stored in the CAMs at the CC|SE interface during the first charge.

2.3.2 Advantages and Challenges of RFCs

This section provides a concise overview of the advantages and challenges associated with RFCs. In addition to the economic perspective, the cell concept is also examined from the physicochemical point of view.

I. Advantages

As described in the previous section 2.3.1, the SME in RFCs is formed by electrodeposition of sodium extracted from the CAM on a CC during the first charge. Hence, no additional sodium metal reservoir is required at the negative electrode during cell assembly and the energy density can be further improved compared conventional SIBs.[128] Accordingly, the volumetric and gravimetric energy densities on the cell level (excluding the cell casing) are improved by roughly 17 % and 6 %, respectively, when the SME is formed through electrodeposition instead of added during cell fabrication (see section 6.1 for details on the calculation). Theoretically, the energy density can be further enhanced when the density of the SE is reduced, for example by replacing NZSP, e.g., with a closo-borate $Na_2B_{12}H_{12}$.[20]

The primary benefit of RFCs is to circumvent the handling and processing of sodium metal during cell manufacturing, as the following issues are avoided. First of all, the energetically intensive production of sodium metal can be prevented.[124] Sodium metal is normally produced by electrolysis of molten sodium chloride. However, to obtain a high-purity grade, additional distillation processes of the raw sodium metal are requried.[129] Secondly, the processing of a sodium foil by shaping an ingot is not necessary. Typically, an areal capacity of 5 mAh cm^{-2} is targeted for commercial battery applications which equals an electrode thickness of roughly 45 μm for sodium. The soft nature and viscosity of sodium pose a challenge for the rolling and cutting process.[38] Thirdly, the high reactivity of sodium towards moisture and oxygen requires processing in an inert atmosphere to minimize degradation or formation of a passivation layer. In contrast to lithium, an inert nitrogen atmosphere would be sufficient for sodium.[80] Nevertheless, the necessary infrastructure for the production under inert atmospheres (e.g., dry rooms or gloveboxes) in large-scale production lines is both complex and costly.

The circumvention of sodium metal during the fabrication of cells not only rationalizes the production process but also substantially reduces the associated material consumption and thus the costs. In addition, the synthesis of the cathode active materials often requires only cheap raw materials such as sodium carbonate.[38] Also, a high-purity of the electrodeposited sodium metal electrode can be expected due to the single ion conduction of the SE.[130] This makes RFCs an attractive cell concept to realize sodium SSBs.

II. Challenges

Besides the advantages of RFCs, the concept possesses also challenges. Given that RFCs operate without an excess of alkali ions, any parasitic reactions such as SEI formation on the Me|SE interface, ultimately result in a reduction in capacity.[124] This encompasses the formation of "dead" alkali metal, which arises from filament or dendrite growth that detach from the negative electrode upon cycling. But also contact loss due to volume expansion during cycling causes a decay in the capacity, particularly in the cathode composite.[131] To counteract the capacity fading, two ways are possible. First, an excess of alkali ions could be added to the cells by using a P/N ratio above unity. Second, the columbic efficiency of each cycle could be improved by suppressing side reactions and contact loss. While the first attempt would be efficient to compensate a capacity fading in the first hundred cycles, it also decreases the energy density of the cell.[124] The second attempt would be more reasonable, however, to compete with current battery technologies in terms of cycle numbers and energy density, a Coulomb efficiency close to 100 % would be necessary for RFCs.[124]

Another challenge arises from the necessity of stack pressure during operation to maintain the physical contact within SSBs and in particular in RFCs.[14] Controlling the pressure in SSBs is not trivial, as the thickness of the cell stack varies in the range of several tens of micrometers upon cycling. This is particularly important for RFCs, where the relative thickness variations are even more pronounced. While on the laboratory-level different cell casings exist, which compensate the volume change of the cell, suitable cell designs and pressure management systems on an application-orientated level are still pending.

The initial formation of the alkali metal electrode through electrodeposition is one of the key steps for the feasibility of RFCs. Ideally, a dense and uniform metal electrode is required, as illustrated in **Figure 4**. Various processes take place during the electrodeposition at a CC|Me interface, which affect the resulting electrode morphology and hence their electrochemical performance. Given this central role for the working principle of RFCs, the cathodic deposition of a parent metal at a solid|solid interface is discussed in the following section.

2.3.3 Cathodic Deposition of Alkali Metals at a Solid|Solid Interface

The process of nucleation and subsequent growth of a metal on a foreign or native substrate driven by an external electric field is denoted as electrocrystallization, electrodeposition or cathodic metal deposition.[132] The cathodic deposition of a metal at an electrode in an LE has been the subject of extensive and different nucleation and growth mechanism have been proposed.[132] In contrast, the knowledge about cathodic deposition at CC|SE interfaces is rare, as the buried nature of the interfaces complicates the characterization.[56] The analysis of the nucleation process is particularly difficult to carry out using analytical microscopy techniques due to the nanoscale dimensions of the nuclei and the brief time span of the process. As a result, often only the early growth process and the morphological evolution is captured by microscopic techniques.

Depending on the material system and deposition conditions various morphological phenomena of as-deposited metals at a CC|SE interface have been reported so far.[56] One of the most prominent morphologies observed during the cathodic deposition is the growth of whiskers which have been first reported for silver ion conductors. For example, the growth of whisker arrays has been observed for planar silver electrodes,[133] while at microelectrodes the morphology depends strongly on the applied current.[134,135] The growth of whiskers has also been observed at other SE substrates, such as LLZO[136] or NZSP[137] by using microelectrode setups but also at CC|SE interfaces, such as stainless steel|Li_2S-P_2S_5,[138] Cu|LLZO,[139] Cu|LiPON,[140] or Cu|NZSP.[40]

Besides the growth of whiskers, also lateral dendritic growth along the surface of an SE has been observed on LLZO or silver bromide.[81,134] The phenomenon is rarely investigated and only occurs at very high local current densities. However, in a joint collaboration between Justus-Liebig University and Research Center Jülich, the lateral growth of sodium on NZSP was analyzed, revealing that this phenomenon can cause short circuiting in symmetrical Na|NZSP|Na cells.[137] Additional micromanipulator experiments demonstrated that the tendency of lateral growth on NZSP is higher compared to LLZO at comparable experimental conditions.[81,137] Hence, the occurrence of lateral dendritic growth is more severe for sodium, especially when high charging rates are required.

Apart from cathodic metal deposition along the surface and out of the SE substrate, the metal can also grow into the SE, which is referred to as dendrites. Dendrite growth into the SE can be caused by current focusing and a non-uniform ion flux at the interface, originating, for example, from insufficient contact between the electrode/CC and the SE, surface contaminations or surface defects. In polycrystalline SEs, also the different conductivity behavior of grain boundaries (GBs) could promote an inhomogeneous ion flux and thus preferential spots for cathodic deposition.[141] However, the formation and propagation of dendrites is quite complex and different mechanisms and reasons are proposed in literature.[142] The interested reader is therefore referred to the review article from Krauskopf et al. about the degradation mode I.[56] In short, the local deposition of the metal, e.g., at a surface flaw causes mechanical stress, which could initiate the formation of cracks. Once a crack is formed, preferential deposition at the metal tip results in a Poiseuille pressure and propagates the crack. Hence, with proceeding deposition the crack propagates through the SE, resulting ultimately in cell failure.[142] However, surface defects do not automatically result in dendrite formation. When the redistribution of the deposited metal through creep and vacancy transport is faster compared to the metal deposition rate, a morphologically stable interface can be maintained. On the opposite, a faster deposition rate results in a pile up of deposited metal and unstable growth which could initiate cracks in the SE.[143]

The formation of dendrites can also originate from metal nucleation inside the SE during cathodic deposition which is referred to as the degradation mode II in literature. This degradation mode was reported in high temperature Na/S-batteries using a BASE as separator.[144] The root cause for internal sodium nucleation was attributed to a partial electronic conductivity in the BASE where GBs and intergranular phases are probably involved. A similar correlation was observed when comparing the partial electronic conductivity and the critical current density of various lithium ion conductors.[145,146] Nevertheless, the underlying mechanism is still under debate. In a collaboration between Justus-Liebig University and Karlsruhe Institute of Technology, the sodium nucleation inside BASE was confirmed by in situ TEM. By analyzing the microstructure of the BASE and correlating the electrical field distribution, a simplified model is proposed to identify preferred nucleation spots. Accordingly, the formation of sodium filaments was preferentially observed at spots where the ion migration across the GB is blocked.[147] At such ionic bottlenecks, the chemical potential of sodium μ_{Na} can exceed the standard chemical potential of sodium μ^0_{Na} and initiate nucleation.[148] Further research is necessary to gain a fundamental understanding of the degradation mode II.

Besides the different growth phenomena during cathodic deposition also the lateral distribution of the deposited alkali metal is important, as a dense and uniform metal layer is desired for RFCs. The distribution and number of the formed lithium “nuclei” at a Cu|LiPON interface was indirectly examined by visualizing the morphological alternations of the thin film copper CC caused by the grown lithium underneath.[140,149] An increase of the current density results in a significant increase in the number of formed lithium particles, whereas the nuclei number decreases at elevated temperatures. In addition, the particle size and shape also changed.[149] At low current densities and temperatures, the formation of needle-like structures and large particles is observed. At high current densities and elevated temperatures, the formed particles have a spherical shape and are smaller in size. Similar results and trends were observed for polycrystalline LLZO.[139] Furthermore, for both systems, the nucleation overpotential η_{Nuc}, which is given by the difference between the initial potential drop and the potential plateau during the growth stage, increases with applied current density. This fits well with the observed size and number of the formed lithium particles, as η_{Nuc} is inverse proportional to the critical nucleation radius according to the classical theory for homogeneous nucleation.[150] In view of achieving a uniform coverage during cathodic deposition, higher current densities are beneficial. Practically, also pulsed deposition protocols might be applicable, as prolonged high current densities could trigger dendritic growth as described above.[139]

The early growth stadium of sodium at a solid|solid interface was analyzed on a nanoscale-level by in situ TEM, revealing particles with a polyhedral shape and oriented growth behavior.[151,152] Similar results were observed for the cathodic deposition at a Cu|NZSP interface, where sodium was deposited only at a contact spot between CC and SE (c.f. section 3.2), highlighting the importance of the initial CC|SE interface preparation.[40,128]

Ideally, the initial CC|SE interface should ensure an intimate physical contact with a low adhesion energy between CC and SE, as the nucleation process requires the separation of the interface.[153] A high adhesion energy would impede the nucleation process by increasing the critical nucleation radius. The nucleation and separation of the CC|SE interface causes mechanical stress which could trigger different scenarios. First, the SE might be damaged by crack formation or spallation close to the interface as reported for the Cu|NZSP interface.[40] On the opposite, whisker growth can penetrate the CC, as often reported when using thin film CCs.[136,139,140] Second, vertical whisker growth can separate the CC|SE interface, resulting in gap formation and decrease of the electrochemically active contact area, as observed at Cu|NZSP or Cu|Li_6PS_5Cl interfaces.[154] Third, the mechanical stress plastically deforms the deposited metal, which expands laterally and delaminates the CC from the SE.[153] The latter scenario would be most beneficial for RFCs, as it facilitates lateral growth. Another possibility to enhance the lateral distribution is by applying a stack pressure, as demonstrated by Kazyak et al. for lithium deposition at a Cu|LLZO interface.[155] In contrast, no substantial enlargement of the contact area was observed for sodium deposition at a Cu|NZSP interface at elevated stack pressures, which might be due to different mechanical or frictional behavior (c.f. section 3.2).[40] The different phenomena and possibilities of metal growth at a CC|SE interface are summarized in **Figure 5**.

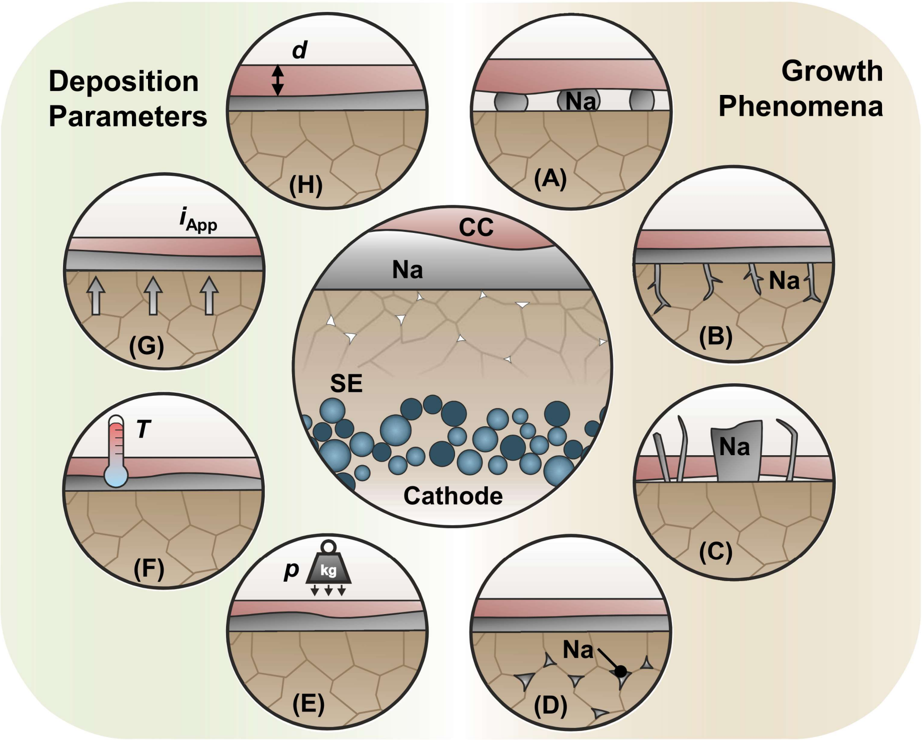

Figure 5: Schematic illustration of cathodic deposition of an alkali metal at a Me|SE interface. An optimal deposition of a dense and uniform SME is depicted in the center of the figure. Different growth phenomena are illustrated such as (A) island growth, delamination and gap formation, (B) dendrite formation starting from the electrode, (C) whisker growth and penetration of CC, and (D) sodium nucleation inside the SE are shown on the right side of the illustration. Parameters that affect the cathodic metal deposition are illustrated on the left side, including (E) stack pressure p, (F) temperature T, (G) applied current density I, and (H) thickness of the current collector. Figure modified from T. Fuchs, Morphological Challenges at the Interface of Lithium

Metal and Electrolytes in Garnet-type Solid-State Batteries. Dissertation, Justus Liebig University, Gießen, 2022.[156]

In recent years, various interlayer and seed layer concepts have been proposed as potential means of improving the lateral distribution and achieving uniform coverage of an electrodeposited lithium metal electrode in RFCs. In particular, by introducing a (amorphous) carbon-based interlayer with embedded silver nanoparticles, a dense and uniform lithium metal electrode between the interlayer and the CC is formed.[157] Although a remarkable cycling stability is achieved, the underlying mechanism is still under debate. Bruce and co-workers found that the graphite material is first lithiated electrochemically, followed by lithium deposition and chemical reaction with silver forming an Ag-Li alloy. Accordingly, the graphite is the electrochemically active species and not the silver.[158] By comparing graphite with an amorphous carbon interlayer, a more homogeneous and selective deposition of lithium between the interlayer and the CC was obtained for the latter one. This is explained by the isotropic lithium transport in an amorphous carbon compared to graphite.[159] In contrast, Ceder and co-workers suggest that enhanced deposition performance is derived from the formation of a Li-Ag alloy.[160] The huge volume expansion during alloy formation extrudes the lithium metal out of the interlayer towards the CC, due to a stronger adhesion between interlayer and SE. The volume expansion during alloy formation might also play a role in the working principle of seed layer concepts. Here, alloy nanoparticles are placed in-between the CC and SE to enhance the nucleation and growth of the metal electrode.[161] Nevertheless, the impact of interlayer and seed layer concepts on sodium systems have not yet been extensively studied, providing an opportunity for further characterization.[162]

2.4 The Role of Microstructure in Metal Electrodes

The previous chapters discussed the importance of a morphological stable Me|SE interface to ensure a reversible operation of an alkali metal electrode upon cycling. In particular, in section 2.2.4, different possibilities to suppress pore formation during anodic dissolution are elaborated, which are mainly based on optimization of the mobility of vacancies in the metal or by increasing the mass transport towards the electrode, e.g., by increasing the stack pressure. Both properties also play a crucial role during cathodic metal deposition, as outlined in section 2.3.3. As is generally known in the field of metallurgy, the microstructure of a material has a significant impact on its mechanical properties and transport processes within the material itself.[56] Therefore, this chapter focuses on the relationship between the microstructure of an alkali metal electrode and the electrochemical performance in SSBs. Starting with a brief definition of the term *microstructure*, the current state of research in the battery community is briefly summarized in section 2.4.1. Furthermore, the relationship between the microstructure and transport by diffusion as well as the mechanical properties are elaborated in section 2.4.2 and 2.4.3, respectively.

2.4.1 The Microstructure of Alkali Metal Electrodes

Most materials such as metals, minerals, or ceramics are polycrystalline. The grains in a material are rarely randomly orientated according to the crystallographic orientation and distribution. This means that a pattern of certain grain orientation or tendency of preferred grain orientation is often found, which is referred to as *texture*.[163] However, texture only describes an average fraction of preferred grain ordination in a given volume. In contrast, the term *microstructure* includes additionally the spatial location of grains. Hence, the microstructure is the collection of crystallinity features in a material, such as, grain size, grain orientation, grain boundaries, phases, dislocations, strain and interfaces, which determine the material properties.[164,165] Besides TEM and synchrotron-based techniques, EBSD is the most common technique to analyze the microstructure of different materials. For a detailed description of the working principle of the mentioned techniques, the reader is referred to Ref [164]. In short, for EBSD analysis, a primary electron beam is focused on a crystalline sample at an incident angle of 70°. First, the electron beam is quasi-elastically scattered over a wide angle within the sample and diverges from a point source below the sample surface. The diverged electrons impinge on different crystal planes in all directions and form paired large-angle cones (also known as Kikuchi cones) whenever the Bragg condition is satisfied.[163,166] The Kikuchi cones represent a single lattice plane, which is detected by a phosphorous screen. By scanning the electron beam along a sample surface, crystallographic information is obtained in a lateral dimension, which allows the analysis of the material microstructure.

The microstructure of alkali metals has been rarely investigated in the literature and is often not considered in the field of battery research, despite the fact that a potential influence of the microstructure on electrochemical performance has been postulated.[167–169] The work by Singh and Fuchs and co-workers on the electrochemical dissolution behavior of different heat-treated lithium metal foils demonstrated the significant influence of different metal grain sizes on the battery performance, and motivated a detailed characterization of the electrode microstructure.[94,170] However, the sample preparation and characterization of the alkali metal microstructure is extremely challenging. The high reactivity of the alkali metal towards residual moisture or oxygen causes a surface passivation layer that drastically complicates the microstructural analysis by EBSD or TEM.[171] Therefore, only few reports exists that visualize the microstructure of lithium metal foils.[171,172] The third publication of this doctoral thesis provides a reliable protocol to characterize not only the microstructure of foils, but also to visualize the microstructure of electrodeposited alkali metals at solid|solid interfaces.[41] In particular, for the first time, the microstructure of sodium has been analyzed and the microstructural evolution during cathodic deposition as well as anodic dissolution has been investigated for both, sodium and lithium metal electrodes (c.f. section 3.3).

2.4.2 Effect of Microstructure on Self-Diffusion in Metals

At thermal equilibrium, vacant lattice sites are the dominating atomic defects in metals. Accordingly, the dominating mechanism for self-diffusion in a metal matrix is mediated by vacancies. An atom diffuses by transition into a neighboring vacant site. Consequently, atoms traverse a crystal by engaging in a series of site exchanges with vacancies that are intermittently present in their vicinity. The exchange jump rate Γ of vacancy-mediated jumps of an atom into a vacant site lattice is given by the molar equilibrium vacancy fraction x_V^eq and the exchange rate ω_V:[173]

$$\Gamma = \omega_\mathrm{V} \cdot x_\mathrm{V}^\mathrm{eq} = v^0 \cdot \exp\left(-\frac{G_\mathrm{V}^\mathrm{F}}{k_\mathrm{B}T}\right) \cdot \exp\left(-\frac{G_\mathrm{V}^\mathrm{M}}{k_\mathrm{B}T}\right) \tag{8}$$

Considering equation (4) and replacing the exchange rate ω_V by equation (9), it becomes evident that the exchange jump rate of a vacancy depends upon on the free enthalpy of vacancy formation G_V^F and the free enthalpy of vacancy migration G_V^M multiplied by the attempt frequency v^0.

$$\omega_\mathrm{V} = v^0 \cdot \exp\left(-\frac{G_\mathrm{V}^\mathrm{M}}{k_\mathrm{B}T}\right) \tag{9}$$

The self-diffusion coefficient D_SD for a monovacancy mechanism in an elemental crystal is a product of the exchange jump rate Γ, a correlation factor f, a geometric factor g and the lattice parameter a.

$$D_\mathrm{SD} = f \cdot g \cdot a^2 \cdot \Gamma \tag{10}$$

According to equations (8) and (10), D_SD depends on the temperature and often follows an Arrhenius-type behavior. Typically, D_SD is strongly affected by the temperature and varies by several orders of magnitude. Often an upward curvature in the Arrhenius plot is observed, when the temperature approaches the melting point T_m of the metal. Although monovacancies are the most prevalent defect in metals, the probability of divacancy formation increases with elevating the temperature. As a rule of thumb, when approaching a temperature $T \approx 0.66\ T_\mathrm{m}$, diffusion mediated by divacancies also contributes substantially to the overall diffusion in the metal. Hence, the total diffusivity is then given by the sum of monovacancy and divacancy diffusion contribution. For example, in the case of silver, the divacancy concentration at $T \approx 0.66\ T_\mathrm{m}$ is roughly 10 %, while it is negligible below $T \approx 0.5\ T_\mathrm{m}$.[173,174] In particular, in face-centered cubic metals, divacancies exhibit higher mobility compared to monovacancies, rendering them a more effective diffusion vehicle. An upward curvature in the Arrhenius plot is also observed for sodium and the formation of divacancies at room temperature is also likely, as the homologous temperature of sodium $T_\mathrm{H,Na} \approx 0.8$.[100]

Apart from the temperature, the self-diffusion in a metal also depends on the pressure according to the pressure-dependency of the free enthalpy of vacancy formation and migration (see equation (8)). Compared to the temperature, the effect of pressure is less pronounced, and usually the diffusivity decreases by less than a factor of ten when the external pressure is altered by about 1 GPa.[173] At such pressure region, sodium would already be plastically deformed. It can thus be concluded that the effect of stack pressure on the self-diffusion of sodium is negligible, given the fact that the expected stack pressure for battery applications falls within the range of a few MPa.[173,175]

In the previous paragraphs, only atomic point defects, such as vacancies, have been considered as diffusion vehicles for self-diffusivity in metals. However, metals are mostly polycrystalline and consist of structural features where the jump rate is enhanced along dislocations, grain boundaries, or along free surfaces.[176] While atomic migration through the lattice is characterized by a diffusion length of $\sqrt{Dt}$, the migration along fast diffusion pathways is much faster, as schematically illustrated in **Figure 6a.**

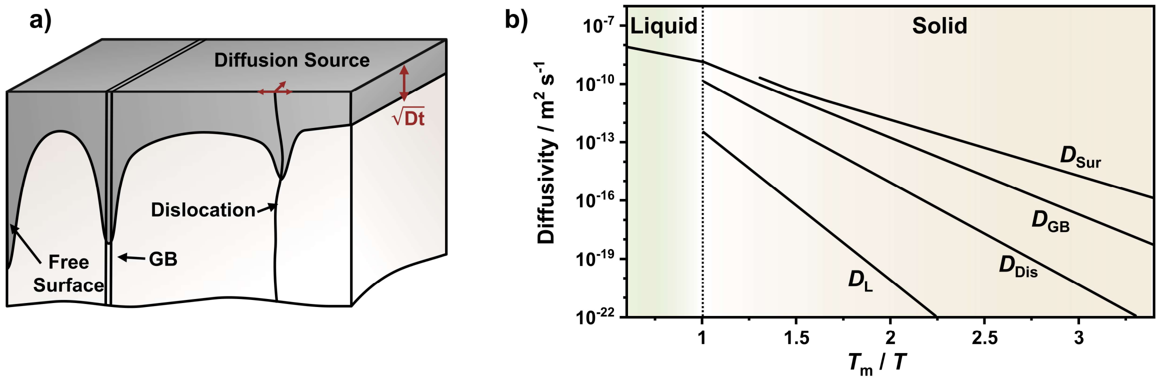

Figure 6: a) Sketch of fast diffusion pathways in a polycrystalline metal, including dislocations, grain boundaries and free surface. b) Schematic illustration of the temperature dependence of various high diffusivity pathways in a metal. The diffusivity in the lattice is denoted by D_L, while D_{Dis}, D_{GB} and D_{Sur} denote the diffusivity along dislocations, grain boundaries, and free surfaces, respectively. The data presented represent an average of different metals according to reference [173]. Figure modified from H. Mehrer, Diffusion in Solids: Fundamentals, Methods, Materials, Diffusion-Controlled Processes, Springer, Springer Series in Solid-State Sciences, Volume 155, 2007.[173] Copyright © Springer-Verlag Berlin Heidelberg. Reproduced with permission from Springer Nature.

Figure 6b illustrates the diffusivity of various diffusion pathways in an average polycrystalline metal across different temperatures. The atomic migration through the lattice has the lowest diffusion coefficient D_L, as the atomic migration is subject to the most significant constraints and exhibits the largest activation enthalpy ΔH. By increasing the disorder in a dislocation core and having a less packed structure in GBs, the atomic motion is further enhanced. Free surfaces exhibit the fastest diffusivity, as atomic motion is mediated not only by vacancies but also by ad-atoms. The respective hierarchy for high diffusivity pathways in comparison to lattice diffusion, as well as the corresponding activation enthalpies, are presented in equations (11) and (12).[173]

$$D_\mathrm{L} \ll D_\mathrm{Dis} \leq D_\mathrm{GB} \leq D_\mathrm{Sur} \tag{11}$$

$$\Delta H_\mathrm{L} > \Delta H_\mathrm{Dis} \geq \Delta H_\mathrm{GB} > \Delta H_\mathrm{Sur} \tag{12}$$

In general, the atomic motion along dislocations and GBs is several orders of magnitude faster compared to lattice diffusion (see **Figure 6b**). This difference is even more pronounced at lower temperatures, due to the different activation enthalpies. Additionally, the diffusivity along GBs also depends on their type, e.g., twisted or rotated GBs as well as high-angle or low-angle GBs. Theoretical calculations for different GBs in lithium metal revealed a difference of a factor of ten for various GB types. Accordingly, the overall (self)-diffusivity in a polycrystalline material depends strongly on the dislocation and GB density and their different types.[173] Hence, the microstructure of metal electrodes is of great interest for their practical application in SSBs. For example, theoretical calculations for lithium metal have shown that a grain size in the order of 1 µm (and thus a high fraction of GBs) is required to meet the current performance goals for SSBs.[177] In contrast, a typical grain size for a lithium foil is roughly 150 µm.[94] To meet the given performance goals, an optimized metal microstructure is required. Although sodium has a higher overall diffusivity, its grain size is even larger than that of lithium.[41] Thus, the necessity of a tailored microstructure to achieve the performance goals is likely for SMEs.

2.4.3 Effect of Microstructure on Mechanical Properties

A major challenge for the reversible operation of an SME arises from contact loss at the Me|SE interface upon cycling, e.g., by the formation of pores during anodic dissolution. One strategy to maintain interfacial contact is to deform the metal electrode mechanically by applying a stack pressure (c.f. section 2.2.3). Consequently, the mechanical properties of the metal electrode are crucial because they determine at which external stress (stack pressure) mechanical deformation occurs.

In principle, the deformation of a material can be classified as either elastic or plastic.[116] If the applied external stress exceeds the yield strength of a material, it will undergo plastic deformation by the movement of dislocations. Besides defect concentration, stress rate, and impurity concentration, the yield strength also depends on the microstructure, e.g., the grain size.[56,170] If the grain size decreases, the density of GBs in a given volume increases. However, GBs act as a barrier to dislocation movement. High stresses are required for a dislocation to cross a GB due to the random orientation of the slip planes of adjacent grains.[170] Therefore, dislocations will accumulate at GBs. The higher the density of GBs (or, the smaller the grain size), the greater the restraint on dislocation movement and hence the strength of the material. This phenomenon is empirically described by the Hall-Petch relationship.[170]

Plastic deformation of a material can also occur due to creep, where in principle two different creep mechanisms are present in a metal, namely power-law creep (see equation (7) in section 2.2.3) or diffusional creep.[116] Depending on the microstructure, temperature and applied external stress, different creep mechanisms dominate the plastic deformation. In general, at low stresses, diffusional creep is rate determining, while at high stresses, power-law creep via dislocation climb is the dominant mechanism.[178] In particular, the strain rates of diffusional creep depend on the grain size as well as on the diffusivity in the material. At low temperatures (and stresses), the motion of atoms is mainly mediated by the lattice, which is referred to as Nabarro-Herring creep.[170] At elevated temperatures, the net flux of atoms is predominantly mediated by diffusion along GBs, which is referred to as Coble creep.[170,178] Accordingly, the types of GBs as well as the grain size and defect density in the material affect the plastic deformation. In contrast, the strain rate for power-law creep is independent of the grain size but depends on the mobility of dislocations.

Apart from plastic deformation, the microstructure affects the elastic properties of alkali metals. For instance, the orientation-dependent characterization of the elastic response of lithium revealed a strongly anisotropic elastic behavior.[172] As sodium metal exhibits the same space group, an anisotropic elastic behavior is likely.[179,180]

Sodium exhibits a yield strength of around 0.2 – 0.3 MPa and power-law creep through dislocation climb via lattice diffusion is the predominately creep mechanism for time-dependent plastic deformation at room temperature.[115,181,182] Accordingly, the effect of grain size and microstructure on the plastic deformation of sodium would be negligible in view of much higher applicable stack pressures in SSBs. However, the mechanical properties of sodium are often investigated by using ingots with dimensions in the mm or cm range, while properties such as the yield strength can drastically increase at smaller lengths and geometries.[183] In view of metal films and lower temperatures, diffusional creep might play a role for the plastic deformation of the SME and thus also its microstructure.[180] Another aspect which has not yet been addressed in literature is, that the microstructure of a metal electrode alters during electrodeposition by the motion of GBs (see section 3.3).[41] Thus, the mechanical properties of the metal electrode would alter during cycling.

The application of stack pressure is a viable strategy to maintain the interfacial contact at the Me|SE interfaces in SSBs also for practical battery applications.[14] Accordingly, the mechanical properties of the metal electrode as well as possible changes are of central interest to ensure a stable battery operation in practice.

3 Results

At the beginning of this doctoral thesis in 2019, a fundamental understanding of the kinetics at the Na|NZSP interface was very limited. While the interface as such had been addressed in several reports, there was a lack of analysis regarding degradation phenomena, morphological evolution during metal dissolution and deposition, and charge transfer processes. Additionally, the microstructure and texture of the SME and their influence on the microscopy processes and interface morphology had not been considered. Therefore, the objective of this doctoral thesis was to study the Na|NZSP interface systematically by characterizing the SME during cycling in terms of the interfacial kinetics, morphological evolution, and microstructure.

The first publication of this doctoral thesis contributes to a better understanding of the Na|NZSP interface and provides a systematic approach to separate and quantitatively compare different microscopic processes regarding the performance limit. Moreover, the morphological evolution of the SME was characterized under anodic current load. Publication II deals with the electrodeposition of sodium at a Cu|NZSP interface and the effect of current density and stack pressure on the resulting morphological evolution of the sodium metal. Publication III targets the microstructural analysis of alkali metals by developing a reliable workflow for sample and cross-section preparation. Accordingly, the microstructure of electrodeposited and dissolved alkali metals at solid|solid interfaces were explored and visualized in this publication.

3.1 Publication I: "*Kinetics and Pore Formation of the Sodium Metal Anode on NASICON-Type $Na_{3.4}Zr_2Si_{2.4}P_{0.6}O_{12}$ for Sodium Solid-State Batteries*"

In the first publication of this doctoral thesis, a systematic approach was developed to characterize the interfacial kinetics of the alkali metal|SE interface. Therefore, sodium metal in contact with NZSP was characterized under equilibrium and non-equilibrium conditions by EIS, in situ XPS, TEM, and SEM.

By combining the results from time-dependent EIS with in situ XPS and TEM characterization, the formation of a kinetically stabilized interphase was observed when NZSP is contacted with sodium. Moreover, pressure and temperature-dependent EIS analysis revealed that insufficient physical contact causes an interface-related impedance, due the current constriction phenomenon. From an electrochemical perspective, the Na|NZSP interface is dominated by the current constriction phenomenon caused by insufficient contact, which is much more significant than the interphase formation and charge transfer process. This phenomenon was also observed during anodic dissolution experiments. Gradual EIS characterization indicated contact loss due to the formation of pores as the dissolution progressed, which has been confirmed by FIB-SEM cross-sectioning. Additionally, different geometric shapes of the pores were observed at the interface, when the stack pressure was altered. Finally, the evolution of the interfacial pore morphology after anodic dissolution in a subsequent resting phase was monitored by EIS, revealing a dynamic reorganization of the interfacial morphology.

Overall, the first publication demonstrates the compatibility of sodium and NZSP and identifies contact loss due to pore formation by anodic dissolution as the rate-limiting process of the SME. Consequently, concepts to suppress or prevent the formation of pores are necessary to improve the performance of the SME. The detailed impedance analysis provides a fundamental basis for the interpretation of the impedance spectra of the Na|NZSP interface and enables the characterization of the interfacial morphology even during electrochemical dissolution and deposition – as demonstrated in publication II. Moreover, the morphology of interfacial pores varies at different stack pressures and exhibits dynamic behavior after anodic dissolution due to creep. Accordingly, resting periods and the cycling protocol can significantly impact the performance of the SME and should be considered for battery applications.

The experiments were designed and planned by the first author, supported by Dr. T. Fuchs and Dr. S. Burkhardt, under the supervision of Prof. M. Rohnke and Prof. J. Janek. The solid electrolyte was synthesized by Dr. Q. Ma. The first author performed the electrochemical characterization, XPS, FIB-SEM and in situ SEM analysis. The TEM characterization was carried out by Z. Ding. The XPS data were analyzed and interpreted by T. Ortmann and Dr. J. Sann. Dr. J. K. Eckhardt, Dr. T. Fuchs and Dr. S. Burkhardt assisted in the interpretation of the electrochemical impedance spectroscopy data. The TEM data were analyzed and interpreted by Z. Ding, Prof. C. Kübel, and T. Ortmann. The manuscript was written by the first author supported by Dr. S. Burkhardt, Prof. M. Rohnke, Dr. Q. Ma and Prof. J. Janek. All authors discussed the results and revised the manuscript.

This study was part of the research within the Cluster of Excellence for Post Lithium-Ion Storage.

Reprinted without modification according to the creative commons license CC BY-NC 4.0 DEED (https://creativecommons.org/licenses/by-nc/4.0/) from Ortmann, T.; Burkhardt S.; Eckhardt J. K.; Fuchs, T.; Ding Z.; Sann J.; Rohnke M.; Ma, Q.; Tietz F.; Fattakhova-Rohlfing D.; Kübel C.; Guillon O.; Heiliger C.; Janek J. Kinetics and Pore Formation of the Sodium Metal Anode on NASICON-Type $Na_{3.4}Zr_2Si_{2.4}P_{0.6}O_{12}$ for Sodium Solid-State Batteries. *Adv. Energy Mater.* **2023**, *13*, 2202712. https://doi.org/10.1002/aenm.202202712. Advanced Energy Materials published by Wiley-VCH GmbH.

RESEARCH ARTICLE

ADVANCED ENERGY MATERIALS
www.advenergymat.de

Kinetics and Pore Formation of the Sodium Metal Anode on NASICON-Type $Na_{3.4}Zr_2Si_{2.4}P_{0.6}O_{12}$ for Sodium Solid-State Batteries

*Till Ortmann, Simon Burkhardt, Janis Kevin Eckhardt, Till Fuchs, Ziming Ding, Joachim Sann, Marcus Rohnke, Qianli Ma, Frank Tietz, Dina Fattakhova-Rohlfing, Christian Kübel, Olivier Guillon, Christian Heiliger, and Jürgen Janek**

In recent years, many efforts have been made to introduce reversible alkali metal anodes using solid electrolytes in order to increase the energy density of next-generation batteries. In this respect, $Na_{3.4}Zr_2Si_{2.4}P_{0.6}O_{12}$ is a promising solid electrolyte for solid-state sodium batteries, due to its high ionic conductivity and apparent stability versus sodium metal. The formation of a kinetically stable interphase in contact with sodium metal is revealed by time-resolved impedance analysis, in situ X-ray photoelectron spectroscopy, and transmission electron microscopy. Based on pressure- and temperature-dependent impedance analyses, it is concluded that the $Na|Na_{3.4}Zr_2Si_{2.4}P_{0.6}O_{12}$ interface kinetics is dominated by current constriction rather than by charge transfer. Cross-sections of the interface after anodic dissolution at various mechanical loads visualize the formed pore structure due to the accumulation of vacancies near the interface. The temporal evolution of the pore morphology after anodic dissolution is monitored by time-resolved impedance analysis. Equilibration of the interface is observed even under extremely low external mechanical load, which is attributed to fast vacancy diffusion in sodium metal, while equilibration is faster and mainly caused by creep at increased external load. The presented information provides useful insights into a more profound evaluation of the sodium metal anode in solid-state batteries.

1. Introduction

In view of the worldwide increasing demand for storage and supply of electrical energy, the development of powerful rechargeable postlithium-ion energy storage concepts is intensifying.[1] Sodium-based battery concepts are gaining more attention in research due to the high abundance, feasible accessibility, and low reversible standard potential (E_H(Na) = −2.71 V vs standard hydrogen electrode) of sodium. In particular, to increase the energy density of current sodium-ion batteries huge efforts are made to replace hard carbon (roughly 530 mAh g^{-1})[2] with the sodium metal anode (1165 mAh g^{-1}).[3,4] However, side reactions and the formation of dendrites leading to capacity loss, short circuits, and cell failure have so far prevented the use of sodium metal anodes in room temperature liquid electrolyte-based batteries.[5]

Inorganic ceramic solid electrolytes (SE) like Na-β''-alumina (BASE) or

T. Ortmann, S. Burkhardt, T. Fuchs, J. Sann, M. Rohnke, J. Janek
Institute for Physical Chemistry
Justus Liebig University Giessen
35392 Giessen, Germany
E-mail: juergen.janek@phys.chemie.uni-giessen.de

T. Ortmann, S. Burkhardt, J. K. Eckhardt, T. Fuchs, J. Sann, M. Rohnke, C. Heiliger, J. Janek
Center for Materials Research (ZfM)
Justus Liebig University Giessen
35392 Giessen, Germany

The ORCID identification number(s) for the author(s) of this article can be found under https://doi.org/10.1002/aenm.202202712.

DOI: 10.1002/aenm.202202712

J. K. Eckhardt, C. Heiliger
Institute for Theoretical Physics
Justus Liebig University Giessen
35392 Giessen, Germany

Z. Ding, C. Kübel
Technische Universität Darmstadt
64289 Darmstadt, Germany

Z. Ding, C. Kübel
Institut of Nanotechnology (INT) and Helmholtz Institut Ulm (HIU)
Karlsruhe Institute of Technology (KIT)
76344 Eggenstein-Leopoldshafen, Germany

Q. Ma, F. Tietz, D. Fattakhova-Rohlfing, O. Guillon
Forschungszentrum Jülich GmbH
Institute of Energy and Climate Research
Materials Synthesis and Processing (IEK-1)
52425 Jülich, Germany

D. Fattakhova-Rohlfing
Department of Engineering and Center for Nano integration
Duisburg-Essen (CENIDE)
Universität Duisburg-Essen
47057 Duisburg, Germany

$Na_3Zr_2Si_2PO_{12}$ (NZSPO) are often discussed as a possible solution to overcome this issue since their high mechanical strength may prevent the growth of dendrites through the separator.[6] Additionally, replacing potentially toxic and flammable liquid electrolytes by inorganic solid electrolytes may enhance safety and environmental compatibility.[7]

NZSPO belongs to a solid solution with the general composition $Na_{1+x}Zr_2Si_xP_{3-x}O_{12}$ ($0 < x < 3$) and was first synthesized in 1976.[8,9] Compared to BASE with its highly anisotropic layered structure, advantages of NZSPO are its 3D conduction pathways and lower sintering temperature for achieving a comparable ionic conductivity of 0.7 mS cm^{-1} at 25 °C.[9] In recent years, lots of efforts have been made to improve the ionic conductivity of NZSPO up to 4 mS cm^{-1} (25 °C) through a wide variety of doping and synthesis protocols.[10–13] An optimum ionic conductivity is obtained at a Na$^+$ content of $x \approx 3.3$ per formula unit, which can be explained by an enhanced correlated migration process.[14] This compositional optimization was already reported in 1979,[15] but did not find attention in the scientific community. However, it recently motivated the re-investigation of the above solid solution and resulted in the ionic conductivity of 5.5 mS cm^{-1} (25 °C) for the composition $Na_{3.4}Zr_2Si_{2.4}P_{0.6}O_{12}$ (NZSP0.4).[16]

Unfortunately, contact of sodium metal with SEs often results in a large interfacial resistance R_{Int}, due to impeded ion transport across the interface, which degrades the cell performance. To reduce R_{Int} various approaches such as the introduction of artificial interlayers and coatings or surface treatments have been applied. In the case of BASE and NZSPO, the interfacial resistance R_{Int} was reduced from a few kΩ cm^2 to a several tens or hundreds Ω cm^2 using various interlayers based on polymers,[17,18] titanium dioxide,[19] graphene,[20] cotton fibers,[21] AlF_3,[22] or tin coatings.[23,24] A similar reduction of R_{Int} is achieved by improving the interfacial contact due to high external stack pressures or a reduced surface tension of Na by employing Na/SiO_2 composite anodes.[25,26] Removing surface contaminations like carbonates and hydroxyl groups by heat treatments decreases the interfacial resistance $R_{\text{Int}} < 15$ Ω cm^2.[27,28] In recent reports, Ma et al. reduced the interfacial resistance of NZSP0.4 below 1.0 Ω cm^2, which is attributed to a self-forming thin Na_3PO_4 layer formed on the surface of the ceramic during sintering.[16,29,30] However, a detailed analysis and interpretation of the Na|NZSP0.4 interface is still missing.

The term "interfacial resistance" R_{Int} is often used in the literature as a general term assigned to an impedance contribution in the medium- and low-frequency range of the spectrum, describing the interfacial behavior of a metal|SE interface. Unfortunately, mostly it is not properly considered that the "interfacial resistance" is composed of different processes including charge transfer (CT) processes, formation of a solid electrolyte interphase (SEI) and current constriction (CC). Especially, the CC phenomenon is not well established in the field of all-solid-state batteries and therefore often neglected. For the Na|BASE and Li|$Li_{6.25}Al_{0.25}La_3Zr_2O_{12}$ (LLZO) interface, it has been shown that an increase in resistance/overvoltage occurs primarily due to pore formation near the interface.[31,32] As insufficient contact at the "parent" metal|SE interface leads to the CC phenomenon, it is likely that the measured interfacial contribution estimated by impedance spectroscopy is dominated by CC.[28,33]

In contrast to the charge transfer process or the ion transport within the SE, the CC effect is not an independent microscopic electric migration process, but rather a mere geometric effect. CC occurs at spatially distributed microcontacts between the metal anode and the solid electrolyte separator, where dissolution and deposition of the metal take place. It strongly depends on the interfacial morphology as recently systematically studied by Eckhardt et al.[34,35] According to their work, CC should be distinguished in "dynamic" and "static" constriction: The impact of dynamic constriction depends on the excitation frequency of an applied electric AC field, while the static constriction effect is independent of external influences, e.g., when the electrode area is smaller than that of the SE.[34,35] Especially dynamic CC is strongly affected by the interfacial morphology of pores formed during anodic dissolution. The presence of microcontacts, however, does not require anodic dissolution to occur, since it can also originate from insufficient physical contact upon cell assembly or incomplete insulating interlayers like surface contaminations.[36,37] Evidence for CC can arise from a similar activation energy for the apparent interface resistance and the ion transport within the SE, as this indicates transport limitation by the SE in the constriction zone.[38] For the Na|NZSPO interface, significantly different activation energies $E_{\text{a,Int}}$ have been reported (0.6 eV[26] and 0.39 eV[39]) which were not assessed with respect to the corresponding bulk properties. Activation energies can vary significantly depending on the manufacturing process of the SE (microstructure) as well as on electrode preparation.[40]

With respect to the formation of microcontacts at the metal|SE interface under an external current load, it is worth noting that kinetic studies of the anodic dissolution of metals at a solid|solid phase boundary have been part of research decades ago. For instance, processes taking place during the anodic dissolution of the "parent" metals (Me) Ag and Cu at the Me|SE phase boundary and the resulting changes at the interface have been investigated in detail.[41–43] Anodic dissolution of metals at the phase boundary leads to the formation of metal vacancies at the interface between both solids. Without an external load the regeneration of the original interface can be achieved by the diffusion of vacancies into the bulk or diffusion-based creep mechanisms like Coble and Nabarro–Hering creep.[41,44] In case of faster dissolution compared to the regeneration of the interface, the contact area will be reduced and no stationary state is reached. Despite the decrease of the contact area, metal dissolution can occur by anodic dissolution of ad-atoms, which are transported to the interface by surface diffusion along the pore walls. By dissolving these metal atoms, extended pores are formed, which in turn affect the current distribution at the interface.[42] Additionally, surface diffusion allows size equilibration of formed pores driven by the minimization of the surface energy, which is similar to the Ostwald ripening of particles ("electrochemical Ostwald ripening").[45]

The mechanical stability of the interface is affected by the pores formed during anodic dissolution. Movement and relaxation of dislocations in the metal may breakdown the pore morphology even causing oscillatory effects at the interface.[41] These effects

---

C. Kübel
Karlsruhe Nano Micro Facility (KNMF)
Karlsruhe Institute of Technology (KIT)
76344 Eggenstein-Leopoldshafen, Germany
O. Guillon
Jülich Aachen Research Alliance
JARA-Energy
52425 Jülich, Germany

are even more pronounced when external load is applied since higher strain rates are achieved by different creep mechanisms.[44] Especially for sodium, creep is enhanced due to low yield strength and high homologous temperature (T_h = 0.8) at ambient temperatures.[46,47] Additionally, the grain size and dislocation density affect the mechanical properties such as yield strength and therefore influences the interfacial kinetic behavior.[48]

Superposition of different phenomena like interfacial degradation, charge transfer, current constriction, as well as regeneration under current load may take place simultaneously at the Na|NZSP0.4 interface. However, a systematic study to distinguish these processes is still missing in literature. It is worth to add that the formation of a highly heterogeneous interface during anodic dissolution (discharge of the cell) will cause highly inhomogeneous current distributions during subsequent cathodic deposition (plating, during charge of the cell), and therefore, will inevitably cause cell failure.

To answer the open questions and get deeper insight into the sodium anode kinetics on NZSP0.4, we performed a series of experiments under various conditions. First, we consider the thermodynamic stability of NZSP0.4 against sodium metal and analyzed the interface using time-resolved impedance analysis combined with in situ X-ray photoelectron spectroscopy (XPS) and transmission electron microscopy (TEM).

Second, we studied the kinetics of the anodic sodium dissolution by pressure- and temperature-dependent impedance analysis. Clearly, the interface contribution observed by impedance spectroscopy is mainly caused by insufficient mechanical contact.[34,35] Based on these results, CC is identified as dominated process at the interface rather than SEI formation and CT process.

Third, anodic dissolution is examined electrochemically under different external (mechanical) loads, and the interface is visualized on the basis of cross sections using focused ion beam scanning electron microscopy (FIB-SEM) and prepared under cryogenic conditions. In vacuum with low external loads (p = 10^{-3} Pa), lens-shaped pores were observed, whereas at higher loads (p = 0.3 MPa), no regular structures can be identified. Finally, the temporal development of the dissolved interface is analyzed electrochemically and equilibration of the interface is observed at open-circuit voltage (OCV).

2. Results and Discussion

2.1. Stability of $Na_{3.4}Zr_2Si_{2.4}P_{0.6}O_{12}$ Versus Na

From a theoretical point of view, the electrochemical stability window of $Na_{1+x}Zr_2Si_xP_{3-x}O_{12}$ with $x = 2$ extends from ≈1 to 3.4 V versus Na^+/Na.[49,50] Increasing the Si/P ratio decreases the thermodynamic driving force of the decomposition in contact with sodium.[51] A similar shift for the stability window is obtained by density functional theory calculation.[52] To date, only $Na_3Zr_2Si_2PO_{12}$ has been investigated experimentally for its stability. Although apparently the same compound was used in various studies, the resistances obtained for the formed interphase range from tens of Ω cm^2 to several hundred Ω cm^2.[39,52,53] Likewise, the temporal development of the interphases differs significantly in the studies, too. Due to these variations, NZSP0.4 in contact with sodium is analyzed in detail. A detailed characterization of the used solid electrolyte material is given in Figure S1 (Supporting Information).

2.1.1. Time-Dependent Impedance Analysis of the Na|NZSP0.4 Interface

For time-dependent impedance analyses, symmetrical Na|NZSP0.4|Na cells were assembled in a specially designed pressure setup (see the Experimental Section for a more detailed description). Experiments were conducted in an Ar-filled glovebox to ensure immediate impedance recording after assembly (time delay <1 min). In **Figure 1**a, the development of the total impedance over time is depicted. After assembly one semicircle with an apex frequency of 1.57 MHz and a corresponding capacity of 4.5 nF cm^{-2} can be identified in the Nyquist plot. The observed contribution is attributed to grain boundary transport (GB) within the solid electrolyte, as the bulk transport process is beyond the measured frequency range (see Figure S2, Supporting Information). During data acquisition, only slight changes in the apex frequency (1.4 MHz) and the capacitance (4.3 nF cm^{-2}) were observed, while the real part of the impedance increases by 6 Ω cm^2. No additional and clearly

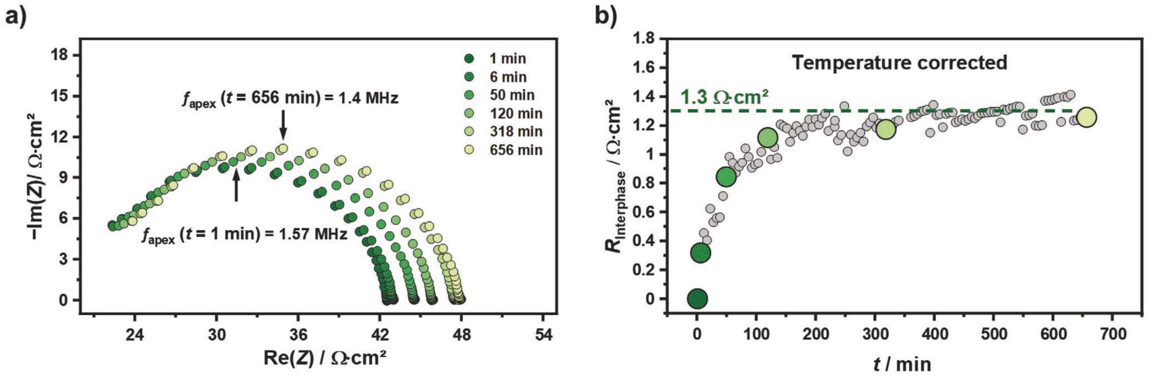

Figure 1. a) Time evolution of the impedance of a symmetrical Na|NZSP0.4|Na cell. Time delay between assembly and recording was <1 min. b) Temporal development of the temperature-corrected resistance of the interface (gray) and the corresponding values determined from the impedance spectra depicted in a) (green). Elimination of temperature fluctuations relies on the temperature dependence of the bulk and grain boundary impedance of the SE. A detailed description can be found in the Supporting Information.

separated contribution in the impedance data—which could indicate the formation of an interphase—was observed. However, it might be possible that the time constants of the GB and the interphase impedance are too close or that the impact of the interphase is below the detection limit given by the experimental setup used.

We like to note (see the Experimental Section) that the impedance measurements were conducted in a glovebox, as transfer to a climate chamber would have taken too long. While this helped to quickly observe the impedance after cell assembly, the glovebox was not perfectly temperature-controlled. A temperature-correction for the measured impedance data was carried out to verify that the observed resistance increase is not caused by the temperature-dependence of the ionic conductivity of NZSP0.4. A detailed description of the procedure is given in Figure S3 (Supporting Information).

The temperature-corrected impedance spectra measured under equilibrium conditions show that any interphase resistance $R_{\text{Interphase}}$ is negligibly small as can be seen in Figure 1b. Additionally, the time dependence of $R_{\text{Interphase}}$ indicates a self-limiting behavior. When the measurement was repeated three times, a mean resistance increase of about 1.3 Ω cm^2 was observed due to interphase growth (for details see Figure S3b,c, Supporting Information).

However, as a high uncertainty is obtained for $R_{\text{Interphase}}$ from a formal error analysis, the same experiments were also carried out in a controlled temperature environment. Sealing and temperature stabilization of the cell to 25 °C led to a time delay of 18 min between assembly and start of data acquisition. A similar increase of the total impedance as well as a similar time course support the previous results, as shown in Figure S3d (Supporting Information). We assume that this small change in resistance is indeed caused by degradation at the Na|NZSP0.4 interface, i.e., by SEI formation.

2.1.2. In Situ XPS and TEM Characterization of the Na|NZSP0.4 Interface

To investigate the degradation processes at the Na|NZSP0.4 interface, chemical and structural analyses were carried out by in situ XPS and TEM. First, the surface of the pristine NZSP0.4 was characterized by XPS. Detail spectra of the elements in the SE as well as the C 1s signal are depicted in Figure S4 (Supporting Information). The binding energies (BE) obtained are in good agreement with those of NZSPO.[26,52,53] Since the substitution of $(PO_4)^{3-}$ by tetrahedral $(SiO_4)^{4-}$ in the crystal structure does not affect the chemical environment of phosphorous and silicon, no shifts in binding energy were expected and this is confirmed by the experimental data. When NZSPO is exposed to ambient atmosphere a contamination layer containing carbonates and hydroxyl groups is formed.[27,54] Along the C 1s spectrum, mainly C–C bonds and a small fraction of C–O bonds were found, probably originating from the residual atmosphere inside the XPS chamber. As no further signal (e.g., carbonate) is identified in the C 1s spectra, the presence of a surface contamination layer is excluded for the material investigated.

Chemical changes of the interface by successive deposition of sodium on NZSP0.4 via sputter deposition inside the XPS chamber were monitored by intermittent XPS. **Figure 2**a–c depicts the development of the Zr 3d, Na 1s, and O 1s signals with increasing amount of deposited sodium. The evolution of a shoulder at lower binding energies in the Zr 3d signal indicates the reduction of Zr^{4+} to Zr suboxides by deposited sodium (Figure 2a). Figure 2d shows the corresponding fit of the last XP spectrum, where the shoulder at lower binding energies is described using two suboxides compounds with binding energies of E_b(Zr 3d) = 180.9 eV and E_b(Zr 3d) = 180.0 eV. Similar binding energies have been reported for the Zr signal in the case of $Na_3Zr_2Si_2PO_{12}$ after contacting with sodium metal.[39,52] Accordingly, the signal at E_b(Zr 3d) = 180.0 eV would indicate a species with an oxidation state between Zr^{1+} and Zr^{2+}, whereas the signal at E_b(Zr 3d) = 180.9 eV indicates species with an oxidation state between Zr^{2+} and Zr^{3+}.[55,56] A reliable identification of reduced Zr species is challenging as more suboxides could be present or phases with varying oxygen content formed leading to broadening of the signal. However, to analyze the development of the reduced Zr species during sodium deposition, we assume to have only two suboxides.

As shown in Figure 2e, after 15 min of sodium deposition, no change in the relative atomic fractions of Zr 3d(SE) and Zr 3d(sub-oxides) was observed. Based on the signal attenuation of the Zr 3d region, roughly 1 nm of Na had been deposited after 15 min, indicating a very thin interfacial layer.

XP spectra of the Si 2p and P 2p regions are shown in Figure S5 (Supporting Information). Only in the first Si 2p spectrum a slightly asymmetric peak shape was observed, which is probably caused by a cleaning step of the surface using an argon sputter gun. Due to the similar binding energy (E_b(Si 2p) = 101.0 eV) compared to an untreated surface (E_b(Si 2p) = 101.2 eV, see Figure S4c, Supporting Information) the effect can be neglected. However, apart from attenuation, no changes in the XP spectra were detected in the Si 2p region during sodium deposition, as well as in the P 2p region. Consequently, Si and P are either not reduced or they form volatile and unstable decomposition products that cannot be detected by XPS.[52]

Before deposition, only one signal at E_b(Na 1s) = 1071.1 eV was observed in the Na 1s region, which is assigned to sodium ions (Na^+ signal) in the SE (Figure 2b). After the first deposition cycles, a shoulder appears at lower BE of the Na 1s line, which develops into a separated line with a binding energy E_b(Na 1s) = 1069.1 eV. This is evidence for the formation of metallic sodium on the SE, which can be confirmed by the observation of plasmon patterns at binding energies of E_b(Na 1s) = 1074.9 eV and E_b(Na 1s) = 1080.8 eV.[57] The area below the sodium signal increases after the first deposition of sodium metal. Since differences in BE between different Na^+ ion-containing compounds are very small (<0.5 eV), a differentiation is challenging. However, an oxidation of freshly deposited sodium can be inferred from the increase in area.

The evaluation of the O 1s signal, shown in Figure 2c, is complicated due to superposition with sodium Auger electrons. In addition, depending on the chemical environment, sodium Auger electrons have different energies.[58] Therefore, refer-

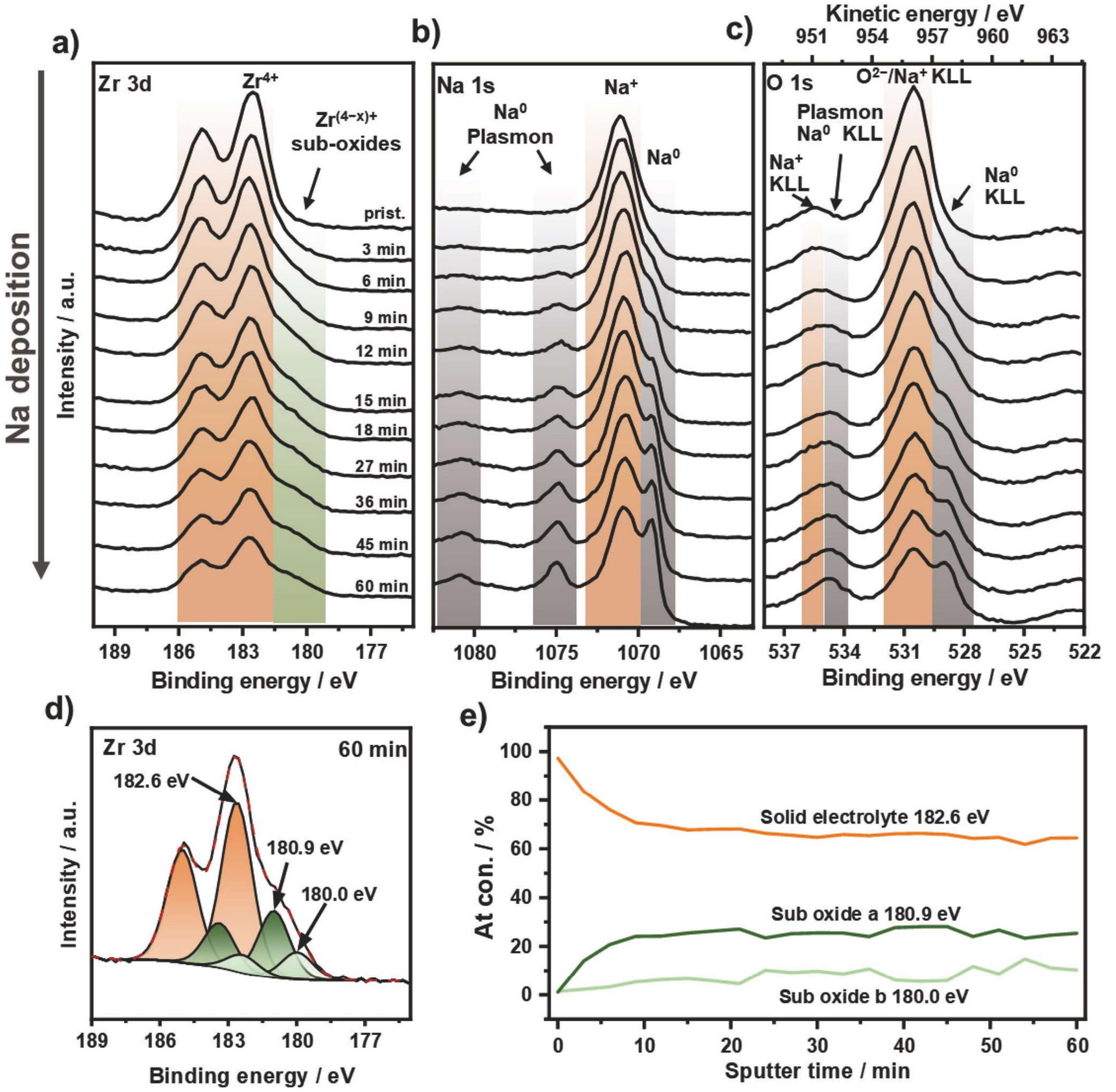

Figure 2. a–c) XP spectra of Zr 3d, Na 1s, and O 1s after different sodium deposition times. Binding energies of the SE, metallic sodium, and reduced spices are highlighted in orange, gray, and green, respectively. The color coding is maintained in d) and e). d) Detail spectra of Zr 3d after a sodium deposition time of 60 min. Beside the main peak of the SE two further suboxide signals at 180.9 and 180.0 eV are used for fitting of Zr 3d signal. e) Relative atomic concentrations in the Zr 3d region with increasing deposition time of sodium. After 15 min, no further change in the composition of the Zr 3d signal was detected indicating a self-limiting reaction.

ences of sodium Auger emissions are necessary to assess their influence in the O 1s region and to interpret the O 1s spectrum properly. Assuming that Auger electrons of Na^+ have a similar kinetic energy, Na_2O can be used as a reference material to distinguish between Na^0- and Na^+-KLL emissions. Hence, the signal at E_b = 535.6 eV (E_{Kin}(photoelectron(PE)) = 951.0 eV) can be ascribed to the Auger process Na^+-$KL_1L_{2,3}$.[59] The main signal at E_b = 530.5 eV originates from the oxygen lattice of the SE and attenuates with increasing deposition time. This signal includes Na^+ Auger electrons, which is obvious from the emission pattern, making reliable fitting challenging.[59] Therefore, the formation of Na_2O postulated by Gao et al. cannot be confirmed based on the results obtained.[54] Finally, the formation of metallic sodium was observed by the Na^0-$KL_1L_{2,3}$ emission at E_{Kin}(PE) = 957.6 eV with an associated plasmon at E_{Kin}(PE) = 951.9 eV.

By comparing the sodium signals (PE and Auger electrons) obtained from metallic sodium with a reference sample (freshly prepared sodium foil) calibrated to the Fermi level, a shift of roughly 2.5 eV to lower energies was found as can be seen in Figure S6 (green curves) as well as Tables S1 and S2 (Supporting Information). For Na|NZSPO interface a band bending of 0.1–0.6 eV due to the formation of a degradation layer at the interface has already been reported.[54,60] However, a band bending of 2.5 eV in the case of NZSP0.4 is rather unlikely, which is why we suspect an additional effect. When sodium is placed on an electronically insulating tape a similar shift of about 2.3 eV for the metallic sodium signals, including the Fermi level, to lower BE is observed (Figure S6 light orange curves, Supporting Information). Therefore, we suspect that the observed shift is mainly a sodium-specific effect in combination with electronically insulating measurement setups. We assume that an equilibration of Fermi levels of sodium in contact with electronically insulating material does not occur. The shift of 2.2–2.3 eV is close to the open circuit voltage of a sodium-oxygen cell (2.27–2.33 V).[61] As residual oxygen is present inside the XPS chamber, the formation of Na_2O in contact with sodium is likely. As Na_2O is a poorly conducting solid electrolyte and if thin enough, it can separate sodium metal from residual oxygen, thus forming a sodium-oxygen cell. During XPS measurements the surface potential is set to zero by the applied neutralization. Referencing to the cathode active material (which might be Na_2O_2, NaO_2, or O_2) leads to a lowering of the Fermi level in the sodium electrode, resulting in a lower binding energy. Despite a very low oxygen partial pressure inside the XPS chamber, a potential difference of roughly 1.95–2 V can be expected for a local sodium-oxygen galvanic cell.[62] A superposition of both effects might be a possible explanation for the observed shift.

The newly formed Na|NZSP0.4 interface was characterized 8 h after the last step of sodium deposition. As shown in Figure S7 (Supporting Information), no further changes in the Zr 3d, Si 2p, and P 2p signals were observed. Only a decrease of the metallic sodium signals in the Na 1s and O 1s region is found, which is due to the reaction with residual atmosphere (especially oxygen). This is shown by quantifying the absolute signal areas in Table S3 (Supporting Information), since the amount of oxygen increases while all other areas remain unchanged.

To analyze and visualize the morphology and thickness of the interfacial degradation layer, TEM characterization was conducted. For the sample preparation a symmetric Na|NZSP0.4|Na cell was assembled and stored until the formation of the interphase has been finished. To excavate the interface by removing one electrode without damaging the formed interphase, one sodium electrode was anodically dissolved. Immediately after removal, a copper layer (120 nm) was deposited thermally on the exposed interface as protection layer to avoid changes. In addition, a Pt layer was deposited for the preparation of the electron transparent lamella by FIB milling technique. A detailed description of the preparation is given in Section S5 and Figure S8, Supporting Information).

The lamella was tilted until the surface of the NZSP0.4 was aligned parallel to the electron beam and high-angle annular dark-field (HAADF) scanning transmission electron microscopy (STEM) images were recorded. Besides the NZSP0.4 (**Figure 3**a, right side) and the deposited protection layer (Figure 3a, left side), an additional layer on the surface of the SE with an increased signal intensity can be observed in the HAADF image. However, clear identification of the formed interphase is not possible as no clear morphology change compared to the SE is found. Therefore, energy-dispersive X-ray spectroscopy (EDX) analysis was performed to characterize the elemental distribution of the layered system. The measured region is highlighted in Figure 3b and the corresponding spectra are shown in Figure 3c.

A similar elemental composition is obtained for the protection layer (region A) as well as the bright layer on the surface of the NZSP0.4 (region B) which mainly consist of sodium, oxygen, copper and platinum. As no zirconium (Zr-K_α line, Zr-L_α overlap with Pt-M_α line) and only slight amounts of silicon are observed in region B, we do not suspect that this interphase originate from the degradation of NZSP0.4 in contact with sodium, since a formed interphase should contain all the elements of the participating reactants.

The presence of sodium and oxygen in the region A and B originates from the preparation process of the specimen as residual sodium will be left at the surface after removing the sodium electrode. Despite a copper protection layer, the residual sodium degrades even in inert atmosphere during further preparation of the lamella. Additionally, the preparation process also explains the presence of platinum directly on the surface of NZSP0.4 as the copper layer does not have a proper contact to the SE and deposition of platinum into the gap is likely to occur during preparation of the lamella.

Finally, the regions near the surface (C) and the bulk (D) of the NZSP0.4 sample were analyzed. Comparing both spectra, a similar elemental composition is observed indicating that no changes in the near-surface region of the SE occurred. A reliable quantification of the SE is not possible as the P signal cannot be clearly separated from the Zr-L_α signal. All other elements of the NZSP0.4 can be identified in the spectra. The presence of a Cu signal in regions C and D is probably due to the copper background of the cryo transfer holder. The experiment was repeated for a second specimen showing similar results as can be seen in Figure S9 (Supporting Information).

In summary, when contacting NZSP0.4 with sodium a kinetically stabilized interphase is formed, which appears to prevent further degradation of NZSP0.4. This interphase causes a minor increase of $R_{\mathrm{Interphase}}$ by about 1.3 Ω cm^2 and could not be identified well via TEM. We therefore assume that NZSP0.4 forms a very thin kinetically stable interface with a low charge transfer resistance.

2.2. Charge Transfer and Current Constriction at the Na|NZSP0.4 Interface

Different processes take place at the interface influencing the interfacial kinetics such as charge transfer, space charge layer formation, defect relaxation, crystallization phenomena, diffusion, or current constriction.[38] Usually, any low-frequency impedance of the Na|NZSPO interface is considered as an interface-related impedance and assigned to charge transfer, however, without clear proof.[20,24,54] As discussed in the

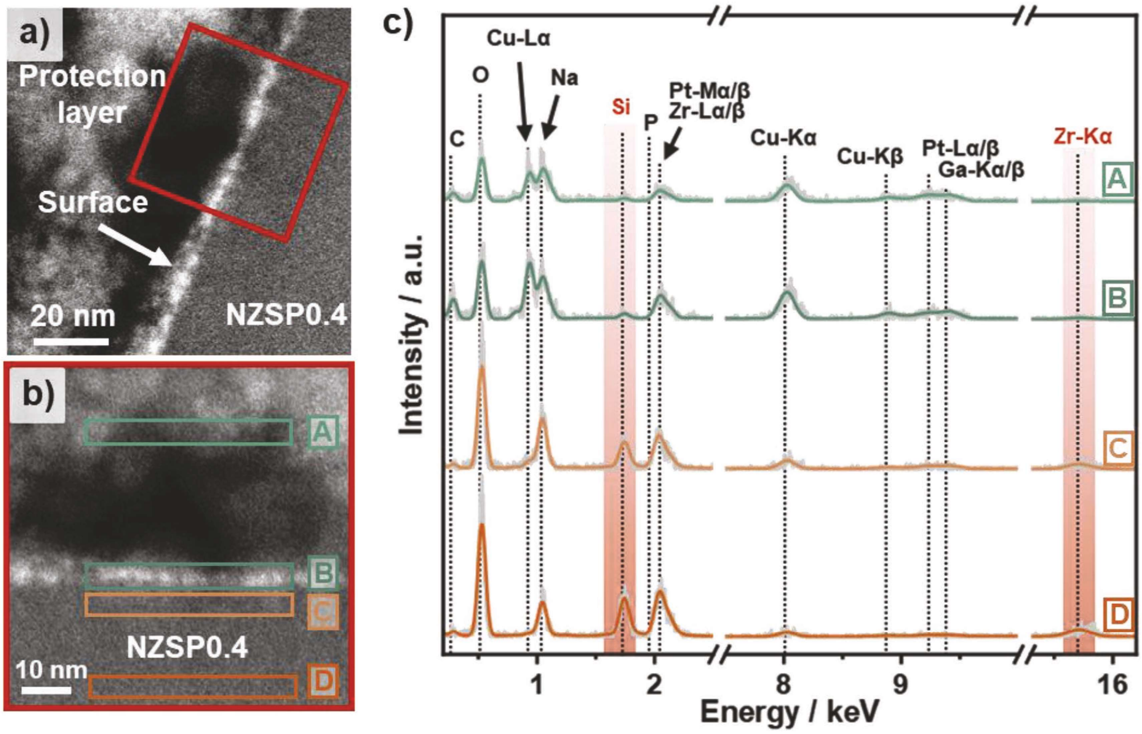

Figure 3. a) High-angle annular dark-field (HAADF) scanning transmission electron microscopy (STEM) image of the prepared electron transparent lamella from the Na|NZSP0.4 interface. Based on different morphologies, the NZSP0.4 solid electrolyte separates clearly from the deposited protection layer. b) HAADF-STEM image of the red marked region in a) at higher magnification. c) Energy-dispersive X-ray spectroscopy (EDX) spectra of selected regions which are highlighted in green and orange in (b). The measured spectra are shown in light gray, while the model spectra are presented in the respective color (orange and green). No changes in the elemental composition are observed in the near-surface region of the NZSP0.4 compared to the bulk.

Introduction, contact loss and the rise of current constriction at a few remaining contact points lead to an additional impedance contribution in the low-frequency region. Pressure- and temperature-dependent potentiostatic electrochemical impedance spectroscopy (PEIS) analysis allows to estimate whether the effect of current constriction or charge transfer is dominating the overall interfacial resistance, as has been shown for the Li|LLZO interface.[33]

2.2.1. Pressure-Dependent PEIS Analysis of Na|NZSP0.4 Interface

The physical contact area between parent metal and the SE can be adjusted by applying external force (pressure). Since the interfacial contact area between parent metal and SE is proportional to the number of microcontacts, R_{Int} should decrease upon increasing the contact area, density, and size of microcontacts. To investigate the role of these microcontacts, a $\mathrm{Na_{bc}}$|NZSP0.4|$\mathrm{Na_{id}}$ cell was assembled whereby one electrode has a low load-bearing contact area denoted as $\mathrm{Na_{bc}}$ in the following. The other sodium electrode, called $\mathrm{Na_{id}}$ (ideally reversible), can be seen as a quasi-reference electrode (QRE), as described in detail in the Experimental Section.

The contact at the $\mathrm{Na_{bc}}$|NZSP0.4 interface was adjusted by applying external load to the $\mathrm{Na_{bc}}$|NZSP0.4|$\mathrm{Na_{id}}$ cell. The external force was gradually increased, and each force was applied for 30 s. After each step, the force was released so that the interfacial contact area does not change during the impedance analysis. The obtained impedance spectra are shown in **Figure** 4a. With an initial force of roughly 1 N, clearly two semicircles are observed at an apex frequency of 1.08 MHz and 88 kHz and with capacitances of 4 and 34 nF $\mathrm{cm^{-2}}$, respectively. The contribution in the high-frequency range can be assigned to the GBs in NZSP0.4 and the one in the lower-frequency range to the interface (see Section S2 for details, Supporting Information).

The impedance data were fitted with the equivalent circuit shown in Figure 4a. The results for the interfacial resistance R_{Int} and capacitance C_{Int} at different loads are shown in Figure 4b. Starting from $R_{\mathrm{Int}} =$ 53 Ω $\mathrm{cm^2}$, the interfacial resistance declines with increasing force and becomes 7 Ω $\mathrm{cm^2}$ at an applied force of 215 N (details for normalization are given in Section S6, Supporting Information). The changes in resistance with increasing external load are significantly larger compared to the small resistance of the electrode interphase (as determined in Section 2.1.1), and thus, we can neglect the latter. The

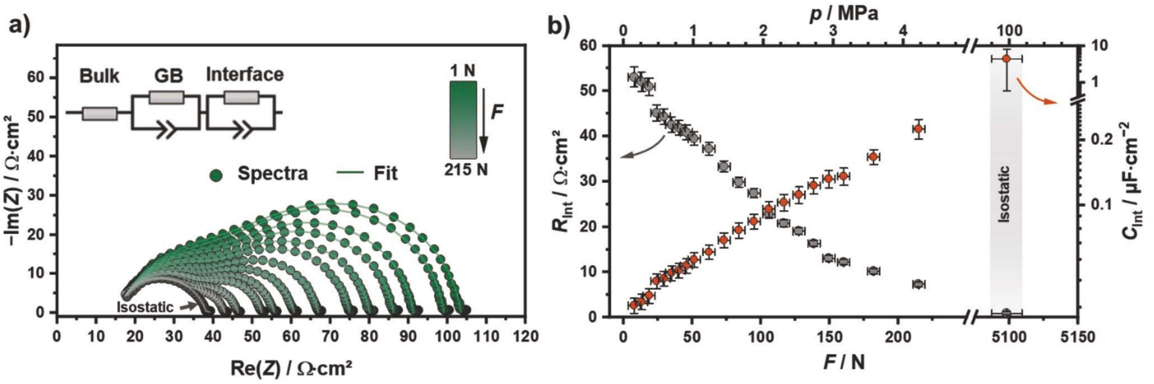

Figure 4. a) Impedance data of a sodium WE attached to a NZSP0.4|Na_{id} half-cell. The external force was gradually increased. At each step a uniaxial force was applied for 30 s. The impedance spectrum labeled with "isostatic" was obtained with an isostatic pressure of 100 MPa applied for 15 min. All impedance spectra were recorded at a base external force of 1 N to avoid changes of the contact area during the measurement. The equivalent circuit depicted in (a) was used for fitting of the impedance data, which is visualized as lines. b) Resistances and capacitances of the interface contribution as a function of the external force. Shown uncertainties originate from the fitting process and were given by the software used. With increasing force, the capacitance rises, whereas the resistance falls. The given pressure is estimated by the applied force and the geometric electrode area after the experiment.

local pressure on the scale of the microcontacts is unknown as the electrode and contact area of the sodium foil increases during force application due to plastic flow, and therefore, we prefer to report force rather than pressure. The pressure given in Figure 4b is related to the geometric electrode area after the experiment to give an estimate of the pressure.

At high isostatic pressures of 100 MPa, R_{Int} is significantly reduced to less than 1 Ω cm^2. However, an interfacial resistance can still be identified in the impedance spectrum, as can be seen from the asymmetric impedance shape in Figure 4a and is even more evident in the distribution of relaxation times (DRT) analysis (see Figure S10a and the Experimental Section for details, Supporting Information). The observed R_{Int} might be caused by degradation of the sodium electrode due to long exposure to glovebox atmosphere rather than to $R_{\mathrm{Interphase}}$.

The interfacial capacitance shows an opposite trend compared to the resistance and rises with increasing force. This also indicates that the contact area between the sodium electrode and NZSP0.4 is increasing, i.e., the interfacial contact is improving, increasing the double layer capacitance at the interface.[34]

In addition to the external (mechanical) load during the contacting of sodium and SE, the time period and the directional anisotropy of the load (uniaxial vs isostatic) are also decisive for the interfacial contact. Three Na_{bc}|NZSP0.4|Na_{id} cells were assembled whereby different external loads at defined time periods were applied to prepare the working electrode (WE). The corresponding impedances are shown in **Figure 5**a.

Even at a uniaxial pressure of 1.7 MPa, no interfacial contribution was detected in the Nyquist plot, which is verified by DRT analysis (Figure S10b, Supporting Information). When the external load was increased to 11 MPa (uniaxial) or 100 MPa (isostatic), there was only a slight decrease in the total impedance of 2.5 Ω cm^2, which clearly shows that the interfacial contact is nearly optimal, even at low loads. A reason for this might be the surface roughness of the SE, as a rough surface leads to higher local stress and plastic flow even at minor external loads. When an ideal interfacial contact is already achieved at minor loads, further increase of pressure does not significantly reduce the total impedance.

The influence of the specific processing to establish the Na|NZSP0.4 interfacial contact gets even clearer when comparing a gradual load increase (Figure 4a) and a one-step load preparation protocol (Figure 5a). While a stepwise increase of the load yields an interfacial contribution of about 25 Ω cm^2 when reaching 1.7 MPa, no contribution was observed by a one-step load preparation. We interpret this apparent discrepancy as follows:

When sodium is pressed onto the SE, point contacts are initially present at the interface. Due to a significantly higher contact stress at these contact points compared to the bulk material, the dislocation density is locally increased. A higher dislocation density leads to strain hardening, which in turn requires higher pressures for the deformation of sodium. However, the locally increased dislocation density will decrease by recovery and recrystallization processes, which in turn proceeds with time. Therefore, strain hardening is normally not observed for sodium due to the high homologous temperature (T_h = 0.8) at ambient temperature, which enhances recovery. However, as high strain rates and short relaxation times (1 min) were used for the stepwise pressing, complete recovery is unlikely, resulting in strain hardening at the interface. Additionally, sodium gets harder by increasing the strain rate.[46] The recovery (annihilation of dislocations) and recrystallization is a function of time.[63] Second, the longer handling inside the glovebox of the previous experiment led to a formation of surface contaminations like sodium oxide. Such contamination may enhance the effective yield strength.[64] The formed contaminations may also explain the small but present interfacial contribution after applying a pressure of 100 MPa in the previous experiment compared to the impedance data shown in Figure 5a.

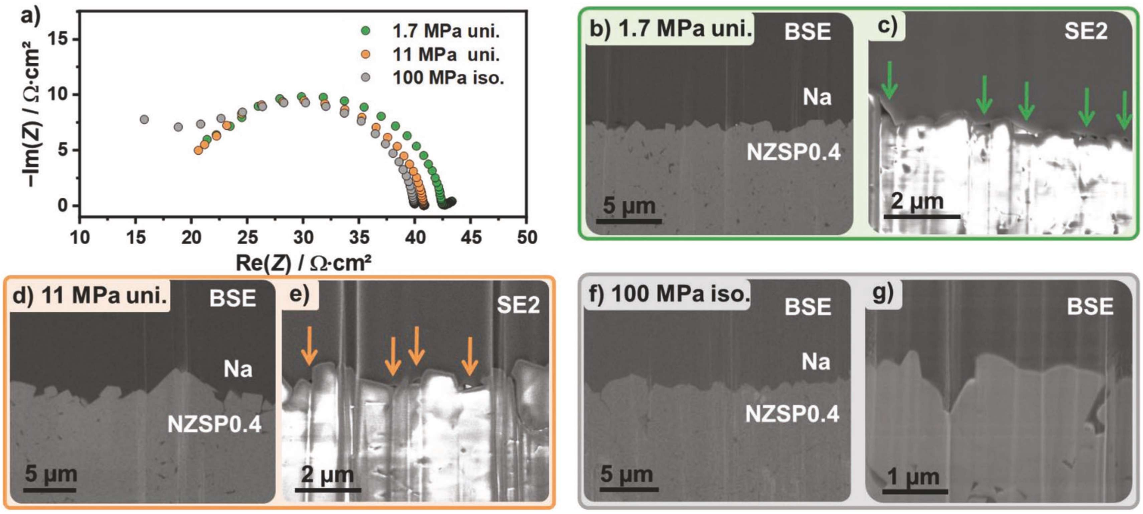

Figure 5. a) Impedance spectra of three different Na|NZSP0.4|Na_{id} cells with the WE pressed on the SE at 1.7 MPa for 60 s, 11 MPa for 60 s, and 100 MPa for 900 s. The abbreviations "iso." and "uni." represent isostatic and uniaxial pressure. For each pressure, cross-sections of the Na|NZSP0.4 interface are shown at low magnification b), d), and f) and at high magnification in (c), (e), and (g). Images described with BSE indicate a back-scattered electron image, whereas SE2 describes a secondary electron image. The arrows indicate pores at the Na|NZSP0.4 interface.

Cross-sections of Na|NZSP0.4 interfaces are shown in Figure 5b–g for differently applied pressures. For all pressures, full interfacial contact is seen in the backscattered electron images at low magnification level. However, by increasing the magnification, pores with a size of a few hundred nanometers are visible at the interface assembled with a pressure of 1.7 MPa. The number of pores as well as their size decreased after applying 11 MPa, but pores were still present. Only at an isostatic pressure of 100 MPa an apparently fully contacted interface was achieved without pores at the interface.

From a geometrical point of view, if an electrically insulating pore is present between the sodium and the SE, there should be a (dynamic) constriction-induced contribution in the resulting impedance spectra.[34,35] Surprisingly, despite the presence of pores at the interface at 1.7 and 11 MPa, the constriction contribution cannot be clearly identified in the associated impedances. One possible explanation for this could be the similar time constant of the pore-induced current constriction and that of the SE grain boundary transport process.

Current constriction is also affected by distribution of the contact area at the interface as a finer distribution leads to a less pronounced constriction effect in the impedances, i.e., the constriction resistance decreases.[34] A finer distribution minimizes the distance between the center of the contact spots and the centers of the pores. As can be seen in Figure 5c–e, pores are only formed in "valleys" due to the higher surface roughness of the SE (R_a = 0.19 µm). Thereto, smaller pores with a finer distribution are observed which may result in difficult separation of the CC signal and the GB transport contribution. Similar behavior has been observed at the Li|LLZO interface, where the CC signal vanishes almost completely despite a native passivation layer between metal electrode and the SE.[37] Accordingly, the surface roughness of the SE plays an important role for the impedance behavior of the metal|SE interface.

2.2.2. *Temperature-Dependence of the Impedance*

To gain a deeper understanding of the interfacial kinetics between sodium and NZSP0.4, temperature-dependent impedance analyses were performed. Three types of cells with different interfacial contact were analyzed and the activation energies E_a for each transport process including bulk, GB, and interface were determined based on the brick layer model.[65] The respective impedance spectra and Arrhenius plots are shown and discussed in Figure S11 (Supporting Information). The values for the activation energies determined are summarized in Table S4 (Supporting Information). Independent of the cell type (electrode material and interfacial contact) similar values of $E_{a,bulk}$ = 0.26 eV and $E_{a,GB}$ = 0.36 eV are obtained. Only for Na_{bc}|NZSP0.4|Na_{id} cells an additional interfacial contribution is observed in the low-frequency range with an activation energy $E_{a,Int}$ = 0.37 eV, which is quite similar to $E_{a,GB.}$

As mentioned above, non-ideal electrode contacts give rise to a constriction impedance, as recently discussed by Eckhardt et al.[34,35] In the following, we will discuss whether the concept of current constriction applies to the Na_{bc}|NZSP0.4 interface.

Pressure-dependent experiments demonstrate that poor interfacial contact is the major issue for a high interface-related resistance, which vanishes completely after increasing the external load. Additionally, no further contributions can be resolved by impedance analysis at near-ideal contact situations, and the bulk and GB activation barriers are similar to those of symmetrical Au|NZSP0.4|Au cells. This implies that the charge transfer between electrode, interlayer and solid electrolyte is not the rate-determining step. As shown in Section 2.1.1, any charge transfer step, even involving the thin SEI interlayer, corresponds to a resistance contribution of only about 1.3 Ω cm².

Due to current constriction, an inhomogeneous potential distribution is caused near the interface in the SE which homogenizes when going into the bulk of the SE. Hence, the volume of the SE near the interface is influenced by the inhomogeneous potential, i.e., by current constriction.[34] The microstructure (grains and grain boundaries) within this volume strongly affects the activation energy of the constriction resistance, as the CC effect does not reflect an independent microscopic electric migration process. For the limiting case of a Na|single crystal SE interface a similar activation energy of bulk $E_{\mathrm{a,bulk}}$ and constriction $E_{\mathrm{a,CC}}$ is expected since the ion transport in the SE is the limiting step.[66,67] In the case of a Na|polycrystalline SE, grain boundaries affect the total conductivity. Depending on the grain boundary arrangement (number of grain boundaries at the interface and grain size) near the Na|SE interface and on the relaxation time of different charge transport processes, the activation energy of the constriction resistance $E_{\mathrm{a,CC}}$ may approach that of the grain boundaries $E_{\mathrm{a,GB}}$.[35,68] Therefore an activation energy between $E_{\mathrm{a,bulk}}$ and $E_{\mathrm{a,GB}}$ is expected for $E_{\mathrm{a,CC}}$. Such a behavior has been observed for the Na|BASE interface as well as for the Li|LLZO interface.[28,33] In the case of the $\mathrm{Na_{bc}}$|NZSP0.4 interface, $E_{\mathrm{a,Int}}$ (0.37 eV) is equal to $E_{\mathrm{a,GB}}$ and significantly larger than $E_{\mathrm{a,bulk}}$ (0.26 eV). The higher activation energy of the interface $E_{\mathrm{a,Int}}$ can be explained by two effects. Given the small grain size (see Figure S1, Supporting Information), the high GB density should result in an $E_{\mathrm{a,CC}}$ close to $E_{\mathrm{a,GB}}$.[35] Second, LLZO as well as BASE are stable in contact with their alkali metal, while this is not the case for NZSP0.4. Hence, the formed interphase will also influence the overall ion transport across the interface. Depending on the activation energy of the $\mathrm{Na^+}$ ion transport through the formed interphase, $E_{\mathrm{a,Interphase}}$, the determined $E_{\mathrm{a,Int}}$ will be higher ($E_{\mathrm{a,Interphase}} > E_{\mathrm{a,CC}}$) or lower ($E_{\mathrm{a,Interphase}} < E_{\mathrm{a,CC}}$). If $E_{\mathrm{a,Interphase}} > E_{\mathrm{a,CC}}$, this would lead to a higher $E_{\mathrm{a,Int}}$ even when the total increase in resistance is comparably small.

Based on these results, we conclude that charge transfer at the Na|NZSP0.4 interface is not the rate-determining step, but current constriction. The vanishing interface impedance at increased external loads as well as the similar values of $E_{\mathrm{a,Int}}$ and $E_{\mathrm{a,GB}}$ give evidence for this interpretation.

2.3. Na|NZSP0.4 Interface During Anodic Dissolution

Recent studies have shown that the overpotential at alkali metal|SE interfaces increases during anodic dissolution of the metal, while it remains unchanged during deposition.[31,69] The rising overpotential is explained by local loss of contact and the formation of pores at the interface. Hence, the pore formation during anodic dissolution is the limiting phenomenon during the cycling of metal|SE interfaces as inverting the current direction leads to dendrite formation due to current focusing. To monitor the evolution of the Na|NZSP0.4 interface during anodic dissolution, an alternating approach comprising chronopotentiometry (CP) and PEIS has been used as a dissolution protocol. During dissolution, the current density was incrementally increased from 67 to 340 µA cm^{-2}.

With proceeding dissolution, an additional contribution in the mid-/low-frequency range (<100 kHz) of the measured impedance spectra was observed in the Nyquist plots depicted in **Figure 6**a. This additional impedance contribution is attributed to the CC effect at the interface. The equivalent circuit depicted in Figure 6a was used for fitting the impedance data. The series resistance describing bulk transport in the solid electrolyte was assumed to be constant. The results are summarized in Figure 6b. Within the first 200 min, all resistances remain unchanged (see Figure 6b), which is in accordance with the constant potential curve depicted in Figure 6c. After 350 min, R_{Int} rises strongly until the experiment was finished, while R_{bulk} and R_{GB} do not change significantly. Clearly, R_{Int} is mainly responsible for the increasing overpotential (see Figure 6c) during anodic dissolution. C_{Int} decreases with increasing dissolution time highlighting the contact loss at the interface and is consistent with the described CC effect.[34,35] After reaching

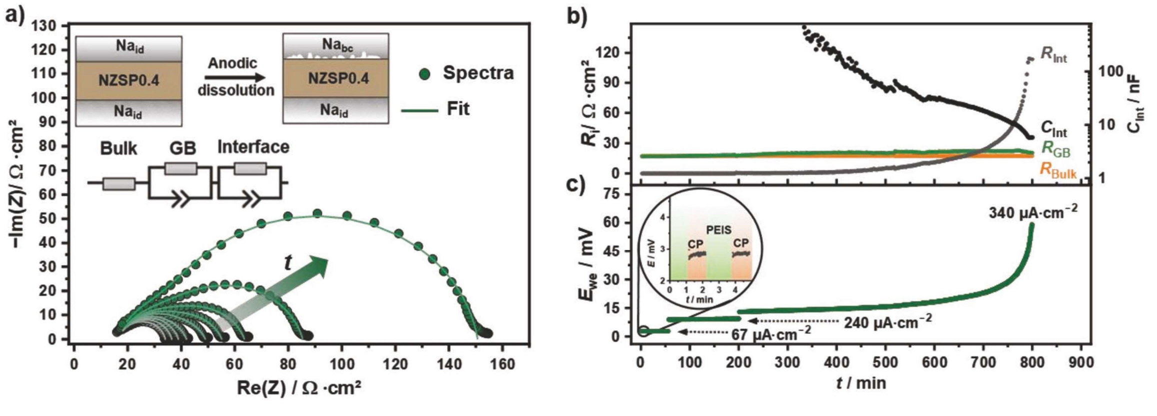

Figure 6. Anodic dissolution of sodium at the Na|NZSP0.4 interface with an applied uniaxial pressure of 11 MPa to gain an ideally reversible electrode ($\mathrm{Na_{id}}$). The dissolution was conducted at 25 °C without external load, despite a small pressure required for contacting the current collectors. The sodium electrode was dissolved in intervals of 60 s by chronopotentiometry (CP) and then characterized by PEIS. a) Selected impedance spectra during anodic dissolution. With increasing dissolution time, an interface-related contribution forms at low frequencies. b) Temporal evolution of determined resistances for bulk, grain boundary, and interface as well as the capacitance of the interface. c) Voltage profile of the anodic dissolution at current densities of 67, 240, and 340 µA cm^{-2} up to a cut-off voltage of 60 mV.

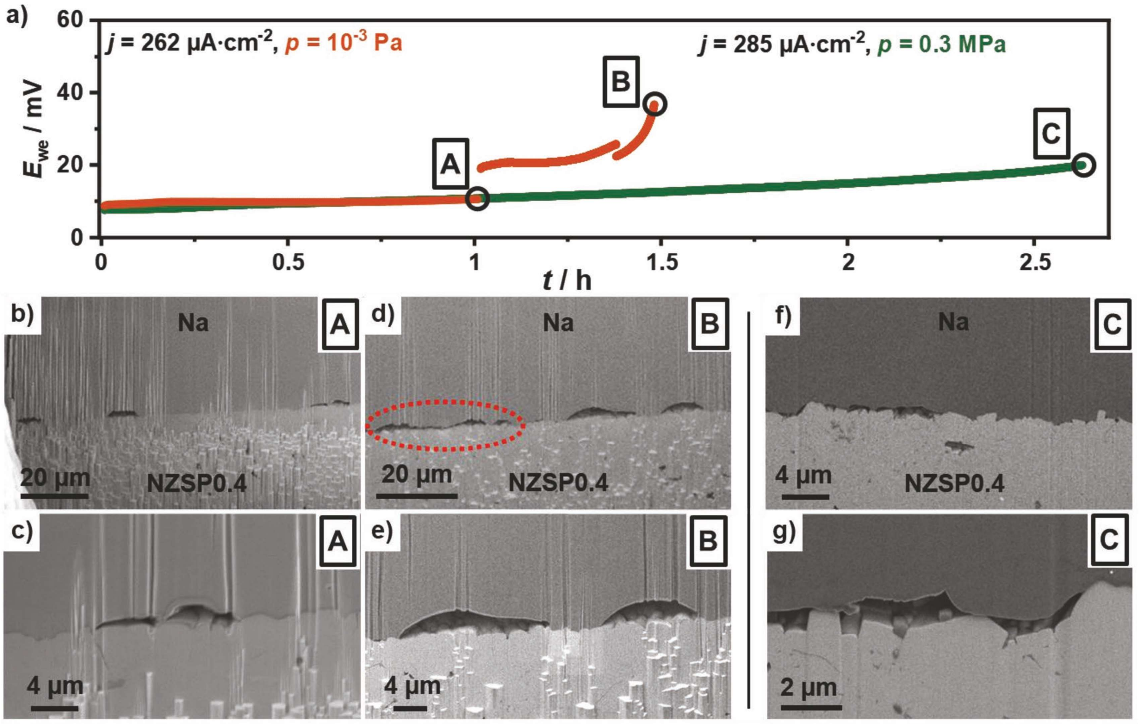

Figure 7. a) Voltage profile of a symmetric Na_{id}|NZSP0.4|Na_{id} cell in which one electrode was anodically dissolved in vacuum (orange) and at an external pressure of 0.3 MPa (green). The marked points A, B, and C show after which dissolution times cross-sections of the interface have been prepared and investigated. Cross-section of the Na|NZSP0.4 interface after a dissolution time of 1 h in vacuum at b) low and c) high magnification. Cross-section of the interface after a dissolution time of 1.5 h in vacuum at d) low and e) high magnification. The red circle indicates an insulating gap at the interface. Cross-section after a dissolution time of 2.5 h with external load of 0.3 MPa at f) low and g) high magnification.

the cut-off voltage of 60 mV after 700 min a total amount of 28 µmol sodium was dissolved, which corresponds to a thickness of about 16 µm normalized to the geometric electrode area.

Following the anodic dissolution steps, the activation energies of the different resistance contribution were determined. The activation energies for bulk, grain boundary, and interface (see Table S4, Supporting Information) agree with the results of the previous section and give a consistent picture. Regardless of whether contact loss results from insufficient pressure during preparation or from anodic dissolution, the rate-limiting step is not affected. It is current constriction, which originates from the pores at the interface, thereby increasing the overvoltage.

The interface morphology formed during anodic dissolution was visualized by FIB-SEM cross-section. For preparation of the cross-section, the dissolution was paused and cells were transferred to the FIB-SEM system. After imaging the dissolution experiment with the same cell was continued. A strong dependence of the pore morphology on the applied external load is observed. Two symmetrical Na_{id}|NZSP0.4|Na_{id} cells were assembled and anodic dissolution was carried out at different external loads. To minimize the influence of creep and plastic deformation driven by an external load on the formed pore morphology, dissolution of one cell was performed inside the vacuum of an SEM at a pressure of $p = 10^{-3}$ Pa. Detailed information on the experimental set up is given in the Experimental Section. The obtained potential profile is given in **Figure 7**a. Starting with a potential of about 8 mV, a constant voltage plateau at $E_{WE} = 10$ mV was observed within the first hour. In the subsequently recorded cross-sections at the interface in Figure 7b,c, individual and separate lens-shaped pores can be seen. However, a larger part of the sodium electrode is still in contact with the SE. Upon further dissolution, a potential step from 10 to 20 mV is observed, which is due to different temperatures during individual dissolution steps. Since the experiments were conducted inside an SEM, exact temperature control was not possible. After a total dissolution time of 80 min, the initially flat potential profile develops into a steep increase. To visualize the pore morphology before complete contact loss is approached, the dissolution was stopped at a cut-of voltage of 36 mV. An increase in pore size after the second dissolution step is obvious, while maintaining a lens-shaped form (Figure 7d,e). Besides the growth of pores, very shallow pores are also observed leading to a large insulating gap at the interface (Figure 6d red circle). Therefore, the interfacial contact area between sodium and NZSP0.4 is drastically reduced to a few contact points explaining the steep increase in overpotential.

In the second case, an external load of 0.3 MPa was applied, while a current density comparable to the previous cell was used for anodic dissolution. At a comparable initial potential of 9 mV, no constant plateau was observed with an external pressure, but rather a linear increase until a cut-off voltage of 20 mV was reached (Figure 7a, green curve). Even after a dissolution time of 2.5 h, no steep increase of the potential was observed. The amount of sodium dissolved under low-potential conditions can be significantly increased with external pressure.

Compared to the previous cross-sections, no lens-shaped pores were obtained when dissolving anodically with external pressure. Still, large regions with interfacial contact are present at the interface (Figure 7f), while small pores were found only at some spots (Figure 7g). In these regions of contact loss, only "pillars" of the SE were still in contact with the electrode, while "valleys" were no longer in contact. Especially, small grains located in "valleys" were not contacted to the sodium electrode, introducing and enhancing the CC at this interface.

When comparing the result of the experiments conducted at different pressures, it must be noted that the time delay between the preparation of cross-sections and the end of anodic dissolution differed significantly. While a cross-section was prepared immediately after anodic dissolution in the SEM (at $p = 10^{-3}$ Pa), the external pressure of 0.3 MPa acted significantly longer in the corresponding experiment (10 h after end of anodic dissolution). A direct comparison between the two series of measurements is therefore challenging. Nevertheless, with an external pressure and a subsequent resting phase, a significantly higher amount of sodium can be dissolved without deteriorating the interfacial contact significantly.

2.4. Temporal Evolution of the Interface after Anodic Dissolution

Finally, the temporal evolution of the Na|NZSP0.4 interface after anodic dissolution was examined by impedance spectroscopy. For this purpose, a sodium anode in a symmetrical Na_{id}|NZSP0.4|Na_{id} cell was dissolved at a current density of 350 µA cm^{-2} under atmospheric pressure. Immediately after completion of the anodic dissolution, impedance spectra were recorded in intervals of 5 min to monitor the development of the interface behavior. To record changes of the interface during dissolution, galvanostatic electrochemical impedance spectroscopy (GEIS) was used.

Similar potential curves (**Figure 8**a) and a comparable impedance evolution (Figure 8b,c) were observed for continuous anodic dissolution, analogous to the successive dissolution in Figure 5a,c. After the dissolution had been finished, a strong decrease of the total resistance by several hundred Ω cm^2 is seen in Figure 8d,e. Within the first 20 min of this relaxation period the drop of resistance is pronounced. After 13 h of rest, the total resistance is only 7 Ω cm^2 higher than in the initial state indicating recovery of the interface. During the transition of the dissolution to the relaxation phase, a "swerving" as well as a "rolling in" of the impedance shape in the low-frequency range is monitored. The reason for this is the nonstationary interface state since significant changes of the interface take place during the impedance recording. This shows that strong relaxation effects occur at the interface directly after dissolution.

Following the resting phase, a second anodic dissolution of the same electrode was performed, whereby a potential curve similar to the first dissolution was obtained. In Figure 8f,g, the Nyquist plot of the pristine cells, after the dissolution and completion of the relaxation are shown. A decrease of impedance is also observed after a second dissolution step, which reached nearly the initial state indicating repeated equilibration at the Na|NZSP0.4 interface after continuous dissolution. Comparing the dissolved amounts of sodium, only one sixth (1.2 µm) could be dissolved during the second dissolution compared to the first dissolution step (7 µm). Thus, despite nearly identical impedances after resting, irreversible changes to the pristine interface are caused.

To check whether the observed and described equilibration is caused by the external load even when only atmospheric pressure was applied, the experiment was repeated at a pressure of 10^{-3} Pa. Figure S12 (Supporting Information) shows the potential curves and the impedances recorded during relaxation. Abrupt changes of the potential curve toward the end of the dissolution are probably due to the electronic contacting of the cell inside the vacuum chamber. The results obtained during the first dissolution step are identical to those obtained with atmospheric pressure. In the subsequent resting phase, also a decrease in total resistance is monitored, which indicates dynamic processes at the Na|NZSP0.4 interface even at extremely low external loads. Compared to the previous experiment, the equilibration of the interface after anodic dissolution is clearly less pronounced as the total resistance tends to a higher value (120 Ω cm^2) compared to the initial resistance of the pristine cell (42 Ω cm^2). Furthermore, only 73 nm of sodium can be dissolved in a following dissolution step.

We like to note that the quantity used to assess the equilibration of the interface is the current constriction contribution in the measured impedance. The impedance contribution of current constriction is affected by the properties characterizing an interface, e.g., contact area, pore size, and distribution of contact points.[34,35] Thus, the observed equilibration and the measured impedance contribution result from a change of the interfacial properties after dissolution and cannot be assigned only to an improvement of the contact area. Reduction of the pore size can occur through diffusion of vacancies into the bulk of the metal. Also, ad-atom diffusion can change the pore structure so that the surface energy is minimized (Ostwald ripening). Both processes show a pronounced time dependence with respect to changes in the pore morphology at the interface. Besides diffusion and energy minimization, mechanical properties of the metal electrode, especially creep, affect the interfacial pore morphology, too. Depending on temperature, microstructure (grain size and shape), dislocation density and applied stress, different mechanisms of creep dominate the deformation of polycrystalline materials. Due to the high homologous temperature and the low yield strength (0.2–0.3 MPa), deformation of sodium at room temperature and atmospheric pressure is mainly dominated by dislocation climbing, rate-limited by lattice diffusion.[46,47] At low external stress, the deformation of sodium is dominated by lattice diffusion, known as Nabarro–Herring creep.[70] Compared to diffusion-based creep mechanisms such as Nabarro–Herring and Coble creep, higher strain rates are obtained with dislocation creep, which explains the larger amount of dissolved sodium at higher external load.[44]

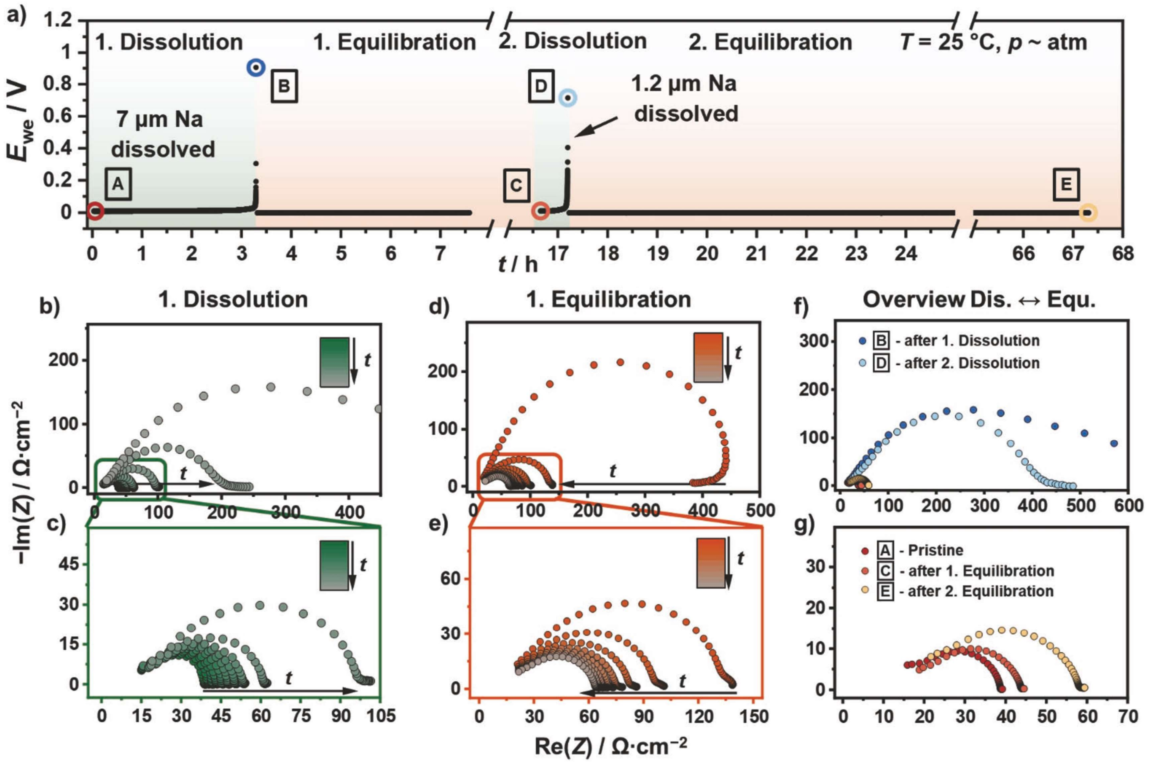

Figure 8. a) Voltage curve of a symmetric $Na_{id}|NZSP0.4|Na_{id}$ cell dissolved anodically by galvanostatic electrochemical impedance spectroscopy at a current density of 350 µA cm^{-2}. After reaching the cut-off voltage of 1 V, the electrode was analyzed by PEIS in intervals of 5 min until the change of the real part of the impedance is <1 Ω. The described procedure was repeated with the same electrode. b) Development of impedance (GEIS measurement) during anodic dissolution of the WE with an enlarged section in (c). Analogous to the previous measurements, impedance increases with increasing dissolution time. d) Obtained impedance data during equilibration period are shown in (d) and (e). A clear drop of the total resistance can be seen in (d), which is close to the original impedance. Representation of selected impedance spectra (marked as colored points in (a)) before and after a dissolution step as well as after completion of the relaxation of the entire measurement protocol are given in (f) and (g).

We assume that the observed interface equilibration is mainly due to creep of sodium, in addition to the minimization of surface energies and the annihilation of vacancies. When lowering the external stress to a minimum (10^{-3} Pa) equilibration is still observed, which is attributed to vacancy diffusion, meaning diffusion due to a concentration gradient. Since creep is pressure- and time-dependent, the amount of sodium that can be dissolved after equilibration is also determined by the dissolution protocol. For instance, a stepwise dissolution could dissolve significantly more sodium (16 µm) compared to a continuous dissolution (7 µm), similarly to the effect of a discontinuous charging and discharging protocols known from rechargeable lithium metal[71] or lithium-ion-batteries.[72] This is especially crucial for real battery applications, in which significantly different dissolution protocols would be needed depending on the required application.

3. Conclusions

In this study, a detailed electrochemical analysis of the interfacial behavior of NZSP0.4 in contact with sodium is presented. Exploring its thermodynamic stability, the formation of a kinetically stabilized interlayer (SEI) within 4 h after contacting through the reduction of zirconium monitored by in situ XPS was observed. The influence of the formed interphase resistance $R_{\mathrm{Interphase}}$ is below 2 Ω cm^2 and could not be fully resolved by impedance spectroscopy, but clearly identified by TEM. We conclude that the SEI formation of NZSP0.4 allows stable operation of the sodium anode.

In the next step, we measured the interfacial impedance at different pressures and temperatures under equilibrium conditions. We found that the interface contribution to the impedance spectrum at low frequencies is caused by current constriction, i.e., by non-ideal physical contact between sodium and NZSP0.4 due to insufficient mechanical pressure. Based on the similarity of the determined activation energies for $E_{a,\mathrm{Int}}$ and $E_{a.\mathrm{GB}}$, as well as a completely vanishing interfacial resistance at high mechanical pressures, neither the formed SEI nor the charge transfer limit the ion transport across the Na|NZSP0.4 interface.

Third, we studied the formed interfacial morphology at the Na|NZSP0.4 interface during anodic dissolution of the metal electrode at different external loads. Impedances recorded during anodic dissolution support the conclusion of current constriction being the origin of the interfacial resistance R_{Int}. Visualization of the interfacial morphology by FIB-SEM after anodic dissolution reveals the formation of lens-shaped pores when no external pressure was applied during dissolution, whereas with external load, smaller, shallower insulating gaps were observed.

Finally, the temporal evolution of the interfacial morphology after anodic dissolution was analyzed by means of time-resolved impedance spectroscopy. Independent of an external pressure, a decrease of the interfacial contribution with time was observed in the impedance spectra after anodic dissolution, which we interpret as dynamic change of the interfacial pore structure. The cause of equilibration without external pressure is attributed to diffusion of vacancies (like Nabarro–Herring creep) as well as ad-atoms. Applying an external pressure leads to a pronounced equilibration which is attributed to a more enhanced dislocation creep of sodium. Accordingly, for real battery applications, resting periods for equilibration of interfaces play a central role to maintain interfacial contact in addition to external load.

To gain a better understanding of the equilibration, further studies are necessary regarding the influence of current density and temperature. Based on the results, the sodium metal anode could show less degradation due to pore formation during cell discharge compared to the lithium metal anode especially in low temperature regions—which may also reduce the dendrite risk during charging.

4. Experimental Section

Synthesis of Solid Electrolyte: NZSP0.4 powder was synthesized on a 1 kg scale using a solution-assisted solid-state reaction method (SA-SSR).[16] $NaNO_3$ (VWR), $ZrO(NO_3)_2$ (Aldrich), $Si(OCH_2CH_3)_4$ (Merck), and $NH_4H_2PO_4$ (Merck) were used as starting materials with a purity of >99%. Stoichiometric amounts of $NaNO_3$ and $ZrO(NO_3)_2$ were dissolved in deionized water. A stoichiometric amount of $Si(OCH_2CH_3)_4$ was also added to the solution while stirring. When $Si(OCH_2CH_3)_4$ was hydrolyzed, the stoichiometric amount of $NH_4H_2PO_4$ was added to the system during stirring. The whole mixture was dried at 85 °C. The dried powder was calcined at 800 °C for 3 h. After calcination, a white powder was obtained. The calcined powder was then milled in ethanol with zirconia balls on a milling bench for 48 h, and dried at 70 °C for 12 h. NZSP0.4 powder was put into a cylindrical pressing mold (diameter of 13 mm) and pressed with a uniaxial pressure of about 100 MPa at room temperature. The pressed pellets were sintered at 1280 °C for 5 h. The obtained pellets were white in color and had a thickness of about 2 mm and a diameter of 10 mm. The relative density of the sintered pellets was >95%.

Materials Characterization: The synthesized NZSP0.4 SE was characterized using a PANalytical Empyrean powder diffractometer in Bragg–Brentano Θ–Θ geometry. A Cu K$\alpha_{1,2}$ radiation ($\lambda(\alpha_1) = 1.540\,596$ Å, $\lambda(\alpha_2) = 1.544\,410$ Å) X-ray source was used and operated at 40 kV and 40 mA. Measurements were recorded in the 2Θ range of 10°–90° with a step size of 0.026° using a PIXcel3D 1×1 detector. For the measurement, the sample was manually ground and placed on a (911) orienting silicon zero background holder. Examinations of the microstructure of the surface were carried out using a Carl Zeiss Ultra field emission SEM instrument (Merlin). Surface roughness of the SE was determined using a profilometer (Alpha-Step D-600 Stylus, KLA Tencor). The R_a value was averaged from three measurements with a scan length of 0.5 mm and a force of 1 mg.

Cell Assembling/Preparation: For electrochemical characterization of bulk and grain boundary properties, symmetrical Au|NZSP0.4|Au cells with blocking electrodes were analyzed. Gold electrodes with thicknesses of 200 nm were prepared by thermal evaporation. The electrode area was determined by evaluating optical images of the electrodes utilizing the software package ImageJ.[73] NZSP0.4 was used without any further surface treatment or polishing step. Afterward the cells were sealed in pouch bags to ensure inert atmosphere during measurements.

All impedance measurements for the study of the interfaces were performed on symmetrical Na|NZSP0.4|Na cells. A straightforward analysis of both interfaces by impedance spectroscopy is only possible in the case of identical interfaces in equilibrium. If this condition is not fulfilled, the introduction of a reference electrode is necessary to distinguish both interfaces. Since establishing a reference electrode for ceramic solid electrolytes is challenging, a QRE was used to monitor changes in an interface as has been shown for the Li|LLZO interface.[33] Using a two-electrode setup, one electrode has to be a resistance-free quasireversible interface, as demonstrated by Krauskopf et al.[33] By applying high external pressure, a virtually resistance-free interface Na|NZSP0.4 has also been obtained (see results). If a “normal” sodium electrode (working electrode, WE) with a higher interfacial resistance is combined with a QRE Na|NZSP0.4 half-cell, the contribution of the CE is minimized, and quasi only the WE is monitored.

For preparation of QRE Na|NZSP0.4 half-cells sodium foils were freshly prepared in an Ar-filled glovebox. Surface impurities were mechanically removed from a sodium ingot. The resulting clean sodium was pressed gradually to a foil with a thickness of ≈150 µm using a hand press. Electrodes with a diameter of 6 mm were then punched out and attached to a copper foil (10 mm in size). Before placing the sodium foil on the SE, the sodium surface was mechanically cleaned again. The other side of the SE was covered with a thin copper foil to protect the surface during the pressing process. Subsequently, the sodium foil was pressed onto the SE with a uniaxial load of 11 MPa for 1 min. For pressure control, an in-house built pressure setup equipped with a compression load cell FC22 (TE Connectivity) was used. Afterward, the cells were vacuum-sealed four times in plastic envelopes (CPR GmbH, Sonodome) and pressed isostatic at 100 MPa for 15 min at room temperature. To ensure that the formation of the interlayer was complete, the QRE half-cells were stored for 24 h in Ar atmosphere. The preparation of the sodium WEs varied and will be described for each experiment individually. A schematic illustration of the preparation process is shown in Figures S13 (Supporting Information).

To study the influence of pressure on the Na|NZSP0.4 interface, a sodium foil was pressed onto a QRE half-cell. Thereto, the cell was sandwiched between two Ni current collectors in a home-made pressure setup. The targeted pressure was maintained for 20 s and released afterward to a base load corresponding to 1 N (about 20 kPa). Reaching the base pressure, impedance spectra were recorded in the frequency range between 7 MHz and 10 Hz with a voltage amplitude of 10 mV using an SP-300 potentiostat (BioLogic Sciences Instruments). Afterward, the force was increased to a higher value than before, maintained for 20 s and released to the base pressure, followed by an impedance measurement. The procedure was repeated several times until a force of 215 N (about 4.2 MPa) was reached. The experiment was conducted in an Ar-filled glove box at room temperature.

For time-dependent impedance measurements, sodium WE was attached on a NZSP0.4|Na_{id} QRE half-cell using a uniaxial pressure of 11 MPa for 1 min. Directly after assembly, impedances were measured at intervals of 5 min with the previously described SP-300 potentiostat in the frequency range between 7 MHz and 100 Hz. To account for temperature fluctuations inside the glovebox, a thermocouple 306 (VOLTCRAFT) was placed next to the cell, tracking the temperature every minute.

Temperature dependence of symmetrical Na|NZSP0.4|Na and Au|NZSP0.4|Au cells was studied inside a climate chamber LabEvent

(Weisstechnik) between –40 and 40 °C. Impedance spectra were recorded in the frequency range from 7 MHz to 1 Hz with a voltage amplitude of 10 mV using a VMP-300 (BioLogic Sciences Instruments) potentiostat. Cells were sealed in pouch bags to ensure inert atmosphere during measurement.

GEIS measurements were performed in the frequency range between 7 MHz and 100 Hz with an applied direct current of about 300 µA cm^{-2} and a current amplitude of 30 µA cm^{-2} using SP-150 or VMP-300 potentiostats (BioLogic Sciences Instruments). Experiments under vacuum conditions were carried out inside an SEM chamber. The cells were contacted via a micromanipulator. A detailed explanation of the set-up and methodology is given in literature.[74,75] After the anodic dissolution was completed, PEIS measurements were performed in intervals of 7 min to monitor relaxation of the interface using the same instrumental parameters as described above.

Impedance data were analyzed by using Relaxis3 software (rhd instruments). Data points in the higher and lower frequency range with a relative error greater than 5% in Kramers–Kronig tests were not included in the data evaluation. Impedance spectra recorded above –30 °C were fitted with an additional *RQ*-element as the SE bulk contribution shifts into the measured frequency range. In impedance spectra below –30 °C the bulk contribution is described by a simple resistor. To eliminate the temperature variation of the time-dependent measurement series in the glovebox, the real part of the impedance was corrected as described in the Supporting Information. All impedance spectra were normalized to the geometric electrode area unless otherwise stated. The thickness of the SE has to be considered additionally when bulk and grain boundary (GB) properties are examined, which is roughly 2 mm for the samples investigated.

DRT analyses were carried out with the software package Relaxis3 (rhd instruments). The real and imaginary parts were considered for the analysis and 200 points were used for interpolation. The second derivative of the distribution function $\gamma(\tau)$ was used in the Tikhonov regularization problem. Calculations were performed using a regularization parameter $\lambda = 10^{-6}$.

In Situ X-Ray Photoelectron Spectroscopy: All XPS analyses were performed with a PHI5000 Versa Probe II system (Physical Electronics GmbH). A home-built sample holder was used for sputtering sodium metal on top of the electrolyte. Detailed information about the sample holder and the procedure of the in situ XPS sputtering can be found in previous reports.[76] In short, sodium is attached to a sail with an 85° angle of inclination by using copper tape and aligned to an Ar^{+}-ion gun. The SE is attached underneath the sail with nonconductive adhesive tape. By sputtering the sodium foil, a plasma is generated through which sodium is deposited on the SE. The reaction layer (i.e., the interphase) obtained is subsequently characterized by XPS. Spectra were monitored as a function of deposition time on top of the electrolyte. Sputtering of sodium was carried out with 4 kV Ar^{+}-ion gun in intervals of 3 min with a total sputtering time of 60 min.

For analysis, monochromatic Al K$_{\alpha}$ radiation (1486.6 eV) was used. The X-ray source was operated at 50 W with a voltage of 17 kV and a beam diameter of 200 μm. Spectra were recorded with a step size and dwell time per step of 0.1 eV and 50 ms, respectively. A pass energy for the analyzer of 46.95 eV was used to record XP spectra between the sodium deposition steps. Additionally, for XP spectra before, directly after and 8 h after the sodium deposition were recorded with an analyzer pass energy of 23.5 eV. For charge neutralization a combination of ion and low-energy electron beam was applied during the measurements.

Data evaluation was carried out with the software CasaXPS (Version 2.3.22, Casa Software Ltd.). XP spectra were calibrated to 284.8 eV using the aliphatic carbon C 1s signal. A Shirley-type background with a Gaussian–Lorentzian function (GL(30)) line shape was utilized for the signal evaluation. Additionally, fitting constraints were used, such as the FWHM constraint, energy splitting values known in the literature due to spin–orbit coupling and the resulting area ratios.

Focused Ion Beam Scanning Electron Microscopy: Cross-sections of the electrode|SE interface were carried out with a XEIA3 system (TESCAN GmbH). Samples were attached to a Leica stub with adhesive copper tape and transferred using the Leica EM VCT500 system (Leica Microsystems GmbH). Before milling, the samples were cooled to –133 °C by liquid nitrogen and cooling was maintained during the analysis. Xe^{+} ions with an energy of 30 kV were used in all experiments. Beam currents for milling and polishing were set to 2 µA and 30 nA. For preparation of the electron transparent specimen an Auriga system (Carl Zeiss NTS GmbH) with a liquid nitrogen stage (GATAN GmbH; operation temperature: –185 °C) has been used. Thinning process of the TEM lamella was performed using Ga^{+} ions with 30 kV high tension energy and beam current of 240 pA.

Transmission Electron Microscopy: TEM analysis was performed at the aberration corrected (STEM) Themis 300 system (Thermo Fischer Scientific) using a beam energy of 300 kV and a screen current of 100 pA. EDX analysis was conducted with a Super-X EDX detector. Characterization was carried out under cryogenic conditions (–185 °C) using a liquid nitrogen cooled 915 cryo transfer holder (GATAN GmbH). Data evaluation was conducted using Velox software package (Thermo Fischer Scientific).

Supporting Information

Supporting Information is available from the Wiley Online Library or from the author.

Acknowledgements

This work contributes to the research performed at CELEST (Center for Electrochemical Energy Storage Ulm-Karlsruhe) and was funded by the German Research Foundation (DFG) under Project ID 390874152 (POLiS Cluster of Excellence). Financial support by the BMBF Cluster of Competence FESTBATT (S.B., Project No. 03XP0180) is also acknowledged. J.K.E. acknowledges financial support by the DFG via the GRK (Research Training Group) 2204 “Substitute Materials for sustainable Energy Technologies.” The authors acknowledge the Karlsruhe Nano Micro Facility (KNMFi) at KIT for providing TEM access. Experimental support by Dr. Klaus Peppler and Dr. Boris Mogwitz (JLU Giessen) is acknowledged.

Open access funding enabled and organized by Projekt DEAL.

Conflict of Interest

The authors declare no conflict of interest.

Author Contributions

T.O., T.F., and S.B. designed the experiments. Q.M. prepared the solid electrolyte. T.O. performed all XPS experiments, impedance analysis and cross sections experiments. T.F. supported in situ SEM studies. T.O. and J.S. interpreted the XPS. T.O., S.B., J.K.E., and T.F. interpreted impedance analysis. Z.D. performed TEM sample preparation and characterization. T.O., Z.D., and C.K. interpreted TEM analysis. T.O., S.B., M.R., Q.M., and J.J. wrote the manuscript. All authors discussed the results and contributed to the preparation of the manuscript. C.K., O.G., and C.H. reviewed and edited the manuscript.

Data Availability Statement

The data that support the findings of this study are available from the corresponding author upon reasonable request.

Keywords

current constriction, impedance spectroscopy, interphase growth, NASICON electrolytes, SEI formation, sodium metal anodes

Received: August 8, 2022
Revised: September 28, 2022

---

[1] J. Janek, W. G. Zeier, *Nat. Energy* **2016**, *1*, 1167.
[2] B. Xiao, T. Rojo, X. Li, *ChemSusChem* **2019**, *12*, 133.
[3] J. Cui, A. Wang, G. Li, D. Wang, D. Shu, A. Dong, G. Zhu, J. Luo, B. Sun, *J. Mater. Chem. A* **2020**, *8*, 15399.
[4] X. Xia, C.-F. Du, S. Zhong, Y. Jiang, H. Yu, W. Sun, H. Pan, X. Rui, Y. Yu, *Adv. Funct. Mater.* **2022**, *32*, 2110280.
[5] M. D. Slater, D. Kim, E. Lee, C. S. Johnson, *Adv. Funct. Mater.* **2013**, *23*, 947.
[6] C. Monroe, J. Newman, *J. Electrochem. Soc.* **2004**, *151*, A880.
[7] Z. Zhang, Y. Shao, B. Lotsch, Y.-S. Hu, H. Li, J. Janek, L. F. Nazar, C.-W. Nan, J. Maier, M. Armand, L. Chen, *Energy Environ. Sci.* **2018**, *11*, 1945.
[8] U. von Alpen, M. Bell, H. Hofer, *Solid State Ionics* **1981**, *3–4*, 215.
[9] J. B. Goodenough, H. Y.-P. Hong, J. A. Kafalas, *Mater. Res. Bull.* **1976**, *11*, 203.
[10] Y. B. Rao, K. K. Bharathi, L. N. Patro, *Solid State Ionics* **2021**, *366–367*, 115671.
[11] Z. Yang, B. Tang, Z. Xie, Z. Zhou, *ChemElectroChem* **2021**, *8*, 1035.
[12] A. G. Jolley, G. Cohn, G. T. Hitz, E. D. Wachsman, *Ionics* **2015**, *21*, 3031.
[13] Q. Ma, M. Guin, S. Naqash, C.-L. Tsai, F. Tietz, O. Guillon, *Chem. Mater.* **2016**, *28*, 4821.
[14] Z. Zhang, Z. Zou, K. Kaup, R. Xiao, S. Shi, M. Avdeev, Y.-S. Hu, D. Wang, B. He, H. Li, X. Huang, L. F. Nazar, L. Chen, *Adv. Energy Mater.* **2019**, *9*, 1902373.
[15] J. A. Kafalas, J. R. Cava, in *Proc. Int. Conference on Fast Ion Transport in Solids, Electrodes, and Electrolytes* (Eds: P. Vashishta, J. N. Mundy, G. K. Shenoy), Elsevier North Holland, Amsterdam **1979**, pp. 419–422.
[16] Q. Ma, C.-L. Tsai, X.-K. Wei, M. Heggen, F. Tietz, J. T. S. Irvine, *J. Mater. Chem. A* **2019**, *7*, 7766.
[17] W. Zhou, Y. Li, S. Xin, J. B. Goodenough, *ACS Cent. Sci.* **2017**, *3*, 52.
[18] X. Yu, A. Manthiram, *Matter* **2019**, *1*, 439.
[19] J. Yang, Z. Gao, T. Ferber, H. Zhang, C. Guhl, L. Yang, Y. Li, Z. Deng, P. Liu, C. Cheng, R. Che, W. Jägermann, R. Hausbrand, Y. Huang, *J. Mater. Chem. A* **2020**, *8*, 7828.
[20] E. Matios, H. Wang, C. Wang, X. Hu, X. Lu, J. Luo, W. Li, *ACS Appl. Mater. Interfaces* **2019**, *11*, 5064.
[21] T. Wu, Z. Wen, C. Sun, X. Wu, S. Zhang, J. Yang, *J. Mater. Chem. A* **2018**, *6*, 12623.
[22] X. Miao, H. Di, X. Ge, D. Zhao, P. Wang, R. Wang, C. Wang, L. Yin, *Energy Storage Mater.* **2020**, *30*, 170.
[23] X. Chi, F. Hao, J. Zhang, X. Wu, Y. Zhang, S. Gheytani, Z. Wen, Y. Yao, *Nano Energy* **2019**, *62*, 718.
[24] M. M. Gross, L. J. Small, A. S. Peretti, S. J. Percival, M. A. Rodriguez, E. D. Spoerke, *J. Mater. Chem. A* **2020**, *8*, 17012.
[25] H. Fu, Q. Yin, Y. Huang, H. Sun, Y. Chen, R. Zhang, Q. Yu, L. Gu, J. Duan, W. Luo, *ACS Mater. Lett.* **2020**, *2*, 127.
[26] Y. Uchida, G. Hasegawa, K. Shima, M. Inada, N. Enomoto, H. Akamatsu, K. Hayashi, *ACS Appl. Energy Mater.* **2019**, *2*, 2913.
[27] J. A. S. Oh, Y. Wang, Q. Zeng, J. Sun, Q. Sun, M. Goh, B. Chua, K. Zeng, L. Lu, *J. Colloid Interface Sci.* **2021**, *601*, 418.
[28] M.-C. Bay, M. Wang, R. Grissa, M. V. F. Heinz, J. Sakamoto, C. Battaglia, *Adv. Energy Mater.* **2020**, *10*, 1902899.
[29] E. Quérel, I. D. Seymour, A. Cavallaro, Q. Ma, F. Tietz, A. Aguadero, *J. Phys. Energy* **2021**, *3*, 44007.
[30] C.-L. Tsai, T. Lan, C. Dellen, Y. Ling, Q. Ma, D. Fattakhova-Rohlfing, O. Guillon, F. Tietz, *J. Power Sources* **2020**, *476*, 228666.
[31] D. S. Jolly, Z. Ning, J. E. Darnbrough, J. Kasemchainan, G. O. Hartley, P. Adamson, D. E. J. Armstrong, J. Marrow, P. G. Bruce, *ACS Appl. Mater. Interfaces* **2020**, *12*, 678.
[32] H. Koshikawa, S. Matsuda, K. Kamiya, M. Miyayama, Y. Kubo, K. Uosaki, K. Hashimoto, S. Nakanishi, *J. Power Sources* **2018**, *376*, 147.
[33] T. Krauskopf, H. Hartmann, W. G. Zeier, J. Janek, *ACS Appl. Mater. Interfaces* **2019**, *11*, 14463.
[34] J. K. Eckhardt, P. J. Klar, J. Janek, C. Heiliger, *ACS Appl. Mater. Interfaces* **2022**, *14*, 35545.
[35] J. K. Eckhardt, T. Fuchs, S. Burkhardt, P. J. Klar, J. Janek, C. Heiliger, *ACS Appl. Mater. Interfaces* **2022**, *14*, 42757.
[36] J. Fleig, *Solid State Ionics* **1998**, *113–115*, 739.
[37] S.-K. Otto, T. Fuchs, Y. Moryson, C. Lerch, B. Mogwitz, J. Sann, J. Janek, A. Henss, *ACS Appl. Energy Mater.* **2021**, *4*, 12798.
[38] T. Krauskopf, F. H. Richter, W. G. Zeier, J. Janek, *Chem. Rev.* **2020**, *120*, 7745.
[39] C. Wang, H. Jin, Y. Zhao, *Small* **2021**, *17*, e2100974.
[40] S. Ohno, T. Bernges, J. Buchheim, M. Duchardt, A.-K. Hatz, M. A. Kraft, H. Kwak, A. L. Santhosha, Z. Liu, N. Minafra, F. Tsuji, A. Sakuda, R. Schelm, S. Xiong, Z. Zhang, P. Adelhelm, H. Chen, A. Hayashi, Y. S. Jung, B. V. Lotsch, B. Roling, N. M. Vargas-Barbosa, W. G. Zeier, *ACS Energy Lett.* **2020**, *5*, 910.
[41] J. Janek, *Solid State Ionics* **1997**, *101*, 721.
[42] S. Majoni, J. Janek, *Ber. Bunsengesellschaft phys. Chem.* **1998**, *102*, 756.
[43] M. Rohnke, C. Rosenkranz, J. Janek, *Solid State Ionics* **2006**, *177*, 447.
[44] P. M. Sargent, M. F. Ashby, *Scr. Metall.* **1984**, *18*, 145.
[45] A. Schröder, J. Fleig, D. Gryaznov, J. Maier, W. Sitte, *J. Phys. Chem. B* **2006**, *110*, 12274.
[46] M. J. Wang, J.-Y. Chang, J. B. Wolfenstine, J. Sakamoto, *Materialia* **2020**, *12*, 100792.
[47] C. D. Fincher, Y. Zhang, G. M. Pharr, M. Pharr, *ACS Appl. Energy Mater.* **2020**, *3*, 1759.
[48] D. K. Singh, T. Fuchs, C. Krempaszky, P. Schweitzer, C. Lerch, F. H. Richter, J. Janek, *Adv. Funct. Mater.*, https://doi.org/10.1002/adfm.202211067.
[49] H. Tang, Z. Deng, Z. Lin, Z. Wang, I.-H. Chu, C. Chen, Z. Zhu, C. Zheng, S. P. Ong, *Chem. Mater.* **2018**, *30*, 163.
[50] V. Lacivita, Y. Wang, S.-H. Bo, G. Ceder, *J. Mater. Chem. A* **2019**, *7*, 8144.
[51] J. Maier, U. Warhus, E. Gmelin, *Solid State Ionics* **1986**, *18–19*, 969.
[52] Z. Zhang, S. Wenzel, Y. Zhu, J. Sann, L. Shen, J. Yang, X. Yao, Y.-S. Hu, C. Wolverton, H. Li, L. Chen, J. Janek, *ACS Appl. Energy Mater.* **2020**, *3*, 7427.
[53] S. Wang, H. Xu, W. Li, A. Dolocan, A. Manthiram, *J. Am. Chem. Soc.* **2018**, *140*, 250.
[54] Z. Gao, J. Yang, H. Yuan, H. Fu, Y. Li, Y. Li, T. Ferber, C. Guhl, H. Sun, W. Jägermann, R. Hausbrand, Y. Huang, *Chem. Mater.* **2020**, *32*, 3970.
[55] Z. Bastl, A. I. Senkevich, I. Spirovová, V. Vrtílková, *Surf. Interface Anal.* **2002**, *34*, 477.
[56] C. Morant, J. M. Sanz, L. Galán, L. Soriano, F. Rueda, *Surf. Sci.* **1989**, *218*, 331.
[57] S. P. Kowalczyk, L. Ley, F. R. McFeely, R. A. Pollak, D. A. Shirley, *Phys. Rev. B* **1973**, *8*, 3583.
[58] Q. Wu, *Solid State Ionics* **2004**, *167*, 155.
[59] A. Barrie, F. J. Street, *J. Electron Spectrosc. Relat. Phenom.* **1975**, *7*, 1.
[60] Z. Gao, J. Yang, G. Li, T. Ferber, J. Feng, Y. Li, H. Fu, W. Jägermann, C. W. Monroe, Y. Huang, *Adv. Energy Mater.* **2022**, *12*, 2103607.

[61] K. Song, D. A. Agyeman, M. Park, J. Yang, Y.-M. Kang, *Adv. Mater.* **2017**, *29*, 1606572.

[62] B. Lee, D.-H. Seo, H.-D. Lim, I. Park, K.-Y. Park, J. Kim, K. Kang, *Chem. Mater.* **2014**, *26*, 1048.

[63] B. Verlinden, *Thermo-Mechanical Processing of Metallic Materials*, Elsevier, Amsterdam **2010**.

[64] X. Zhang, Q. J. Wang, K. L. Harrison, S. A. Roberts, S. J. Harris, *Cell Rep. Phys. Sci.* **2020**, *1*, 100012.

[65] J. T. S. Irvine, D. C. Sinclair, A. R. West, *Adv. Mater.* **1990**, *2*, 132.

[66] J. Fleig, J. Maier, *J. Electroceram.* **1997**, *1*, 73.

[67] J. Fleig, J. Maier, *Electrochim. Acta* **1996**, *41*, 1003.

[68] J. K. Eckhardt, S. Burkhardt, J. Zahnow, M. T. Elm, J. Janek, P. J. Klar, C. Heiliger, *J. Electrochem. Soc.* **2021**, *168*, 090516.

[69] J. Kasemchainan, S. Zekoll, D. S. Jolly, Z. Ning, G. O. Hartley, J. Marrow, P. G. Bruce, *Nat. Mater.* **2019**, *18*, 1105.

[70] J. Fiala, L. Kloc, J. Čadek, *Mater. Sci. Eng., A* **1991**, *137*, 163.

[71] M. Z. Mayers, J. W. Kaminski, T. F. Miller, *J. Phys. Chem. C* **2012**, *116*, 26214.

[72] S. Zhu, C. Hu, Y. Xu, Y. Jin, J. Shui, *J. Energy Chem.* **2020**, *46*, 208.

[73] C. A. Schneider, W. S. Rasband, K. W. Eliceiri, *Nat. Methods* **2012**, *9*, 671.

[74] T. Krauskopf, R. Dippel, H. Hartmann, K. Peppler, B. Mogwitz, F. H. Richter, W. G. Zeier, J. Janek, *Joule* **2019**, *3*, 2030.

[75] T. Krauskopf, B. Mogwitz, H. Hartmann, D. K. Singh, W. G. Zeier, J. Janek, *Adv. Energy Mater.* **2020**, *10*, 2000945.

[76] S. Wenzel, T. Leichtweiss, D. Krüger, J. Sann, J. Janek, *Solid State Ionics* **2015**, *278*, 98.

3.2 **Publication 2: "*Deposition of Sodium Metal at the Copper-NaSICON Interface for Reservoir-Free Solid-State Sodium Batteries*"**

The second publication of this doctoral thesis reports the formation of a SME at the CC|SE interface for reservoir-free sodium SSBs. For this purpose, the nucleation and growth of electrodeposited sodium at a Cu|NZSP interface was investigated at various current densities and stack pressures.

Based on the results presented in publication I, the morphological evolution of the electrodeposited sodium was monitored by EIS in combination with light and electron microscopy. Irrespective of the chosen deposition parameters, only minor changes in the impedance data after the first deposition step indicated that the lateral distribution of sodium is mainly influenced by the nucleation process. It was found that an increase of the current density improved the lateral distribution of the electrodeposited sodium. In contrast, only a slight improvement in the coverage of sodium by plastic deformation was observed when the applied stack pressure exceeded the yield strength of the electrodeposited sodium. Cross-sections of the interface revealed dense and uniform sodium layers between copper and NZSP, ideal for reservoir-free batteries. However, besides layer formation, islands and whiskers were observed, which caused gaps by separating the copper CC from the NZSP SE. Despite the observation of local spallation and cracks in the NZSP after electrodeposition by cross-sectioning and in situ TEM analysis, there was no evidence of detrimental dendrite formation causing short circuits according to the impedance analysis. The early growth of electrodeposited sodium was visualized by in situ TEM. It was found that faceted sodium whiskers appeared solely at contact spots between the copper CC and NZSP SE. This highlights the significance of the cell preparation process in terms of combining the SE and the CC and provides a first insight into the microstructure of electrodeposited SMEs. On the macroscopic scale, no mechanical failure, e.g., penetration by sodium whisker, was observed for the copper CC with a thickness of several micrometers. Deformation and expansion were found for thin copper CCs by TEM. Consequently, CC with a minimum thickness and mechanical stability are required for RFCs.

Overall, the second publication demonstrates the electrodeposition of dense and uniform sodium layers/islands at a CC|SE interface. This knowledge is essential for the initial formation step of an SME to realize reservoir-free solid-state battery concepts. Moreover, the study expands the knowledge about the influence of the current density and stack pressure on the lateral distribution and morphological interface evolution, providing a basis to further optimize electrodeposited SMEs.

The experiments were designed and planned by the first author, assisted by Dr. T. Fuchs under the supervision of Prof. M. Rohnke and Prof. J. Janek. The solid electrolyte was synthesized by Dr. Q. Ma and Dr. F. Tietz. Electrochemical experiments and postmortem optical and electron microscopy were performed by T. Ortmann. The in situ TEM characterization was carried out by Z. Ding. The corresponding data were interpreted by Z. Ding, Prof. C. Kübel, and T. Ortmann. The electrochemical impedance spectroscopy data were interpreted by Dr. J. K. Eckhardt and T. Ortmann. The manuscript was written by the first author and revised by eight co-authors.

This study was part of the research within the Cluster of Excellence for Post Lithium-Ion Storage.

Reprinted without modification according to the creative commons license CC BY-NC 4.0 DEED (https://creativecommons.org/licenses/by-nc/4.0/) from Ortmann, T.; Fuchs, T.; Eckhardt J. K.; Ding Z.; Ma, Q.; Tietz F.; Kübel C.; Rohnke M.; Janek J. Deposition of Sodium Metal at the Copper-NaSICON Interface for Reservoir-Free Solid-State Sodium Batteries. *Adv. Energy Mater.* **2023**, 2302729. https://doi.org/10.1002/aenm.202302729. Advanced Energy Materials published by Wiley-VCH GmbH.

RESEARCH ARTICLE

ADVANCED ENERGY MATERIALS
www.advenergymat.de

Deposition of Sodium Metal at the Copper-NaSICON Interface for Reservoir-Free Solid-State Sodium Batteries

Till Ortmann, Till Fuchs, Janis K. Eckhardt, Ziming Ding, Qianli Ma, Frank Tietz, Christian Kübel, Marcus Rohnke, and Jürgen Janek**

"Anode-free" solid-state battery concepts are explored extensively as they promise a higher energy density with less material consumption and simple anode processing. Here, the homogeneous and uniform electrochemical deposition of alkali metal at the interface between current collector and solid electrolyte plays the central role to form a metal anode within the first cycle. While the cathodic deposition of lithium has been studied intensively, knowledge on sodium deposition is scarce. In this work, dense and uniform sodium layers of several microns thickness are deposited at the Cu|$Na_{3.4}Zr_2Si_{2.4}P_{0.6}O_{12}$ interface with high reproducibility. At current densities of ≈1 mA•cm^{-2}, relatively uniform coverage is achieved underneath the current collector, as shown by electrochemical impedance spectroscopy and 3D confocal microscopy. In contrast, only slight variations of the coverage are observed at different stack pressures. Early stages of the sodium metal growth are analyzed by in situ transmission electron microscopy revealing oriented growth of sodium. The results demonstrate that reservoir-free ("anode-free") sodium-based batteries are feasible and may stimulate further research efforts in sodium-based solid-state batteries.

1. Introduction

Sodium solid-state batteries gain increasing research interest following the fast rise of sodium-ion batteries because of the potential use of sodium metal as anode material in combination with a solid electrolyte (SE) separator.[1–4] Sodium metal has a high specific capacity (q_{th} = 1165 mAh•g^{-1}) and low standard potential (E_{H} = −2.71 V vs standard hydrogen electrode), which can significantly increase energy and power density compared to carbon-based anodes.[5,6] Achieving a reversible sodium metal anode, however, poses several challenges – including a clean interface with sufficient interfacial contact, and an electrochemically stable interface with a solid electrolyte.[7] In addition, the high reactivity of sodium metal requires inert atmosphere conditions during processing, which increases the production costs of sodium solid-state batteries.[8,9]

"Zero-excess" or "reservoir-free" cell concepts, also often called "anode-free", could be a possible solution to these challenges and are encountering a rapidly growing research activity.[9–12] Most cathode active materials are synthesized in the discharged (sodiated or pre-sodiated) state.[13] During the first charge of a cell, sodium ions are extracted from the cathode active material and electrodeposited on a current collector (CC) (e.g., aluminum or copper), forming the sodium metal anode in situ.[14,15] This further increases the volumetric

---

T. Ortmann, T. Fuchs, J. K. Eckhardt, M. Rohnke, J. Janek
Institute for Physical Chemistry
Justus Liebig University Giessen
35392 Giessen, Germany
E-mail: marcus.rohnke@phys.chemie.uni-giessen.de;
juergen.janek@phys.chemie.uni-giessen.de
T. Ortmann, T. Fuchs, J. K. Eckhardt, M. Rohnke, J. Janek
Center for Materials Research (ZfM)
Justus Liebig University Giessen
35392 Giessen, Germany

The ORCID identification number(s) for the author(s) of this article can be found under https://doi.org/10.1002/aenm.202302729

DOI: 10.1002/aenm.202302729

Z. Ding, C. Kübel
Department of Materials & Earth Sciences
Technische Universität Darmstadt
64289 Darmstadt, Germany
Z. Ding, C. Kübel
Institute of Nanotechnology (INT) and Helmholtz Institute Ulm (HIU)
Karlsruhe Institute of Technology (KIT)
76344 Eggenstein-Leopoldshafen, Germany
Q. Ma, F. Tietz
Institute of Energy and Climate Research
Materials Synthesis and Processing (IEK-1)
Forschungszentrum Jülich GmbH
52425 Jülich, Germany
C. Kübel
Karlsruhe Nano Micro Facility (KNMF)
Karlsruhe Institute of Technology (KIT)
76344 Eggenstein-Leopoldshafen, Germany

and gravimetric energy density of reservoir-free cells compared to conventional Na|SE|Cathode battery architectures including a sodium foil. It also reduces production costs and energy consumption during cell manufacture by avoiding the need to produce and process sodium metal foils or layers.[9]

However, the successful operation of reservoir-free cells also poses a number of challenges. For instance, the uniform and reversible metal deposition on the CC plays a key role.[9] While the influence of (modified) CC material,[14–18] deposition protocol,[19] external stack pressure,[13] and electrolyte composition[20,21] on the cathodic deposition of sodium at a CC|liquid electrolyte interface have been studied, less is known about the deposition at CC|SE interface.[22]

The cathodic deposition of a parent metal on a SE has early been studied by silver deposition on AgX (X = Cl, Br) revealing a preferential nucleation at surface defects like surface scratches.[23–25] As shown by microelectrode experiments, the silver morphology strongly depends on the applied current density.[24] Later, the cathodic deposition of lithium at a CC|LiPON interface was systematically investigated by Motoyama et al.[26–28] By increasing the current density j_{app}, a growing number of lithium nuclei N_{Li} are formed per interface area, leading to more uniform deposition, while increasing the temperature decreases N_{Li} and affects the lithium morphology.[27] Since LiPON is an amorphous SE, lithium deposition was also studied at CC|$\mathrm{Li_{6+x}La_3Zr_{2-x}M_xO_{12}}$ (with M = Al, Ta) (LLZO) interfaces to evaluate the influence of grain boundaries and surface defects. As with LiPON, N_{Li} increases with higher j_{app}, with preferential nucleation observed at surface defects.[12,29,30] Recently, lithium deposition under a CC has been investigated in bulk solid-state batteries, showing the importance of the interfacial adhesion between CC and SE on the nucleation and growth behavior.[31] Moreover, the stack pressure was shown to affect the lateral growth behavior of lithium at the Cu|LLZO interface.[32] The operating principle of solid-state reservoir-free cells has already been demonstrated for lithium by electrodeposition of reasonable capacities of 5 mAh•cm^{-2} that corresponds to a layer thickness $d_{\mathrm{Li}} \approx 24$ µm.[31,33–35] For the same capacity, the layer thickness would nearly double in the case of sodium ($d_{\mathrm{Na}} \approx 44$ µm), due to the higher molar volume of sodium metal.

Based on the low interface-related resistance and the formation of a kinetically stabilized interphase in contact with sodium, $\mathrm{Na_{3.4}Zr_2Si_{2.4}P_{0.6}O_{12}}$ (NZSP) is an ideal SE to study the deposition of sodium at a CC|SE interface.[36–39] Copper was chosen as the current collector material because of its ease of processing on a laboratory scale and to avoid alloying effects with sodium. The nucleation and growth of sodium at the interface between copper and NZSP has not yet been studied and a detailed analysis of the evolution of the interfacial morphology at different deposition conditions is lacking in the literature.

In this study, we investigate the deposition of sodium at a Cu|NZSP interface at different current densities and stack pressures. Time-dependent impedance spectroscopy is used to analyze the morphological evolution during deposition, followed by 3D profiling of the copper current collector by confocal microscopy. An increase in current density results in more uniform sodium deposition. In contrast, no significant change in the sodium coverage is observed with increasing stack pressure. The growth of dense and uniform sodium layers between copper and NZSP is shown by cross-sections prepared via focused ion beam-scanning electron microscopy (FIB-SEM). In addition, island and whisker growth are observed, leading to the formation of gaps between copper and NZSP. In situ transmission electron microscopy (TEM) further reveals the growth of sodium whiskers with a faceted microstructure.

2. Results and Discussion

For the characterization of sodium deposition, Cu|NZSP|Na$_{\mathrm{id}}$ cells with a copper layer thickness of 5 µm were assembled. An ideal sodium counter electrode (Na$_{\mathrm{id}}$) acts as a sodium reservoir and quasi-reference electrode. A quasi-reference electrode is an electrode that shows no significant interfacial polarization and has a stable potential despite low current load, as demonstrated by Krauskopf et al.[36,40] Two series of measurements were performed to investigate the influence of current density j_{app} and external pressure p on sodium deposition. While a constant pressure of 2 MPa was used for the current density series, a constant current of 200 µA•cm^{-2} was used for the stack pressure series. An overview of the cell preparation and the selected j_{app} and p is shown in Figure S1 (Supporting Information).

2.1. Potential Profiles

Figure 1a,b shows the potential profiles of the performed current density and stack pressure series. The parameters (j_{app} and p) of the two measurement series were chosen such that the measurement at 200 µA•cm^{-2} and 2 MPa (light green curve) is included in both series (see Figure S1b, Supporting Information). Starting from an open circuit voltage of 1.0–2.1 V, all voltage profiles show a strong initial drop below the standard potential of sodium $E_{\mathrm{H}}(\mathrm{Na^+/Na})$ at the beginning of the deposition. Afterward, the voltage generally increases and turns into a plateau, which remains always below $E_{\mathrm{H}}(\mathrm{Na^+/Na})$. The initial potential drop can be attributed to the nucleation of sodium at the current collector and the subsequent plateau at higher potentials to the growth of the formed nuclei.[26,41,42]

The onsets of sodium deposition for the current density and stack pressure series are shown magnified in Figure 1c,d. The voltage profiles are slightly shifted along the x-axis to give a better overview of the individual curves. With increasing j_{app}, less fluctuations are observed in the potential curves during the first deposition step. While at atmospheric pressure (labeled with "ATM") a "smoother" potential profile is observed during the initial growth, slight fluctuations are present when a stack pressure is applied.

Fluctuations were also reported during the initial growth of lithium at a Cu|LLZO interface, while none are observed during electrodeposition from liquid electrolytes or thin film current collectors in contact with a SE.[12,26,27,32,42] A relationship between the fluctuations and the interfacial morphology, including the delamination of the copper current collector, is therefore likely.[32] Thus, for the Cu|NZSP interface the fluctuations may be due to changes in the interfacial morphology, including possible damage of the SE near the Na|NZSP interface. However, it is unclear why this phenomenon preferentially occurs at low current densities and stack pressures.

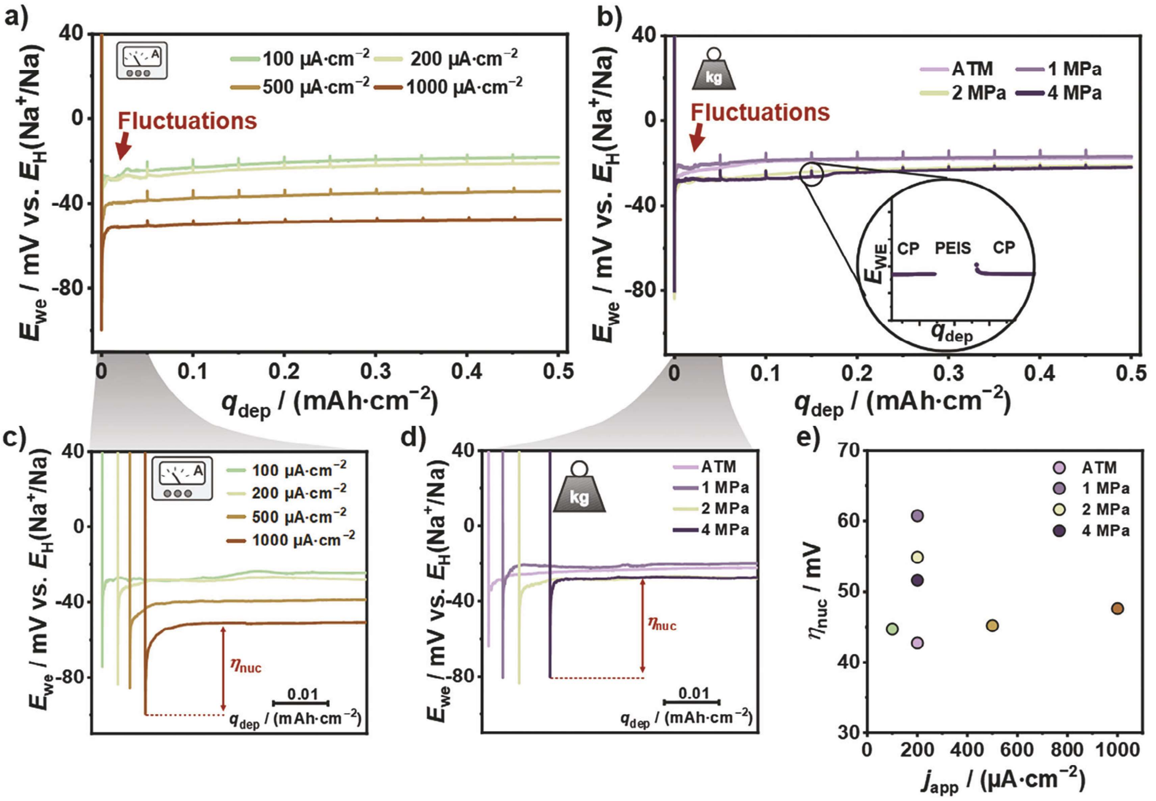

Figure 1. Potential profile of cathodic deposition of sodium at a Cu|NZSP interface at various a) current densities and b) stack pressures. A pressure of 2 MPa was applied for measurements at different current densities. Depositions at atmospheric pressures (ATM) and different stack pressures were performed at a current density of j_{app} = 200 µA•cm^{-2}. The pictogram insert in (a) and (b) indicates the individual measurement series. Measurements were conducted at 25 °C and a sodium amount corresponding to an areal charge q_{dep} of 0.5 mAh•cm^{-2} was deposited at the Cu|NZSP interface in all cells. Impedance spectra were recorded after each 0.05 mAh•cm^{-2} deposition step to characterize the evolution of the Cu|NZSP interface. The impedance measurements result in the small and regular dips in the potential profile for each cell. The initial drop in the potential profile for both series is depicted at higher magnification for c) current density and d) stack pressure series to visualize the nucleation overpotential η_{nuc}. The potential curves were slightly shifted along the *x*-axis to give a better overview of their individual course. The corresponding scale is given by the black bar. The determined η_{nuc} for the current densities (green and brown points) and stack pressure series are shown in e). For the determination of η_{nuc}, the difference between the voltage drop and the average voltage plateau in the range between 0.05 and 0.25 mAh•cm^{-2} was extracted from the graphs.

The nucleation overpotential η_{nuc} was calculated for all measurements by the difference between the initial potential drop and the potential plateau (see Figure 1c,d).[41] The values of η_{nuc} are summarized in Figure 1e. For both series of measurements, only small changes in the range of a few mV were observed for η_{nuc}, which does not allow an identification of a clear trend. In the case of the nucleation of lithium at the Cu|LiPON interface, a significant increase in η_{nuc} was observed at higher j_{app}, especially at elevated temperatures (60 to 100°C).[27] In the case of sodium nucleation, it might be possible to identify a trend of η_{nuc} by expanding the parameter window, which will be part of future studies.

After nucleation and early growth ($q_{dep} > 0.05$ µAh•cm^{-2}), a constant potential for all measurements is observed, indicating a stable growth of sodium at the Cu|NZSP interface. However, considering the current density series (green to brown curves), doubling of the deposition potential is usually expected by doubling j_{app}, which is not observed. This is due to the dependence of the potential on the total resistance of the cell. This resistance varies depending on the interfacial contact between sodium and NZSP and volume of the SE actively involved in transport. This also explains why different growth overpotentials η_{growth} are obtained for the same j_{app}. The non-linear behavior shows that the nucleation and growth is influenced by the deposition conditions. A more detailed analysis of the individual changes is possible by electrochemical impedance spectroscopy and is discussed in the following section.

2.2. Electrochemical Impedance Spectroscopy

Electrochemical impedance spectroscopy enables the identification and quantification of individual processes such as ionic transport, interface-related processes or chemical degradation in

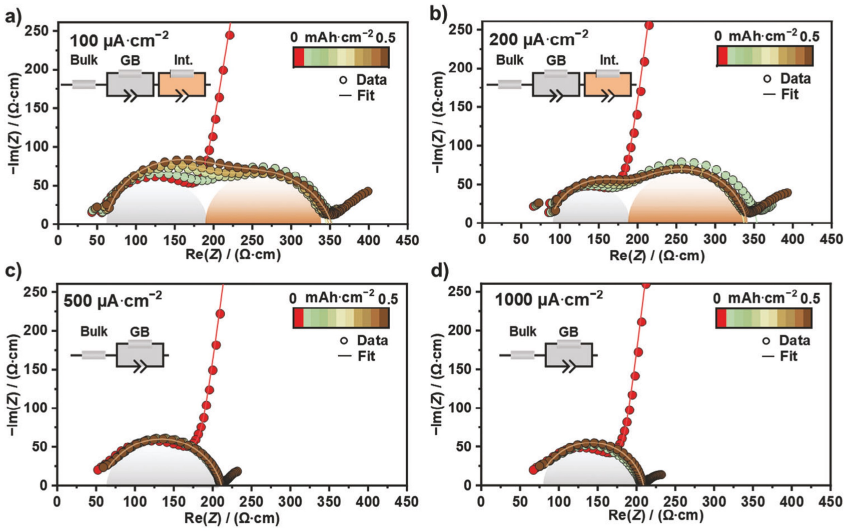

Figure 2. Development of the impedance spectra during cathodic deposition of sodium at the Cu|NZSP interface at various current densities. All impedance data are normalized with respect to the cell constant instead of the electrode area. The grain boundary transport contribution is highlighted by a gray area while the interface-related contribution is indicated by an orange background. The inserted equivalent circuit diagram was used to fit the impedance data except for the pristine cells (red dots). Here, the blocking behavior of the copper electrode was fitted by a *Q*- instead of an *RQ*-element. The evolution of the extracted fitting parameters R_{SE}, R_{Int}, and C_{Int} with progressing sodium deposition is shown in Figure 3.

electrochemical cells.[43] Apart from microscopic transport processes such as transport across grain boundaries or charge transfer at phase boundaries, additional non-microscopic transport contributions can occur in impedance spectra such as geometric current constriction. The latter results from insufficient physical contact at the alkali metal|SE interface and shows the same signature in the impedance spectrum as a true migration process, i.e., a semicircle in the Nyquist diagram.[44] This is due to the dynamic nature of the conduction behavior of pores at the interface in the measured frequency range. At low excitation frequencies, ionic charge transport is blocked by an insulating gap at the metal|SE interface, while at higher frequencies, charge transport can occur across the gap by a dielectric displacement current.[44] As a result, the SE volume actively involved in transport is reduced in the direct current range, leading to the increase in the impedance. In particular, for the Li|LLZO and Na|NZSP interfaces, it has been demonstrated that the interface-related impedance contribution R_{Int} is dominated by this geometric phenomenon.[36,40,45]

Note that current constriction is a purely geometric effect and is given by the morphology of the interface. A systematic investigation of the influence of contact area, contact area distribution, electrode area, and gap height on the current constriction phenomenon was reported in detail by Eckhardt et al.[44–46] For example, a decrease of the contact area leads to an increase of the current constriction resistance R_{cstr}, while a finer spatial distribution of contact at constant contact area would decrease R_{cstr}. Furthermore, the constriction capacity C_{cstr} is strongly affected by the interfacial morphology, meaning the shape of gaps (height and contact area). Thus, time-resolved electrochemical impedance spectroscopy is a suitable tool to qualitatively monitor the evolution of the interfacial morphology during sodium deposition at the Cu|NZSP interface.

However, to unambiguously monitor changes at the Cu|NZSP interface, changes at the counter electrode|SE interface must be avoided. As shown in a previous work, an ideal sodium electrode Na_{id} does not show any interfacial polarization in contact with NZSP and thus no interface-related contribution in the impedance spectrum.[36] Moreover, a Na_{id} electrode can still serve as a quasi-reference electrode even when small amounts (<0.5 mAh•cm^{-2}) of sodium are anodically dissolved at a Na_{id}|NZSP interface.[36] Thus, changes of the interface-related impedance in the performed measurement series can be assigned to the Cu|NZSP interface, whereby $R_{Int} \approx R_{cstr}$.

For both measurement series, cells were characterized in intervals of 0.05 mAh•cm^{-2}, as can be seen by the short breaks in the potential profiles (Figure 1a,b). A detailed explanation of the impedance data is given based on the current density series shown in **Figure 2**. This is followed by a discussion of the stack pressure series. For better comparison, the impedances of the different samples were normalized to the cell constant instead of the working electrode area. This is necessary because the cells have slightly different thicknesses due to the polishing process. Thus, all resistances are given in Ω•cm instead of Ω•cm^2, while capacities are given in nF•cm^{-1} instead of nF•cm^{-2}.

2.2.1. Current Density Series

For pristine cells (red data points), only one semicircle in the high-frequency range is observed in the Nyquist plot with

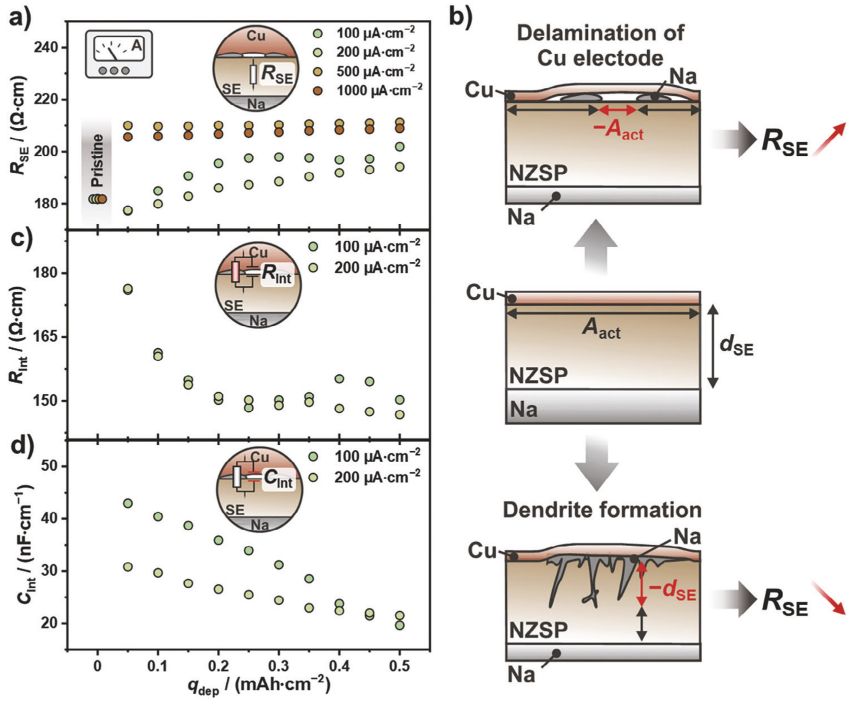

Figure 3. a) Evolution of the solid electrolyte resistance R_{SE} (sum of R_{Bulk} and R_{GB}) during cathodic deposition of sodium at the Cu|NZSP interface for various current densities. Deposition was carried out at $p = 2$ MPa and $T = 25$ °C. Impedance data were fitted using the equivalent circuit models depicted in Figure 2 and normalized with respect to the cell constant. Due to the normalization to the cell constant, all pristine cells have the same R_{SE}. For a better overview, the R_{SE} of the pristine cells were slightly shifted and highlighted in gray. b) Scheme illustrating the influence of delaminating copper from NZSP (upper part) and dendrite formation (bottom part) on R_{SE} during cathodic deposition. The formation of an interfacial gap leads to a reduction in the electrode area A_{act} actively involved in transport in the frequency range of the grain boundary transport process, and thus to an increase of R_{SE}. In contrast, the distance between opposing electrodes decreases on average when sodium penetrates the SE. This is similar to reducing the effective thickness of the SE, resulting in a decrease of R_{SE}. c) Evolution of interface-related resistance R_{Int} and d) capacity C_{Int} at various j_{app}. The respective errors resulting from the fitting are shown in Figure S3 (Supporting Information).

a strong polarization in the low-frequency range. The high-frequency impedance contribution corresponds to the transport across grain boundaries (GB) and the low-frequency polarization originates from the ion blocking behavior of the copper electrode. The bulk impedance of NZSP is not captured in the measured frequency range and no contribution is observed with respect to the charge transfer at the NZSP|Na$_{id}$ interface.[47]

Independent of the current density, after the first sodium deposition interval at the working electrode (copper electrode), the interface polarization turns into a non-blocking behavior with a small tail in the low-frequency range. The non-blocking behavior indicates the formation of a sodium electrode. The small tail in the low-frequency range is frequently observed at metal|SE interfaces and is probably due to diffusion processes of the metal at the interface.[43] However, the real origin is not yet clarified so far. A second semicircle in the mid-frequency range in the Nyquist plot appears at low j_{app} (100 and 200 µA•cm^{-2}), while no contributions can be resolved at higher j_{app}. According to the distribution of relaxation times analysis, very weak signals are observed for long relaxation times at 500 µA•cm^{-2}, whereas no signals are present at 1000 µA•cm^{-2}, as shown in Figure S2 (Supporting Information). The second semicircle in the Nyquist plot can be assigned to the Cu|NZSP interface and arises due to the current constriction phenomenon. As no additional interface-related impedance contribution is present at high j_{app}, such electrodes can be considered as a quasi-reference electrode, since charge transfer and SEI formation are negligible at the Na|NZSP interface.[36]

With progressing sodium deposition changes in the high- and mid-frequency range are observed, which are more pronounced at lower j_{app}. To analyze the evolution of the individual contributions in more detail, the impedance data were fitted using the equivalent circuit inserted in Figure 2. First, the evolution of the SE impedance contribution (high-frequency region) during sodium deposition is analyzed in more detail, that is, the total resistance R_{SE}, which is the sum of R_{Bulk} and R_{GB}, shown in **Figure 3**a. It should be noted that the direct comparison of R_{SE} of the pristine cell (q_{dep} = 0 mAh•cm^{-2}) and after the first deposition interval (q_{dep} = 0.05 mAh•cm^{-2}) is hampered because different equivalent circuits are used for fitting to account for the transition from blocking to non-blocking behavior of the working electrode. Small deviations in determining R_{SE} occur if the fitting model is altered, resulting in a small offset. We could compensate this difference numerically, as R_{SE} should of course not depend on the fit model, but we prefer not to modify the data analysis in this way.

As sodium deposition progresses, a slight increase of R_{SE}, especially at lower j_{app}, is observed for the measurement series indicating an increase of the cell constant. A similar trend is also deduced from the distribution of relaxation times analysis shown in Figure S2 (Supporting Information). The increase of R_{SE} can be attributed to delamination of the copper electrode and the NZSP due to vertical growth of sodium, resulting in gaps at the interface.[31] Above a certain gap height and width, they are no longer dielectrically shorted even in the frequency range of the grain boundary transport process.[48] As shown schematically in Figure 3b, this reduces the electrode area that is actively involved in transport and thus increases the cell constant. At higher j_{app}, the impact of gap formation on R_{SE} is less pronounced, indicating more uniform deposition of sodium.

Based on the evolution of R_{SE}, detrimental dendrite growth during deposition is unlikely. As shown in Figure 3b, metal infiltration into the SE would lead on average to a reduction in cell thickness and thus to a reduction of the cell constant. This would lead to a decrease of R_{SE} as it was observed in the case of the lithium plating at a Cu|LLZO interface.[29] However, it cannot be completely ruled out that dendrites are formed in this work, since dendrite growth and gap formation have an opposing effect on the evolution of R_{SE}. Therefore, it is possible that dendrites form but they cannot be identified from R_{SE} because the evolution of R_{SE} seems to be dominated by the gap formation.

Figure 3c shows the evolution of R_{Int} at 100 and 200 µA•cm^{-2} determined based on the given equivalent circuit depicted in Figure 2. No clearly separated interface-related contribution can be identified in the Nyquist plots and distribution of relaxation time analysis (Figure S2, Supporting Information) for 500 and 1000 µA•cm^{-2}. To properly fit the impedance data, the equivalent circuit has been changed from *R-RQ-RQ* to *R-RQ* for these current densities. Accordingly, no interface-related contribution (R_{Int} and C_{Int}) is gained from the fitting and shown in the Figure 3.

At low current densities, only slight changes of R_{Int} are observed, limited to the first two deposition cycles. This suggests that the interfacial contact area between sodium and NZSP is already defined after the first sodium deposition cycles and does not change significantly with longer deposition time. As systematically investigated by Fleig et al. and Eckhardt et al., the constriction resistance depends strongly on the contact area as well as its spatial distribution at the interface.[45,46,49] Accordingly, R_{Int} decreases with increasing contact area or with finer distribution of the contact spots. Thus, it is challenging to derive the contact area directly from R_{Int}. A finer spatial distribution of contact could be achieved, for example, by the formation of new sodium nuclei at the Cu|NZSP interface during the deposition. However, after the initial nucleation, the formation of new sodium nuclei at the Cu|NZSP interface is unlikely because η_{growth} is usually smaller than η_{nuc}. In contrast, an increase in the contact area can be achieved, for example, by sodium deposition on the surface of existing sodium nuclei or by plastic flow of the already deposited sodium. As the applied stack pressure (2 MPa) is higher than the yield strength of polycrystalline bulk sodium ($\sigma_{Na} \approx 0.2$–0.3 MPa), plastic flow of sodium is likely.[31,50] If the contact area is enlarged by plastic flow of sodium, no change of R_{Int} would be expected when the stack pressure is below its yield strength. As can be seen in **Figure 4**, R_{Int} remains constant during deposition when no stack pressure is applied. This supports our conclusion that the decrease of R_{Int} and thus an increase of the contact area is due to plastic flow of sodium. A more detailed discussion of the influence of stack pressure on the evolution of R_{Int} is given in Section 2.2.2.

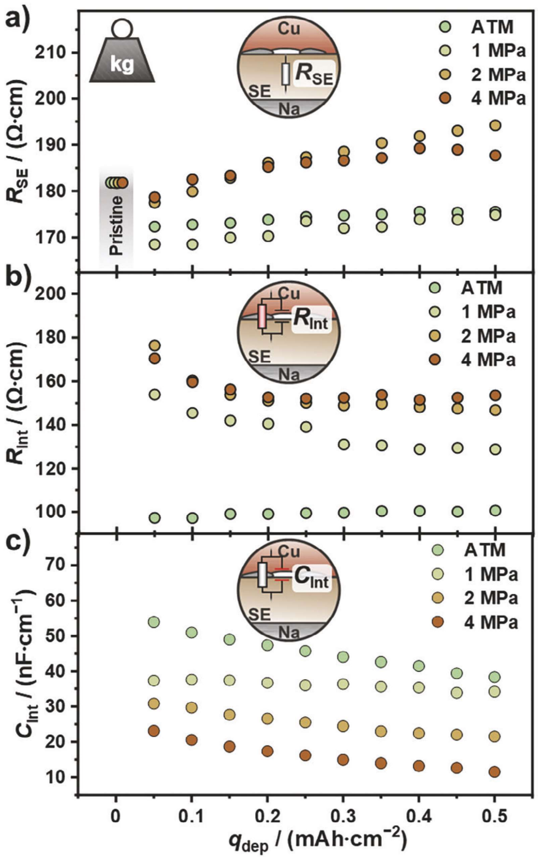

Figure 4. Evolution of solid electrolyte resistance R_{SE} (sum of R_{Bulk} and R_{GB}), interface-related resistance R_{Int}, and interface-related capacity C_{Int} at different stack pressures. Deposition was carried out at j_{app} = 200 µA•cm^{-2} and $T = 25$ °C. Impedance data were fitted using the equivalent circuit given in Figure S4 (Supporting Information) and normalized to the cell constants. Due to the normalization to the cell constant, all pristine cells have the same R_{SE}. For a better overview, the R_{SE} of the pristine cells were slightly shifted and highlighted in gray. Independent of the stack pressure, R_{SE} increases slightly as deposition progresses. R_{Int} initially decreases when stack pressure is applied, while it remains unchanged at atmospheric pressure. C_{Int} decreases slightly during the deposition of all measurements. The errors bars of the fitting are presented in Figure S5 (Supporting Information).

The direct current resistances R_{DC} (sum of R_{SE} and R_{Int}) of the cells provide further information about the interface morphology. In a first approximation R_{DC} is inversely proportional to the contact area. This relationship suggests that the lower the R_{DC}, the larger the contact area. Consequently, a larger contact area between sodium and NZSP is achieved at higher current densities (see Figure 2).

The interfacial capacity C_{Int} depends on the morphology of the interface, i.e., the contact area and the height of the formed gap.[44] Figure 3d shows the evolution of C_{Int}, which decreases for both current densities. The reduction of C_{Int} would mean an increase of the gap height if the contact area remains almost unchanged. This is consistent with the observed trend of R_{SE}, which indicates a decrease in the electrode area actively involved in transport due to gap formation. An increase in the gap distance between copper and NZSP may be caused by vertical sodium growth. According to the trend in Figure 3d, vertical growth would be more pronounced at lower j_{app}. We like to emphasize that only the trend of the individual contributions (R_{SE}, R_{Int}, C_{Int}) was considered and analyzed qualitatively. A quantitate evaluation is not meaningful as the changes of the individual contributions are very small. With respect to a formal error analysis, shown in Figure S3 (Supporting Information), a quantitative change of a contribution is in the range of the fitting error.

2.2.2. Stack Pressure Series

Analogous to impedance analysis for the current density series, the influence of stack pressure on sodium deposition is discussed based on the evolution of the impedance. **Figure 4** shows the evolution of R_{SE}, R_{Int}, and C_{Int} during sodium deposition at different stack pressures. The corresponding impedance spectra and underlying distribution functions are shown in Figure S4 (Supporting Information). Starting with the evolution of R_{SE}, a sharp decrease is observed after the first deposition step for all stack pressures that is probably due to the different equivalent circuit models used. With progressing sodium deposition, a significant increase of R_{SE} is only observed at 2 MPa within the range of uncertainty, as shown in Figure S5 (Supporting Information). However, according to the results of the previous and also the following section, an increase of R_{SE} and thus gap formation is also likely at other stack pressures.

The evolution of R_{Int} for the stack pressure series is shown in Figure 4b. The corresponding formal errors for R_{Int} are given in Figure S5 (Supporting Information). Starting with the evolution of R_{Int} at atmospheric pressure, R_{Int} remains unchanged throughout the sodium deposition process. This indicates that the interfacial contact area as well as its distribution does not change significantly during deposition. In contrast, R_{Int} decreases within the first deposition intervals and flattens afterward, when a stack pressure above 1 MPa is applied. The reduction of R_{Int} results from a rise in the contact area due to plastic flow of sodium, caused by the stack pressure, which exceeds the yield strength of polycrystalline bulk sodium ($\sigma_{\mathrm{Na}} \approx$ 0.2–0.3 MPa).[50]

However, this raises the question of why no continuous flow and thus no continuous decrease of R_{Int} is observed during deposition, especially when the stack pressure is elevated up to 4 MPa. This can be explained by the following reasons: First, the yield strength and flow stress strongly depends on the temperature, strain-rate, and aspect ratio.[50,51] Especially, at low aspect ratios (height/length), like metal films, the flow stress is drastically increased under compression.[51] Second, frictional and adhesive forces at the interfaces additionally result in a hydrostatic pressure and thus reduce the plastic deformation of alkali metals.[50,52]

With the initial lateral deformation of sodium, the contact area between Na|CC and Na|SE increases and thus also frictional and adhesive forces. Furthermore, the aspect ratio decreases with lateral deformation, reinforcing the trend and resulting in a significant increase in flow stress. Consequently, the lateral deformation slows down and does not continue to increase the electrode area even though the applied stack pressure exceeds the yield strength of the polycrystalline bulk sodium.[50] Therefore, we attribute the initial decrease of R_{Int} to an increase of the contact area by plastic flow of sodium. With increasing contact area the plastic flow is reduced by additional frictional and adhesive forces and thus R_{Int} remains unchanged.

The direct current resistance R_{DC} (shown in Figure S4Supporting Information) slightly decreases with decreasing the stack pressure as the lowest interface contribution is obtained at atmospheric pressure. Similar to the current density series, only slight changes of the direct current resistance, and thus the contact area, can be observed after the first sodium deposition intervals. This suggest that the interfacial contact area is mainly determined by the nucleation process. Hence, the stack pressure might affect the nucleation process. However, whether the stack pressure influences the lateral distribution of nuclei or the nucleation process itself requires further characterization, which will be investigated in future studies.

Finally, the evolution the interface-related capacity C_{Int} is shown in Figure 4c. Independent of the stack pressure, C_{Int} continues to decrease with progressing electrodeposition, indicating that the gap height is increasing, and thus supporting the trend and interpretation of the evolution of R_{SE}.

Based on the impedance analysis, the current density appears to have a stronger impact on interfacial morphology and the coverage of sodium than the stack pressure. According to the classical nucleation theory for electrodeposition from liquid electrolytes, the critical nucleation radius decreases with increasing η_{nuc} and the areal nucleation density increases.[41] In the case of a solid|solid interface, the mechanical work during nucleation needs to be considered additionally.[26] For Li deposition at Cu|LiPON and Cu|LLZO interfaces, an increase in areal nuclei density was observed with increasing current density, although there were no large changes in η_{nuc}.[12,27] For verification of the trend obtained from the electrochemical characterization, the samples were examined by light and electron microscopy to visualize the sodium deposition.

2.3. Characterization of Copper Electrodes after Cathodic Deposition

2.3.1. Light Microscopy

In addition to electrochemical characterization, copper electrodes were imaged from the top by light microscopy after deposition of $q_{\mathrm{dep}} = 0.5$ mAh•cm^{-2} (corresponding to a sodium layer thickness of 4.4 µm assuming homogeneous deposition over the entire copper electrode). **Figure 5** shows the optical images (upper

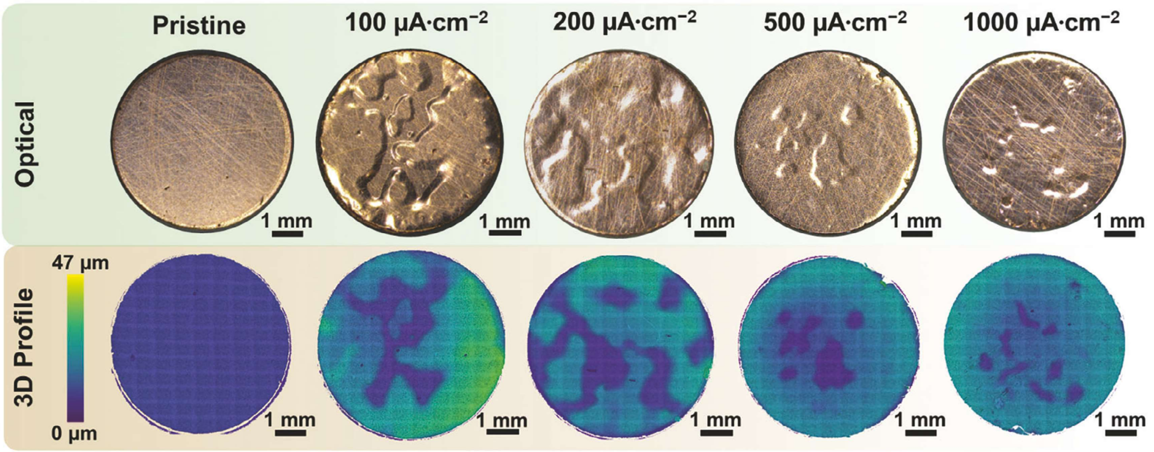

Figure 5. Optical microscopy images of copper electrode after cathodic deposition of $q_{\text{dep}} = 0.5$ mAh•cm^{-2} (upper row) at different current densities. The specimens were slightly tilted to improve the visibility of the topography in the optical images. In addition, the copper electrodes were imaged by confocal microscopy to generate a 3D representation (bottom row). Based on the optical and 3D confocal profiles, a more uniform coverage of the electrode is observed with increasing j_{app}.

row) and the corresponding 3D confocal microscopy profiles (bottom row) for the current density series. Starting from a smooth and flat pristine copper electrode, the optical images clearly show that the topography changes significantly, indicating inhomogeneous sodium growth underneath. It is also worth noting that no sodium whiskers grew through the copper electrode. The topographic changes of the copper electrode at different j_{app} are consistent with the trend of the impedance analysis. The 3D profiles reveal that the elevated areas of the copper electrode quantitatively increase as j_{app} increases, as shown in Figure 5 and Figure S6a (Supporting Information). Since the same amount of sodium was deposited in all measurements, stronger vertical growth must occur at smaller contact areas and vice versa. For instance, the absolute height difference at 100 µA•cm^{-2} is larger than for 1000 µA•cm^{-2}. Accordingly, the electrode area actively involved in transport is smaller at 100 µA•cm^{-2} than at 1000 µA•cm^{-2}, which supports our conclusion of better coverage at higher j_{app}.

For the stack pressure series, the elevated area of the copper electrode is smaller at atmospheric and low stack pressure (1 MPa) compared to high stack pressures (2 and 4 MPa), as can be seen in Figures S7 and S6b (Supporting Information). On the contrary, according to the direct current resistances R_{DC}, an opposite trend of the contact area is observed and thus is inconsistent with the 3D confocal microscopy profiles. This discrepancy is probably due to the mismatch between the elevated area and the actual contact area in the optical data, as described in Section 2.3.2. In general, the absolute height difference is higher at atmospheric pressure than with additional stack pressure. This is consistent with the trend of R_{Int}, since no plastic deformation and thus no lateral expansion of the sodium whiskers due to plastic flow is expected. Consequently, the height of an average whisker is higher for lower contact areas as the amount of sodium deposited remains constant. Similar behavior was also observed for the lithium deposition at the Cu|LLZO interface, where vertical growth was less pronounced when a stack pressure was applied.[32]

2.3.2. Cross Sections of the Cu|Na|NZSP Interface

Since light microscopy only gives an overview of the surface of the copper electrode, additional cross-sections were prepared by FIB-SEM to visualize the deposited sodium in more detail. Multiple cross-sections per sample were prepared and linked to the position on the copper electrode in the 3D confocal microscopy profiles. **Figure 6** shows the cross-sections for the sample deposited at 200 µA•cm^{-2} and 2 MPa.

Starting with cross-section C1, a dense and uniform sodium layer with good contact to the NZSP and a thickness of 8.8 µm is found. The thickness is very well in line with the height difference obtained from the 3D profile at position C1. The thickness of ≈9 µm already indicates that there is no uniform sodium deposition over the entire copper electrode as the expected mean film thickness is 4.4 µm. Surprisingly, a discrepancy between the elevated area in the 3D profile and the sodium underneath is observed in the other cross-sections (C2-C4), revealing that the elevated area is not equal to the contact area between sodium and NZSP. For instance, a mismatch can result from the formation of gaps, as shown at positions C3 and C4. This can be caused by island or whisker growth. When sodium grows, the copper electrode near the island/whisker can be raised if the electrode is locally not bonded properly to the NZSP.[31,32] Although the lifted area in the 3D profiles does not correspond to the real contact area, it can provide information on the distribution of deposited sodium underneath the copper electrode.

The observation of large gaps supports the results of our impedance analysis given in Section 2.2. The increase in R_{SE} during deposition is associated with a reduction of the electrode area actively involved in transport, even at high frequencies, leading to

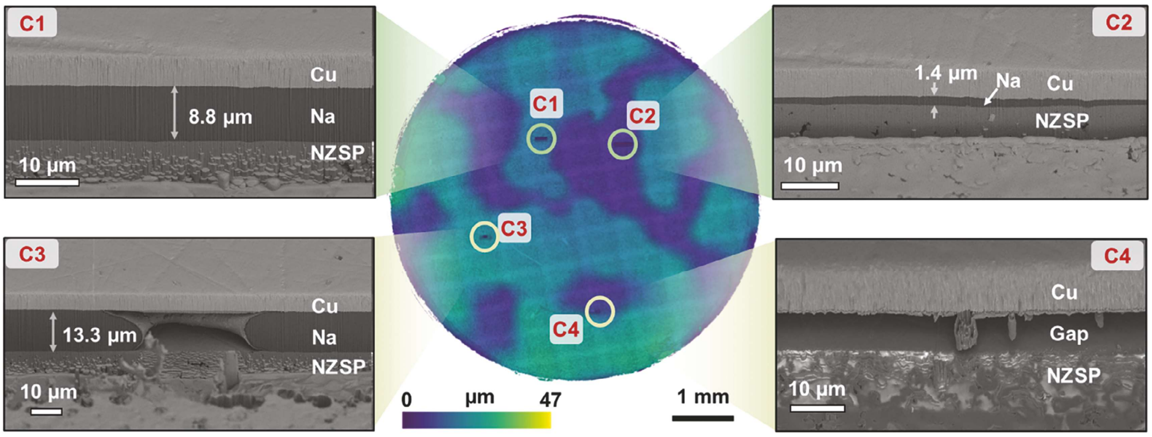

Figure 6. FIB-SEM cross-sections of selected spots on the copper electrode to visualize the sodium growth underneath. The positions are correlated with the corresponding 3D confocal microscopy profile as indicated by the labels C1-C4. The topography of the electrode in the 3D profile is indicated by the color bar shown on the bottom side. A total amount of sodium corresponding to $q_{\mathrm{dep}} = 0.5$ mAh•cm^{-2} was deposited at $j_{\mathrm{app}} = 200$ µA•cm^{-2}, $p = 2$ MPa, and $T = 25$ °C. Homogeneous deposition of a dense sodium layer with a homogeneous interfacial contact can be observed at position C1 and C2. Position C3 visualizes a region near the edge of a sodium island while at position C4 copper and NZSP is separated by a gap. The thickness of the deposited sodium varies between 1.4 and 13.3 µm.

a change in the cell constant. The formation of such gaps may be due to the preparation of the copper electrode, as they are less pronounced when a copper foil is laminated on a SE.[12,31,32] Lamination at elevated temperatures (<800 °C) and pressures (≈3 MPa) may improve the bonding between copper and SE.

Compared to the Cu|NZSP interface prepared by thermal evaporation, a small gap of ≈100 nm can be observed already in the pristine sample by Xe$^+$ FIB-SEM cross sections, as shown in Figure S8a–g (Supporting Information). When a TEM lamella of the stack prepared via Ga$^+$ FIB is prepared, an almost covering copper layer with small voids in the layer is obtained, as can be seen in Figure S8h,i (Supporting Information). It is unclear whether these voids were created by the FIB preparation or during the evaporation process. Therefore, it must be assumed that the copper electrode is not directly bonded to the solid electrolyte in some areas. Without direct bonding to the SE, there is no counterforce to push the copper electrode toward the SE when nearby vertical sodium growth lifts the electrode. Larger gaps have also been observed when the current collector is pressed only on a lithium SE, as in the case of Cu|Li_6PS_5Cl.[35]

Further cross-sections with the corresponding assignment to the respective 3D profile are shown in Figures S9–S11 (Supporting Information). Despite several cross-sections per sample, it is not possible to correlate the frequency of occurrence of growth features with the respective deposition parameters. This is because the cross sections provide only a local view. Therefore, only the generally observed phenomena of sodium deposition at the Cu|NZSP interface are described and summarized in **Figure 7**. Besides the formation of gaps, which occurs in all samples, mostly dense and uniform sodium layers with a conformal contact between sodium and NZSP are observed (Figure 7a,b). It is noteworthy that voids in the SE near the interface are not filled with sodium and no spallation of the SE is observed. The deposited sodium can adapt to the geometrical conditions, even if the sodium layers are very thin (Figure 7c) or located in edge regions of the layer (Figure 7d). As shown in Figure 7e,f, besides a homogeneous deposition, the growth of small islands and whiskers can be observed leading to gap formation as discussed previously. Additionally, in the case of whisker growth no fracturing of the SE near the interface takes place.

Nevertheless, it cannot be ruled out that damage occurs near the Na|NZSP interface. As can clearly be seen in Figure 7g,h, parts of the SE are pulled out of the surface and voids in the SE are filled with sodium. Despite this spallation, a uniform sodium layer is obtained between the pulled-out SE and the remaining SE, which can be unambiguously concluded from the negative imprint in the remaining SE. The reason for the fracture has not been fully clarified. It cannot be excluded that sodium does nucleate inside the SE causing a high mechanical stress that leads to the formation of cracks. It is suggested that the root cause of the nucleation is related to the partial electronic conductivity of the SE.[53,54] In addition, the driving force for metal nucleation inside the SE needs to be considered.[7] Hence, nucleation can occur when the chemical potential of sodium inside the SE μ_{Na} exceeds the chemical potential of sodium metal μ^0_{Na}.[55] Such an “overshoot” of μ_{Na} can be caused by local ionic transport limitations or differences in transference number.[55,56] Moreover, to initiate sodium nucleation an overpotential has to be overcome that depends on the mechanical back stress of the respective SE.[57] For example, nucleation of sodium within the solid electrolyte has been observed for the sodium beta-alumina solid electrolyte.[56,58]

As the NZSP was polished prior to copper deposition, minor damages may have been induced, which led to local predetermined breaking points and further defects. These may act as preferred sites for nucleation and locally reduced fracture toughness of NZSP. However, the spallation of the SE appears to be very local, as can be seen in Figure 7g,d. Despite the presence of

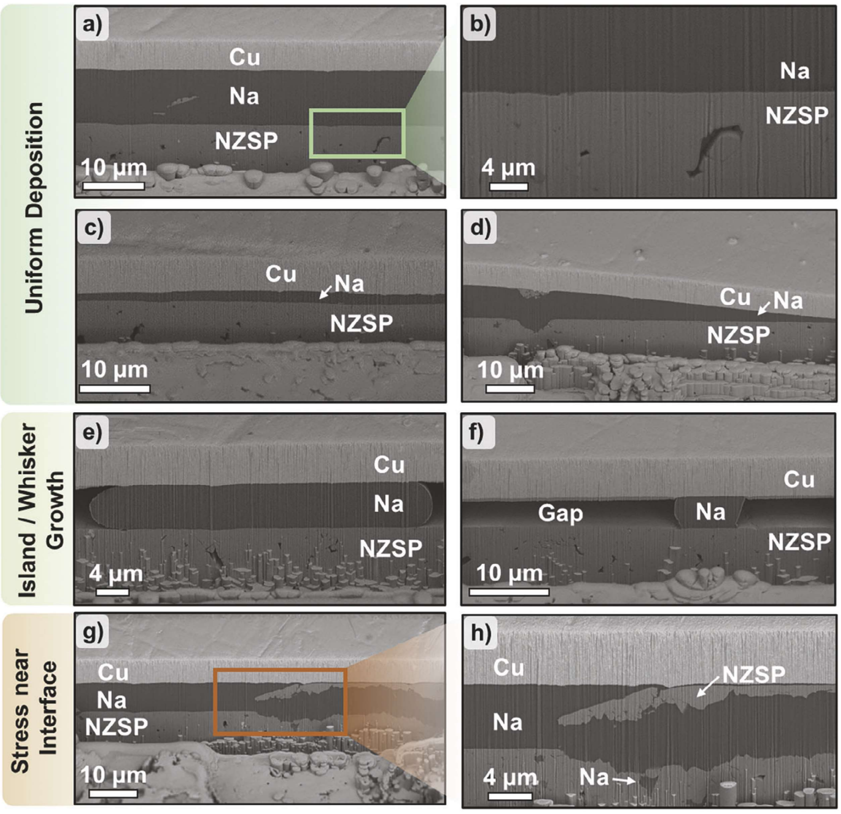

Figure 7. Compilation of FIB-SEM cross sections of differently observed phenomena during cathodic deposition of sodium at the Cu|NZSP interface. The formation of thick and uniform sodium layers with an optimal physical contact to the solid electrolyte are shown in (a) and (b). In addition, thin and wedge-shaped layers are observed in (c) and (d) with a proper contact to the copper electrode and the NZSP solid electrolyte. In contrast, island and whisker growth lead to gap formation between copper and NZSP as shown in (e) and (f). Moreover, NZSP grains near the interface break out and pores near the interface can be filled with sodium as identified in (g) and (h). The different morphologies and contrasts of NZSP result from the fact that both the crater wall (upper part) and the crater floor (lower part) are shown.

fractures, uniform deposition is again observed only a few micrometers next to it.

The cross sections generally show dense and uniform sodium deposition, which is required for sodium solid-state reservoir-free cells. Whisker growth, that is, out-of-plane or vertical growth, is not beneficial for the cycling of reservoir-free cells, as it leads to a reduction in the electrode area. However, it is not critical as no damage to the SE is observed in general. Clearly, spallation of the SE would lead to a degradation of the interface during cycling and may develop into a critical microstructural defect.

2.4. Characterization of Early Stages of Sodium Growth by In Situ Transmission Electron Microscopy (TEM)

For better understanding of the processes during early growth at the nanoscopic level, the sodium deposition at the Cu|NZSP interface was characterized by in situ TEM. A schematic representation of the experimental setup is depicted in Figure S12 (Supporting Information). Sodium growth at the interface was induced by applying a bias of 6.3 V and the morphological evolution has been recorded through time-series of high-angle annular dark-field scanning transmission electron microscopy images.

Starting from the pristine sample, besides a few close contact spots between copper and NZSP, several voids are present within the copper layer, as can be seen in **Figure** 8a. Moreover, a small crack in the SE is present near the interface, which is outlined with a green arrow in Figure 8b. The crack might be due to the polishing procedure of the SE or introduced by the ion milling.

During biasing, sodium nucleates at a close contact point shown in Figure 8c, highlighting the importance of physical contact between the copper and NZSP. With further biasing, a sodium whisker grows, which is highlighted by a brown dotted frame in Figure 8d. A polyhedral shape can be recognized. This might indicate a faceted single whisker, which is also observed in a second in situ TEM experiment, shown in FigureS13a,b (Supporting Information). We would like to note that the sample history of the second electron-transparent lamella differs from that of the first lamella, which is described in more detail in Section S5 (Supporting Information). However, such an oriented sodium

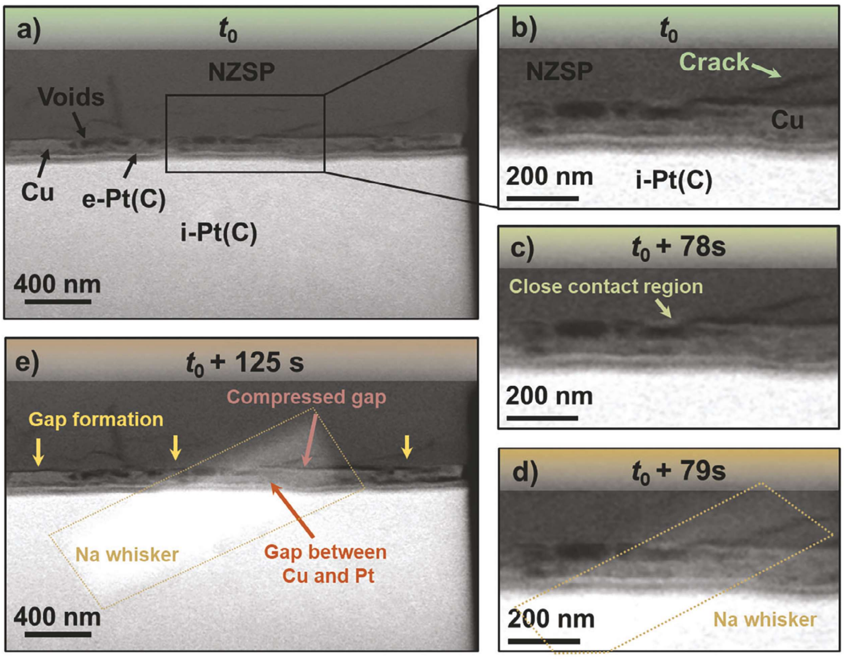

Figure 8. Time-resolved high-angle annular dark-field scanning transmission electron microscopy images of a Cu|NZSP interface during biasing. To initiate sodium deposition, the voltage was gradually increased and image acquisition was started when a voltage of 6.3 V was reached. This time is referred to as t_0. The pristine lamella is shown in (a) and (b). For processing of the lamella, a platinum protection layer was deposited via electron-beam (denoted as e-Pt(C)) followed by an ion-beam deposition referred to i-Pt(C). An initial crack near the Cu|NZSP interface is marked by a green arrow. c) After 78 s of polarization a sodium particle nucleates at a close contact spot highlighted with a light green arrow. During further polarization, the sodium particle grows into a polyhedral-shaped whisker. d) With progressing biasing, the formed whisker grows maintaining its shape (e). Furthermore, gap formation between the NZSP and copper layer (yellow arrows) as well as between the copper and platinum protection layer (orange arrow) is observed. Surprisingly, some gaps are also compressed as highlighted by a red arrow in (e).

growth has been observed previously in other TEM studies at (multiwall) carbon nanotube matrix.[59,60]

Moreover, the initial crack in Figure 8b (highlighted by the green arrow) does not further propagate during sodium nucleation and growth (Figure 8d). Therefore, existing cracks are not necessarily the starting point for further damage to the SE. On the contrary, damage to the SE due to the deposition cannot be completely ruled out. As shown in Figure S13c (Supporting Information), a crack forms in the SE near the interface. The formation of the crack may arise from mechanical stress generated by the deposition of sodium within the SE (see explanation in Section 2.3.2) or at the Cu|NZSP interface. Furthermore, the resulting crack can also serve as nucleation point. As can be seen in Figure S13d (Supporting Information), a second whisker is formed at the location of the previous crack. It is not clear whether the second whisker forms independently by plating inside the SE or whether a junction of the first whisker creates an electrical connection to the copper electrode and causes the formation.

The formation and growth of the sodium whisker also influences the copper current collector. In Figure 8e and Video S1 (Supporting information), gaps between copper and NZSP become enlarged or formed (indicated by yellow arrows), and compressed (indicated by red arrow). It is unclear if these phenomena are solely a result of the mechanical stress caused by the deposition of sodium as enlargement and compression are two opposite effects. Moreover, a minor expansion of the copper layer and detachment from the platinum protective layer (orange arrow) indicate additional factors that contribute to the observed changes in the electrode, beyond mechanical stress. However, small voids are also observed at the Cu|NZSP interface after sodium deposition, suggesting that sodium deposition bears the risk of delaminating copper from NZSP and agrees with the previous results (cf. Figure S13b, Supporting Information).

Note that we cannot exclude an influence of the specific lamella geometry in the operando experiments on the observed whisker growth. However, we assume that the faceted whisker growth of sodium is a general phenomenon that would also be observed in extended 3D samples.

3. Conclusions

In this work, we demonstrate the deposition of dense sodium layers with several microns thickness at the Cu|NZSP interface that are of comparable quality to reported electrodeposited lithium films.[31,32,35,61] To the best of our knowledge, there have not been reports on “anode-free” sodium deposition published yet. The electrodeposition and growth of sodium was studied at different current densities and stack pressures. Based on impedance analysis and optical microscopy, we conclude that a more homogeneous sodium distribution underneath the copper electrode can be achieved at higher current densities, whereas the stack pressure has a minor impact on the sodium distribution within the examined parameter window. We conclude that this interesting difference to lithium plating is due to the higher plasticity of sodium, which operates at room temperature quite close to its melting point.

FIB-SEM cross-sections show the deposition of dense and uniform sodium layers ideal for reservoir-free cells. Beside the layers, island, and whisker growth of sodium is also observed at the Cu|NZSP interface, leading to the formation of larger gaps due to incomplete physical contact between the copper electrode and the SE. The relevance of the initial physical contact is demonstrated by in situ TEM studies, as electrochemical sodium deposition only occurs at contact sites showing orientated growth of sodium whiskers. In addition, FIB-SEM cross-sections and in situ TEM characterizations reveal that sodium deposition can lead to crack formation and spallation of grains from the SE near the interface. However, based on the electrochemical impedance analysis, no detrimental dendrite formation is observed, even at higher current densities.

In order to obtain dense and homogeneous sodium layers, attention should be paid to the physical contact between the current collector and the SE, as well as to an adequate electrochemical deposition protocol. For example, ion beam sputtering of the copper layer could improve the interfacial contact between copper and NZSP compared to thermal evaporation technique due to the higher energy input of particles during deposition.[62] Moreover, pulse techniques with high current densities could be used to promote a homogeneous lateral sodium metal distribution but minimize damage to the solid electrolyte. We conclude that “reservoir-free” cell concepts can be realized for sodium solid-state batteries and hope to motivate further research in this field.

4. Experimental Section

Preparation of Reservoir-Free Cells: The NZSP solid electrolyte was synthesized via solution-assisted solid-state reaction (SA-SSR) as described elsewhere.[63] After sintering the NZSP pellets have a relative density of > 95%. For cell preparation, an ideally reversible sodium electrode was attached on one side of a NZSP pellet using a uniaxial load of 11 MPa for 1 min followed by additional isostatically pressing at 100 MPa for 15 min, as described previously.[36] The opposite side of the pellets was gradually polished with SiC grinding paper (Buehler Ltd., USA) starting from P400 up to P4000. A 5 µm copper layer was deposited on the polished surface by thermal evaporation in a home-built evaporation chamber.[29] During evaporation of copper the pressure inside the chamber was below 10^{-2} Pa. Before sealing of the Cu|NZSP|Na_{id} assembly in an Ar-filled pouch bag, the copper electrode was covered by a nickel disc (thickness 1 mm) to ensure a homogeneous pressure distribution during electrochemical experiments. For measurements carried out at atmosphere pressures, the pouch bags were sealed under vacuum. The nickel disc was polished with an AutoMet 300 polishing machine (Buehler Ltd. USA) using a 1 µm polycrystalline diamond suspension (MetaDi Supreme, Buehler Ltd., USA). Preparation and assembling were conducted in an Ar-filled glovebox. A schematic illustration of the cell preparation, including the cell dimensions, is shown in Figure S1a (Supporting Information).

Electrochemical Characterization: Electrochemical measurements were conducted using a VMP-300 potentiostat (BioLogic, France) in a controlled temperature environment (LabEvent climate chamber, Weisstechnik, Germany) at 25 °C. The external load during cathodic deposition was maintained by an in-house build pressure frame equipped with an FC22 (TE Connectivity) force sensor.[40] For the characterization of the evolution of the Cu|NZSP interface, an alternating approach of chronopotentiometry and potentiostatic electrochemical impedance spectroscopy was used for cathodic deposition. A total amount of sodium corresponding to 0.5 mAh•cm^{-2} was cathodically deposited at the Cu|NZSP interface for all cells. Assuming an ideally uniform deposition of sodium across the entire copper electrode, a theoretical mean layer thickness of 4.4 µm would be expected. Impedance spectra were recorded after each deposition step of 0.05 mAh•cm^{-2} in a frequency range from 7 MHz to 100 Hz with a voltage amplitude of 10 mV.

Impedance data were analyzed using the Relaxis3 software package (rhd Instruments, Germany). The Kramers-Kronig test was used to check the spectra before fitting. Frequencies with relative residuals > 2% were not considered for fitting. The ionic blocking (polarization) behavior of the copper electrode in the pristine cells was fitted by a Q-element. The model used to fit the impedance data during cathodic sodium deposition is shown in the respective figures. All impedance data were normalized to the total conduction volume of NZSP using the fitted bulk and grain boundary resistance of the pristine cell. The specified errors of the determined resistances and capacitances were estimated by a formal error estimation based on the mathematical errors of the fit.

Distribution of relaxation times were analyzed by the software package Relaxis3 (rhd Instruments, Germany). The real and imaginary parts of the data set were considered for the evaluation. For solving the Tikhonov regularization problem, the second derivative of the distribution function $\gamma(\tau)$ was used. Calculations were performed with a shape factor of 0.5, a regularization parameter $\lambda = 10^{-6}$, and Gaussian basic functions.

3D Confocal Microscopy: After cathodic deposition, the copper electrodes were imaged by digital microscopy (Emspira 3, Leica Microsystems GmbH, Germany). The samples were slightly tilted to better visualize the topography of the copper electrodes. In addition, 3D confocal microscopy profiles of the copper electrodes were generated with an optical 3D profiler (S Neox confocal microscope, Sensofar, Spain) using the SensoSCAN 6.7 software package. The 3D profiles were processed and evaluated using the SensoVIEW 1.9.2 software package. The recorded 3D profiles were leveled by the other part of the copper electrode. Missing or unmeasured data points were reconstructed by interpolation (bicubic). Determination of the elevated area was conducted by the same software package.

Focused Ion Beam Scanning Electron Microscopy: Cross-sections of the Cu|Na|NZSP interface were prepared by FIB-SEM using a XEIA3 system (TESCAN GmbH, Czech Republic). The samples were transferred from a glovebox to a XEIA3 system under inert gas conditions using a Leica EM VCT500 transfer shuttle (Leica Microsystems GmbH, Germany). Prior to milling, the samples were cooled to a temperature of −143 K by liquid nitrogen, which was maintained during analysis. The cross-sections were milled with Xe^+ ions with an energy of 30 kV. Beam currents of 100–300 nA and 3–30 nA were used for milling and polishing. The cross sections were imaged by SEM using a low-energy back scattered electron detector (LE-BSE).

In Situ Transmission Electron Microscopy: For in situ TEM experiments, first a 120 nm thick copper film was deposited on a NZSP pellet by thermal evaporation. From this sample, a thick lamella with the Cu|NZSP interface was prepared using a Strata 400 S FIB microscope (FEI Company, USA) and attached to a copper TEM grid.[64] To protect the copper layer, a platinum protection layer was deposited by the electron and ion beam on the surface before milling. The final TEM lamella was obtained by thinning with a Ga^+ ion beam using an Auriga 60 CrossBeam FIB (Carl Zeiss NTS GmbH, Germany) following the cryogenic FIB processing routine for SE.[64]

TEM characterization was carried out using a probe-corrected Themis 300 system (Thermo Fisher Scientific, USA) operated at 300 kV and the in situ biasing was conducted using the scanning tunneling microscopy holder (ZEPtools Technology Company, PicoFemto double-tilt holder, China) inside the TEM. After establishing contact of the grounded tungsten tip with the platinum layer of the TEM lamella, a biasing voltage of 4 and 6.3 V was applied between the copper TEM grid and the tungsten tip, respectively. The experimental setup is illustrated in Figure S12 (Supporting Information). Meanwhile, time-dependent series of high-angle annular dark-field scanning transmission electron microscopy images were acquired to record the morphological changes during biasing. The electron beam diameter was nominally 170 pm with nominal screen current of 100 pA.

Supporting Information

Supporting Information is available from the Wiley Online Library or from the author.

Acknowledgements

This work contributes to the research performed at CELEST (Center for Electrochemical Energy Storage Ulm-Karlsruhe) and was funded by the German Research Foundation (DFG) under Project ID 390874152 (POLiS Cluster of Excellence). The authors acknowledge the Karlsruhe Nano Micro Facility (KNMFi) at KIT for providing TEM access.

Open access funding enabled and organized by Projekt DEAL.

Conflict of Interest

The authors declare no conflict of interest.

Author Contributions

T.O. and T.F. designed the experiments. Q.M. and F.T prepared the solid electrolyte. T.O. prepared all cell and performed impedance analysis and cross sections experiments. T.O. and J.K.E. interpreted impedance analysis. Z.D. performed TEM sample preparation and characterization. T.O., Z.D., and C.K. interpreted TEM analysis. T.O., M.R., and J.J. wrote the manuscript. All authors discussed the results and contributed to the preparation of the manuscript.

Data Availability Statement

The data that support the findings of this study are available under DOI 10.5281/zenodo.10117406.

Keywords

anode-free-cell, impedance spectroscopy, in situ electron microscopy, sodium deposition

Received: August 18, 2023
Revised: November 14, 2023
Published online:

---

[1] J. Janek, W. G. Zeier, *Nat. Energy* **2023**, *8*, 230.
[2] C. Zhao, L. Liu, X. Qi, Y. Lu, F. Wu, J. Zhao, Y. Yu, Y.-S. Hu, L. Chen, *Adv. Energy Mater.* **2018**, *8*, 1703012.
[3] A. Banerjee, K. H. Park, J. W. Heo, Y. J. Nam, C. K. Moon, S. M. Oh, S.-T. Hong, Y. S. Jung, *Angew. Chem., Int. Ed.* **2016**, *55*, 9634.
[4] L. Zhou, J. D Bazak, B. Singh, C. Li, A. Assoud, N. M. Washton, V. Murugesan, L. F. Nazar, *Angew. Chem., Int. Ed.* **2023**, *62*, e202300404.
[5] M. D. Slater, D. Kim, E. Lee, C. S. Johnson, *Adv. Funct. Mater.* **2013**, *23*, 947.
[6] B. Xiao, T. Rojo, X. Li, *ChemSusChem* **2019**, *12*, 133.
[7] T. Krauskopf, F. H. Richter, W. G. Zeier, J. Janek, *Chem. Rev.* **2020**, *120*, 7745.
[8] Z. Lu, H. Yang, Q.-H. Yang, P. He, H. Zhou, *Angew. Chem., Int. Ed.* **2022**, *61*, e202200410.
[9] C. Heubner, S. Maletti, H. Auer, J. Hüttl, K. Voigt, O. Lohrberg, K. Nikolowski, M. Partsch, A. Michaelis, *Adv. Funct. Mater.* **2021**, *31*, 2106608.
[10] Q. Ni, Y. Yang, H. Du, H. Deng, J. Lin, L. Lin, M. Yuan, Z. Sun, G. Sun, *Batteries* **2022**, *8*, 272.
[11] O. Lohrberg, K. Voigt, S. Maletti, H. Auer, K. Nikolowski, C. Heubner, A. Michaelis, *Adv. Funct. Mater.* **2023**, *33*, 2214891.
[12] T. Fuchs, J. Becker, C. G. Haslam, C. Lerch, J. Sakamoto, F. H. Richter, J. Janek, *Adv. Energy Mater.* **2023**, *13*, 2203174.
[13] A. Willow, H. E. M. Hussein, S. Vajirakaphan, A. Chasri, S. Margadonna, *Front. Energy Res.* **2022**, *10*, 825.
[14] F. Mazzali, M. W. Orzech, A. Adomkevicius, A. Pisanu, L. Malavasi, D. Deganello, S. Margadonna, *ACS Appl. Energy Mater.* **2019**, *2*, 344.
[15] C. Wang, Y. Zheng, Z.-N. Chen, R. Zhang, W. He, K. Li, S. Yan, J. Cui, X. Fang, J. Yan, G. Xu, D. Peng, B. Ren, N. Zheng, *Adv. Energy Mater.* **2023**, *13*, 4.
[16] H. Li, H. Zhang, F. Wu, M. Zarrabeitia, D. Geiger, U. Kaiser, A. Varzi, S. Passerini, *Adv. Energy Mater.* **2022**, *12*, 2202293.
[17] B. Ma, Y. Lee, P. Bai, *Adv. Sci.* **2021**, *8*, 2005006.
[18] A. P. Cohn, N. Muralidharan, R. Carter, K. Share, C. L. Pint, *Nano Lett* **2017**, *17*, 1296.
[19] M. Tanwar, H. K. Bezabh, S. Basu, W.-N. Su, B.-J. Hwang, *ACS Appl. Mater. Inter.* **2019**, *11*, 39746.
[20] J. Seok, J.-H. Hyun, A. Jin, J. H. Um, H. D. Abruña, S.-H. Yu, *ACS Appl. Mater. Inter.* **2022**, *14*, 10438.
[21] R. Cao, K. Mishra, X. Li, J. Qian, M. H. Engelhard, M. E. Bowden, K. S. Han, K. T. Mueller, W. A. Henderson, J.-G. Zhang, *Nano Energy* **2016**, *30*, 825.
[22] X. Wang, C. Zhang, M. Sawczyk, J. Sun, Q. Yuan, F. Chen, T. C. Mendes, P. C. Howlett, C. Fu, Y. Wang, X. Tan, D. J. Searles, P. Král, C. J. Hawker, A. K. Whittaker, M. Forsyth, *Nat. Mater.* **2022**, *21*, 1057.
[23] A. Spangenberg, J. Fleig, J. Maier, *Adv. Mater.* **2001**, *13*, 1466.
[24] K. Peppler, J. Janek, *Solid State Ionics* **2006**, *177*, 1643.
[25] K. Peppler, M. Pölleth, S. Meiss, M. Rohnke, J. Janek, *Z. Phys. Chem.* **2006**, *220*, 1507.
[26] M. Motoyama, M. Ejiri, Y. Iriyama, *J. Electrochem. Soc.* **2015**, *162*, A7067.
[27] M. Motoyama, M. Hirota, T. Yamamoto, Y. Iriyama, *ACS App. Mater. Inter.* **2020**, *12*, 38045.
[28] M. Motoyama, M. Ejiri, T. Yamamoto, Y. Iriyama, *J. Electrochem. Soc.* **2018**, *165*, A1338.
[29] T. Krauskopf, R. Dippel, H. Hartmann, K. Peppler, B. Mogwitz, F. H. Richter, W. G. Zeier, J. Janek, *Joule* **2019**, *3*, 2030.
[30] S. Kim, C. Jung, H. Kim, K. E. Thomas-Alyea, G. Yoon, B. Kim, M. E. Badding, Z. Song, J. Chang, J. Kim, D. Im, K. Kang, *Adv. Energy Mater.* **2020**, *10*, 1903993.
[31] M. J. Wang, E. Carmona, A. Gupta, P. Albertus, J. Sakamoto, *Nat. Commun.* **2020**, *11*, 5201.
[32] E. Kazyak, M. J. Wang, K. Lee, S. Yadavalli, A. J. Sanchez, M. D. Thouless, J. Sakamoto, N. P. Dasgupta, *Matter* **2022**, *5*, 3912.
[33] B. J. Neudecker, N. J. Dudney, J. B. Bates, *J. Electrochem. Soc.* **2000**, *147*, 517.
[34] Y.-G. Lee, S. Fujiki, C. Jung, N. Suzuki, N. Yashiro, R. Omoda, D.-S. Ko, T. Shiratsuchi, T. Sugimoto, S. Ryu, J. H. Ku, T. Watanabe, Y. Park, Y. Aihara, D. Im, I. T. Han, *Nat. Energy* **2020**, *5*, 299.
[35] J. A. Lewis, S. E. Sandoval, Y. Liu, D. L. Nelson, S. G. Yoon, R. Wang, Y. Zhao, M. Tian, P. Shevchenko, E. Martínez-Pañeda, M. T. Mcdowell, *Adv. Energy Mater.* **2023**, *13*, 2204186.

[36] T. Ortmann, S. Burkhardt, J. K. Eckhardt, T. Fuchs, Z. Ding, J. Sann, M. Rohnke, Q. Ma, F. Tietz, D. Fattakhova-Rohlfing, C. Kübel, O. Guillon, C. Heiliger, J. Janek, *Adv. Energy Mater.* **2023**, *13*, 2202712.

[37] J. A. S. Oh, Y. Wang, Q. Zeng, J. Sun, Q. Sun, M. Goh, B. Chua, K. Zeng, L. Lu, *J. Colloid Interf. Sci.* **2021**, *601*, 418.

[38] E. Quérel, I. D. Seymour, A. Cavallaro, Q. Ma, F. Tietz, A. Aguadero, *J. Phys. Energy* **2021**, *3*, 044007.

[39] E. Quérel, N. J. Williams, I. D. Seymour, S. J. Skinner, A. Aguadero, *Chem. Mater.* **2023**, *35*, 853.

[40] T. Krauskopf, H. Hartmann, W. G. Zeier, J. Janek, *ACS Appl. Mater. Inter.* **2019**, *11*, 14463.

[41] A. Pei, G. Zheng, F. Shi, Y. Li, Y. Cui, *Nano Lett.* **2017**, *17*, 1132.

[42] P. Xu, X. Li, M.-Y. Yan, H.-B. Ni, H.-H. Huang, X.-D. Lin, X.-Y. Liu, J.-M. Fan, M.-S. Zheng, R.-M. Yuan, Q.-F. Dong, *J. Mater. Chem. A* **2021**, *9*, 22892.

[43] J. T. S. Irvine, D. C. Sinclair, A. R. West, *Adv. Mater.* **1990**, *2*, 132.

[44] J. K. Eckhardt, T. Fuchs, S. Burkhardt, P. J. Klar, J. Janek, C. Heiliger, *ACS App. Mater. Inter.* **2022**, *14*, 42757.

[45] J. K. Eckhardt, T. Fuchs, S. Burkhardt, P. J. Klar, J. Janek, C. Heiliger, *Adv. Mater. Inter.* **2023**, *10*, 2202354.

[46] J. K. Eckhardt, P. J. Klar, J. Janek, C. Heiliger, *ACS Appl. Mater. Inter.* **2022**, *14*, 35545.

[47] S. Lunghammer, Q. Ma, D. Rettenwander, I. Hanzu, F. Tietz, H. M. R. Wilkening, *Chem. Phys. Lett.* **2018**, *701*, 147.

[48] D. K. Singh, T. Fuchs, C. Krempaszky, P. Schweitzer, C. Lerch, F. H. Richter, J. Janek, *Matter* **2023**, *6*, 1463.

[49] J. Fleig, J. Maier, *J. Am. Ceram. Soc.* **1999**, *82*, 3485.

[50] M. J. Wang, J.-Y. Chang, J. B. Wolfenstine, J. Sakamoto, *Materialia* **2020**, *12*, 100792.

[51] A. Masias, N. Felten, J. Sakamoto, *J. Mater. Res.* **2021**, *36*, 729.

[52] C. G. Haslam, J. B. Wolfenstine, J. Sakamoto, *J. Power Sources* **2022**, *520*, 230831.

[53] F. Aguesse, W. Manalastas, L. Buannic, J. M. Lopez Del Amo, G. Singh, A. Llordés, J. Kilner, *ACS Appl. Mater. Inter.* **2017**, *9*, 3808.

[54] F. Han, A. S. Westover, J. Yue, X. Fan, F. Wang, M. Chi, D. N. Leonard, N. J. Dudney, H. Wang, C. Wang, *Nat. Energy* **2019**, *4*, 187.

[55] Y. Dong, Z. Zhang, A. Alvarez, I.-W. Chen, *Acta Mater.* **2020**, *199*, 264.

[56] L. C. De Jonghe, *J. Electrochem. Soc.* **1982**, *129*, 752.

[57] R. Raj, J. Wolfenstine, *J. Power Sources* **2017**, *343*, 119.

[58] L. C. De Jonghe, L. Feldman, A. Beuchele, *J. Mater. Sci.* **1981**, *16*, 780.

[59] L. Geng, C. Zhao, J. Yan, C. Fu, X. Zhang, J. Yao, H. Sun, Y. Su, Q. Liu, L. Zhang, Y. Tang, F. Ding, J. Huang, *J. Mater. Chem. A* **2022**, *10*, 14875.

[60] Q. Liu, L. Zhang, H. Sun, L. Geng, Y. Li, Y. Tang, P. Jia, Z. Wang, Q. Dai, T. Shen, Y. Tang, T. Zhu, J. Huang, *ACS Energy Lett* **2020**, *5*, 2546.

[61] C. Haslam, J. Sakamoto, *J. Electrochem. Soc.* **2023**, *170*, 040524.

[62] M. Ohring, *The Materials Science of Thin Films*, Academic Press, Cambridge, Massachusetts, USA **2022**.

[63] Q. Ma, C.-L. Tsai, X.-K. Wei, M. Heggen, F. Tietz, J. T. S. Irvine, *J. Mater. Chem. A* **2019**, *7*, 7766.

[64] Z. Ding, Y. Tang, V. S. K. Chakravadhanula, Q. Ma, F. Tietz, Y. Dai, T. Scherer, C. Kübel, *Microscopy* **2023**, *74*, 326.

3.3 Publication 3: *"Imaging the Microstructure of Lithium and Sodium Metal in "Anode-Free" Solid-State Batteries using EBSD"*

In the third publication of this doctoral thesis, the microstructure of electrodeposited lithium and sodium metal at solid|solid interfaces is analyzed by electron backscatter diffraction. For this purpose, lithium and sodium metal foils with different grain sizes were characterized by EBSD to study potential grain growth during characterization. Additionally, a workflow for the microstructural characterization of buried interfaces by ion beam milling was established. The microstructure of electrodeposited lithium and sodium metal at three relevant interfaces for reservoir-free cell concepts, namely Cu|LLZO, StS|LPSCl, and Al|NZSP, was imaged based on the established workflow. Besides the reservoir-free configuration, electrodeposition at the Li|LLZO and Na|NZSP interfaces of the respective alkali metals was also examined. An in situ EBSD experiment was designed to characterize the evolution of the microstructure during cathodic deposition and anodic dissolution of the respective metal anode.

For the first time, the microstructure of sodium metal foils has here been visualized by EBSD revealing a grain size of several hundred micrometers, which is larger compared to lithium metal. The grain size of sodium and lithium can be altered by quenching molten alkali metal using liquid N_2. For both metals, no substantial grain growth was observed within a period of two weeks. Furthermore, the microstructure remained unchanged when the samples were processed by a plasma-focused ion beam under cryogenic conditions. Large angle grain boundaries perpendicular to the SE surface were observed in both electrodeposited sodium and lithium. Furthermore, there was no correlation between the grain size of the deposited alkali metal and the electrode material or the SE. In situ EBSD experiments revealed a lateral motion of the grain boundaries in addition to the vertical growth of the metal grains. This results in the merging of neighboring grains and a reduction in the total grain number as electrodeposition progresses. The formation of pores was observed during the anodic dissolution of the metal anode. Pore formation occurred preferentially in the interior of a grain localized at the interface.

Overall, the third publication establishes a workflow and demonstrates the characterization of the microstructure of highly reactive alkali metals as well as its evolution during cathodic deposition and anodic dissolution using EBSD. The study highlights the importance of the metal electrode microstructure and reveals its correlation with electrochemical performance. The established method and knowledge open a new perspective on metal anodes in general and help to design and evaluate new concepts to improve the cycling performance of metal anodes in SSBs.

Dr. T. Fuchs and T. Ortmann contributed equally to this work by designing and conducting the experiments, which were supported by J. Becker. T. Ortmann mainly conducted the experiments for sodium, while T. Fuchs carried out the experiments for lithium. The preparation of the solid electrolyte and the cells including the electrochemical cycling was supported by C. G. Haslam, V. K. Singh, M. Ziegler and J. Becker. The EBSD experiments were supported by Dr. B. Mogwitz and Dr. K. Peppler. The first draft of the manuscript was written by Dr. T. Fuchs and T. Ortmann and revised by twelve co-authors. The work was supervised by Prof. M. Rohnke, Prof. L. Nazar, Prof. J. Sakamoto and Prof. J. Janek.

This study was part of the research within the Cluster of Excellence for Post Lithium-Ion Storage.

Reprinted without modification according to the creative commons license CC BY-NC 4.0 (https://creativecommons.org/licenses/by-nc/4.0/) from Fuchs, T., Ortmann, T., Becker, J., Haslam, G. C., Ziegler, M., Singh, V. K., Rohnke, M., Mogwitz, B., Peppler, K., Nazar, L. F., Sakamoto, J., Janek, J. Imaging the microstructure of lithium and sodium metal in anode-free solid-state batteries using electron backscatter diffraction. *Nat. Mater.* **2024**, *23*, 1678-1685. https://doi.org/10.1038/s41563-024-02006-8. Nature Materials published by Springer Nature Limited.

nature materials

Article https://doi.org/10.1038/s41563-024-02006-8

Imaging the microstructure of lithium and sodium metal in anode-free solid-state batteries using electron backscatter diffraction

Received: 23 May 2024

Accepted: 22 August 2024

Till Fuchs [1,6], **Till Ortmann** [1,6], **Juri Becker** [1], **Catherine G. Haslam** [2,3], **Maya Ziegler** [1], **Vipin Kumar Singh** [4], **Marcus Rohnke** [1], **Boris Mogwitz** [1], **Klaus Peppler** [1], **Linda F. Nazar** [4], **Jeff Sakamoto** [5] & **Jürgen Janek** [1]

'Anode-free' or, more fittingly, metal reservoir-free cells could drastically improve current solid-state battery technology by achieving higher energy density, improving safety and simplifying manufacturing. Various strategies have been reported so far to control the morphology of electrodeposited alkali metal films to be homogeneous and dense, but until now, the microstructure of electrodeposited alkali metal is unknown, and a suitable characterization route is yet to be identified. Here we establish a reproducible protocol for characterizing the size and orientation of metal grains in differently processed lithium and sodium samples by a combination of focused ion beam and electron backscatter diffraction. Electrodeposited films at Cu|Li$_{6.5}$Ta$_{0.5}$La$_3$Zr$_{1.5}$O$_{12}$, steel|Li$_6$PS$_5$Cl and Al|Na$_{3.4}$Zr$_2$Si$_{2.4}$P$_{0.6}$O$_{12}$ interfaces were characterized. The analyses show large grain sizes (>100 µm) within these films and a preferential orientation of grain boundaries. Furthermore, metal growth and dissolution were investigated using in situ electron backscatter diffraction, showing a dynamic grain coarsening during electrodeposition and pore formation within grains during dissolution. Our methodology and results deepen the research field for the improvement of solid-state battery performance through a characterization of the alkali metal microstructure.

Solid-state batteries (SSBs) have gained substantial attention for their potential to surpass lithium-ion batteries as advanced energy storage devices[1–3]. Major advancement is expected by the successful implementation of lithium metal anodes in SSBs, enabled by chemically stable solid electrolytes (SEs)[4,5], and owing to lithium's high theoretical specific capacity of 3,861 mAh g^{-1} and low redox potential of −3.04 V. Similar advantages are expected by the use of sodium metal anodes in sodium-based SSBs[6–8].

'Anode-free' or, more fittingly, reservoir-free cells (RFCs) emerged as an alternative to using alkali metal foils for cell fabrication[9–11]. Instead, the metal is deposited onto a specially designed current collector (CC) in the first charging step, eliminating the need for costly handling of reactive alkali metal foils. This approach increases energy density by reducing unnecessary weight while also simplifying fabrication and enhancing safety during storage.

The main challenge of RFCs is controlling the morphology and microstructure of plated alkali metal at the CC|SE interface. Strategies to control the alkali metal layer include specialized plating protocols, engineered CC materials, seed layers and applying pressure during

---

[1] Institute of Physical Chemistry and Center for Materials Research, Justus Liebig University Giessen, Giessen, Germany. [2] Department of Materials Science and Engineering, University of Michigan, Ann Arbor, MI, USA. [3] Department of Mechanical Engineering, University of Michigan, Ann Arbor, MI, USA. [4] Department of Chemistry and the Waterloo Institute for Nanotechnology, University of Waterloo, Waterloo, Ontario, Canada. [5] Materials Department, University of California Santa Barbara, Santa Barbara, CA, USA. [6] These authors contributed equally: Till Fuchs, Till Ortmann. e-mail: Till.Fuchs@pc.jlug.de; Juergen.Janek@phys.chemie.uni-giessen.de

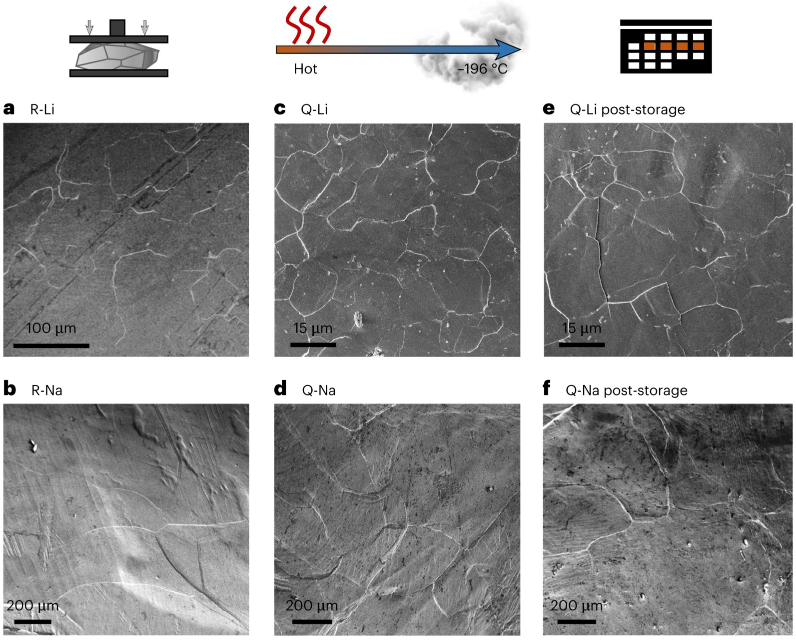

Fig. 1 | Top-view SEM images obtained from freshly pressed alkali metal foils. R-Li and R-Na denote pristine lithium and sodium foils, while quenched metal foils are labelled as Q-Li and Q-Na. **a**–**d**, Large grains are visible for lithium (**a**) and sodium (**b**) as well as small grains for lithium (**c**) and sodium (**d**). **e**,**f**, After a wait time of several calendar days, two new foils were prepared from the quenched metal, for lithium (**e**) and sodium (**f**).

plating[11–17]. Despite intense investigation of the morphology of the metal deposited in RFCs[11–13,18], its microstructure, including the grain size and orientation, is yet completely unknown[19,20]. Based on previous work, we expect that the microstructure will impact the anode performance by influencing, for example, the pore formation and spatially inhomogeneous plating[19,21,22].

Another unknown effect concerns alkali metal grain growth during storage at room temperature. Typically, metals show microstructural changes at homologous temperatures (T_{H}) of around 0.4–0.6 (ref. 23). As T_{H}(Li) = 0.61 and T_{H}(Na) = 0.80 at room temperature exceed this, it is reasonable to assume that the microstructure of alkali metals is always close to equilibrium, given enough time to anneal. Recent investigations of lithium suggest that its microstructure is actually tunable by a different thermal processing, suggesting slow grain coarsening[21,22]. Interestingly, electrodeposited silver is initially nanocrystalline but anneals during the first hours until grain growth stops at around 40 µm, even at a much lower T_{H}(Ag) of 0.23 at room temperature[24,25]. It is possible that the initially stated rule of thumb about recrystallization at $T_{\mathrm{H}} > 0.4$ may not hold for lithium and sodium.

The most suitable technique to analyse the microstructure of metals and its evolution is electron backscatter diffraction (EBSD). EBSD offers quantitative information on the grain size and orientation, grain boundaries and possibly even dislocations and strain within large single grains[26–28]. However, a very well-defined sample surface with regard to its flatness, crystallinity and chemical composition is required. Thin (<50 nm) degradation layers typically found on lithium[29,30] mask the electron diffraction pattern due to the very low probe depth of EBSD (~20 nm). Very few EBSD analyses of lithium foils[26,31–33] exist so far, and to the best of our knowledge, no data have been reported for sodium or electrodeposited alkali metals.

To solve this issue, this work presents a protocol to analyse the microstructure of lithium and sodium foils as well as deposited films in RFCs using EBSD. The success relies on operation in inert gas or high vacuum in all steps, a delicate focused ion beam (FIB) cutting/polishing under cryogenic conditions, and an EBSD system with high sensitivity. First, the results presented here indicate that substantial grain growth of lithium and sodium occurs neither during room temperature storage despite the high T_{H}, nor during cryogenic FIB preparation. Second, we analyse the microstructure of lithium electrodeposited at $\mathrm{Cu|Li_{6.5}Ta_{0.5}La_3Zr_{1.5}O_{12}}$ (Cu|LLZO) and stainless-steel|$\mathrm{Li_6PS_5Cl}$ (SS|LPSCl) interfaces as well as sodium plated at a carbon-coated $\mathrm{Al|Na_{3.4}Zr_2Si_{2.4}P_{0.6}O_{12}}$ (Al|NZSP) interface, showing distinctly columnar growth of large grains. These observations offer the first views into the electrochemical growth of unexpected large metal grains and open up a multitude of options for follow-up work on the correlation of electrochemical performance and microstructure of alkali metal anodes.

The major goal of this work was to analyse the grain size and orientation of electrodeposited alkali metal films in RFCs as well as to image pore formation after electrodissolution—in representative cross-sections—to advance the understanding of microstructure–property relations. However, before the results could be interpreted reliably, a protocol is required that does not alter the metal grain size, including artefacts created by heating during preparation and subsequent annealing. Furthermore, it was necessary to determine if and to what extent lithium and sodium anneal/recrystallize at room temperature. The following section answers these questions, while the subsequent section showcases the first results obtained from electrodeposited films within RFCs.

Protocol for alkali metal microstructure analysis by EBSD

Lithium foils with varying microstructures were already prepared by Singh et al.[21,22]. However, while electrodeposited silver and copper films show microstructural changes during room temperature storage[24,34],

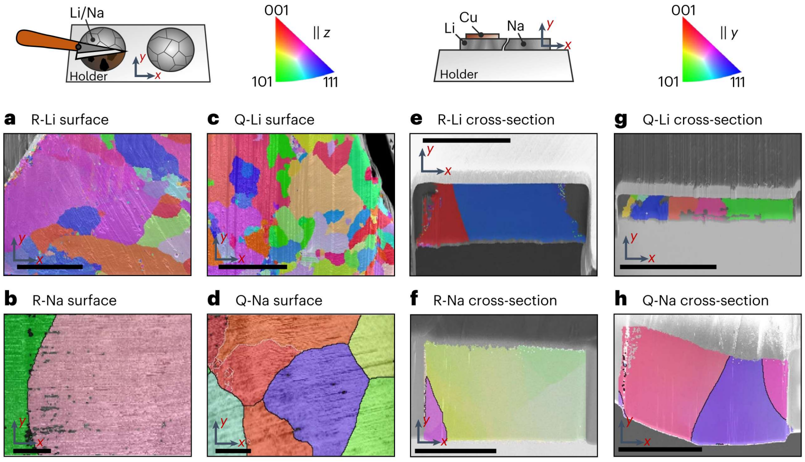

Fig. 2 | IPF maps of alkali metal foils with different thermal processing histories. a–d, Top-view IPF maps of freshly cut samples of R-Li (**a**), R-Na (**b**), Q-Li (**c**) and Q-Na (**d**). **e–h**, IPF maps of cross-sections prepared via cryogenic FIB of R-Li (**e**), R-Na (**f**), Q-Li (**g**) and Q-Na (**h**). Scale bars, 200 µm.

it is unclear if this can be applied to (electrodeposited) lithium and sodium. Therefore, four different metal foils were prepared for analysis as described in Methods.

Top-view scanning electron microscopy (SEM) images of each foil obtained directly after preparation are shown in Fig. 1a–d. Figure 1e,f shows top-view images of quenched lithium and sodium referred to as Q-Li and Q-Na after several days of room temperature storage, to reveal information about possible grain growth. First, lines and multiple triple junctions are found on the freshly prepared metal foils. These are assumed to be grain boundaries made visible by preferential degradation or morphological changes induced during pressing[21,22]. Interestingly, sodium foils show less pronounced lines, possibly due to differences in mechanical properties, impurity level and surface chemistry.

With apparent grain sizes of ~100–300 µm for the reference lithium foil (R-Li) and 10–50 µm for Q-Li, we confirm that thermal processing strongly influences the lithium microstructure[21,22]. Furthermore, no visible grain growth occurred during room temperature storage of Q-Li despite its high T_H. With less pronounced white lines, the reference sodium foil (R-Na) shows larger grains close to the millimetre range and Q-Na grain sizes of about 200–600 µm. Note that the grains were sometimes larger than the SEM field of view, which makes statistical grain size analysis difficult. However, upon comparison, it is also striking that the microstructure of sodium could be altered by thermal processing. Furthermore, Q-Na stored for 2 days does not show grain growth caused by room temperature annealing, which is confirmed below.

The apparent lack of grain growth despite the high T_H may be explained considering two stages. Small grains are expected to grow rapidly driven by the reduction of interfacial grain boundary energies, as, for example, in the case of electrodeposited silver[25]. However, with increasing grain size, the driving force to mitigate interfacial grain boundary energies decreases, slowing down further growth.

To validate these initial findings, we used EBSD to analyse freshly prepared surfaces of each foil as depicted in Fig. 2a–d. Exemplary Kikuchi patterns are depicted in Supplementary Figs. 1 and 2, proving that crystalline, sufficiently passivation-free surfaces were obtained. The inverse pole figure (IPF) maps confirm that the grains identified in Fig. 1 are body-centered cubic metal grains with different orientations. Due to the large grain size of R- and Q-Na, several spots were characterized by EBSD as presented in Supplementary Figs. 3 and 4. Similar grain sizes are observed for R-Li and R-Na with EBSD characterization compared with the initial SEM analysis as well as for their quenched counterparts. This controlled grain size change fits well to what was observed for lithium[21,22] and has not been previously shown for sodium. As the time between quenching the metal and cooling for analysis was minimized (that is, 20 min for Q-Na), substantial grain growth is not expected to have occurred. Moreover, no substantial grain growth of Q-Na at room temperature was observed after approximately 2 weeks, as demonstrated by the IPF in Supplementary Fig. 4. Therefore, grain growth of lithium at room temperature is also unlikely due to its lower T_H. Interestingly, the lithium grains do not follow a typical Voronoi shape. A more regular grain shape is expected, as seen for sodium. We assume that these shape distortions were induced by the high ductility of the metal during preparation, where a blade was run across the sample surface.

These results for thermally prepared alkali metals are consistent and demonstrate the efficacy of our protocol. However, electrodeposited metal films in RFCs are buried between a CC and an SE separator, and surface EBSD analysis is not suitable for these films. Here, cross-section preparation by cryogenic FIB is required to enable the analysis of electrodeposited metal layers perpendicular to the interface. Therefore, a second step was necessary to exclude local alterations of the microstructure by the cryogenic FIB preparation. Hence, cross-sections of samples shown in Fig. 2a–d were analysed using EBSD (Fig. 2e–h). A second IPF map in the *x* direction of the sample in Fig. 2g is shown in Supplementary Fig. 5, to showcase that the large green grain actually consists of multiple, coincidentally oriented similarly in the *y* direction. IPF maps of aged sodium cross-sections are depicted in Supplementary Fig. 6.

Although the analysis area of a cross-section is smaller than a surface view, substantial differences between thermally processed metal foils and reference foils are observed for both lithium and sodium, consistent with previous results. Furthermore, all cross-sectional maps predominantly show vertical grain boundaries. This probably occurs due to the high aspect ratio of the analysed foils and the grain size being larger than the foil thickness or potentially during texturing when pressing ingots to a foil. This also explains why more curved grain boundaries are observed for thicker sodium foils in Fig. 2f,h with a lower aspect ratio.

Local grain growth during cryogenic FIB preparation is thereby excluded, and the alkali metal microstructure remains unaltered.

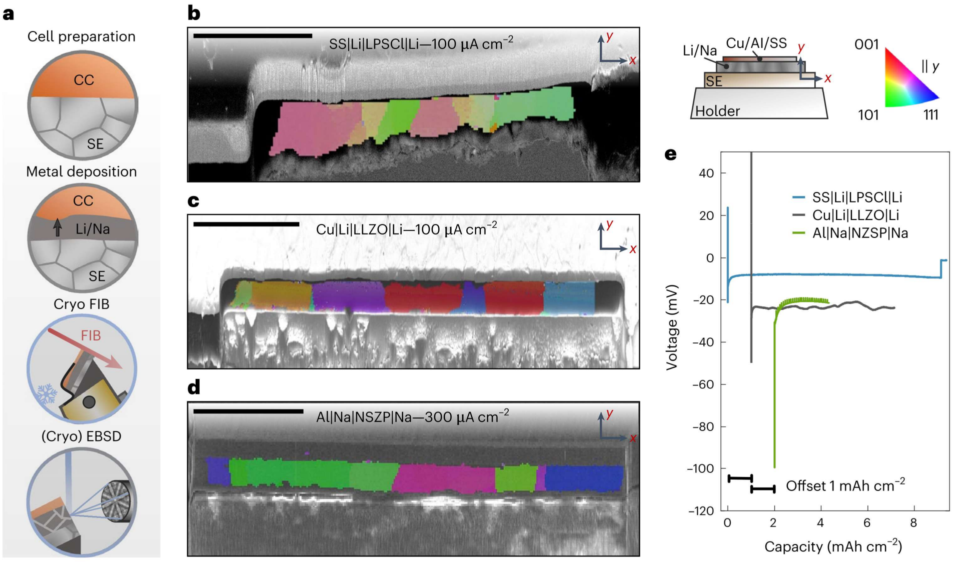

Fig. 3 | Microstructural analysis of electrodeposited lithium and sodium at different CC|SE interfaces using FIB cross-sections and EBSD. **a**, Overview of the analysis protocol to image the microstructure of electrodeposited alkali metal films. **b**,**c**, Cross-sectional IPF maps of lithium plated at the SS|LPSCl (**b**) and Cu|LLZO (**c**) interface. **d**, A cross-sectional IPF map of sodium plated at the Al|NZSP interface. IPF maps are given parallel to the *y* direction as indicated by the sketch in the upper right of the figure. Scale bars, 100 μm. **e**, The corresponding voltage profiles during electrodeposition for every layer.

These findings are supported by the lack of microstructural changes after a second milling step of a cross-section (Supplementary Fig. 7). Overall, this confirms that our cryogenic FIB protocol is suitable to analyse the microstructure of alkali metal cross-sections, including electrodeposited films at CC|SE interfaces. We could further confirm that the white lines on the surfaces as seen by SEM in Fig. 1 indicate grain boundaries in most cases, as elaborated in Supplementary Fig. 8.

The microstructure of electrodeposited alkali metal films

Next, the EBSD analysis is focused on the microstructure of alkali metal films electrodeposited within RFCs. Different RFCs were prepared, namely, SS|LPSCl|Li, Cu|LLZO|Li and Al|NZSP|Na cells, representing today's most investigated SEs paired with alkali metal anodes. The metal was deposited within each cell on the respective CC. Figure 3a shows the protocol needed to obtain cross-sectional EBSD images thereof, with the three respective IPF maps shown in Fig. 3b–d. The corresponding voltage profiles during plating are shown in Fig. 3e.

Both lithium films were deposited with 100 μA cm^{-2}, at the SS|LPSCl interface with 15 MPa and at the Cu|LLZO interface with 5 MPa. Sodium was electrodeposited at the carbon-coated Al|NZSP interface with 300 μA cm^{-2} at 3 MPa. These parameters were chosen on the basis of experience to yield a homogeneously deposited film[11,35]. Impedance spectra before and after electrodeposition of each cell are depicted in Supplementary Fig. 9, showing a characteristic change from a blocking impedance of the working electrode to the signature of a reversible alkali metal electrode, confirming nucleation and subsequent growth of a metal layer[11,35,36]. All three voltage profiles display a characteristic nucleation overpotential in line with previous results, followed by a stable plateau, during which layer growth occurs[11,35]. The magnitude of the overvoltage is also similar to what was previously reported with 10–20 mV for lithium deposition and around 80 mV for sodium deposition[35,36]. For lithium plated at the SS|LPSCl interface, a sudden voltage drop indicates a short circuit from dendrite formation, confirmed by impedance data showing substantially lowered resistance (Supplementary Fig. 9). However, the resulting film could still be analysed.

Subsequently, each sample was prepared for EBSD analysis according to the description given in Methods. It is striking that the average grain size of each electrodeposited metal film is quite large, especially compared with other electrodeposited metals[25,28,34,37]. The grain width for deposited lithium at the SS|LPSCl interface and CC|LLZO interface is around 20–100 μm and 10–100 μm, respectively. Sodium deposited at the carbon-coated Al|NZSP interface shows a grain width around 10–150 μm. A second cross-section of the sodium film in Supplementary Fig. 10 confirms the given grain size. However, compared with the alkali metal foils analysed in Figs. 1 and 2, the grain size is smaller, further indicating the absence of substantial room temperature storage grain growth in electrodeposited films, although the impurity content is expected to be lower.

Another observation is that all grain boundaries are perpendicular to the CC|SE interface, which marks a major difference between the Li/Na|SE interface of an electrodeposited metal compared with an as-built Li/Na|SE interface using foils. In the latter case, grains are larger and grain boundaries are randomly oriented. This has implications for the subsequent discharge performance of the anode, as the microstructure will probably affect the pore formation[21,22]. Additionally, for the lithium film plated at the Cu|LLZO interface, two small grains are observed that do not span the whole thickness of the film. A larger magnification of these areas is visible in Supplementary Fig. 11.

Interestingly, similar predominant columnar grain growth has also been observed for electrodeposited nickel using cross-sectional EBSD analysis, although these grains did not span the whole thickness[37]. While the grain size is nearly constant for nickel films, the fraction of columnar grains increases with thickness. A similar phenomenon is not observed here, as the columnar grains appear to grow along the whole layer. On the contrary, electrodeposited silver films do not show this columnar grain growth[24]. A reason could be that silver shows room

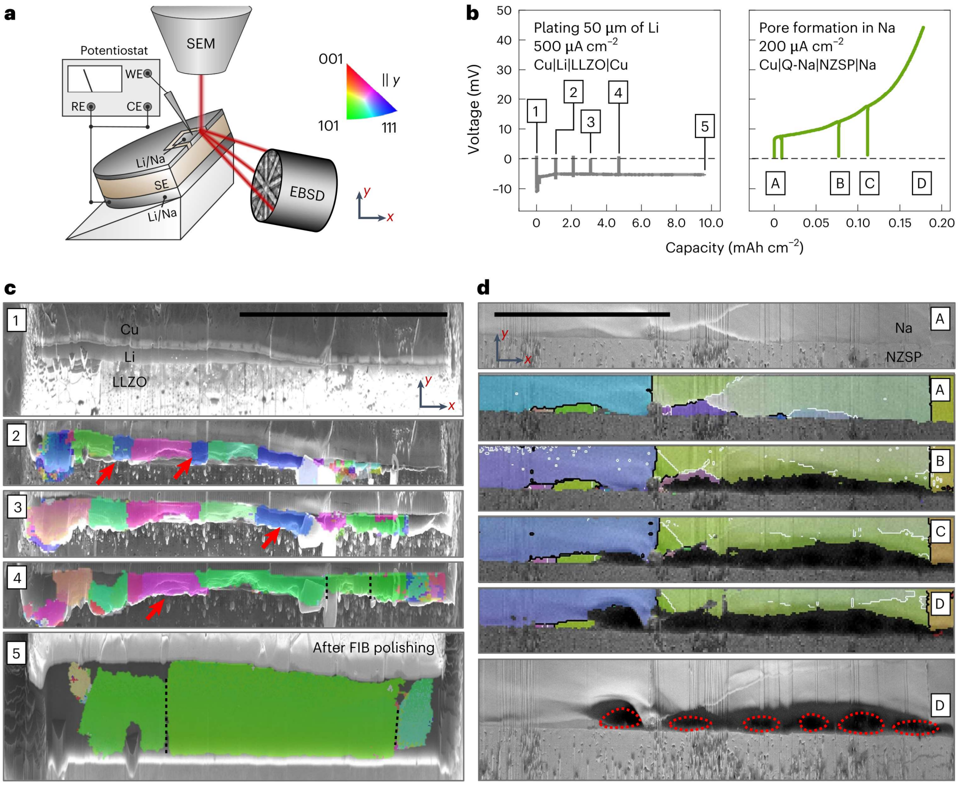

Fig. 4 | Analysis of the microstructural evolution during electrodeposition and electrodissolution of an alkali metal electrode in contact with an SE. **a**, Schematic depiction of the in situ EBSD setup whereby RE, WE and CE denote the reference, working and counter electrode, respectively. **b**, The voltage profiles for plating 50 µm lithium at the Cu|Li|LLZO interface and stripping sodium until pore formation at the Cu|Q-Na|NZSP interface. **c**,**d**, The microstructure evolution for lithium plating (**c**) and sodium stripping (**d**). The red arrows indicate grains disappearing during film growth in **c**, and the red outlines indicate pores formed during stripping in **d**. The map provided in **c** step 5 was acquired after a 2 week storage period and second FIB polishing step. Scale bars, 100 µm.

temperature grain annealing within hours, thereby changing the initial grain microstructure present during electrodeposition. This supports the conclusion that plated alkali metals do not show grain growth at room temperature, unlike silver and copper. However, microstructural changes during deposition may still occur, as discussed later. A direct correlation between CC/SE microstructure and the alkali metal microstructure cannot be observed, as discussed in Supplementary Figs. 12 and 13.

As the process of grain growth and evolution during electrodeposition is yet elusive, in situ EBSD analysis was performed. Here, cross-sections of Cu|Li|LLZO|Li and Cu|Q-Na|NZSP|Na were charged and discharged inside the SEM, respectively, and stopped for intermittent EBSD analysis. Around 2 µm of lithium was deposited at the Cu|LLZO interface before cross-section preparation to fix the CC on the SE. Further, microelectrodes were prepared via FIB at the cross-section to ensure that changes occur in the field of view. The described setup is depicted in Fig. 4a. An overview SEM image is shown in Supplementary Fig. 14a before deposition with front-view images of the pristine cross-section provided in Supplementary Fig. 14b,c. The left section of Fig. 4b shows the voltage profile during deposition of lithium with 1,000 µA cm^{-2} initially followed by ~500 µA cm^{-2}. The initial higher voltage ensures homogeneous layer growth. The observed voltage profile is mostly flat, hinting at dendrite-free lithium deposition of 10 mAh cm^{-2}, corresponding to a layer of ~50 µm thickness. The right side of Fig. 4b shows the voltage profile obtained for stripping of the sodium electrode with a typical increase of voltage indicative of pore formation. Both measurements were paused for intermittent EBSD analysis as visible in the potential profiles, which is shown in Fig. 4c,d.

Figure 4c(1) shows an SEM image of the pristine cross-section of Cu|Li|LLZO. The lithium reservoir is not freshly deposited and also too thin to obtain EBSPs of sufficient quality to generate an IPF map. However, upon depositing around 10–15 µm of additional lithium, the IPF map depicted in Fig. 4c(2) was obtained. Herein, several grains around 10–30 µm wide are visible. Surprisingly, after another ~5 µm of lithium deposition, fewer but wider grains are visible in the next IPF map in Fig. 4c(3). Two small blue grains close to a <111> orientation from the previous map apparently fused into larger neighbouring grains close to a <101> orientation (green). After another deposition step, IPF map Fig. 4c(4) shows even wider grains, with another blue grain from the previous map being fused to a neighbouring green grain.

After another long deposition step resulting in around 20 µm of additional lithium, multiple grains have fused together forming a large grain with >100 µm width, again close to a <101> orientation as visible in Fig. 4c(5). As the observed grain boundaries are mostly vertically oriented, lateral motion of grain boundaries is assumed to be responsible for the observed changes. This post-deposition map was

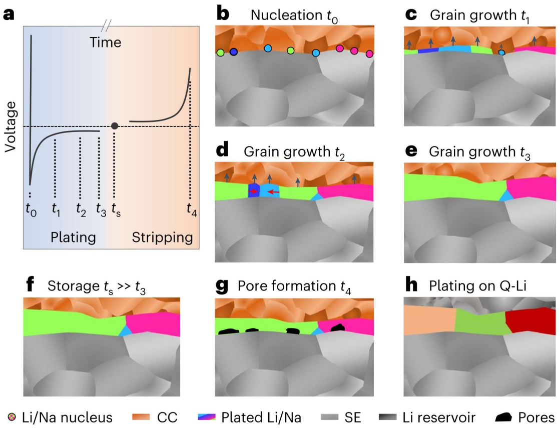

Fig. 5 | Schematic evolution and the origin of the observed columnar microstructure of deposited alkali metal films in RFCs during electrochemical deposition and dissolution. a–**g**, A schematic voltage profile of one cycle of a metal electrode (**a**) with the corresponding schematized metal microstructures upon nucleation (**b**) followed by grain growth at t_1 (**c**), t_2 (**d**) and t_3 (**e**), after storage (**f**) and after pore formation induced by electrochemical dissolution (**g**). **h**, The schema of the metal microstructure plated on a lithium reservoir.

acquired after 2 weeks of room temperature storage and additional FIB polishing, with top- and front-view images depicted in Supplementary Fig. 14g,h. Additionally, the map in Supplementary Fig. 15a acquired directly after the deposition shows the same microstructure. Small deviations were visible in the map directly acquired after plating, which can be seen in Supplementary Fig. 15a. This is due to the lithium being partly squeezed outside of the prepared electrode area (Supplementary Fig. 14d). The uneven film morphology at the interface also explains the low indexing rate of the shown IPF maps, as the sample is not perfectly tilted at 70° at every spot. Interestingly, our analysis also confirms the absence of grain growth during storage. Additionally, Supplementary Fig. 15b,c depicts the maps of Fig. 4c(4,5) with the IPF in the x direction, showing that the large green grains actually consist of more grains, coincidentally oriented similarly in the y direction. These grain boundaries are indicated with dashed black lines in every map in the y direction. Furthermore, Supplementary Fig. 15d depicts the cross-section shown in Fig. 4c(5) after storage and additional FIB polishing, further confirming the absence of grain growth during storage. We consider these results gained from the in situ analysis as highly important, that is, microstructural changes are now shown to occur during the deposition process but to stop once the deposition is finished. This is also explored for sodium metal deposition as discussed in Supplementary Fig. 16.

To further study the dependence of pore formation on the anode microstructure, a sodium anode was stripped with intermittent EBSD analysis. A typical voltage profile is achieved with an initial small increase evolving into a step increase, as shown in Fig. 4b. This signature voltage profile clearly indicates pore formation[6,38–40]. The corresponding IPF maps and forward-scatter electron images are shown in Fig. 4d. Starting from an optimal interfacial contact between sodium and NZSP (Fig. 4d(A)), a dark region close to the interface emerges (Fig. 4d(B)) after the first stripping interval, attributed to pores. Likewise, the generation of secondary electrons decreases, leading to darker areas in the images (Supplementary Fig. 17a,b).

Interestingly, the pores formed mainly within the green grain, while the vertical grain boundaries on both sides remain intact (Fig. 4d(C)). As stripping progresses, another pore nucleates within the large blue grain starting from a grain boundary, supporting the previous description. Moreover, the pores within the green grain further grow into its bulk (Fig. 4d(D)). Despite geometrical correction, the size and shape of the pores might not be fully captured, appearing larger due to the high tilting angle of 70° for EBSD analysis, as visible in Supplementary Fig. 17c. Finally, the cross-section was polished again to confirm that the pores resulted from anodic dissolution of sodium (Supplementary Fig. 17d).

Clearly, this observation of preferential pore formation in grains—not in grain boundaries—is at first glance counter-intuitive, but is a direct proof for the fast diffusion of vacancies along grain boundaries[41]. Pore nuclei at grain boundaries can be closed faster by diffusion within the grain boundary than within the bulk. The microstructure strongly influences the pore formation and, thus, the physical contact at the interface, which drastically affects the performance of the metal anode.

Grain evolution during cycling

In the following, a mechanism behind the microstructural evolution during stripping and plating of alkali metal is proposed and schematically depicted in Fig. 5.

Figure 5a shows a schematic of a voltage profile during electrochemical deposition of alkali metals on an inert CC with subsequent storage and dissolution. The metal nucleation at t_0 evolves into the early stages of grain formation and growth (Fig. 5b), which is followed by mostly vertical grain growth at t_1 with different rates (Fig. 5c,d). If the growth rates of neighbouring grains are dissimilar, it also seems to be possible that the growth of slower growing grains is limited compared with the faster-growing neighbouring grains as shown in Fig. 5d,e or Supplementary Fig. 11, leading to truncated V-shaped grains. Furthermore, the observed grain density is lower than what would be expected for each nucleus growing into a columnar grain[12,13]. One reason is that neighbouring nuclei may exhibit a similar orientation, thus directly fusing together to form a single grain upon contact as depicted with the pink nuclei in Fig. 5b,c.

During the whole deposition process between t_0 and t_3, lateral grain ripening occurs with some grain boundaries moving into adjacent grains as depicted with red arrows in Fig. 5d, thus widening the average lateral grain dimensions and reducing the grain density. The reason and magnitude of this ripening is yet elusive and may be related to abnormal grain growth or ‘secondary recrystallization’, which is dependent on the interface and grain boundary energies[42]. This may also be another reason for the occurrence of truncated V-shaped grains. To elucidate this, further studies will focus on more detailed investigations of the current density and thickness dependence of the film microstructure.

After a prolonged room temperature storage at t_s, the microstructure remains unchanged (Fig. 5f). If this microstructure is then subjected to anodic dissolution until pore formation, the pores predominantly form within grains at the interface and not at grain boundaries, where vacancy accumulation is less likely during stripping (Fig. 5g). Grain boundaries as two-dimensional defects typically have a higher free energy compared with the bulk, meaning that the oxidation of a metal atom, and thus vacancy injection, is thermodynamically favoured. However, fast transport of vacancies along grain boundaries—as reported as a result of computational work by Yoon et al.—might be the reason for a kinetic stabilization of the interface, as vacancy accumulation is hindered[41]. Therefore, the growth of pores where the grain boundaries within the metal meet the interface is suppressed.

As the pores formed during anodic dissolution seem to form preferentially within grains and not at grain boundaries, we conclude that it is possible to tune the electrochemical properties, such as available stripping capacity[38,43], by controlling the microstructure. Following this reasoning, achieving a microstructure with small grains would be desired[41]. The nucleation density mainly depends on applied current density and temperature as well as the surface properties of the SE[12,13,36].

Additionally, our in situ EBSD results further show that not only the grain nucleation is important to control the resulting microstructure, but also the growth process. Potentially, the applied current density will also influence the grain ripening during electrodeposition. Similarly, applying stack pressure may be a suitable tool to guide the lateral expansion of the growing grains[11].

In addition, based on our evidence, controlling the microstructure of the CC and SE may not be a successful path to influence the deposited metal microstructure. Lithium plated on a lithium foil matches neither the microstructure of the SE nor the foil but plates with a similar, columnar shape as in the case of plating on an inert CC in a reservoir-free setup (Fig. 5h). The microstructure of the deposited metal is still substantially different and has lower overall grain sizes compared with those of commonly used metal foils.

Based on our results, the merging of grains is caused by the movement of grain boundaries. Thus, the microstructure of electrodeposited alkali metals is tunable by modifying the mobility and movement of grain boundaries. The mobility of grain boundaries in metals is diminished by impurities, even at low concentrations[44]. Therefore, the implementation of tailored impurities such as seed layers or particles at the metal|SE interface could affect the mobility of grain boundaries and, thus, the resulting microstructure. For example, an enhanced stripping performance for electrodeposited lithium was observed when gold particles were situated at the Cu|LLZO interface during the initial electrodeposition of lithium[14], potentially leading to smaller grains. The mobility of grain boundaries is also prevented by introducing mechanical barriers, such as geometric constrictions present in three-dimensional SE host structures, as demonstrated for LLZO and NZSP by Wachsman and coworkers[45,46]. Our analyses on the metal microstructure offer valuable insights to explain the mechanism behind the metal growth when using three-dimensional hosts or seed layers previously overlooked in literature.

The results of this work highly motivate further research on the influence of deposition parameters and seed layer concepts or geometrical confinements at the interface on the resulting electrode microstructure and thereby subsequent electrochemical performance. Both ex situ and in situ experiments will help to develop more advanced plating and stripping strategies for enhanced performance.

We developed an analysis protocol to reliably analyse the microstructure of alkali metal foils both from the surface and cross-sections using EBSD. We conclude that the microstructure of both lithium and sodium can be tailored by thermal processing, yielding grain sizes between 10–200 µm (lithium) and 200–600 µm (sodium). Grain growth can be ruled out for these foils during both room temperature storage and cryogenic FIB preparation.

This further allowed the analysis of the grain size and orientation of electrodeposited metal for three different CC|SE combinations, namely, Cu|LLZO, SS|LPSCl and Al|NZSP. We show that the grain width in electrodeposited films in RFCs ranged between 10 µm and 100 µm while the height depends on the film thickness ('row of teeth' microstructure). Grain boundaries are predominantly perpendicular to the CC|SE interface, which is distinctively different from the microstructure of metal foils and thereby will influence the electrochemical performance. Interestingly, microstructural changes could be observed neither for deposited lithium nor sodium during storage. Moreover, the deposited metal microstructures were influenced neither by the SE nor the CC. Instead, we conclude the deposited metal microstructure is dominated by the used charging protocol, that is, current density and especially the capacity (layer thickness) and applied pressure—which opens a wide range of opportunities for optimization in practice.

In situ EBSD analysis during cross-sectional deposition and dissolution further revealed the evolution of the microstructure, where small grains are annealed in a process similar to Ostwald ripening in the case of lithium. Additionally, it was shown that pore formation during discharge of the metal anode predominantly occurs at the interface between the bulk of the grain and the SE. The locations where the metal grain boundaries meet the interface are mostly left intact, probably due to faster metal and vacancy diffusion along grain boundaries.

In general, this analysis advances the investigation of metal electrodes and the understanding of their microstructural evolution. A reliable analysis protocol is presented to characterize the microstructure of deposited lithium or sodium, and the presented results will help to optimize alkali metal electrodes to tune their electrochemical performance.

Online content

Any methods, additional references, Nature Portfolio reporting summaries, source data, extended data, supplementary information, acknowledgements, peer review information; details of author contributions and competing interests; and statements of data and code availability are available at https://doi.org/10.1038/s41563-024-02006-8.

References

1. Janek, J. & Zeier, W. G. A solid future for battery development. *Nat. Energy* **1**, 16141 (2016).
2. Li, M., Lu, J., Chen, Z. & Amine, K. 30 years of lithium-ion batteries. *Adv. Mater.* **30**, 1800561 (2018).
3. Randau, S. et al. Benchmarking the performance of all-solid-state lithium batteries. *Nat. Energy* **5**, 259–270 (2020).
4. Krauskopf, T., Richter, F. H., Zeier, W. G. & Janek, J. Physicochemical concepts of the lithium metal anode in solid-state batteries. *Chem. Rev.* **120**, 7745–7794 (2020).
5. Zhang, Z. et al. New horizons for inorganic solid state ion conductors. *Energy Environ. Sci.* **11**, 1945–1976 (2018).
6. Ortmann, T. et al. Kinetics and pore formation of the sodium metal anode on NASICON-type $Na_{3.4}Zr_2Si_{2.4}P_{0.6}O_{12}$ for sodium solid-state batteries. *Adv. Energy Mater.* **13**, 2202712 (2023).
7. Chu, I. H. et al. Room-temperature all-solid-state rechargeable sodium-ion batteries with a Cl-doped Na_3PS_4 superionic conductor. *Sci. Rep.* **6**, 33733 (2016).
8. Sayahpour, B. et al. Quantitative analysis of sodium metal deposition and interphase in Na metal batteries. *Energy Environ. Sci.* **17**, 1216–1228 (2024).
9. Spencer-Jolly, D. et al. Structural changes in the silver–carbon composite anode interlayer of solid-state batteries. *Joule* **7**, 503–514 (2023).
10. Lee, Y.-G. et al. High-energy long-cycling all-solid-state lithium metal batteries enabled by silver–carbon composite anodes. *Nat. Energy* **5**, 299–308 (2020).
11. Wang, M. J., Carmona, E., Gupta, A., Albertus, P. & Sakamoto, J. Enabling 'lithium-free' manufacturing of pure lithium metal solid-state batteries through in situ plating. *Nat. Commun.* **11**, 5201 (2020).
12. Motoyama, M., Hirota, M., Yamamoto, T. & Iriyama, Y. Temperature effects on Li nucleation at Cu/LiPON interfaces. *ACS Appl. Mater. Interfaces* **12**, 38045–38053 (2020).
13. Fuchs, T. et al. Current-dependent lithium metal growth modes in 'anode-free' solid-state batteries at the Cu|LLZO interface. *Adv. Energy Mater.* **13**, 2203174 (2023).
14. Haslam, C. & Sakamoto, J. Stable lithium plating in 'lithium metal-free' solid-state batteries enabled by seeded lithium nucleation. *J. Electrochem. Soc.* **170**, 040524 (2023).
15. Xu, S. et al. Three-dimensional, solid-state mixed electron-ion conductive framework for lithium metal anode. *Nano Lett.* **18**, 3926–3933 (2018).
16. Kazyak, E. et al. Understanding the electro-chemo-mechanics of Li plating in anode-free solid-state batteries with operando 3D microscopy. *Matter* **5**, 3912–3934 (2022).
17. Sandoval, S. E. et al. Structural and electrochemical evolution of alloy interfacial layers in anode-free solid-state batteries. *Joule* **7**, 2054–2073 (2023).

18. Motoyama, M., Ejiri, M. & Iriyama, Y. Modeling the nucleation and growth of Li at metal current collector/LiPON interfaces. *J. Electrochem. Soc.* **162**, A7067–A7071 (2015).
19. Sandoval, S. E. & McDowell, M. T. Lithium metal anodes in solid-state batteries: metal microstructure matters. *Matter* **6**, 2101–2102 (2023).
20. Westover, A. S. Understanding the complexities of Li metal for solid-state Li-metal batteries. *MRS Bull.* **49**, 503–511 (2024).
21. Singh, D. K. et al. Origin of the lithium metal anode instability in solid-state batteries during discharge. *Matter* **6**, 1463–1483 (2023).
22. Singh, D. K. et al. Overcoming anode instability in solid-state batteries through control of the lithium metal microstructure. *Adv. Funct. Mater.* **33**, 2211067 (2023).
23. Callister, W. D. *Materials Science and Engineering: An Introduction (Eighth Edition)* (John Wiley & Sons, 2009); https://doi.org/10.1016/0261-3069(91)90101-9
24. Hayashi, Y., Shohji, I., Koyama, S. & Miyazawa, H. Change of crystallographic orientation characteristics of (001)-oriented electrodeposited silver films during self-annealing at room temperature. *Procedia Eng.* **184**, 725–731 (2017).
25. Hayashi, Y., Miyazawa, H., Minamitani, K. & Shohji, I. In situ observation of self-annealing behaviors of (001)-oriented electrodeposited silver film by EBSD method. *Mater. Trans.* **57**, 815–818 (2016).
26. Aspinall, J., Armstrong, D. E. J. & Pasta, M. EBSD-coupled indentation: nanoscale mechanics of lithium metal. *Mater. Today Energy* **30**, 101183 (2022).
27. Brodusch, N., Zaghib, K. & Gauvin, R. Electron backscatter diffraction applied to lithium sheets prepared by broad ion beam milling. *Microsc. Res. Tech.* **78**, 30–39 (2015).
28. Bastos, A., Zaefferer, S. & Raabe, D. Three-dimensional EBSD study on the relationship between triple junctions and columnar grains in electrodeposited Co–Ni films. *J. Microsc.* **230**, 487–498 (2008).
29. Otto, S.-K. et al. In-depth characterization of lithium-metal surfaces with XPS and ToF-SIMS: toward better understanding of the passivation layer. *Chem. Mater.* **33**, 859–867 (2021).
30. Otto, S. K. et al. Storage of lithium metal: the role of the native passivation layer for the anode interface resistance in solid state batteries. *ACS Appl. Energy Mater.* **4**, 12798–12807 (2021).
31. Kaboli, S. et al. On high-temperature evolution of passivation layer in Li–10 wt % Mg alloy via in situ SEM-EBSD. *Sci. Adv.* **6**, eabd5708 (2020).
32. Somekawa, H., Nishikawa, K., Moronaga, T. & Ohmura, T. Fabrication of Li anode metal via bulk mechanical property analysis. *J. Power Sources* **569**, 233019 (2023).
33. Darnbrough, E., Aspinall, J., Pasta, M. & Armstrong, D. E. J. Elastic and plastic mechanical properties of lithium measured by nanoindentation. *Mater. Des.* **233**, 112200 (2023).
34. Han, H. et al. The self-annealing phenomenon of electrodeposited nano-twin copper with high defect density. *Front. Chem.* **10**, 1056596 (2022).
35. Ortmann, T. et al. Deposition of sodium metal at the copper–NaSICON interface for reservoir-free solid-state sodium batteries. *Adv. Energy Mater.* **14**, 2302729 (2024).
36. Krauskopf, T. et al. Lithium-metal growth kinetics on LLZO garnet-type solid electrolytes. *Joule* **3**, 2030–2049 (2019).
37. Bastos, A., Zaefferer, S., Raabe, D. & Schuh, C. Characterization of the microstructure and texture of nanostructured electrodeposited NiCo using electron backscatter diffraction (EBSD). *Acta Mater.* **54**, 2451–2462 (2006).
38. Krauskopf, T., Hartmann, H., Zeier, W. G. & Janek, J. Toward a fundamental understanding of the lithium metal anode in solid-state batteries—an electrochemo-mechanical study on the garnet-type solid electrolyte $Li_{6.25}Al_{0.25}La_3Zr_2O_{12}$. *ACS Appl. Mater. Interfaces* **11**, 14463–14477 (2019).
39. Zaman, W. et al. Temperature and pressure effects on unrecoverable voids in Li metal solid-state batteries. *ACS Appl. Mater. Interfaces* **15**, 37401–37409 (2023).
40. Barai, P. et al. Study of void formation at the lithium|solid electrolyte interface. *Chem. Mater.* **36**, 2245–2258 (2024).
41. Yoon, J. S., Sulaimon, H. & Siegel, D. J. Exploiting grain boundary diffusion to minimize dendrite formation in lithium metal-solid state batteries. *J. Mater. Chem. A* **11**, 23288–23299 (2023).
42. Thompson, C. V. Grain growth in thin films. *Annu. Rev. Mater. Sci.* **20**, 245–268 (1990).
43. Lee, K., Kazyak, E., Wang, M. J., Dasgupta, N. P. & Sakamoto, J. Analyzing void formation and rewetting of thin in situ-formed Li anodes on LLZO. *Joule* **6**, 2547–2565 (2022).
44. Rollett, A., Rohrer, G. S. & Humphreys, J. *Recrystallization and Related Annealing Phenomena* (Elsevier, 2017).
45. Alexander, G. V., Shi, C., O'Neill, J. & Wachsman, E. D. Extreme lithium-metal cycling enabled by a mixed ion- and electron-conducting garnet three-dimensional architecture. *Nat. Mater.* **22**, 1136–1143 (2023).
46. Jaschin, P. W., Tang, C. R. & Wachsman, E. D. High-rate cycling in 3D dual-doped NASICON architectures toward room-temperature sodium-metal-anode solid-state batteries. *Energy Environ. Sci.* **17**, 727–737 (2024).

Methods

Materials

Lithium (99.0%) from Goodfellow GmbH and sodium metal supplied by BASF AG were used without further purification for microstructural characterization by EBSD, referred to as R-Li and R-Na. Modification of the microstructure of the alkali metals was induced by melting mechanically cleaned lithium and sodium ingots in stainless-steel crucibles on a hot plate at 400 °C and 250 °C, respectively, followed by quenching in liquid nitrogen inside an argon-filled glovebox. Quenched lithium and sodium are referred to as Q-Li and Q-Na. All visible passivation layers on the metal ingots were mechanical removed. Cross-sections for EBSD analysis were prepared by cutting through an ingot using a microtome blade. To avoid a potential passivation layer 'freezing' the microstructure in place, a fresh foil was prepared from the same quenched ingot after storage.

Counter electrodes attached to LLZO were prepared from a 750 µm lithium foil supplied by Alfa Aesar. For argyrodite-based cells, counter electrodes were prepared from a lithium rod (Albemarle Corporation). The passivation layers on the alkali metals were scraped off before usage. Three different kinds of SE were used. The LLZO was prepared as described in the literature[47], while the LPSCl was a commercial powder by NEI with a particle size of <1 µm. NZSP was synthesized following literature methods[48]. An excess of 4.5% of the sodium precursor and 1.5% of phosphorus precursor was used for the synthesis[49] yielding NZSP pellets with a relative density ≥90% after sintering.

Electrode preparation and electrochemistry

Electrodeposition of lithium and sodium were carried out using three different cell configurations, namely, Cu|LLZO|Li, SS|LPSCl|Li and Al|NZSP|Na. For the garnet-based cells, copper foil (10 µm) was hot-pressed onto the polished pellets at 900 °C in accord with previous literature[11]. In preparation for the in situ EBSD measurement, nominally 2 µm of lithium was plated ex situ at 60 °C under 2.5 MPa stack pressure and current density of 250 µA cm^{-2}. For argyrodite-based cells, LPSCl powder was pressed on stainless-steel foil (20 µm, Goodfellow, AISI 304) at 400 MPa. For the sodium-based RFC configuration, an aluminium sheet was coated with a thin carbon layer via tape casting: namely, carbon black (FW200, Degussa) and poly(vinylidene) fluoride were dispersed in *N*-methyl-2-pyrrolidone with a weight ratio of 95:5 carbon:poly(vinylidene) fluoride. The slurry was rapidly cast onto an aluminium foil (~17 µm) at a thickness of 30 µm at 60 °C followed by a drying process at 80 °C in vacuum for 12 h. Cylindrical electrodes were punched out and isostatically pressed onto a dry polished NZSP pellet (P1000 SiC grinding paper (Buehler)) at 100 MPa for 15 min, resulting in a 1-µm-thick carbon layer between the aluminium foil and NZSP. A sodium counter electrode was prepared as described in a previous report and attached on the opposite side of the NZSP pellet[6]. To ensure a homogeneous pressure distribution of 3 MPa during electrodeposition, the aluminium CC was covered with a nickel disc (thickness ~1 mm) that was polished with an AutoMet300 polishing machine (Buehler) using a 1 µm polycrystalline diamond suspension (MetaDi Supreme, Buehler). The obtained stack was sealed in a pouch bag under vacuum.

Electrochemical deposition was carried out using a potentiostat (Biologic, VMP300) at 25 °C if not specified otherwise in the text and controlled by EC-Lab (V11.2). Impedance measurements were carried out between 7 MHz and 100 mHz if not specified otherwise, with an excitation voltage of 10 mV. The stack pressure during deposition was controlled using an in-house built pressure frame[38]. Connection of the electrode inside the SEM was enabled using a micromanipulator system (Kleindiek Nanotechnik GmbH). In situ EBSD experiments were conducted using an SP200 potentiostat (Biologic) equipped with a low current module.

Cross-section preparation via FIB and TIC and transfer

Small lithium and sodium metal ingots were inserted into a homemade holder tilted at a 70° angle to the horizontal. The metal surface was prepared by cutting it with a microtome blade along the holder at a 70° angle, which is optimal for EBSD analysis, resulting in a surface that was free enough from any passivation to enable the EBSD analysis. For cross-sectional EBSD analysis, passivation-free ingots of lithium and sodium were pressed into metal foils and mounted on a home-built holder with a tilt angle of 20° to the horizontal. Cross-sections perpendicular to the metal surface were processed using a plasma FIB (XEIA3 system, Tescan GmbH). Milling was conducted under cryogenic conditions (−130 °C) using Xe^{+} ions operating at 30 kV with beam currents between 0.1 µA and 2.7 µA. To characterize the electrodeposited lithium and sodium at the CC|SE interface, the assembled Al|Na|NZSP|Na and Cu|Li|LLZO|Li cells were intentionally fractured perpendicular to the sample surface. The fracturing was carried out by using two flat and insulated pliers. The distance between the pliers was kept at several millimetres so as not to press onto the deposited metal beneath the CC near the desired fracture line. Furthermore, the samples were always broken with the electrode of interest being subjected to tensile forces during the fracture. In the case of the SS|Li|LPSCl|Li cells, the CC including the deposited lithium was peeled off from the SE and cut using scissors instead. The cross-sections were further processed according to the previously described plasma FIB approach to achieve clean cross-sections for EBSD mapping. Alternatively, large-area cross-sections for EBSD maps were also prepared at −130 °C with a triple ion beam cutter (EM TIC 3X, Leica Microsystems) equipped with three Ar^{+}-ion guns operating at 6 kV and a current of around 2 mA instead of the FIB.

All sodium samples were transferred under inert gas and cryogenic conditions (−160 °C) between the glovebox and the respective FIB-SEM and high-resolution-SEM using a Leica EM VCT500 transfer system (Leica Microsystems). Lithium samples were transferred under cryogenic conditions from the time of interface preparation via FIB and onwards.

In situ SEM and EBSD

Microstructural characterization was performed using a high-resolution field-emission SEM instrument Gemini SEM 560 (Carl Zeiss Microscopy GmbH) equipped with a Symmetry 3 EBSD detector (Oxford Instruments) operated by Aztec 6.1 software package (Oxford Instruments). EBSPs were recorded at 20 kV excitation voltage and a beam current of 3.4 nA and partially at 10 kV with 12.3 nA for lithium, if the EBSP quality allowed. Exposure time, pattern averaging, background correction and shadow masking were optimized for each sample individually to obtain optimal pattern quality. The EBSPs were indexed via a Hough algorithm with a resolution of 60 and 6–11 bands considering the following phases: cubic Na ($Im\bar{3}m$, Inorganic Crystal Structure Database (ICSD) number 44757), cubic Al ($Fm\bar{3}m$), cubic Cu ($Fm\bar{3}m$) and Li ($Im\bar{3}m$). Hexagonal Na_2O_2 ($P\bar{6}2m$, ICSD 26575) and cubic Na_2O ($Fm\bar{3}m$, ICSD 60435) were only considered to validate that no misindexing occurred due to surface passivation during sample preparation and processing.

Evaluation and post-treatment of the recorded EBSD maps were performed with an AZtecCrystal software package (Oxford Instruments). Besides using a common Hough indexing algorithm, EBSPs were indexed with a dynamic simulated pattern matching algorithm to enhance the indexing rate and reduce misindexed pixels (zero solutions). Based on the crystal structure of lithium and sodium metal, EBSPs of different orientation were simulated and matched with the measured EBSP. First, the recorded EBSPs were calibrated followed by a pixel binning. For indexing, the master pattern was calculated with an orientation spacing of 2° and matched with the measured EBSP. Second, the matched pattern orientation was refined to decrease the deviation. Finally, a matched pattern of a pixel is compared with the next neighbour pixel, and zero solutions were replaced if the band contrast was higher than 10. For post-treatment of sodium-based maps, a Gaussian filter was applied on the measured EBSP to reduce the influence of partially masked EBSPs. The combination of indexing procedures is visualized in Supplementary Figs. 1 and 2.

After the dynamic pattern matching, mathematical data refinement was performed by wild spikes removal followed by replacing zero solution with six neighbours and five neighbours. Pseudo-symmetry removal of 60° <111> for Laue group $m3m$ was only applied after verifying that the respective raw EBSPs are similar. If not otherwise stated, large angle grain boundaries are indicated by black lines with a misorientation of neighbour pixels >10°, while misorientation between 2° and 10° is highlighted by white lines for sodium.

For in situ EBSD experiments on sodium, an NZSP pellet was first cut perpendicular to the sample's surface with a diamond saw. The cross-section was polished with diamond grinding paper using a Leica EM TXP system (Leica Microsystems). The sodium working electrode was prepared from Q-Na with a diameter of 3 mm while the counter electrode consisted of R-Na with a diameter of 8 mm. The circular electrodes were sliced with a microtome blade and positioned under a digital microscope (Emspira 3, Leica Microsystems) to match the polished cross-section of the NZSP pellet. Cross-sections for in situ EBSD experiments on lithium were prepared out by fracturing the respective Cu|Li|LLZO|Li pellet similarly to the post-mortem analysis, followed by FIB polishing and microelectrode preparation. Samples were generally handled in an argon-filled glovebox (<0.1 ppm O_2, <1 ppm H_2O, MBraun).

Data availability

The data that support the findings of this study are available at the open access repository JLUdata under https://doi.org/10.22029/jlupub-18714.

References

47. Taylor, N. J. et al. Demonstration of high current densities and extended cycling in the garnet $Li_7La_3Zr_2O_{12}$ solid electrolyte. *J. Power Sources* **396**, 314–318 (2018).
48. Ma, Q. et al. Room temperature demonstration of a sodium superionic conductor with grain conductivity in excess of 0.01 S cm^{-1} and its primary applications in symmetric battery cells. *J. Mater. Chem. A* **7**, 7766–7776 (2019).
49. Quérel, E. et al. The role of NaSICON surface chemistry in stabilizing fast-charging Na metal solid-state batteries. *J. Phys. Energy* **3**, 044007 (2021).

Acknowledgements

We thank D. K. Singh and D. Raabe for fruitful discussions. This work was conducted as part of the US–German joint collaboration on 'Interfaces and Interphases in Rechargeable Li-metal based Batteries' supported by the US Department of Energy (DOE) and German Federal Ministry of Education and Research (BMBF). This work has been partly funded by the German Federal Ministry of Education and Research (BMBF) under the project 'LiSI2', grant identifier 03XP0509B (T.F. and J.J.), as well as the project 'FB2-Char', grant identifier 03XP0433D (J.J.). This work contributes to the research performed at CELEST (Center for Electrochemical Energy Storage Ulm-Karlsruhe) and was in part (sodium) also funded by the German Research Foundation (DFG) under project ID 390874152 (POLiS Cluster of Excellence) (T.O., M.R. and J.J.).

Author contributions

T.F. and T.O. designed and conducted the experiments, which were additionally supported by J.B. The preparation of the solid electrolyte material and the cells, including the electrochemical cycling, was supported by C.G.H. from J.S.'s group, V.K.S. from L.F.N.'s group, M.Z. and J.B. The EBSD experiments were supported by B.M. and K.P. The original draft was written by T.F. and T.O. and then edited and supervised by M.R., L.F.N., J.S. and J.J.

Funding

Open access funding provided by Justus-Liebig-Universität Gießen.

Competing interests

The authors declare no competing interests.

Additional information

Supplementary information The online version contains supplementary material available at https://doi.org/10.1038/s41563-024-02006-8.

Correspondence and requests for materials should be addressed to Till Fuchs or Jürgen Janek.

Peer review information *Nature Materials* thanks the anonymous reviewers for their contribution to the peer review of this work.

4 Conclusion

In this doctoral thesis, a sodium metal electrode and its interface with a NaSICON-structured solid electrolyte has been systematically studied. The interfacial kinetics during anodic dissolution and cathodic deposition was characterized and the evolution of the interfacial morphology has been examined in detail. The microstructure of sodium metal and its evolution upon charge and discharge was visualized for the first time by using EBSD.

In the first part of this doctoral thesis, the Na|$Na_{3.4}Zr_2Si_{2.4}P_{0.6}O_{12}$ interface was examined under equilibrium conditions. The systematic approach that was used to characterize the interfacial kinetics can serve as an experimental guideline for other SEs in contact with sodium metal. For the Na|NZSP interface, the geometric current constriction phenomenon has been identified as the overall dominant process at the interface, while the charge transfer process as well as the formation of a kinetically stabilized interphase play only a minor role for the interfacial kinetics. Accordingly, the observed interface-related resistance in the impedance spectrum mainly originated from an insufficient physical contact between the SME and the SE. A similar interfacial kinetics was reported for the Li|LLZO and the Na|BASE interface.[77,82] This suggests that, in general, the charge transfer is not the rate-limiting process at a Me|SE interface for an alkali metal electrode in contact with a chemically sufficiently stable SE. The similarities further highlight the importance of the geometric current constriction phenomenon for metal electrodes in SSBs.

As described in section 2.1.2, the relation between the geometric current constriction phenomenon and the interface-related contribution in the impedance enables the monitoring of the interfacial morphology by using EIS. Accordingly, the Na|NZSP interface represents an ideal choice to characterize morphological alternations of the SME during operation, as no significant contribution of other processes (charge transfer and interfacial degradation) are present in the impedance. Thus, the Na|NZSP interface can be considered as the sodium analog to the Li|LLZO model system.

Based on these results, the Na|NZSP interface was examined during anodic dissolution. Clearly, the increase in the potential during dissolution could be attributed to the current constriction contribution in the impedance, indicating the loss of physical contact at the Na|NZSP interface. The formation of pores at the interface has been confirmed by FIB-SEM cross-sectioning, revealing a lens-shaped pore geometry when no additional stack pressure was applied. No regular pore shape has been identified at low stack pressure (0.3 MPa). The impedance evolution in a subsequent resting phase after the anodic dissolution indicated a dynamic behavior of the interfacial morphology. Equilibration was observed even at low stack pressures and is attributed to the creep behavior of sodium. Thus, resting phases play an important role for the interfacial contact in real battery applications.

The cathodic deposition of a sodium metal electrode has been examined at a Cu|NZSP interface to evaluate the feasibility of RFCs. The electrodeposition of dense sodium layers in the micrometer range in between the CC and NZSP was observed. By increasing the current density, a more uniform coverage of sodium over the entire electrode has been achieved, whereas an increase of the stack pressure results only in a minor improvement of the surface coverage. In addition to the formation of sodium layers, the growth of whiskers or island growth can result in the delamination of the CC from the NZSP, leading to the formation of a gap. Furthermore, spallation of the NZSP was observed at local level, which was probably caused by cathodic deposition. The significance of the initial contact between CC and NZSP has been elucidated by in situ TEM. The growth of sodium is restricted to contact spots between Cu and NZSP. In addition, the experiments showed that the sodium filaments tend to grow in a faceted shape. The results showed that RFCs can in principle be realized. However, attention should be paid to the initial Cu|NZSP contact. Pulsed techniques or seed layer concepts might be beneficial to further improve the coverage of the electrode area.

The final section of this doctoral thesis is dedicated to an in-depth examination of the microstructure of alkali metal electrodes, with a particular focus on sodium, in SSBs. A reliable protocol has been developed for the characterization of the microstructure of highly reactive alkali metal foils, as well as for the analysis of cross-sections, using a combination of FIB-SEM and EBSD. A grain size in the range of several hundred micrometers was found for sodium metal ingots. The grain size could be substantially altered by melting of the sodium metal ingot followed by a subsequent quenching in liquid nitrogen. Despite the high homologous temperature of sodium, no substantial grain growth was observed over a resting period of two weeks. This not only demonstrates that the microstructure, e.g., grain size, can be effectively altered by thermal processes, it also suggests that the processing history of commercial sodium as well as the electrode preparation strongly affects the microstructure and thus also the electrochemical performance. This complicates the reproducibility and comparability of published results, as often the sodium source and detailed description of electrode preparation are insufficiently described in battery research.

The microstructure of electrodeposited sodium and lithium layers showed, on average, a smaller grain size than that of the mechanically prepared foils. Independent of the CC and SE materials, the GBs in the alkali metal were predominantly oriented perpendicular to the SE surface. In addition to vertical grain growth during electrodeposition, also lateral growth was observed. By reversing the current direction, pores were preferentially observed at the Na|NZSP interface in the interior of the grain. Based on these results, the microstructural evolution during electrodeposition of alkali metal films in RFCs can be summarized as follows. Metal nuclei first grow preferentially in the vertical direction. With progressing deposition, the number of grains decreases either by fusion of grains with similar orientation or by grain ripening due to the movement of GBs. During anodic dissolution, the preferential formation of pores is attributed to the different diffusivities in the metal bulk. The faster vacancy mobility along GBs compared to the bulk material suppresses the accumulation of vacancies and hence pore formation. It can thus be concluded that the electrochemical performance, for example, the stripping capacity, can be tuned by tailoring the electrode microstructure.

Overall, this doctoral thesis expands the knowledge of the interfacial kinetics of the SME in contact with NaSICON-structured SEs, which is essential for the reversible operation of the SME and of interested not only for SSBs but also for sea water battery types.[184,185] The detailed impedance analysis provides a fundamental basis for the interpretation of EIS spectra, thus helping to avoid misinterpretations. Moreover, the analytical approach described here can be applied to the microstructural characterization of other metal or alloy electrodes, thereby facilitating the correlation of electrochemical performance with the respective microstructure.

5 Outlook

The results provided in this doctoral thesis might be a starting point for further tasks and projects which can be considered in future work. The established preparation protocol of alkali metal electrode for EBSD analysis (see section 3.3) opens the possibility to evaluate the electrochemical performance of metal and alloy electrodes by including their microstructure. In the following, different projects with the focus on the relationship between microstructure and electrochemical performance of electrode materials are briefly presented.

(I) Possibility to control the alkali metal microstructure and influence of impurities

The results of this doctoral thesis emphasize the possibility to alter the microstructure of alkali metals by using thermal treatment (see section 3.3). In view of the electrochemical performance, this raises two questions: First, how does the production of sodium influence the metal microstructure? This includes not only the thermal and mechanical processing, but also the level of impurities. Impurities have a strong influence on crystallization processes and grain growth in a metal. Accordingly, a different microstructure also changes the mechanical properties of the material, as outlined in section 2.4.3, and thus the electrochemical performance. In addition to their impact on the microstructure, impurities also affect the diffusivity of the metal itself. This is due to their influence on the equilibrium defect concentration, including that of vacancies, as well as on the diffusion along fast diffusion pathways. Consequently, a strong impact of the amount and type of impurities on the electrochemical performance can be expected. This leads in a further step to the question of the working principle of alloy electrodes, which at first glance can be understood as a highly contaminated metal electrode. Is the improved electrochemical performance due to a different microstructure, e.g., increased number of fast diffusion pathways, or to improved self-diffusion due to different vacancy concentration and low migration enthalpy?

The second question points towards the controllability of the alkali metal microstructure to tune the electrochemical performance. Is it possible to further tailor the metal microstructure, e.g., by further decreasing the grain size of the metal, by different thermal or mechanical processes, or even by the introduction of an “artificial” impurity? The relationship between microstructure, diffusivity and impurity level in an alkali metal electrode provides a wide variety of parameters to further characterize and improve the electrochemical performance.

(II) Seed and interlayer concepts in RFCs

Uniform formation and coverage of the metal electrode is essential for RFCs. The cathodic metal deposition at the Me|SE can lead to undesirable metal growth as described in section 2.3.3. A possible approach to improve the uniformity of the deposited metal electrode is to introduce a seed layer or interlayer. The main idea behind this concept is to increase the number of nuclei, enhancing the metal diffusivity at the interface or to improve the interfacial contact. Typically, thin metal layers or nanoparticles are used that alloy with the respective alkali metal (see section 2.3.3). The functional principle of these concepts has been demonstrated for lithium-based systems, while the transferability to sodium-based systems has not yet been investigated in detail.[162] In view of the previously mentioned research fields, the impact of the interlayers (and the corresponding deposition parameters such as current density, stack pressure, temperature) on the resulting metal microstructure would be of great interest for the electrochemical performance.

(III) EBSD in the field of battery research

Although EBSD is a well-established method in the field of metallurgy and mineralogy, it is rarely used in the field of battery research. One reason for this is the challenging sample preparation and the tendency of most battery components such as metal electrode or CAMs to form surface passivation or contamination layers. However, the microstructure does not only play a crucial role for metal electrodes but is also of interest for SEs or CAMs. Fracture toughness, stress evolution, and orientation-dependent ion migration are important properties that influence the functionality of battery components. Therefore, it is of interest to explore the capabilities of EBSD (and the sample preparation) as a method to characterize the microstructure of battery components, particularly of SEs and CAMs.

For example, polycrystalline materials with anisotropic ionic conduction behavior, such as layered oxides, are often used as CAMs. During cycling, the insertion and extraction of ions cause the crystal lattice to expand and contract or undergo phase transitions.[186,187] This volume change leads to mechanical stress within the material, which can result in mechanical degradation and influence the electrochemical performance.[187] EBSD could be a useful technique for identifying strained regions and stress hot spots in polycrystalline CAMs, providing insights into the orientation dependence of these processes. This knowledge might be helpful for the optimization of polycrystalline CAMs. Overall, the ability to analyze the microstructure, particularly crystal orientations, makes EBSD a promising technique for battery research.

6 References

(1) Summary for Policymakers. In *Climate Change 2022 – Impacts, Adaptation and Vulnerability*; (IPCC), I. P. o. C. C., Ed.; Cambridge University Press, **2023**, 3–34. DOI: 10.1017/9781009325844.001.

(2) *Global energy transformation*: *A roadmap to 2050*; International Renewable Energy Agency, **2019**.

(3) Denholm, P.; Hand, M. Grid flexibility and storage required to achieve very high penetration of variable renewable electricity. *Energ. Policy* **2011**, *39*, 1817–1830. DOI: 10.1016/j.enpol.2011.01.019.

(4) Gryparis, E.; Papadopoulos, P.; Leligou, H. C.; Psomopoulos, C. S. Electricity demand and carbon emission in power generation under high penetration of electric vehicles. A European Union perspective. *Energy Reports* **2020**, *6*, 475–486. DOI: 10.1016/j.egyr.2020.09.025.

(5) Zhu, Z.; Jiang, T.; Ali, M.; Meng, Y.; Jin, Y.; Cui, Y.; Chen, W. Rechargeable Batteries for Grid Scale Energy Storage. *Chem. Rev.* **2022**, *122* (22), 16610–16751. DOI: 10.1021/acs.chemrev.2c00289.

(6) Schipper, F.; Aurbach, D. A brief review: Past, present and future of lithium ion batteries. *Russ. J. Electrochem.* **2016**, *52*, 1095–1121. DOI: 10.1134/S1023193516120120.

(7) Winter, M.; Barnett, B.; Xu, K. Before Li Ion Batteries. *Chem. Rev.* **2018**, *118* (23), 11433–11456. DOI: 10.1021/acs.chemrev.8b00422.

(8) Armand, M.; Tarascon, J.-M. Building better batteries. *Nature* **2008**, *451*, 652–657. DOI: 10.1038/451652a.

(9) Goodenough, J. B.; Park, K.-S. The Li-ion rechargeable battery: a perspective. *J. Am. Chem. Soc.* **2013**, *135* (4), 1167–1176. DOI: 10.1021/ja3091438.

(10) Habib, K.; Hansdóttir, S. T.; Habib, H. Critical metals for electromobility: Global demand scenarios for passenger vehicles, 2015–2050. *Resour. Conserv. Recy.* **2020**, *154*, 104603. DOI: 10.1016/j.resconrec.2019.104603.

(11) Tabelin, C. B.; Dallas, J.; Casanova, S.; Pelech, T.; Bournival, G.; Saydam, S.; Canbulat, I. Towards a low-carbon society: A review of lithium resource availability, challenges and innovations in mining, extraction and recycling, and future perspectives. *Miner. Eng.* **2021**, *163*, 106743. DOI: 10.1016/j.mineng.2020.106743.

(12) Janek, J.; Zeier, W. G. A solid future for battery development. *Nat. Energy* **2016**, *1*, 1167. DOI: 10.1038/nenergy.2016.141.

(13) Degen, F.; Winter, M.; Bendig, D.; Tübke, J. Energy consumption of current and future production of lithium-ion and post lithium-ion battery cells. *Nat. Energy* **2023**, *8*, 1284–1295. DOI: 10.1038/s41560-023-01355-z.

(14) Janek, J.; Zeier, W. G. Challenges in speeding up solid-state battery development. *Nat. Energy* **2023**, *8*, 230–240. DOI: 10.1038/s41560-023-01208-9.

(15) Delmas, C. Sodium and Sodium-Ion Batteries: 50 Years of Research. *Adv. Energy Mater.* **2018**, *8*, 1703137. DOI: 10.1002/aenm.201703137.

(16) Kundu, D.; Talaie, E.; Duffort, V.; Nazar, L. F. The emerging chemistry of sodium ion batteries for electrochemical energy storage. *Angew. Chem. Int. Ed.* **2015**, *54*, 3431–3448. DOI: 10.1002/anie.201410376.

(17) Rudola, A.; Rennie, A. J. R.; Heap, R.; Meysami, S. S.; Lowbridge, A.; Mazzali, F.; Sayers, R.; Wright, C. J.; Barker, J. Commercialisation of high energy density sodium-ion batteries: Faradion's journey and outlook. *J. Mater. Chem. A* **2021**, *9*, 8279–8302. DOI: 10.1039/D1TA00376C.

(18) Yabuuchi, N.; Kubota, K.; Dahbi, M.; Komaba, S. Research development on sodium-ion batteries. *Chem. Rev.* **2014**, *114* (23), 11636–11682. DOI: 10.1021/cr500192f.

(19) Singh, A. N.; Islam, M.; Meena, A.; Faizan, M.; Han, D.; Bathula, C.; Hajibabaei, A.; Anand, R.; Nam, K.-W. Unleashing the Potential of Sodium-Ion Batteries: Current State and Future Directions for Sustainable Energy Storage. *Adv. Funct. Mater.* **2023**, *33*, 2304617. DOI: 10.1002/adfm.202304617.

(20) Titirici, M.-M.; Adelhelm, P.; Hu, Y.-S., Eds. *Sodium-Ion batteries: Materials, Characterization, and Technology Volume 1 & 2*, Wiley-VCH, **2023**. ISBN: 978-3-527-35112-1.

(21) Tapia-Ruiz, N.; Armstrong, A. R.; Alptekin, H.; Amores, M. A.; Au, H.; Barker, J.; Boston, R.; Brant, W. R.; Brittain, J. M.; Chen, Y.; Chhowalla, M.; Choi, Y.-S.; Costa, S. I. R.; Crespo Ribadeneyra, M.; Cussen, S. A.; Cussen, E. J.; David, W. I. F.; Desai, A. V.; Dickson, S. A. M.; Eweka, E. I.; Forero-Saboya, J. D.; Grey, C. P.; Griffin, J. M.; Gross, P.; Hua, X.; Irvine, J. T. S.; Johansson, P.; Jones, M. O.; Karlsmo, M.; Kendrick, E.; Kim, E.; Kolosov, O. V.; Li, Z.; Mertens, S. F. L.; Mogensen, R.; Monconduit, L.; Morris, R. E.; Naylor, A. J.; Nikman, S.; O'Keefe, C. A.; Ould, D. M. C.; Palgrave, R. G.; Poizot, P.; Ponrouch, A.; Renault, S.; Reynolds, E. M.; Rudola, A.; Sayers, R.; Scanlon, D. O.; Sen, S.; Seymour, V. R.; Silván, B.; Sougrati, M. T.; Stievano, L.; Stone, G. S.; Thomas, C. I.; Titirici, M.-M.; Tong, J.; Wood, T. J.; Wright, D. S.; Younesi, R. 2021 roadmap for sodium-ion batteries. *J. Phys. Energy* **2021**, *3*, 031503. DOI: 10.1088/2515-7655/ac01ef.

(22) Chayambuka, K.; Mulder, G.; Danilov, D. L.; Notten, P. H. L. From Li-Ion Batteries toward Na-Ion Chemistries: Challenges and Opportunities. *Adv. Energy Mater.* **2020**, *10*, 2001310. DOI: 10.1002/aenm.202001310.

(23) Zhao, Y.; Kang, Y.; Wozny, J.; Lu, J.; Du, H.; Li, C.; Li, T.; Kang, F.; Tavajohi, N.; Li, B. Recycling of sodium-ion batteries. *Nat. Rev. Mater.* **2023**, *8*, 623–634. DOI: 10.1038/s41578-023-00574-w.

(24) Slater, M. D.; Kim, D.; Lee, E.; Johnson, C. S. Sodium-Ion Batteries. *Adv. Funct. Mater.* **2013**, *23*, 947–958. DOI: 10.1002/adfm.201200691.

(25) Weiss, M.; Ruess, R.; Kasnatscheew, J.; Levartovsky, Y.; Levy, N. R.; Minnmann, P.; Stolz, L.; Waldmann, T.; Wohlfahrt-Mehrens, M.; Aurbach, D.; Winter, M.; Ein-Eli, Y.; Janek, J. Fast Charging of Lithium-Ion Batteries: A Review of Materials Aspects. *Adv. Energy Mater.* **2021**, *11*, 2101126. DOI: 10.1002/aenm.202101126.

(26) Matei Ghimbeu, C.; Beda, A.; Réty, B.; El Marouazi, H.; Vizintin, A.; Tratnik, B.; Simonin, L.; Michel, J.; Abou-Rjeily, J.; Dominko, R. Review: Insights on Hard Carbon Materials for Sodium-Ion Batteries (SIBs): Synthesis – Properties – Performance Relationships. *Adv. Energy Mater.* **2024**, *14,* 2303833. DOI: 10.1002/aenm.202303833.

(27) Zhu, Y.-E.; Yang, L.; Zhou, X.; Li, F.; Wei, J.; Zhou, Z. Boosting the rate capability of hard carbon with an ether-based electrolyte for sodium ion batteries. *J. Mater. Chem. A* **2017**, *5*, 9528–9532. DOI: 10.1039/C7TA02515G.

(28) Lee, B.; Paek, E.; Mitlin, D.; Lee, S. W. Sodium Metal Anodes: Emerging Solutions to Dendrite Growth. *Chem. Rev.* **2019**, *119* (8), 5416–5460. DOI: 10.1021/acs.chemrev.8b00642.

(29) Hu, Z.; Liu, L.; Wang, X.; Zheng, Q.; Han, C.; Li, W. Current Progress of Anode-Free Rechargeable Sodium Metal Batteries: Origin, Challenges, Strategies, and Perspectives. *Adv. Funct. Mater.* **2024**, *34*, 2313823. DOI: 10.1002/adfm.202313823.

(30) Sun, B.; Li, P.; Zhang, J.; Wang, D.; Munroe, P.; Wang, C.; Notten, P. H. L.; Wang, G. Dendrite-Free Sodium-Metal Anodes for High-Energy Sodium-Metal Batteries. *Adv. Mater.* **2018**, *30*, 1801334. DOI: 10.1002/adma.201801334.

(31) Zhang, Z.; Shao, Y.; Lotsch, B.; Hu, Y.-S.; Li, H.; Janek, J.; Nazar, L. F.; Nan, C.-W.; Maier, J.; Armand, M.; Chen, L. New horizons for inorganic solid state ion conductors. *Energy Environ. Sci.* **2018**, *11*, 1945–1976. DOI: 10.1039/c8ee01053f.

(32) Ohno, S.; Zeier, W. G. Sodium is the new lithium. *Nat. Energy* **2022**, *7*, 686–687. DOI: 10.1038/s41560-022-01084-9.

(33) Kim, J.-J.; Yoon, K.; Park, I.; Kang, K. Progress in the Development of Sodium-Ion Solid Electrolytes. *Small Methods* **2017**, *1*, 1700219. DOI: 10.1002/smtd.201700219.

(34) Lu, Y.; Li, L.; Zhang, Q.; Niu, Z.; Chen, J. Electrolyte and Interface Engineering for Solid-State Sodium Batteries. *Joule* **2018**, *2*, 1747–1770. DOI: 10.1016/j.joule.2018.07.028.

(35) Wu, J.-F.; Zhang, R.; Fu, Q.-F.; Zhang, J.-S.; Zhou, X.-Y.; Gao, P.; Xu, C.-H.; Liu, J.; Guo, X. Inorganic Solid Electrolytes for All-Solid-State Sodium Batteries: Fundamentals and Strategies for Battery Optimization. *Adv. Funct. Mater.* **2021**, *31*, 2008165. DOI: 10.1002/adfm.202008165.

(36) Tang, B.; Jaschin, P. W.; Li, X.; Bo, S.-H.; Zhou, Z. Critical interface between inorganic solid-state electrolyte and sodium metal. *Mater. Today* **2020**, *41*, 200–218. DOI: 10.1016/j.mattod.2020.08.016.

(37) Wang, C.; Zheng, Y.; Chen, Z.-N.; Zhang, R.; He, W.; Li, K.; Yan, S.; Cui, J.; Fang, X.; Yan, J.; Xu, G.; Peng, D.; Ren, B.; Zheng, N. Robust Anode-Free Sodium Metal Batteries Enabled by Artificial Sodium Formate Interface. *Adv. Energy Mater.* **2023**, *13*, 2204125. DOI: 10.1002/aenm.202204125.

(38) Yang, T.; Luo, D.; Liu, Y.; Yu, A.; Chen, Z. Anode-free sodium metal batteries as rising stars for lithium-ion alternatives. *iScience* **2023**, *26* (3), 105982. DOI: 10.1016/j.isci.2023.105982.

(39) Ortmann, T.; Burkhardt, S.; Eckhardt, J. K.; Fuchs, T.; Ding, Z.; Sann, J.; Rohnke, M.; Ma, Q.; Tietz, F.; Fattakhova-Rohlfing, D.; Kübel, C.; Guillon, O.; Heiliger, C.; Janek, J. Kinetics and Pore Formation of the Sodium Metal Anode on NASICON-Type $Na_{3.4}Zr_2Si_{2.4}P_{0.6}O_{12}$ for Sodium Solid-State Batteries. *Adv. Energy Mater.* **2023**, *13*, 2202712. DOI: 10.1002/aenm.202202712.

(40) Ortmann, T.; Fuchs, T.; Eckhardt, J. K.; Ding, Z.; Ma, Q.; Tietz, F.; Kübel, C.; Rohnke, M.; Janek, J. Deposition of Sodium Metal at the Copper-NaSICON Interface for Reservoir-Free

Solid-State Sodium Batteries. *Adv. Energy Mater.* **2024**, *14*, 2302729. DOI: 10.1002/aenm.202302729.

(41) Fuchs, T.; Ortmann, T.; Becker, J.; Haslam, C. G.; Ziegler, M.; Singh, V. K.; Rohnke, M.; Mogwitz, B.; Peppler, K.; Nazar, L. F.; Sakamoto, J.; Janek, J. Imaging the microstructure of lithium and sodium metal in anode-free solid-state batteries using electron backscatter diffraction. *Nat. Mater.* **2024,** *23*, 1678-1685. DOI: 10.1038/s41563-024-02006-8.

(42) Hueso, K. B.; Armand, M.; Rojo, T. High temperature sodium batteries: status, challenges and future trends. *Energy Environ. Sci.* **2013**, *6*, 734–749. DOI: 10.1039/c3ee24086j.

(43) Hueso, K. B.; Palomares, V.; Armand, M.; Rojo, T. Challenges and perspectives on high and intermediate-temperature sodium batteries. *Nano Res.* **2017**, *10*, 4082–4114. DOI: 10.1007/s12274-017-1602-7.

(44) Wang, Y.; Zhou, D.; Palomares, V.; Shanmukaraj, D.; Sun, B.; Tang, X.; Wang, C.; Armand, M.; Rojo, T.; Wang, G. Revitalising sodium–sulfur batteries for non-high-temperature operation: a crucial review. *Energy Environ. Sci.* **2020**, *13*, 3848–3879. DOI: 10.1039/d0ee02203a.

(45) Laskar, A. L.; Chandra, S., Eds. *Superionic solids and solid electrolytes Recent trends*; Materials science and technology series; Acad. Press, **1989**. ISBN: 0124370756.

(46) Goodenough, J. B.; Hong, H.Y.-P.; Kafalas, J. A. Fast Na^+-ion transport in skeleton structures. *Mater. Res. Bull.* **1976**, *11* (2), 203–220. DOI: 10.1016/0025-5408(76)90077-5.

(47) Hong, H.Y.-P. Crystal structures and crystal chemistry in the system $Na_{1+x}Zr_2Si_xP_{3-x}O_{12}$. *Mater. Res. Bull.***1976**, *11* (2), 173–182. DOI: 10.1016/0025-5408(76)90073-8.

(48) Rao, Y. B.; Bharathi, K. K.; Patro, L. N. Review on the synthesis and doping strategies in enhancing the Na ion conductivity of $Na_3Zr_2Si_2PO_{12}$ (NASICON) based solid electrolytes. *Solid State Ionics* **2021**, *366-367*, 115671. DOI: 10.1016/j.ssi.2021.115671.

(49) Jolley, A. G.; Cohn, G.; Hitz, G. T.; Wachsman, E. D. Improving the ionic conductivity of NASICON through aliovalent cation substitution of $Na_3Zr_2Si_2PO_{12}$. *Ionics* **2015**, *21*, 3031–3038. DOI: 10.1007/s11581-015-1498-8.

(50) Deng, Z.; Mishra, T. P.; Mahayoni, E.; Ma, Q.; Tieu, A. J. K.; Guillon, O.; Chotard, J.-N.; Seznec, V.; Cheetham, A. K.; Masquelier, C.; Gautam, G. S.; Canepa, P. Fundamental investigations on the sodium-ion transport properties of mixed polyanion solid-state battery electrolytes. *Nat. Commun.* **2022**, *13*, 4470. DOI: 10.1038/s41467-022-32190-7.

(51) Yang, Y.; Yang, S.; Xue, X.; Zhang, X.; Li, Q.; Yao, Y.; Rui, X.; Pan, H.; Yu, Y. Inorganic All-Solid-State Sodium Batteries: Electrolyte Designing and Interface Engineering. *Adv. Mater.* **2024**, *36*, 2308332. DOI: 10.1002/adma.202308332.

(52) Oh, J. A. S.; Wang, Y.; Zeng, Q.; Sun, J.; Sun, Q.; Goh, M.; Chua, B.; Zeng, K.; Lu, L. Intrinsic low sodium/NASICON interfacial resistance paving the way for room temperature sodium-metal battery. *J. Colloid Interf. Sci.* **2021**, *601*, 418–426. DOI: 10.1016/j.jcis.2021.05.123.

(53) Zhou, W.; Li, Y.; Xin, S.; Goodenough, J. B. Rechargeable Sodium All-Solid-State Battery. *ACS Cent. Sci.* **2017**, *3* (1), 52–57. DOI: 10.1021/acscentsci.6b00321.

(54) Wang, S.; Xu, H.; Li, W.; Dolocan, A.; Manthiram, A. Interfacial Chemistry in Solid-State Batteries: Formation of Interphase and Its Consequences. *J. Am. Chem. Soc.* **2018**, *140* (1), 250–257. DOI: 10.1021/jacs.7b09531.

(55) Lotsch, B. V.; Maier, J. Relevance of solid electrolytes for lithium-based batteries: A realistic view. *J. Electroceram.* **2017**, *38*, 128–141. DOI: 10.1007/s10832-017-0091-0.

(56) Krauskopf, T.; Richter, F. H.; Zeier, W. G.; Janek, J. Physicochemical Concepts of the Lithium Metal Anode in Solid-State Batteries. *Chem. Rev.* **2020**, *120* (15), 7745–7794. DOI: 10.1021/acs.chemrev.0c00431.

(57) Peljo, P.; Girault, H. H. Electrochemical potential window of battery electrolytes: the HOMO–LUMO misconception. *Energy Environ. Sci.* **2018**, *11*, 2306–2309. DOI: 10.1039/c8ee01286e.

(58) Zhu, Y.; He, X.; Mo, Y. Origin of Outstanding Stability in the Lithium Solid Electrolyte Materials: Insights from Thermodynamic Analyses Based on First-Principles Calculations. *ACS Appl. Mater. Inter.* **2015**, *7* (42), 23685–23693. DOI: 10.1021/acsami.5b07517.

(59) Lacivita, V.; Wang, Y.; Bo, S.-H.; Ceder, G. Ab initio investigation of the stability of electrolyte/electrode interfaces in all-solid-state Na batteries. *J. Mater. Chem. A* **2019**, *7*, 8144–8155. DOI: 10.1039/c8ta10498k.

(60) Wu, E. A.; Kompella, C. S.; Zhu, Z.; Lee, J. Z.; Lee, S. C.; Chu, I.-H.; Nguyen, H.; Ong, S. P.; Banerjee, A.; Meng, Y. S. New Insights into the Interphase between the Na Metal Anode and Sulfide Solid-State Electrolytes: A Joint Experimental and Computational Study. *ACS Appl. Mater. Inter.* **2018**, *10* (12), 10076–10086. DOI: 10.1021/acsami.7b19037.

(61) Tang, H.; Deng, Z.; Lin, Z.; Wang, Z.; Chu, I.-H.; Chen, C.; Zhu, Z.; Zheng, C.; Ong, S. P. Probing Solid–Solid Interfacial Reactions in All-Solid-State Sodium-Ion Batteries with First-Principles Calculations. *Chem. Mater.* **2018**, *30* (1), 163–173. DOI: 10.1021/acs.chemmater.7b04096.

(62) Wenzel, S.; Leichtweiss, T.; Krüger, D.; Sann, J.; Janek, J. Interphase formation on lithium solid electrolytes—An in situ approach to study interfacial reactions by photoelectron spectroscopy. *Solid State Ionics* **2015**, *278*, 98–105. DOI: 10.1016/j.ssi.2015.06.001.

(63) Wenzel, S.; Leichtweiss, T.; Weber, D. A.; Sann, J.; Zeier, W. G.; Janek, J. Interfacial Reactivity Benchmarking of the Sodium Ion Conductors Na_3PS_4 and Sodium β-Alumina for Protected Sodium Metal Anodes and Sodium All-Solid-State Batteries. *ACS Appl. Mater. Inter.* **2016**, *8* (41), 28216–28224. DOI: 10.1021/acsami.6b10119.

(64) Ellis, B. L.; Nazar, L. F. Sodium and sodium-ion energy storage batteries. *Curr. Opin. Solid St. M.* **2012**, *16* (4), 168–177. DOI: 10.1016/j.cossms.2012.04.002.

(65) Alt, C. D.; Müller, N. U.C.B.; Riegger, L. M.; Aktekin, B.; Minnmann, P.; Peppler, K.; Janek, J. Quantifying multiphase SEI growth in sulfide solid electrolytes. *Joule* **2024**, *8*, 2755–2776. DOI: 10.1016/j.joule.2024.07.006.

(66) Schwöbel, A.; Hausbrand, R.; Jaegermann, W. Interface reactions between LiPON and lithium studied by in-situ X-ray photoemission. *Solid State Ionics* **2015**, *273*, 51–54. DOI: 10.1016/j.ssi.2014.10.017.

(67) Dai, W.; Qiao, Y.; Ma, Z.; Wang, T.; Fu, Z. All-solid-state thin-film batteries based on lithium phosphorus oxynitrides. *Mater. Futures* **2022**, *1* (3), 32101. DOI: 10.1088/2752-5724/ac7db2.

(68) Gao, H.; Xin, S.; Xue, L.; Goodenough, J. B. Stabilizing a High-Energy-Density Rechargeable Sodium Battery with a Solid Electrolyte. *Chem* **2018**, *4* (4), 833–844. DOI: 10.1016/j.chempr.2018.01.007.

(69) Wang, C.; Jin, H.; Zhao, Y. Surface Potential Regulation Realizing Stable Sodium/$Na_3Zr_2Si_2PO_{12}$ Interface for Room-Temperature Sodium Metal Batteries. *Small* **2021**, *17*, 2100974. DOI: 10.1002/smll.202100974.

(70) Zhang, Z.; Wenzel, S.; Zhu, Y.; Sann, J.; Shen, L.; Yang, J.; Yao, X.; Hu, Y.-S.; Wolverton, C.; Li, H.; Chen, L.; Janek, J. $Na_3Zr_2Si_2PO_{12}$: A Stable Na^+-Ion Solid Electrolyte for Solid-State Batteries. *ACS Appl. Energy Mater.* **2020**, *3* (8), 7427–7437. DOI: 10.1021/acsaem.0c00820.

(71) Quérel, E.; Seymour, I. D.; Cavallaro, A.; Ma, Q.; Tietz, F.; Aguadero, A. The role of NaSICON surface chemistry in stabilizing fast-charging Na metal solid-state batteries. *J. Phys. Energy* **2021**, *3* (4), 44007. DOI: 10.1088/2515-7655/ac2fb3.

(72) Quérel, E.; Williams, N. J.; Seymour, I. D.; Skinner, S. J.; Aguadero, A. Operando Characterization and Theoretical Modeling of Metal|Electrolyte Interphase Growth Kinetics in Solid-State Batteries. Part I: Experiments. *Chem. Mater.* **2023**, *35* (3), 853–862. DOI: 10.1021/acs.chemmater.2c03130.

(73) Irvine, J. T. S.; Sinclair, D. C.; West, A. R. Electroceramics: Characterization by Impedance Spectroscopy. *Adv. Mater.* **1990**, *2* (3), 132–138. DOI: 10.1002/adma.19900020304.

(74) Matios, E.; Wang, H.; Wang, C.; Hu, X.; Lu, X.; Luo, J.; Li, W. Graphene Regulated Ceramic Electrolyte for Solid-State Sodium Metal Battery with Superior Electrochemical Stability. *ACS Appl. Mater. Inter.* **2019**, *11* (5), 5064–5072. DOI: 10.1021/acsami.8b19519.

(75) Gross, M. M.; Small, L. J.; Peretti, A. S.; Percival, S. J.; Rodriguez, M. A.; Spoerke, E. D. Tin-based ionic chaperone phases to improve low temperature molten sodium–NaSICON interfaces. *J. Mater. Chem. A* **2020**, *8*, 17012–17018. DOI: 10.1039/d0ta03571h.

(76) Gao, Z.; Yang, J.; Yuan, H.; Fu, H.; Li, Y.; Li, Y.; Ferber, T.; Guhl, C.; Sun, H.; Jaegermann, W.; Hausbrand, R.; Huang, Y. Stabilizing $Na_3Zr_2Si_2PO_{12}$/Na Interfacial Performance by Introducing a Clean and Na-Deficient Surface. *Chem. Mater.* **2020**, *32* (9), 3970–3979. DOI: 10.1021/acs.chemmater.0c00474.

(77) Bay, M.-C.; Wang, M.; Grissa, R.; Heinz, M. V. F.; Sakamoto, J.; Battaglia, C. Sodium Plating from Na-β″-Alumina Ceramics at Room Temperature, Paving the Way for Fast-Charging All-Solid-State Batteries. *Adv. Energy Mater.* **2020**, *10*, 1902899. DOI: 10.1002/aenm.201902899.

(78) Otto, S.-K.; Fuchs, T.; Moryson, Y.; Lerch, C.; Mogwitz, B.; Sann, J.; Janek, J.; Henss, A. Storage of Lithium Metal: The Role of the Native Passivation Layer for the Anode Interface Resistance in Solid State Batteries. *ACS Appl. Energy Mater.* **2021**, *4* (11), 12798–12807. DOI: 10.1021/acsaem.1c02481.

(79) Otto, S.-K.; Moryson, Y.; Krauskopf, T.; Peppler, K.; Sann, J.; Janek, J.; Henss, A. In-Depth Characterization of Lithium-Metal Surfaces with XPS and ToF-SIMS: Toward Better Understanding of the Passivation Layer. *Chem. Mater.* **2021**, *33* (3), 859–867. DOI: 10.1021/acs.chemmater.0c03518.

(80) Addison, C. C. *The chemistry of the liquid alkali metals*; John Wiley and Sons, **1984**. ISBN: 0-471-90508-9.

(81) Krauskopf, T.; Mogwitz, B.; Hartmann, H.; Singh, D. K.; Zeier, W. G.; Janek, J. The Fast Charge Transfer Kinetics of the Lithium Metal Anode on the Garnet-Type Solid Electrolyte $Li_{6.25}Al_{0.25}La_3Zr_2O_{12}$. *Adv. Energy Mater.* **2020**, *10*, 2000945. DOI: 10.1002/aenm.202000945.

(82) Krauskopf, T.; Hartmann, H.; Zeier, W. G.; Janek, J. Toward a Fundamental Understanding of the Lithium Metal Anode in Solid-State Batteries-An Electrochemo-Mechanical Study on the Garnet-Type Solid Electrolyte $Li_{6.25}Al_{0.25}La_3Zr_2O_{12}$. *ACS Appl. Mater. Inter.* **2019**, *11* (15), 14463–14477. DOI: 10.1021/acsami.9b02537.

(83) Tsai, C.-L.; Lan, T.; Dellen, C.; Ling, Y.; Ma, Q.; Fattakhova-Rohlfing, D.; Guillon, O.; Tietz, F. Dendrite-tolerant all-solid-state sodium batteries and an important mechanism of metal self-diffusion. *J. Power Sources* **2020**, *476*, 228666. DOI: 10.1016/j.jpowsour.2020.228666.

(84) Seymour, I. D.; Quérel, E.; Brugge, R. H.; Pesci, F. M.; Aguadero, A. Understanding and Engineering Interfacial Adhesion in Solid-State Batteries with Metallic Anodes. *ChemSusChem* **2023**, *16*, e202202215. DOI: 10.1002/cssc.202202215.

(85) Liu, T.; Xiang, P.; Li, Y.; Li, Z.; Sun, H.; Yang, J.; Tian, Z.; Yao, X. In Situ Forming Na─Sn Alloy/Na_2S Interface Layer for Ultrastable Solid State Sodium Batteries. *Adv. Funct. Mater.* **2024**, *34*, 2316528. DOI: 10.1002/adfm.202316528.

(86) Jia, J.; Liu, T.; Li, Y.; Yang, J.; He, H.; Zhu, X.; Yao, X. Calcium Doped NASICON Electrolyte with Graphite Coating for Stable All-solid-state Sodium Metal Batteries. *ChemSusChem* **2024**, *17*, e202400481. DOI: 10.1002/cssc.202400481.

(87) Eckhardt, J. K.; Klar, P. J.; Janek, J.; Heiliger, C. Interplay of Dynamic Constriction and Interface Morphology between Reversible Metal Anode and Solid Electrolyte in Solid State Batteries. *ACS Appl. Mater. Inter.* **2022**, *14* (31), 35545–35554. DOI: 10.1021/acsami.2c07077.

(88) Fleig, J. The impedance of imperfect electrode contacts on solid electrolytes. *Solid State Ionics* **1996**, *85*, 17–24. DOI: 10.1016/0167-2738(96)00036-7.

(89) Fleig, J.; Maier, J. Finite element calculations of impedance effects at point contacts. *Electrochim. Acta* **1996**, *41* (7-8), 1003–1009. DOI: 10.1016/0013-4686(95)00431-9.

(90) Meyer, M.; Rickert, H.; Schwaitzer, U. Investigations on the kinetics of the anodic dissolution of lithium at the interface Li/Li_3N. *Solid State Ionics* **1983**, *9-10*, 689–693. DOI: 10.1016/0167-2738(83)90315-6.

(91) Eckhardt, J. K.; Fuchs, T.; Burkhardt, S.; Klar, P. J.; Janek, J.; Heiliger, C. Guidelines for Impedance Analysis of Parent Metal Anodes in Solid-State Batteries and the Role of Current Constriction at Interface Voids, Heterogeneities, and SEI. *Adv. Mater. Interfaces* **2023**, *10*, 2202354. DOI: 10.1002/admi.202202354.

(92) Eckhardt, J. K.; Fuchs, T.; Burkhardt, S.; Klar, P. J.; Janek, J.; Heiliger, C. 3D Impedance Modeling of Metal Anodes in Solid-State Batteries-Incompatibility of Pore Formation and Constriction Effect in Physical-Based 1D Circuit Models. *ACS Appl. Mater. Inter.* **2022**, *14* (37), 42757–42769. DOI: 10.1021/acsami.2c12991.

(93) Eckhardt, J. K.; Burkhardt, S.; Zahnow, J.; Elm, M. T.; Janek, J.; Klar, P. J.; Heiliger, C. Understanding the Impact of Microstructure on Charge Transport in Polycrystalline Materials Through Impedance Modelling. *J. Electrochem. Soc.* **2021**, *168* (9), 90516. DOI: 10.1149/1945-7111/ac1cfe.

(94) Singh, D. K.; Fuchs, T.; Krempaszky, C.; Schweitzer, P.; Lerch, C.; Richter, F. H.; Janek, J. Origin of the lithium metal anode instability in solid-state batteries during discharge. *Matter* **2023**, *6* (5), 1463–1483. DOI: 10.1016/j.matt.2023.02.008.

(95) Rohnke, M.; Rosenkranz, C.; Janek, J. The influence of non-equilibrium defects on the anodic dissolution of a metal into a solid electrolyte. *Solid State Ionics* **2006**, *177* (5-6), 447–456. DOI: 10.1016/j.ssi.2005.12.002.

(96) Majoni, S.; Janek, J. Investigation of charge transport across the Ag|AgI-interface: (II) Dilatometric study of the anodic dissolution of silver. *Berich. Bunsen. Gesell. Phys. Chem.* **1998**, *102* (5), 756–762. DOI: 10.1002/bbpc.19981020509.

(97) Schmalzried, H.; Janek, J. Chemical kinetics of phase boundaries in solids. *Berich. Bunsen. Gesell. Phys. Chem.* **1998**, *102* (2), 127–143. DOI: 10.1002/bbpc.19981020202.

(98) Frank, W.; Breier, U.; Elsässer, C.; Fähnle, M. First-Principles Calculations of Absolute Concentrations and Self-Diffusion Constants of Vacancies in Lithium. *Phys. Rev. Lett.* **1996**, *77* (3), 518–521. DOI: 10.1103/PhysRevLett.77.518.

(99) Smargiassi, E.; Madden, P. A. Free energies of point defects in sodium from first-principles molecular-dynamics simulations. *Phys. Rev. B* **1995**, *51* (1), 129–136. DOI: 10.1103/physrevb.51.129.

(100) Mundy, J. N.; Barr, L. W.; Smith, F. A. Sodium self-diffusion and the isotope effect. *The Philosophical Magazine: A Journal of Theoretical Experimental and Applied Physics* **1966**, *14* (130), 785–802. DOI: 10.1080/14786436608211972.

(101) Seymour, I. D.; Aguadero, A. Suppressing void formation in all-solid-state batteries: the role of interfacial adhesion on alkali metal vacancy transport. *J. Mater. Chem. A* **2021**, *9*, 19901–19913. DOI: 10.1039/D1TA03254B.

(102) Flatscher, F.; Philipp, M.; Ganschow, S.; Wilkening, H. M. R.; Rettenwander, D. The natural critical current density limit for $Li_7La_3Zr_2O_{12}$ garnets. *J. Mater. Chem. A* **2020**, *8*, 15782–15788. DOI: 10.1039/c9ta14177d.

(103) Le Xiang; Li, X.; Xiao, J.; Zhu, L.; Zhan, X. Interface issues and challenges for NASICON-based solid-state sodium-metal batteries. *Advanced Powder Materials* **2024**, *3* (3), 100181. DOI: 10.1016/j.apmate.2024.100181.

(104) Fuchs, T.; Haslam, C. G.; Richter, F. H.; Sakamoto, J.; Janek, J. Evaluating the Use of Critical Current Density Tests of Symmetric Lithium Transference Cells with Solid Electrolytes. *Adv. Energy Mater.* **2023**, *13*, 2302383. DOI: 10.1002/aenm.202302383.

(105) Krauskopf, T.; Mogwitz, B.; Rosenbach, C.; Zeier, W. G.; Janek, J. Diffusion Limitation of Lithium Metal and Li–Mg Alloy Anodes on LLZO Type Solid Electrolytes as a Function of

Temperature and Pressure. *Adv. Energy Mater.* **2019**, *9*, 1902568. DOI: 10.1002/aenm.201902568.

(106) Kasemchainan, J.; Zekoll, S.; Spencer Jolly, D.; Ning, Z.; Hartley, G. O.; Marrow, J.; Bruce, P. G. Critical stripping current leads to dendrite formation on plating in lithium anode solid electrolyte cells. *Nat. Mater.* **2019**, *18*, 1105–1111. DOI: 10.1038/s41563-019-0438-9.

(107) Spencer Jolly, D.; Ning, Z.; Darnbrough, J. E.; Kasemchainan, J.; Hartley, G. O.; Adamson, P.; Armstrong, D. E. J.; Marrow, J.; Bruce, P. G. Sodium/Na β″ Alumina Interface: Effect of Pressure on Voids. *ACS Appl. Mater. Inter.* **2020**, *12* (1), 678–685. DOI: 10.1021/acsami.9b17786.

(108) Lu, Y.; Zhao, C.-Z.; Hu, J.-K.; Sun, S.; Yuan, H.; Fu, Z.-H.; Chen, X.; Huang, J.-Q.; Ouyang, M.; Zhang, Q. The void formation behaviors in working solid-state Li metal batteries. *Sci. Adv.* **2022**, *8* (45), eadd0510. DOI: 10.1126/sciadv.add0510.

(109) Schröder, A.; Fleig, J.; Gryaznov, D.; Maier, J.; Sitte, W. Quantitative model of electrochemical Ostwald ripening and its application to the time-dependent electrode potential of nanocrystalline metals. *J. Phys. Chem. B* **2006**, *110* (25), 12274–12280. DOI: 10.1021/jp060788t.

(110) Janek, J.; Majoni, S. Influence of Mechanical Pressure on Ionic Charge Transport Across the Ag|Agl-Interface - Periodic Oscillations of Interfacial Properties. *DDF* **1996**, *129-130*, 243–252. DOI: 10.4028/www.scientific.net/ddf.129-130.243.

(111) Wenzel S., *Thermodynamic and kinetic instability of inorganic solid electrolytes at lithium and sodium metal electrodes*, Dissertation, Justus Liebig University, Giessen, **2016**.

(112) Oh, J. A. S.; Sun, J.; Goh, M.; Chua, B.; Zeng, K.; Lu, L. A Robust Solid–Solid Interface Using Sodium–Tin Alloy Modified Metallic Sodium Anode Paving Way for All-Solid-State Battery. *Adv. Energy Mater.* **2021**, *11*, 2101228. DOI: 10.1002/aenm.202101228.

(113) Oh, J. A. S.; He, L.; Chua, B.; Zeng, K.; Lu, L. Inorganic sodium solid-state electrolyte and interface with sodium metal for room-temperature metal solid-state batteries. *Energy Storage Materials* **2021**, *34*, 28–44. DOI: 10.1016/j.ensm.2020.08.037.

(114) Fu, H.; Yin, Q.; Huang, Y.; Sun, H.; Chen, Y.; Zhang, R.; Yu, Q.; Gu, L.; Duan, J.; Luo, W. Reducing Interfacial Resistance by Na-SiO_2 Composite Anode for NASICON-Based Solid-State Sodium Battery. *ACS Materials Lett.* **2020**, *2* (2), 127–132. DOI: 10.1021/acsmaterialslett.9b00442.

(115) Wang, M. J.; Chang, J.-Y.; Wolfenstine, J. B.; Sakamoto, J. Analysis of elastic, plastic, and creep properties of sodium metal and implications for solid-state batteries. *Materialia* **2020**, *12*, 100792. DOI: 10.1016/j.mtla.2020.100792.

(116) LePage, W. S.; Chen, Y.; Kazyak, E.; Chen, K.-H.; Sanchez, A. J.; Poli, A.; Arruda, E. M.; Thouless, M. D.; Dasgupta, N. P. Lithium Mechanics: Roles of Strain Rate and Temperature and Implications for Lithium Metal Batteries. *J. Electrochem. Soc.* **2019**, *166* (2), A89-A97. DOI: 10.1149/2.0221902jes.

(117) Zhang, X.; Wang, Q. J.; Peng, B.; Wu, Y. Pressure-Driven and Creep-Enabled Interface Evolution in Sodium Metal Batteries. *ACS Appl. Mater. Inter.* **2021**, *13* (22), 26533–26541. DOI: 10.1021/acsami.0c22006.

(118) Wang, M. J.; Choudhury, R.; Sakamoto, J. Characterizing the Li-Solid-Electrolyte Interface Dynamics as a Function of Stack Pressure and Current Density. *Joule* **2019**, *3* (9), 2165–2178. DOI: 10.1016/j.joule.2019.06.017.

(119) Zhang, X.; Wang, Q. J.; Harrison, K. L.; Roberts, S. A.; Harris, S. J. Pressure-Driven Interface Evolution in Solid-State Lithium Metal Batteries. *Cell Reports Physical Science* **2020**, *1* (2), 100012. DOI: 10.1016/j.xcrp.2019.100012.

(120) Masias, A.; Felten, N.; Garcia-Mendez, R.; Wolfenstine, J.; Sakamoto, J. Elastic, plastic, and creep mechanical properties of lithium metal. *J. Mater. Sci.* **2019**, *54* (3), 2585–2600. DOI: 10.1007/s10853-018-2971-3.

(121) Doux, J.-M.; Nguyen, H.; Tan, D. H. S.; Banerjee, A.; Wang, X.; Wu, E. A.; Jo, C.; Yang, H.; Meng, Y. S. Stack Pressure Considerations for Room-Temperature All-Solid-State Lithium Metal Batteries. *Adv. Energy Mater.* **2020**, *10*, 1903253. DOI: 10.1002/aenm.201903253.

(122) Schnell, J.; Günther, T.; Knoche, T.; Vieider, C.; Köhler, L.; Just, A.; Keller, M.; Passerini, S.; Reinhart, G. All-solid-state lithium-ion and lithium metal batteries – paving the way to large-scale production. *J. Power Sources* **2018**, *382*, 160–175. DOI: 10.1016/j.jpowsour.2018.02.062.

(123) Huang, W.-Z.; Zhao, C.-Z.; Wu, P.; Yuan, H.; Feng, W.-E.; Liu, Z.-Y.; Lu, Y.; Sun, S.; Fu, Z.-H.; Hu, J.-K.; Yang, S.-J.; Huang, J.-Q.; Zhang, Q. Anode-Free Solid-State Lithium Batteries: A Review. *Adv. Energy Mater.* **2022**, *12*, 2201044. DOI: 10.1002/aenm.202201044.

(124) Heubner, C.; Maletti, S.; Auer, H.; Hüttl, J.; Voigt, K.; Lohrberg, O.; Nikolowski, K.; Partsch, M.; Michaelis, A. From Lithium-Metal toward Anode-Free Solid-State Batteries: Current Developments, Issues, and Challenges. *Adv. Funct. Mater.* **2021**, *31*, 2106608. DOI: 10.1002/adfm.202106608.

(125) Zhang, H.; Gao, Y.; Liu, X.; Zhou, L.; Li, J.; Xiao, Y.; Peng, J.; Wang, J.; Chou, S.-L. Long-Cycle-Life Cathode Materials for Sodium-Ion Batteries toward Large-Scale Energy Storage Systems. *Adv. Energy Mater.* **2023**, *13*, 2300149. DOI: 10.1002/aenm.202300149.

(126) Hatzell, K. B. Anode-Less or Anode-Free? *ACS Energy Lett.* **2023**, *8* (11), 4775–4776. DOI: 10.1021/acsenergylett.3c02163.

(127) Neudecker, B. J.; Dudney, N. J.; Bates, J. B. “Lithium-Free” Thin-Film Battery with In Situ Plated Li Anode. *J. Electrochem. Soc.* **2000**, *147* (2), 517. DOI: 10.1149/1.1393226.

(128) Deysher, G.; Oh, J. A. S.; Chen, Y.-T.; Sayahpour, B.; Ham, S.-Y.; Cheng, D.; Ridley, P.; Cronk, A.; Lin, S. W.-H.; Qian, K.; Nguyen, L. H. B.; Jang, J.; Meng, Y. S. Design principles for enabling an anode-free sodium all-solid-state battery. *Nat. Energy* **2024**, *9*. DOI: 10.1038/s41560-024-01569-9.

(129) Holleman, A. F.; Wiberg, N.; Wiberg, E.; Fischer, G. *Anorganische Chemie*, 103. Auflage; de Gruyter, **2017**. ISBN: 978-3-11-026932-1.

(130) Lang, J.; Jin, Y.; Liu, K.; Long, Y.; Zhang, H.; Qi, L.; Wu, H.; Cui, Y. High-purity electrolytic lithium obtained from low-purity sources using solid electrolyte. *Nat. Sustain.* **2020**, *3*, 386–390. DOI: 10.1038/s41893-020-0485-x.

(131) Koerver, R.; Aygün, I.; Leichtweiß, T.; Dietrich, C.; Zhang, W.; Binder, J. O.; Hartmann, P.; Zeier, W. G.; Janek, J. Capacity Fade in Solid-State Batteries: Interphase Formation and Chemomechanical Processes in Nickel-Rich Layered Oxide Cathodes and Lithium Thiophosphate Solid Electrolytes. *Chem. Mater.* **2017**, *29* (13), 5574–5582. DOI: 10.1021/acs.chemmater.7b00931.

(132) Budevski, E.; Staikov, G.; Lorenz, W. J. *Electrochemical Phase Formation and Growth*: *An Introduction to the Initial Stages of Metal Deposition*, Wiley-VCH, **1996**. ISBN: 3-527-29422-8.

(133) Rohnke, M.; Best, T.; Janek, J. Controlled electrochemical growth of silver microwires. *J. Solid State Electrochem.* **2005**, *9*, 239–243. DOI: 10.1007/s10008-004-0619-5.

(134) Peppler, K.; Janek, J. Cathodic deposition of silver on silver bromide at microelectrodes. *Solid State Ionics* **2006**, *177* (19-25), 1643–1648. DOI: 10.1016/j.ssi.2005.12.012.

(135) Spangenberg, A.; Fleig, J.; Maier, J. Electromechanical Writing on Silver Ion Conductors. *Adv. Mater.* **2001**, *13* (19), 1466–1468. DOI: 10.1002/1521-4095(200110)13:19<1466:AID-ADMA1466>3.0.CO;2-#.

(136) Krauskopf, T.; Dippel, R.; Hartmann, H.; Peppler, K.; Mogwitz, B.; Richter, F. H.; Zeier, W. G.; Janek, J. Lithium-Metal Growth Kinetics on LLZO Garnet-Type Solid Electrolytes. *Joule* **2019**, *3* (8), 2030–2049. DOI: 10.1016/j.joule.2019.06.013.

(137) Ma, Q.; Ortmann, T.; Yang, A.; Sebold, D.; Burkhardt, S.; Rohnke, M.; Tietz, F.; Fattakhova-Rohlfing, D.; Janek, J.; Guillon, O. Enhancing the Dendrite Tolerance of NaSICON Electrolytes by Suppressing Edge Growth of Na Electrode along Ceramic Surface. *Adv. Energy Mater.* **2022**, *12,* 2201680. DOI: 10.1002/aenm.202201680.

(138) Nagao, M.; Hayashi, A.; Tatsumisago, M.; Kanetsuku, T.; Tsuda, T.; Kuwabata, S. In situ SEM study of a lithium deposition and dissolution mechanism in a bulk-type solid-state cell with a Li_2S-P_2S_5 solid electrolyte. *Phys. Chem. Chem. Phys.* **2013**, *15*, 18600–18606. DOI: 10.1039/c3cp51059j.

(139) Fuchs, T.; Becker, J.; Haslam, C. G.; Lerch, C.; Sakamoto, J.; Richter, F. H.; Janek, J. Current-Dependent Lithium Metal Growth Modes in "Anode-Free" Solid-State Batteries at the Cu|LLZO Interface. *Adv. Energy Mater.* **2023**, *13*, 2203174. DOI: 10.1002/aenm.202203174.

(140) Motoyama, M.; Ejiri, M.; Iriyama, Y. Modeling the Nucleation and Growth of Li at Metal Current Collector/LiPON Interfaces. *J. Electrochem. Soc.* **2015**, *162*, A7067-A7071. DOI: 10.1149/2.0051513jes.

(141) Cao, D.; Sun, X.; Li, Q.; Natan, A.; Xiang, P.; Zhu, H. Lithium Dendrite in All-Solid-State Batteries: Growth Mechanisms, Suppression Strategies, and Characterizations. *Matter* **2020**, *3* (1), 57–94. DOI: 10.1016/j.matt.2020.03.015.

(142) Ansell, R. O. The chemical and electrochemical stability of beta-alumina. *J. Mater. Sci.* **1986**, *21*, 365–379. DOI: 10.1007/BF01145497.

(143) Wang, M.; Wolfenstine, J. B.; Sakamoto, J. Temperature dependent flux balance of the Li/$Li_7La_3Zr_2O_{12}$ interface. *Electrochim. Acta* **2019**, *296*, 842–847. DOI: 10.1016/j.electacta.2018.11.034.

(144) Jonghe, L. C. de; Feldman, L.; Beuchele, A. Slow degradation and electron conduction in sodium/beta-aluminas. *J. Mater. Sci.* **1981**, *16*, 780–786. DOI: 10.1007/BF02402796.

(145) Aguesse, F.; Manalastas, W.; Buannic, L.; Lopez Del Amo, J. M.; Singh, G.; Llordés, A.; Kilner, J. Investigating the Dendritic Growth during Full Cell Cycling of Garnet Electrolyte in Direct Contact with Li Metal. *ACS Appl. Mater. Inter.* **2017**, *9* (4), 3808–3816. DOI: 10.1021/acsami.6b13925.

(146) Han, F.; Westover, A. S.; Yue, J.; Fan, X.; Wang, F.; Chi, M.; Leonard, D. N.; Dudney, N. J.; Wang, H.; Wang, C. High electronic conductivity as the origin of lithium dendrite formation within solid electrolytes. *Nat. Energy*. **2019**, *4*, 187–196. DOI: 10.1038/s41560-018-0312-z.

(147) Ding, Z.; Tang, Y.; Ortmann, T.; Eckhardt, J. K.; Dai, Y.; Rohnke, M.; Melinte, G.; Heiliger, C.; Janek, J.; Kübel, C. The Impact of Microstructure on Filament Growth at the Sodium Metal Anode in All-Solid-State Sodium Batteries. *Adv. Energy Mater.* **2023**, *13*, 2302322. DOI: 10.1002/aenm.202302322.

(148) Dong, Y.; Zhang, Z.; Alvarez, A.; Chen, I.-W. Potential jumps at transport bottlenecks cause instability of nominally ionic solid electrolytes in electrochemical cells. *Acta Mater.* **2020**, *199*, 264–277. DOI: 10.1016/j.actamat.2020.08.017.

(149) Motoyama, M.; Hirota, M.; Yamamoto, T.; Iriyama, Y. Temperature Effects on Li Nucleation at Cu/LiPON Interfaces. *ACS Appl. Mater. Inter.* **2020**, *12* (34), 38045–38053. DOI: 10.1021/acsami.0c02354.

(150) Pei, A.; Zheng, G.; Shi, F.; Li, Y.; Cui, Y. Nanoscale Nucleation and Growth of Electrodeposited Lithium Metal. *Nano Lett.* **2017**, *17* (2), 1132–1139. DOI: 10.1021/acs.nanolett.6b04755.

(151) Geng, L.; Zhao, C.; Yan, J.; Fu, C.; Zhang, X.; Yao, J.; Sun, H.; Su, Y.; Liu, Q.; Zhang, L.; Tang, Y.; Ding, F.; Huang, J. In situ imaging the dynamics of sodium metal deposition and stripping. *J. Mater. Chem. A* **2022**, *10*, 14875–14883. DOI: 10.1039/d2ta02513b.

(152) Liu, Q.; Zhang, L.; Sun, H.; Geng, L.; Li, Y.; Tang, Y.; Jia, P.; Wang, Z.; Dai, Q.; Shen, T.; Tang, Y.; Zhu, T.; Huang, J. In Situ Observation of Sodium Dendrite Growth and Concurrent Mechanical Property Measurements Using an Environmental Transmission Electron Microscopy–Atomic Force Microscopy (ETEM-AFM) Platform. *ACS Energy Lett.* **2020**, *5* (8), 2546–2559. DOI: 10.1021/acsenergylett.0c01214.

(153) Wang, M. J.; Carmona, E.; Gupta, A.; Albertus, P.; Sakamoto, J. Enabling “lithium-free” manufacturing of pure lithium metal solid-state batteries through in situ plating. *Nat. Commun.* **2020**, *11*, 5201. DOI: 10.1038/s41467-020-19004-4.

(154) Lewis, J. A.; Sandoval, S. E.; Liu, Y.; Nelson, D. L.; Yoon, S. G.; Wang, R.; Zhao, Y.; Tian, M.; Shevchenko, P.; Martínez-Pañeda, E.; McDowell, M. T. Accelerated Short Circuiting in Anode-Free Solid-State Batteries Driven by Local Lithium Depletion. *Adv. Energy Mater.* **2023**, *13*, 2204186. DOI: 10.1002/aenm.202204186.

(155) Kazyak, E.; Wang, M. J.; Lee, K.; Yadavalli, S.; Sanchez, A. J.; Thouless, M. D.; Sakamoto, J.; Dasgupta, N. P. Understanding the electro-chemo-mechanics of Li plating in anode-free solid-state batteries with operando 3D microscopy. *Matter* **2022**, *5* (11), 3912–3934. DOI: 10.1016/j.matt.2022.07.020.

(156) Fuchs T., *Morphological Challenges at the Interface of Lithium Metal and Electrolytes in Garnet-type Solid-State Batteries*. Dissertation, Justus Liebig University, Gießen, **2022**. DOI: 10.22029/jlupub-15629

(157) Lee, Y.-G.; Fujiki, S.; Jung, C.; Suzuki, N.; Yashiro, N.; Omoda, R.; Ko, D.-S.; Shiratsuchi, T.; Sugimoto, T.; Ryu, S.; Ku, J. H.; Watanabe, T.; Park, Y.; Aihara, Y.; Im, D.; Han, I. T. High-energy long-cycling all-solid-state lithium metal batteries enabled by silver–carbon composite anodes. *Nat. Energy* **2020**, *5*, 299–308. DOI: 10.1038/s41560-020-0575-z.

(158) Spencer-Jolly, D.; Agarwal, V.; Doerrer, C.; Hu, B.; Zhang, S.; Melvin, D. L.R.; Gao, H.; Gao, X.; Adamson, P.; Magdysyuk, O. V.; Grant, P. S.; House, R. A.; Bruce, P. G. Structural changes in the silver-carbon composite anode interlayer of solid-state batteries. *Joule* **2023**, *7* (3), 503–514. DOI: 10.1016/j.joule.2023.02.001.

(159) Kim, S.; Yoon, G.; Jung, S.-K.; Park, S.; Kim, J.-S.; Yoon, K.; Lee, S.; Kang, K. High-Power Hybrid Solid-State Lithium–Metal Batteries Enabled by Preferred Directional Lithium Growth Mechanism. *ACS Energy Lett.* **2023**, *8* (1), 9–20. DOI: 10.1021/acsenergylett.2c02150.

(160) Xie, F.; Diallo, M. S.; Kim, H.; Tu, Q. H.; Ceder, G. The Microscopic Mechanism of Lithiation and Delithiation in the Ag/C Buffer Layer for Anode-Free Solid-State Batteries. *Adv. Energy Mater.***2024**, *14*, 2302960. DOI: 10.1002/aenm.202302960.

(161) Haslam, C.; Sakamoto, J. Stable Lithium Plating in “Lithium Metal-Free” Solid-State Batteries Enabled by Seeded Lithium Nucleation. *J. Electrochem. Soc.* **2023**, *170* (4), 40524. DOI: 10.1149/1945-7111/accab4.

(162) Tseng, K.-T.; Lee, K.; Sakamoto, J. Enabling “Sodium–Metal-Free” Manufacturing of Solid-State Batteries. *ACS Energy Lett.* **2024**, 4544–4549. DOI: 10.1021/acsenergylett.4c01724.

(163) Dingley, D. J.; Randle, V. Microtexture determination by electron back-scatter diffraction. *J. Mater. Sci.* **1992**, *27*, 4545–4566. DOI: 10.1007/BF01165988.

(164) Engler, O.; Zaefferer, S.; Randle, V. *Introduction to Texture Analysis*, CRC Press, **2023**. ISBN: 9781003258339.

(165) Hornbogen, E. A systematic description of microstructure. *J. Mater. Sci.* **1986**, *21*, 3737–3747. DOI: 10.1007/BF02431607.

(166) Randle, V. Electron backscatter diffraction: Strategies for reliable data acquisition and processing. *Mater. Charact.* **2009**, *60* (9), 913–922. DOI: 10.1016/j.matchar.2009.05.011.

(167) Sandoval, S. E.; McDowell, M. T. Lithium metal anodes in solid-state batteries: Metal microstructure matters. *Matter* **2023**, *6* (7), 2101–2102. DOI: 10.1016/j.matt.2023.05.017.

(168) Westover, A. S. Understanding the complexities of Li metal for solid-state Li-metal batteries. *MRS Bull.* **2024**, *49* (5), 503–511. DOI: 10.1557/s43577-024-00677-x.

(169) Aspinall, J.; Chart, Y.; Guo, H.; Shrestha, P.; Burton, M.; Pasta, M. Effect of Microstructure on the Cycling Behavior of Li–In Alloy Anodes for Solid-State Batteries. *ACS Energy Lett.* **2024**, *9* (2), 578–585. DOI: 10.1021/acsenergylett.3c02274.

(170) Singh, D. K.; Fuchs, T.; Krempaszky, C.; Mogwitz, B.; Burkhardt, S.; Richter, F. H.; Janek, J. Overcoming Anode Instability in Solid-State Batteries through Control of the Lithium

Metal Microstructure. *Adv. Funct. Mater.* **2023**, *33*, 2211067.
DOI: 10.1002/adfm.202211067.

(171) Brodusch, N.; Zaghib, K.; Gauvin, R. Electron backscatter diffraction applied to lithium sheets prepared by broad ion beam milling. *Microsc. Res. Techniq.* **2015**, *78*, 30–39.
DOI: 10.1002/jemt.22441.

(172) Aspinall, J.; Armstrong, D. E.J.; Pasta, M. EBSD-coupled indentation: nanoscale mechanics of lithium metal. *Materials Today Energy* **2022**, *30*, 101183.
DOI: 10.1016/j.mtener.2022.101183.

(173) Mehrer, H. *Diffusion in Solids*: *Fundamentals, Methods, Materials, Diffusion-Controlled Processes*, Springer, Springer Series in Solid-State Sciences, Volume 155, **2007**.
ISBN: 978-3-540-71486-6

(174) Backus, J. G. E. M.; Bakker, H.; Mehrer, H. Self-Diffusion Measurements in Silver at Low Temperatures Using Single Crystals and Slightly Deformed Crystals. *Phys. Status Solidi B* **1974**, *64* (1), 151–162. DOI: 10.1002/pssb.2220640119.

(175) Nachtrieb, N. H.; Weil, J. A.; Catalano, E.; Lawson, A. W. Self-Diffusion in Solid Sodium. II. The Effect of Pressure. *J. Chem. Phys.* **1952**, *20*, 1189–1194. DOI: 10.1063/1.1700709.

(176) Barnes, R. S. Diffusion of Copper along the Grain Boundaries of Nickel. *Nature* **1950**, *166*, 1032–1033. DOI: 10.1038/1661032a0.

(177) Yoon, J. S.; Sulaimon, H.; Siegel, D. J. Exploiting grain boundary diffusion to minimize dendrite formation in lithium metal-solid state batteries. *J. Mater. Chem. A* **2023**, *11*, 23288–23299. DOI: 10.1039/d3ta03814a.

(178) Ruano, O. A.; Wadsworth, J.; Sherby, O. D. Deformation mechanisms in an austenitic stainless steel (25Cr-20Ni) at elevated temperature. *J. Mater. Sci.* **1985**, *20*, 3735–3744.
DOI: 10.1007/BF01113782.

(179) McDowell, M. T.; Cortes, F. J. Q.; Thenuwara, A. C.; Lewis, J. A. Toward High-Capacity Battery Anode Materials: Chemistry and Mechanics Intertwined. *Chem. Mater.* **2020**, *32* (20), 8755–8771. DOI: 10.1021/acs.chemmater.0c02981.

(180) LePage, W. S.; Chen, Y.; Poli, A.; Thouless, M. D.; Dasgupta, N. P. Sodium mechanics: effects of temperature, strain rate, and grain rotation and implications for sodium metal batteries. *Extreme Mechanics Letters* **2022**, *52*, 101644.
DOI: 10.1016/j.eml.2022.101644.

(181) Sargent, P. M.; Ashby, M. F. Deformation mechanism maps for alkali metals. *Scripta Metall. Mater.* **1984**, *18* (2), 145–150. DOI: 10.1016/0036-9748(84)90494-0.

(182) Fincher, C. D.; Zhang, Y.; Pharr, G. M.; Pharr, M. Elastic and Plastic Characteristics of Sodium Metal. *ACS Appl. Energy Mater.* **2020**, *3* (2), 1759–1767.
DOI: 10.1021/acsaem.9b02225.

(183) Masias, A.; Felten, N.; Sakamoto, J. Characterizing the mechanical behavior of lithium in compression. *J. Mater. Res.* **2021**, *36*, 729–739. DOI: 10.1557/s43578-020-00028-x.

(184) Jung, J.; Hwang, D. Y.; Kristanto, I.; Kwak, S. K.; Kang, S. J. Deterministic growth of a sodium metal anode on a pre-patterned current collector for highly rechargeable seawater batteries. *J. Mater. Chem. A* **2019**, *7*, 9773–9781. DOI: 10.1039/c9ta01718f.

(185) Kim, D. H.; Choi, H.; Hwang, D. Y.; Park, J.; Kim, K. S.; Ahn, S.; Kim, Y.; Kwak, S. K.; Yu, Y.-J.; Kang, S. J. Reliable seawater battery anode: controlled sodium nucleation via deactivation of the current collector surface. *J. Mater. Chem. A* **2018**, *6*, 19672–19680. DOI: 10.1039/c8ta07610c.

(186) Trevisanello, E.; Ruess, R.; Conforto, G.; Richter, F. H.; Janek, J. Polycrystalline and Single Crystalline NCM Cathode Materials—Quantifying Particle Cracking, Active Surface Area, and Lithium Diffusion. *Adv. Energy Mater.* **2021**, *11*, 2003400. DOI: 10.1002/aenm.202003400.

(187) Daubner, S.; Weichel, M.; Schneider, D.; Nestler, B. Modeling intercalation in cathode materials with phase-field methods: Assumptions and implications using the example of $LiFePO_4$. *Electrochim. Acta* **2022**, *421* (4), 140516. DOI: 10.1016/j.electacta.2022.140516.

7 Appendix

7.1 Calculation of Energy Density for Solid-State Sodium Batteries

For a comparison of the gravimetric and volumetric energy density, two different SSBs cell configurations were considered, namely a “classical” set up and an RFC set up. In the “classical” SSB set up, a negative electrode (sodium metal) is introduced already during cell fabrication by attaching a sodium foil on the SE. In contrast, in a RFC the negative electrode is formed by electrodeposition of sodium stored in the CAM on a CC. The parameters used for the calculation of the energy density are listed in Table 1, including the nominal voltage, specific capacity, density and layer thickness. The calculations are based on an areal capacity of 5 $\mathrm{mAh \cdot cm^{-2}}$. For the positive electrode, a composite consisting of NZSP and NVP with a weight ratio of 15:85 % is assumed. For the “classical” a capacity balancing of the electrodes of 1:1 is assumed.[20] Cell casings and battery management systems are not included in the calculation.[128]

Table 1: *Overview of the specific capacity, nominal voltage, and density for sodium metal as negative electrode and sodium vanadium phosphate (NVP) as positive electrode. In addition, the assumed thickness and density of the solid electrolyte (NZSP) and current collector (Al) are listed.*

Parameter	***Na***	***NVP***	***NZSP***	***Al***
Specific capacity	1166 $\mathrm{mAh \cdot g^{-1}}$	118 $\mathrm{mAh \cdot g^{-1}}$	-	-
Nominal voltage vs (Na^+/Na)	0 V	3.4 V	-	-
Density	0.97 $\mathrm{g \cdot cm^{-3}}$	3.21 $\mathrm{g \cdot cm^{-3}}$	3.27 $\mathrm{g \cdot cm^{-3}}$	2.7 $\mathrm{g \cdot cm^{-3}}$
Thickness	-	-	10 µm	15 µm

Based on the given assumptions and the values in Table 1, a gravimetric and volumetric energy density of 233 $\mathrm{Wh \cdot kg^{-1}}$ and 647 $\mathrm{Wh \cdot L^{-1}}$, respectively, is achieved for the “classical” SSB set up. In contrast, for an RFC setup (sodium metal electrode formed in situ), the gravimetric and volumetric energy densities are calculated to be 246 $\mathrm{Wh \cdot kg^{-1}}$ and 779 $\mathrm{Wh \cdot L^{-1}}$, respectively.

7.2 Supporting Information

7.2.1 Publication 1: Kinetics and Pore Formation of the Sodium Metal Anode on NASICON-Type $Na_{3.4}Zr_2Si_{2.4}P_{0.6}O_{12}$ for Sodium Solid-State Batteries

ADVANCED
ENERGY
MATERIALS

Supporting Information

for *Adv. Energy Mater.,* DOI: 10.1002/aenm.202202712

Kinetics and Pore Formation of the Sodium Metal Anode on NASICON-Type $Na_{3.4}Zr_2Si_{2.4}P_{0.6}O_{12}$ for Sodium Solid-State Batteries

*Till Ortmann, Simon Burkhardt, Janis Kevin Eckhardt, Till Fuchs, Ziming Ding, Joachim Sann, Marcus Rohnke, Qianli Ma, Frank Tietz, Dina Fattakhova-Rohlfing, Christian Kübel, Olivier Guillon, Christian Heiliger, and Jürgen Janek**

WILEY-VCH

Supplementary Information

Kinetics and Pore Formation of the Sodium Metal Anode on NASICON-type $Na_{3.4}Zr_2Si_{2.4}P_{0.6}O_{12}$ for Sodium Solid-State Batteries

*Till Ortmann, Simon Burkhardt, Janis Kevin Eckhardt, Till Fuchs, Ziming Ding, Joachim Sann, Marcus Rohnke, Qianli Ma, Frank Tietz, Dina Fattakhova-Rohlfing, Christian Kübel, Olivier Guillon, Christian Heiliger and Jürgen Janek**

Mr. T. Ortmann, Dr. S. Burkhardt, Mr. T. Fuchs, Dr. J. Sann, Dr. M. Rohnke and Prof. J. Janek
Institute for Physical Chemistry, Justus Liebig University Giessen, 35392 Giessen, Germany.
*E-Mail: juergen.janek@phys.chemie.uni-giessen.de

Mr. T. Ortmann, Dr. S. Burkhardt, Mr. J. K. Eckhardt, Mr. T. Fuchs, Dr. J. Sann, Dr. M. Rohnke, Prof. C. Heiliger and Prof. J. Janek
Center for Materials Research (ZfM), Justus Liebig University Giessen, 35392 Giessen, Germany.

Mr. J. K. Eckhardt, Prof. C. Heiliger
Institute for Theoretical Physics, Justus Liebig University Giessen, 35392 Giessen, Germany.

Ms. Z. Ding and Prof. C. Kübel
Technische Universität Darmstadt, 64289 Darmstadt, Germany.

Dr. Q. Ma, Dr. F. Tietz, Prof. D. Fattakhova-Rohlfing and Prof. O. Guillon
Forschungszentrum Jülich GmbH, Institute of Energy and Climate Research, Materials Synthesis and Processing (IEK-1), 52425 Jülich, Germany.

Ms. Z. Ding and Prof. C. Kübel
Institute of Nanotechnology (INT) and Helmholtz Institute Ulm (HIU), Karlsruhe Institute of Technology (KIT), 76344 Eggenstein-Leopoldshafen, Germany.

Prof. D. Fattakhova-Rohlfing
Department of Engineering and Center for Nano integration Duisburg-Essen (CENIDE), Universität Duisburg-Essen, 47057 Duisburg, Germany.

Prof C. Kübel
Karlsruhe Nano Micro Facility (KNMF), Karlsruhe Institute of Technology (KIT), 76344 Eggenstein-Leopoldshafen, Germany.

Prof. O. Guillon
Jülich Aachen Research Alliance, JARA-Energy, 52425 Jülich, Germany.

1. Materials characterization

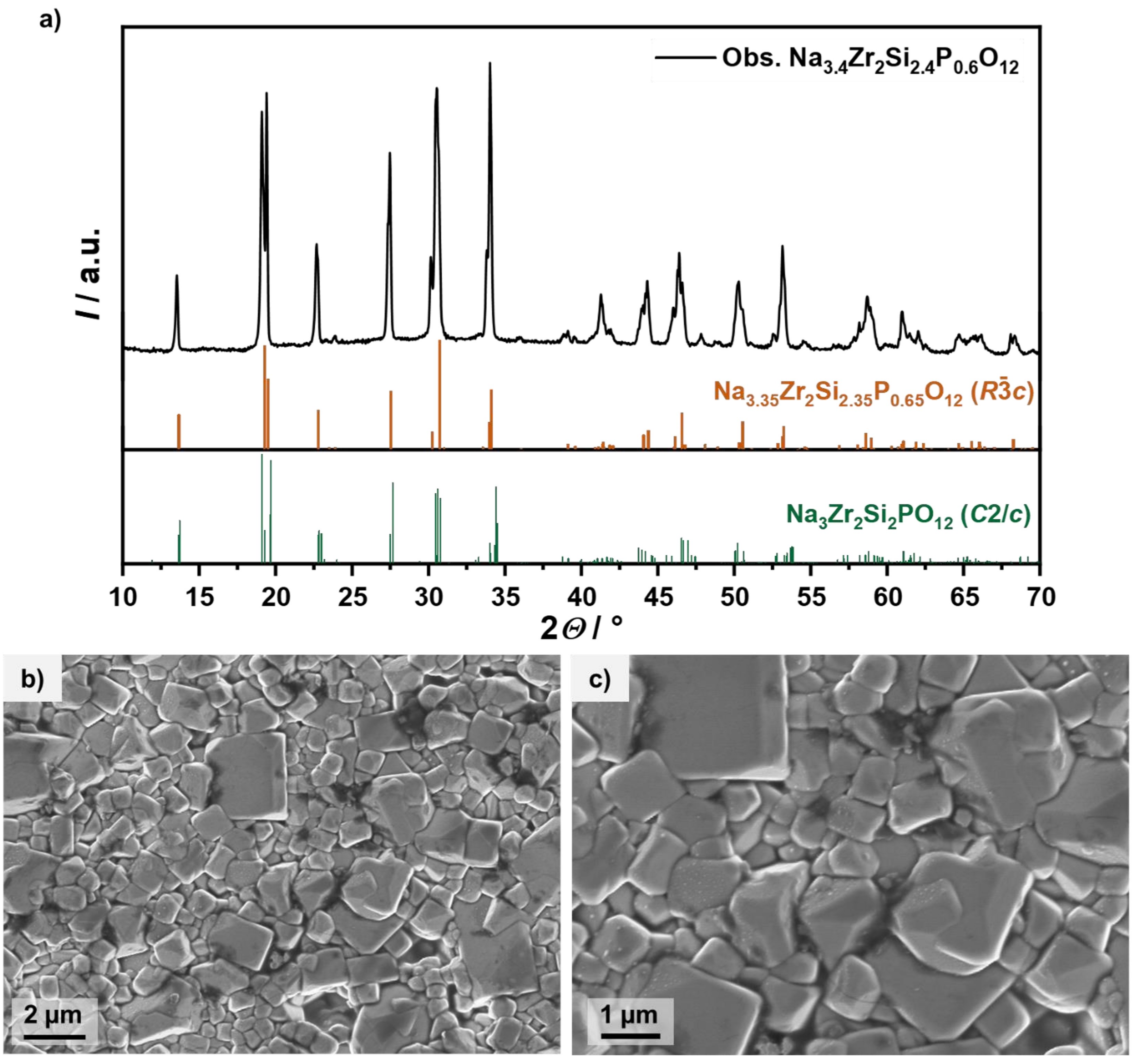

Figure S-1: *a) XRD pattern of the synthesized* $Na_{3.4}Zr_2Si_{2.4}P_{0.6}O_{12}$ *solid electrolyte in comparison to the reference patterns of* $Na_3Zr_2Si_2PO_{12}$ *(C2/c, ICSD000473) and* $Na_{3.35}Zr_2Si_{2.35}P_{0.65}O_{12}$ *(*$R\bar{3}c$*, ICSD 062386). SEM image of the pristine surface of sintered* $Na_{3.4}Zr_2Si_{2.4}P_{0.6}O_{12}$ *at b) low magnification and c) at higher magnification. A crystalline surface with a grain size distribution between about 0.4 µm and 3 µm is visible.*

Based on X-ray diffraction (XRD) analysis, NZSP0.4 solid electrolyte including monoclinic and rhombohedral phase was obtained and used for all experiments (**Figure S-1a**). SEM images indicate a crystalline surface of the material (**Figure S-1b** and **c**). Based on the macroscopic dimensions of the NZSP0.4 separators investigated, the relative density of the separator was >95 %.

2. Impedance analysis of $Na_{3.4}Zr_2Si_{2.4}P_{0.6}O_{12}$

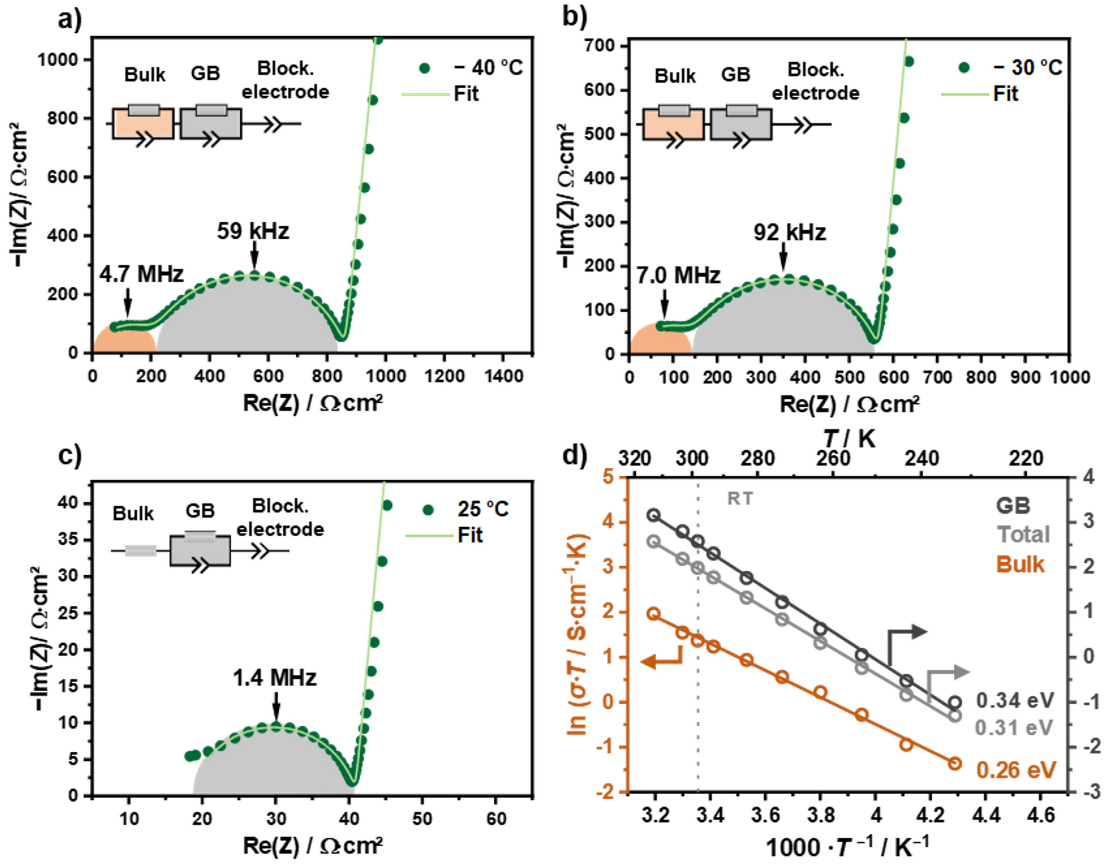

Figure S-2: *Impedance spectra of a symmetric Au|NZSP0.4|Au cell at a) − 40 °C b) − 30 °C and c) 25 °C. The frequency of the bulk contribution shifts outside the measurement range with increasing temperature. Therefore, at temperatures above − 30 °C the bulk is described by a resistance instead of an RQ element. At 25°C, no bulk contribution is observed within the selected frequency range. d) Arrhenius plot and determined activation energy for bulk and grain boundary transport in the temperature range of −40 and 40 °C. For the bulk process the ionic conductivities are shown whereas for grain boundaries only the resistance in dependence of temperature is visualized.*

To characterize the bulk and grain boundary transport processes of the NZSP0.4, impedance analysis of symmetric Au|NZSP0.4|Au cells at different temperatures were recorded and are shown in **Figure S-2a-c**. At −40 °C two separated semicircles are observed in the high- and mid-frequency range with apex frequencies at 4.7 MHz and 59 kHz. In the low-frequency range a strong increase of impedance is obtained. The process at high frequencies (f_{apex}(−40 °C) = 4.7 MHz) is assigned to the bulk transport while the process in the mid-frequency range (f_{apex}(−40 °C) = 59 kHz) is attributed to grain boundary transport, which is in accordance with literature.[1,2] The pronounced polarization at low frequencies is caused by the blocking behavior of the gold electrodes.[3] By elevating the temperature, the apex frequency of bulk transport shifts to higher frequencies ($f_{\mathrm{apex,bulk}}$(−30 °C) = 7.0 MHz) and is beyond the measured frequency range at 25 °C. At elevated temperature the bulk transport is therefore modeled by a serial resistance instead of an *RQ*-element in the equivalent circuit.

Based on the *brick layer model*[2] activation energies for bulk and GB transport process of $E_{\mathrm{a,bulk}}$ = 0.26 eV and $E_{\mathrm{a,GB}}$ = 0.34 eV were determined. The total activation energy $E_{\mathrm{a,tot}}$ = 0.31 eV (for combined bulk and GB resistance) is in good agreement with the literature value for NZSP0.4, whereas a slightly lower $E_{\mathrm{a,bulk}}$ = 0.28 eV is reported.[3] The measurement has been repeated and the mean activation energy for bulk, GB and total transport are summarized in **Table S-4.**

The ionic conductivity of the bulk can be calculated by the following equation:

$$\sigma_{\mathrm{bulk}} = \frac{L}{A \cdot R_{\mathrm{bulk}}} \tag{E1}$$

With the thickness L of the SE pellet, the electrode area A and the measured resistance of the bulk R_{bulk} from impedance analyses an ionic conductivity for bulk transport σ_{bulk} = 1.1 mS·cm^{-1} at −40 °C is obtained. Calculating the GB conductivity σ_{GB} by **Equation 1** is not correct since the volume fraction of the GB is much smaller compared to the volume fraction of the grains in the SE pellet.[4] Hence, for determine σ_{GB} the respective capacitance for bulk C_{bulk} and GB C_{GB} must be considered according to **Equation 2**:

$$\sigma_{\mathrm{GB}} = \frac{L}{A}\left(\frac{C_{\mathrm{bulk}}}{C_{\mathrm{GB}}}\right)\frac{1}{R_{\mathrm{GB}}} \tag{E2}$$

As the C_{bulk} is necessary for determination, σ_{GB} can only calculated for low temperature as $f_{\mathrm{apex,bulk}}$ shifts beyond the measured frequency range. At −40 °C a σ_{GB} = 0.014 mS·cm^{-1} is obtained. However, due to this limitation **Figure S-2d** only shows the temperature dependence of R_{GB} obtained from the respective impedance spectra.

3. Temperature-correction for time-resolved impedance analysis of Na|NZSP0.4 interface

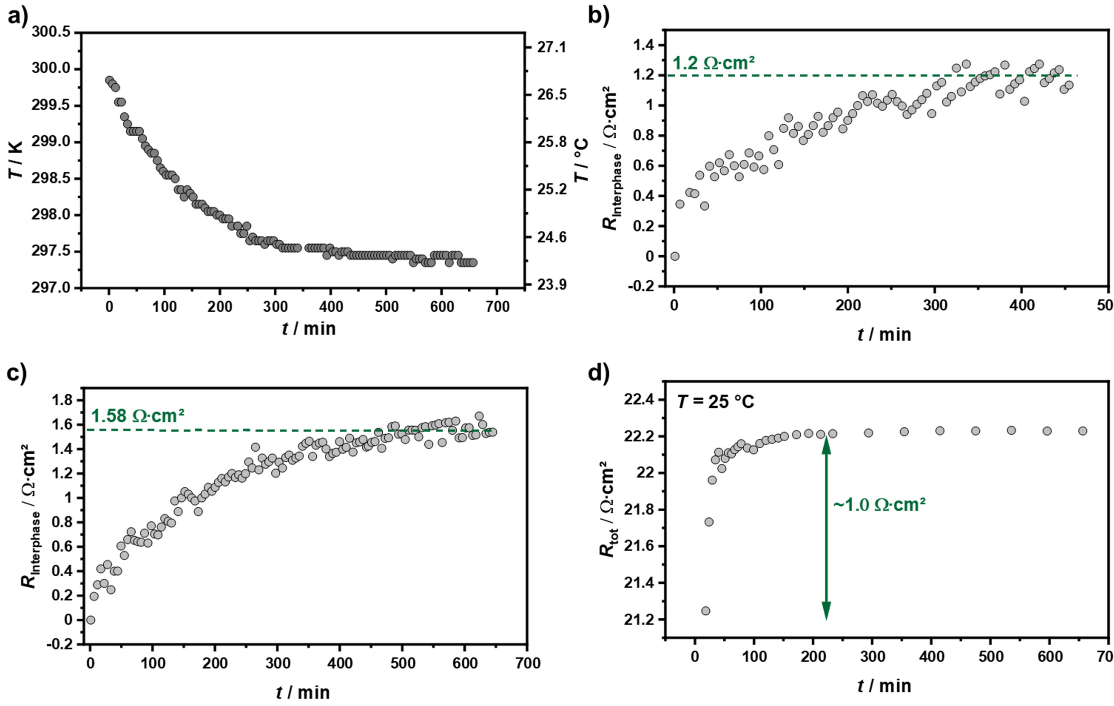

Figure S 3*: a) Temperature profile during time-resolved impedance analysis inside the glovebox. The thermocouple was placed directly next to the electrochemical cell. Representation of the temporal evolution of* $R_{\text{Interphase}}$ *for two independent measurement series shown in b) and c), which have already been corrected for temperature fluctuations during the impedance recording. d) Real part of total resistance of a symmetric Na|NZSP0.4|Na cell at a constant temperature of 25°C as function of time. Time delay between assembly and recording was roughly 18 minutes.*

Figure S-3a shows the temperature profile of the glovebox during impedance analysis indicating a temperature decrease of roughly 2.5 °C. To compensate for temperature changes during measurements we subtracted a correction term R_{Corr} from the measured real part of impedance R_{m} and obtain the real part of resistance of the growing interphase $R_{\text{Interphase}}$ (E3):

$$R_{\text{Interphase}} = R_{\text{m}} - R_{\text{Corr}} \qquad \text{(E3)}$$

R_{Corr} has been calculated based on the temperature dependence of the ionic conductivity of NZSP0.4, which is described in the following:

The ionic conductivity in solid electrolytes can be described using **Equation E4**:[5]

$$\sigma \cdot T = \sigma_0 \cdot \exp\left(\frac{-E_{\text{a}}}{k_{\text{B}}T}\right) \qquad \text{(E4)}$$

were σ describes the conductivity, E_{a} the activation energy, T the absolute temperature and k_{B} the Boltzmann constant. σ_0 is the pre-exponential factor which includes crystallographic properties of the material under consideration. Since the specific conductivity is proportional to the reciprocal resistance, **Equation E4** can be transformed to:

$$\frac{T}{R} = \frac{1}{R_0} \cdot \exp\left(\frac{-E_\mathrm{a}}{k_\mathrm{B}T}\right) \tag{E5}$$

Rearrangement of **Equation E5** leads to:

$$R(T) = T \cdot R_0 \cdot \exp\left(\frac{E_\mathrm{a}}{k_\mathrm{B}T}\right) \tag{E6}$$

If the activation energy E_a and the constant R_0 are known for a material or a specific sample, the resulting resistance R can be calculated for any temperature.

In case of time-dependent impedance analysis, this relationship (**Equation E6**) was used to calculate the influence of temperature fluctuations inside the glovebox on the resistance (ionic conductivity) of NZSP0.4. It is assumed that the temperature only influences the conductivity of the solid electrolyte and not that of a (possible) formed interphase. By means of symmetrical Au|NZSP0.4|Au cells the activation energy for bulk and grain boundary transport was determined as 0.244 eV and 0.357 eV, respectively. These values were obtained from two different cells. The pre-exponential Factor R_0^{-1} is sample-dependent and therefore cannot be taken from measurements with blocking electrodes.

For the determination of R_0 it is assumed that the first recorded impedance spectrum of a measurement series has not yet formed an interlayer. In this case the impedance spectrum contains only the bulk and grain boundary properties of the solid electrolyte. By fitting this first impedance spectrum using an R_bulk–$R_\mathrm{GB}Q_\mathrm{GB}$ equivalent circuit, the resistance of bulk $R_{\mathrm{bulk},t=0}$ and grain boundary $R_{\mathrm{GB},t=0}$ at time $t = 0$ were determined. Based on these resistances combined with the activation energies $E_\mathrm{a,bulk}$ and $E_\mathrm{a,GB}$ as well as the temperature T, R_0 were calculated for bulk and grain boundary transport.

$$R_\mathrm{0,bulk} = \frac{R_{\mathrm{bulk},t=0}}{T} \cdot \exp\left(\frac{-E_\mathrm{a,bulk}}{k_\mathrm{B}T}\right) \tag{E7}$$

$$R_\mathrm{0,GB} = \frac{R_{\mathrm{GB},t=0}}{T} \cdot \exp\left(\frac{-E_\mathrm{a,GB}}{k_\mathrm{B}T}\right) \tag{E8}$$

With the help of the determined factors $R_\mathrm{0,bulk}$ and $R_\mathrm{0,GB}$ and the respective activation energies for bulk $E_\mathrm{a,bulk}$ and grain boundary transport $E_\mathrm{a,GB}$, the resistance of a specific sample can be calculated as a function of temperature.

$$R_\mathrm{bulk}(T) = R_\mathrm{0,bulk} \cdot T \cdot \exp\left(\frac{E_\mathrm{a,bulk}}{k_\mathrm{B}T}\right) \tag{E9}$$

$$R_{\mathrm{GB}}(T) = R_{0,\mathrm{GB}} \cdot T \cdot \exp\left(\frac{E_{\mathrm{a,GB}}}{k_{\mathrm{B}}T}\right) \tag{E10}$$

The addition of $R_{\mathrm{bulk}}(T)$ and $R_{\mathrm{GB}}(T)$ gives the corrected total resistance of the solid electrolyte at a given temperature.

$$R_{\mathrm{Corr}}(T) = R_{\mathrm{bulk}}(T) + R_{\mathrm{GB}}(T) \tag{E11}$$

It must be taken into account that with the described temperature correction a relative error for R_{Corr} of about 50 % is obtained. This is mainly due to the absolute errors of the determined activation energies of bulk and GB obtained from the linear regression. Since the values of R_{Corr} and R_{m} are close to each other, extremely high absolute errors of a factor of 10 result for $R_{\mathrm{Interphase}}$.

4. XPS Analysis of Na|NZSP0.4 Interface

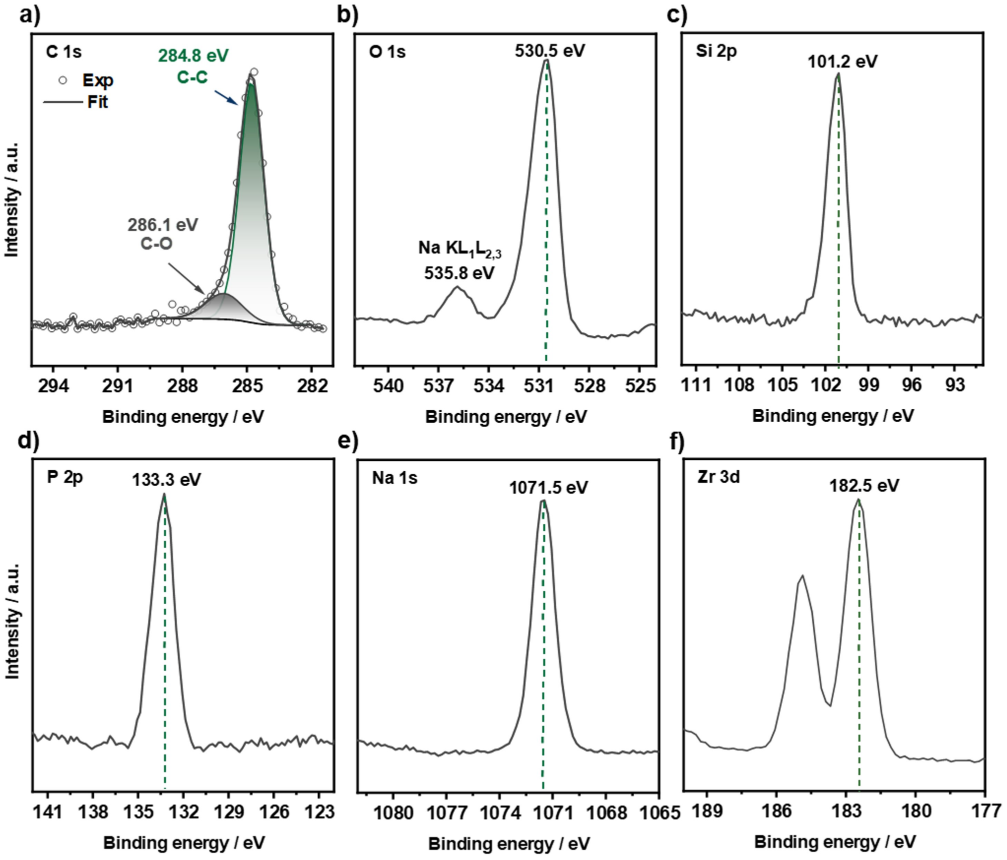

Figure S-4: *Detail XP spectra of a) C 1s, b) O 1s, c) Si 2p, d) P 2p, e) Na 1s and f) Zr 3d of an untreated pristine* $Na_{3.4}Zr_2Si_{2.4}P_{0.6}O_{12}$ *surface.*

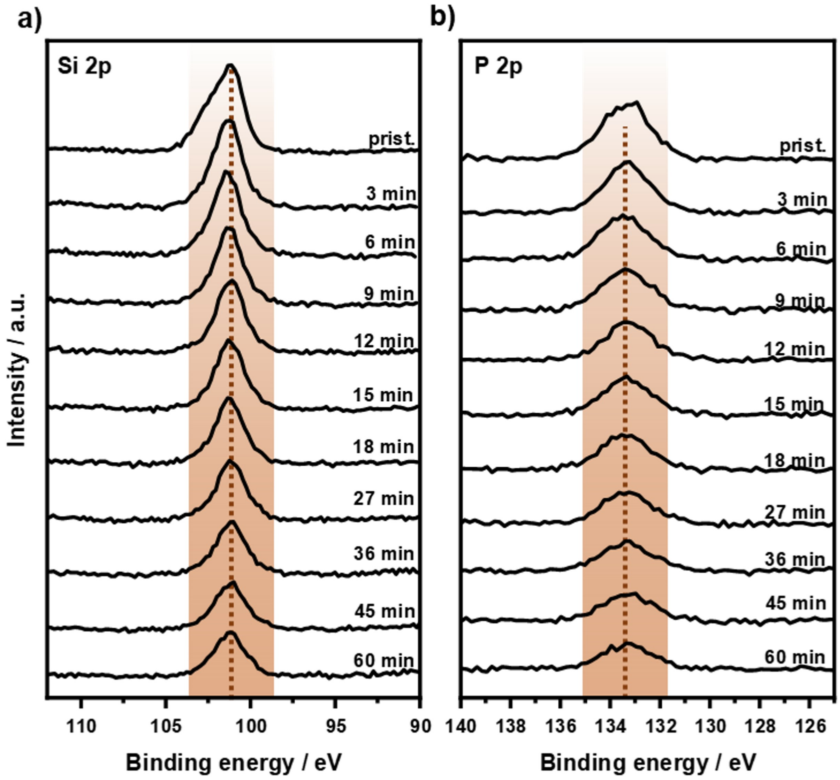

Figure S-5: *XP spectra of a) Si 2p and b) P 2p lines after deposition of different amounts of sodium. No changes in binding energy are observed for both signals. Thus, Si and P are not reduced in contact with sodium or decomposition products are formed that are either volatile or react further with the chamber atmosphere and cannot be detected by XPS.*

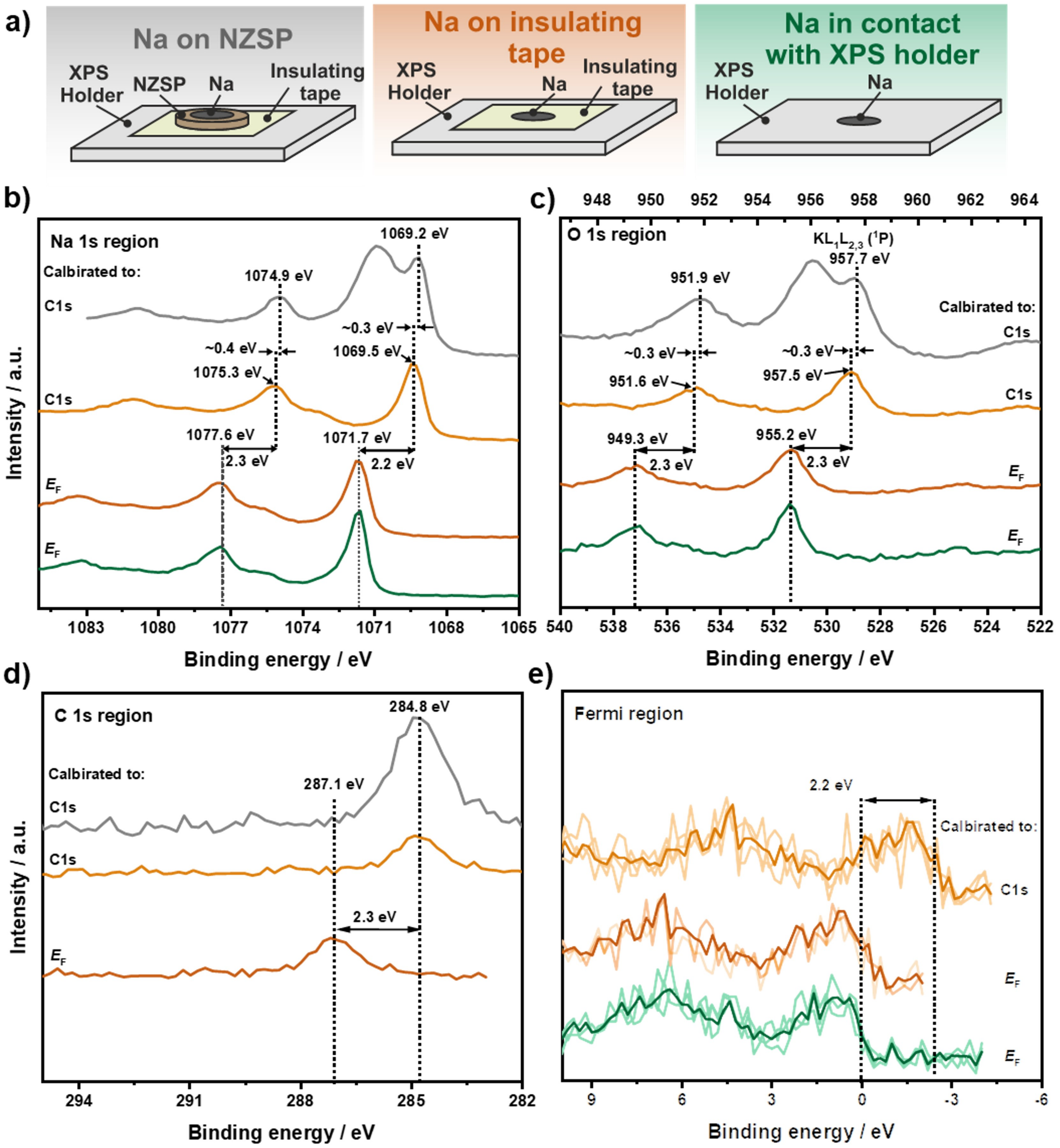

Figure S-6: *Overview of sodium XP spectra at different boundary conditions. Three different measurements were performed with different measurement settings (with and without dual beam neutralization) and measurement setups. a) Sketch of the measurement setups used. Neutralization was used for samples fixed on insulating tape. These spectra are calibrated with the C 1s signal (grey and light orange curves). Additionally, the measurement of sodium metal with neutralization is calibrated to the Fermi level for better comparison, too (dark orange curves). Sodium in direct contact with the sample holder was measured without neutralization and calibrated to Fermi level (green curves). b)-e) XP spectra of Na 1s, O 1s, C 1s and Fermi region for the respective measurement conditions. For the Fermi region, three measurements for each condition (light tint) and the corresponding average value (dark tint) are shown. Independent of the measurement method (with or without neutralization), identical spectra are obtained for sodium metal when calibrating to the Fermi level. However, when an electrically insulating layer between the sodium* *and the sample holder is present and the spectra are calibrated on C 1s signal, a clear shift of roughly 2.5 eV of all sodium signals including the Fermi level to lower energies can be observed compared to the sodium samples directly contacted to the sample holder. The shift indicates that an equilibration of the Fermi levels is not possible when an insulation layer is present between sample and sample holder.*

To the best of our knowledge, only the energy loss of bulk and surface plasmon excitation is known in the literature, but not a suitable fit model for the Na 1s signal or Na Auger emission in the O 1s region for sodium metal.[6] However, to determine the shift of the sodium metal signals in the Na 1s and O 1s region for the different measurement settings, a simplified fit model was designed. We would like to emphasize that the presented fit model is not an ideal description of the Na 1s and Na Auger emission for sodium metal, but it is sufficient to identify relative changes between different measurement conditions.

The presented Na 1s spectrum for sodium metal should contain the main peak as well as the first and second excitations of bulk and surface plasmon. For simplification, all components are assigned to a Gaussian-Lorentzian function (GL(30)) for peak description. In addition, the corresponding energy spacings of the plasmon excitations and full-width-half-maximum < 2 were used as constraints for fitting. A further component was added to the model describing Na^+-species originating from NZSP0.4 and possible sodium containing degradation products, when the sodium metal was deposited on the SE.

For fitting the O 1s region, the Na^0-$KL_1L_{2,3}$ transition with first bulk and surface plasmonic excitation were considered for sodium metal. Analogous to the fitting of the Na1s spectrum, an identical function and constraints were used for the components. For the case of sodium in contact with NZSP0.4, one further component was added describing the oxygen component of the SE. Further Auger signals originating from Na^+ species were neglected. The obtained parameters for Na 1s and O 1s regions of the different measurements are summarized in Figure S-6 and **Table S-1** and **S-2**.

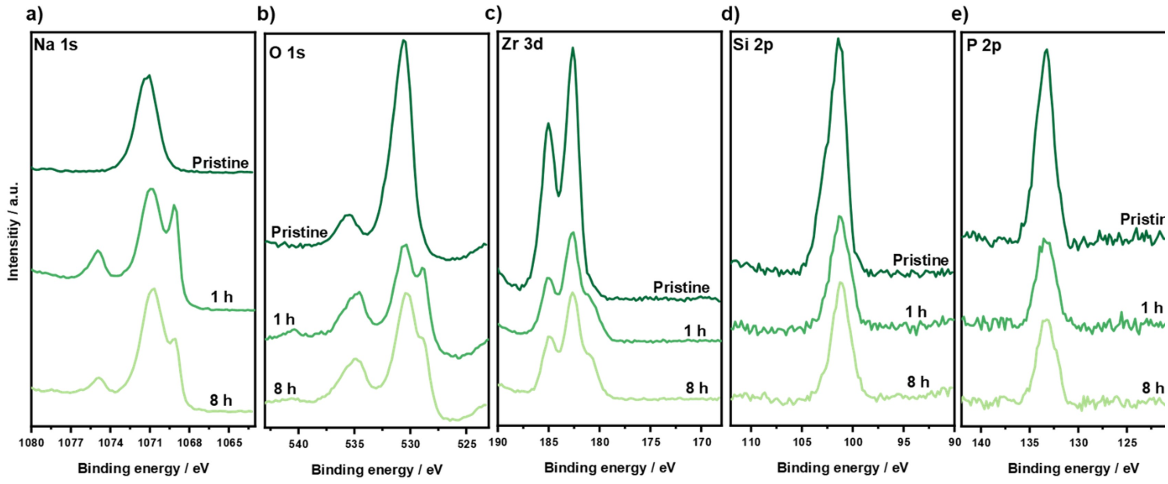

***Figure S-7**: XP Spectra of the solid electrolyte before sodium deposition, after a total deposition time of 1 h and after 8 h of the last deposition cycle. Except for the decrease of the sodium metal signals in the Na 1s and O 1s regions, only the Zr 3d signal profile shows a shoulder at 181.0 eV after sodium deposition.*

5. Transmission electron microscopy of Na|NZSP0.4 interface

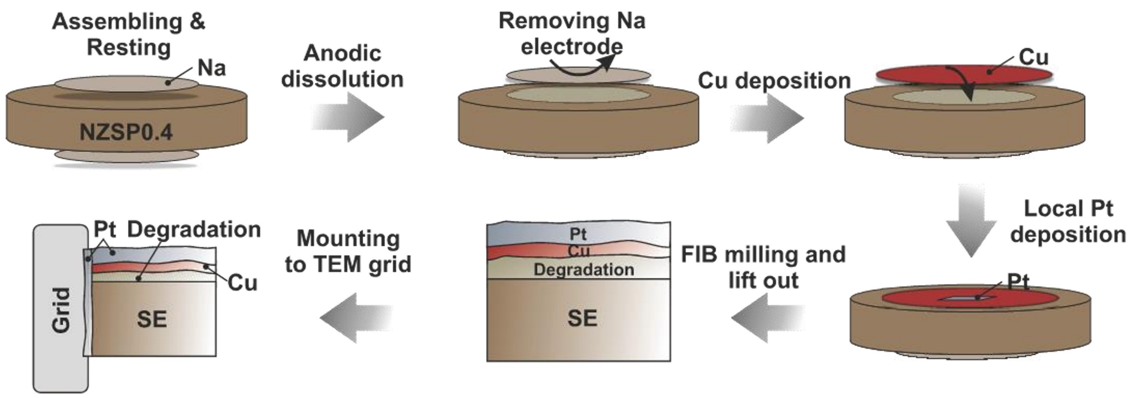

***Figure S-8**: a) Illustration of preparation route of electron transparent specimen for TEM characterization. A tight copper layer was deposited on the NZSP0.4 after removing the sodium electrode to protect the exposed surface. For preparation of the electron transparent specimen and mounting on the TEM grid, deposition of platinum was used.*

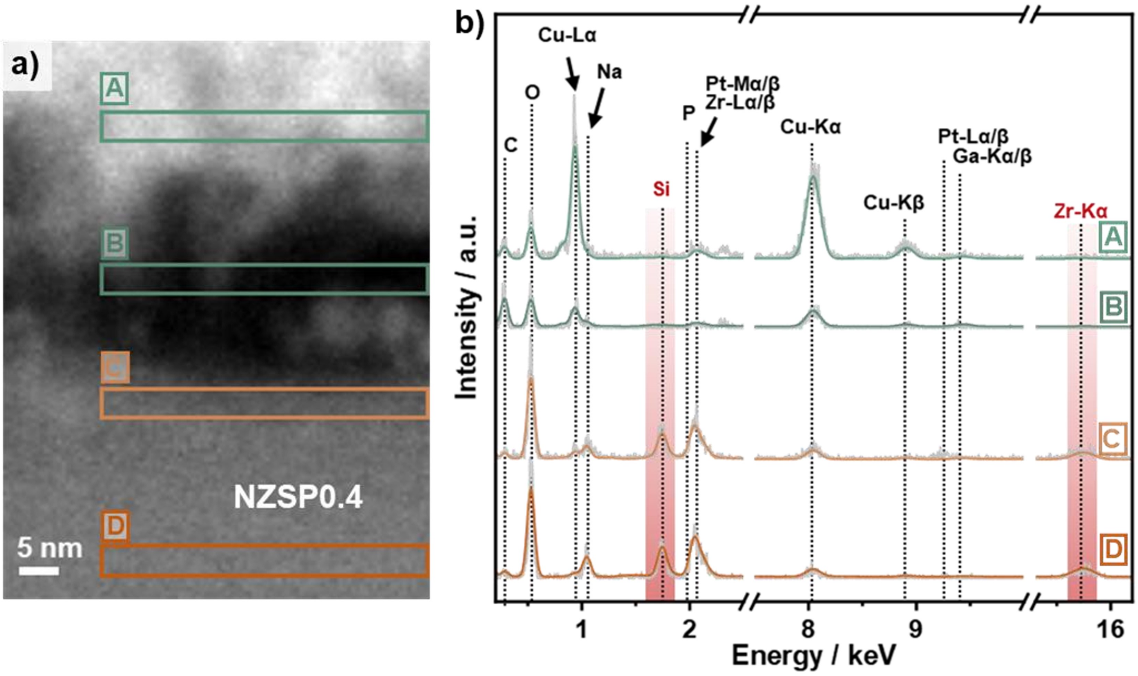

***Figure S-9**: a) HAADF-STEM image of a prepared electron transparent lamella from the Na|NZSP0.4 interface. Based on different morphologies, the NZSP0.4 solid electrolyte separates clearly from the deposit protection layer. b) EDX spectra of selected regions which are highlighted in green and orange in b). The measured spectra are shown in light grey while the model spectra are presented in the respective color (orange and green). Similar to the results shown in **Figure 3**, no obvious changes of the elemental composition in the bulk and near-surface region of the NZSP0.4 are obtained. The present of copper signal inside the NZSP0.4 region is probably caused by the cryo transfer holder system. The protection layer consists mainly of copper and small amounts of platinum. In addition, the present of sodium and oxygen in the protection layer originate from the degradation of residual sodium which have not removed with the bulk sodium electrode.*

6. Normalization of impedance spectra with different geometric electrode areas

For comparing impedance spectra obtained from cells with different electrode size a normalization to the geometric electrode area is not sufficient, since the volume contribution to the overall conductivity of the SE changes, too. This is the case when sodium is gradually attached to an SE by applying a uniaxial force where beside an improvement of interfacial contact also the geometric electrode area increases. In other words, the dynamic constriction (improvement of interfacial contact) is superimposed by a static constriction (change of electrode area) effect.[7] To account for the static constriction effect in the normalization, the ionic bulk conductivity $\sigma_{\mathrm{SE,bulk}}$ of the SE can be used. Since the geometric thickness d and $\sigma_{\mathrm{SE,bulk}}$ are constant during the experiment, the electrode area $A_{\mathrm{El,cal}}$ can be calculated using the fitted series resistor R_{Ser} according to:

$$A_{\mathrm{El,cal}} = \frac{d}{\sigma_{\mathrm{SE}} \cdot R_{\mathrm{Ser}}} \qquad \text{(E12)}$$

This calculated electrode area can be used to normalize the impedance spectra as well as the resistances and capacitances determined from the spectra.

7. Distribution of relaxation times of symmetric Na|NZSP0.4|Na cells

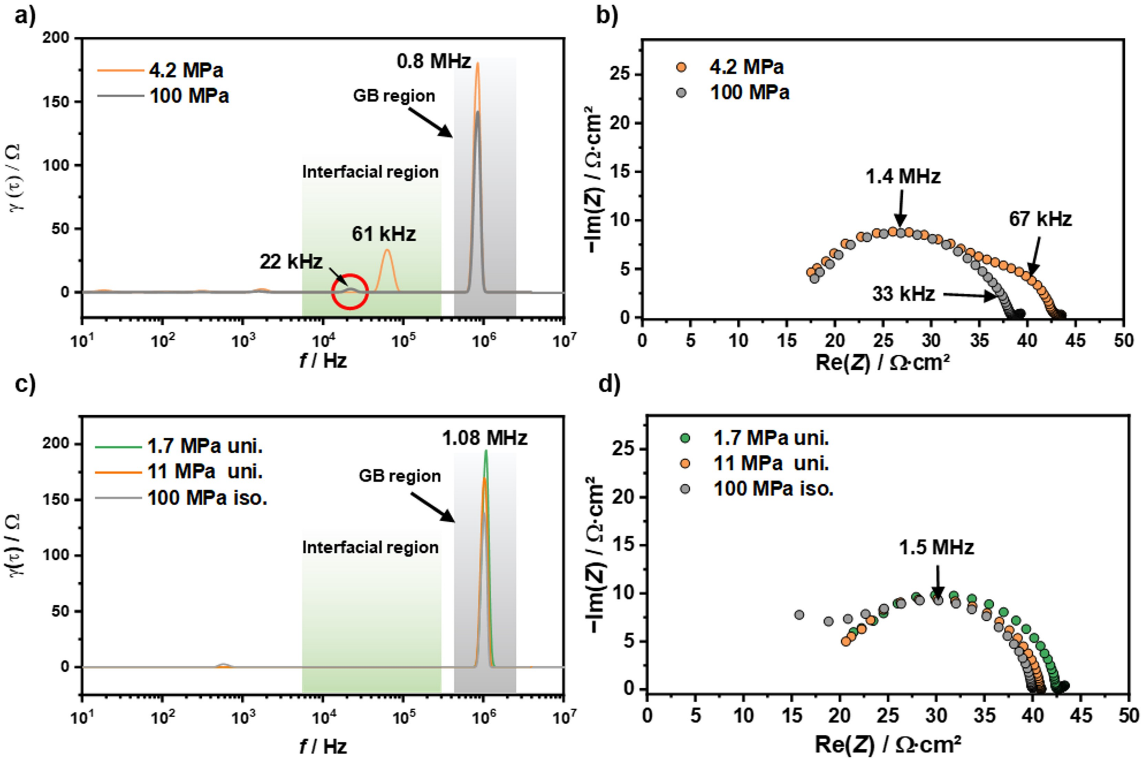

Figure S-10: *a) Representation of selected DRT analyses of the symmetrical cell* $Na_{bc}|NZSP0.4|Na_{id}$*, where the working electrode was pressed on the SE step by step with increasing force/pressure. Shown are the cases after an applied pressure of 4.2 MPa (215 N) and 100 MPa. For comparison, the corresponding Nyquist plots are shown in b). The green background indicates the region in which interface-related signals are expected in the DRT analysis while the grey background indicates the grain boundary region. In both cases, two signals (22 kHz and 61 kHz) are present in this interface-related region, although after a pressure of 100 MPa this is markedly less pronounced (Figure a, outlined in red). c) DRT analyses of* $Na_{bc}|NZSP0.4|Na_{id}$ *cells assembled at three different pressures with the corresponding Nyquist plots in d). In contrast to a), for the sodium working electrodes shown in c) only one pressure step was performed at the indicated pressures. For all three cells, no signal indicating an interfacial contribution was obtained in the DRT analysis (c and d).*

8. Activation energies of Na|NZSP0.4|Na cells with different interfacial contact

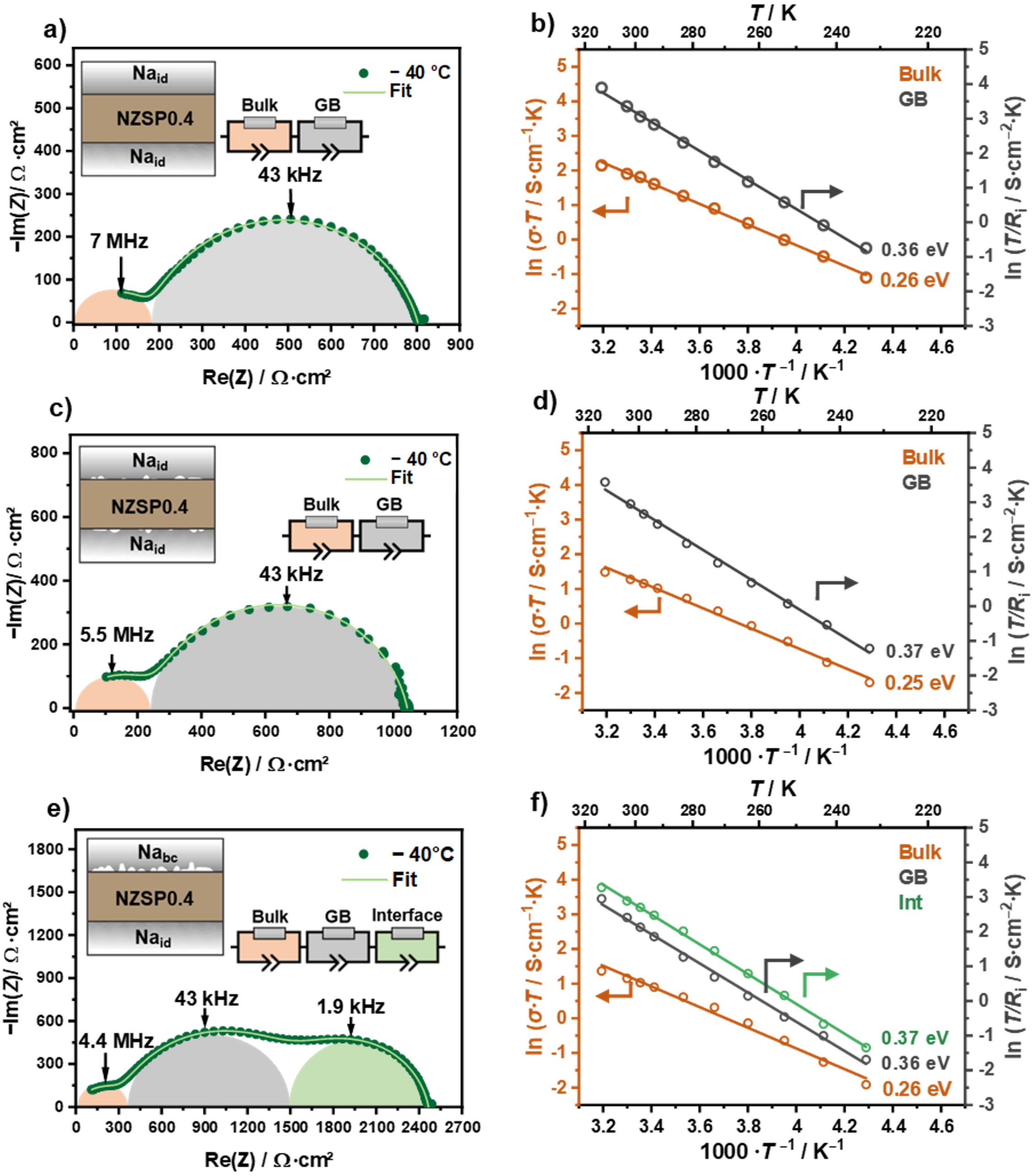

***Figure S-11**: Impedance data (left column) and associated Arrhenius plots (right column) of three Na|NZSP0.4|Na cells which have been assembled with different protocols of attaching the sodium electrodes. The abbreviations "bc" stand for low and "id" ideally reversible electrode. For all cells impedance data at − 40 °C are shown in the left column. Determined activation energies of different processes (bulk, GB and interface) are inserted in the Arrhenius plots for each cell, respectively. For the bulk process the ionic conductivities are shown whereas for grain boundaries and interface process only the resistance in dependence of temperature are visualized.*

Three Na|NZSP0.4|Na cells with different interfacial contact were analyzed by temperature-dependent impedance analysis to determine the activation energies for the bulk, GB, and interface transport processes. Impedance spectra for each cell at −40 °C are on the right-hand side in **Figure S-11** where the corresponding Arrhenius plots are shown on the left-hand side. Starting with an ideal interfacial contact (Figure S-9a) even at low temperatures in the high- and mid-frequency range only bulk and GB transport are observed. No additional interfacial contribution is observed. Furthermore, the apex frequencies as well as the values for $E_{a,\mathrm{bulk}} = 0.26$ eV and $E_{a,\mathrm{GB}} = 0.36$ eV are very similar to those obtained from Au|NZSP0.4|Au cells (see **Table S-4**). Contributions from the interface including the formed interphase are negligibly small.

Even when small pores are present (< 100 nm, compare Figure 4d and e) at the interface, only the bulk and GB contributions are found at −40 °C in the respective impedance (Figure S-11c). Similar to the previous case values for $E_{a,\mathrm{bulk}}$ and $E_{a,\mathrm{GB}}$ are close to those determined in Au|NZSPO0.4|Au cells (see Figure S-11d and Table S-4). Based on this result the prepared electrode can be considered as a QRE.

The WE was then attached using a much lower external load while a QRE was used as counter electrode. Beside bulk and GB processes in the high- and mid-frequency range a clear contribution at 1.4 kHz with $C_{\mathrm{Int}} = 0.1$ μF·cm^{-2} is observed (Figure S-11e) which we can safely attribute to the interface. For the interfacial contribution an activation energy $E_{a,\mathrm{Int}} = 0.37$ eV is determined, which is close to $E_{a,\mathrm{GB}}$ (Figure S-11f). All determined E_a are summarized in Table S-4.

9. Anodic dissolution of Na|NZSP0.4|Na inside SEM chamber ($p = 10^{-3}$ Pa)

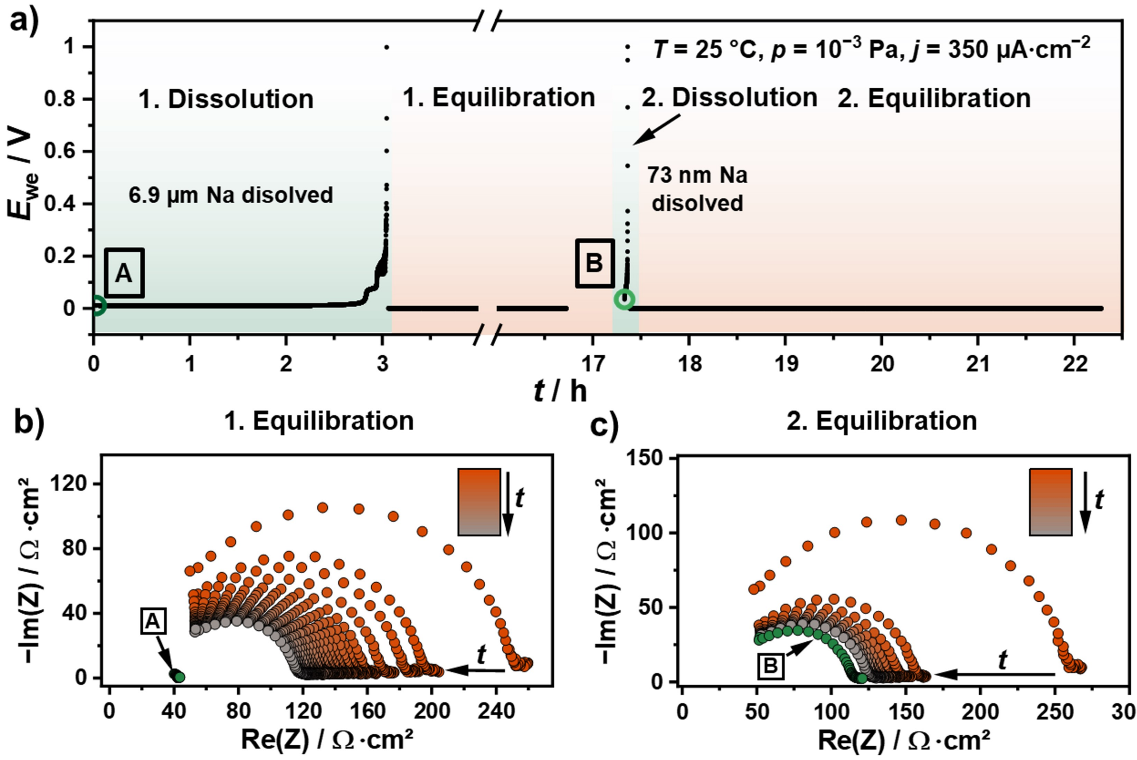

***Figure S-12**: a) Chronopotentiometric curve of a symmetrical $Na_{idR}|NZSP0.4|Na_{idR}$ cell at a current density of 350 µA·cm^{-2} and at a pressure of 10^{-3} Pa. After reaching the cut-off voltage of 1V, the electrode was analyzed by PEIS in intervals of 5 minutes until the changes of the real part of the resistance were less than 1 Ω·cm². The described procedure was repeated again with the same electrode. With the first dissolution around 6.9 µm of sodium was resolved, whereas with the second dissolution only 73 nm could be dissolved. b) Development of impedance during the equilibration period of the anodically dissolved electrode. In green, the pristine impedance is inserted in the figure (also shown in figure a) at point A). A decrease in impedance is also observed in the vacuum, but it does not reach the pristine state. c) Nyquist plot of the second equilibration period.*

10. Schematic illustration of preparation of symmetrical Na|NZSP0.4|Na$_{id}$ cells

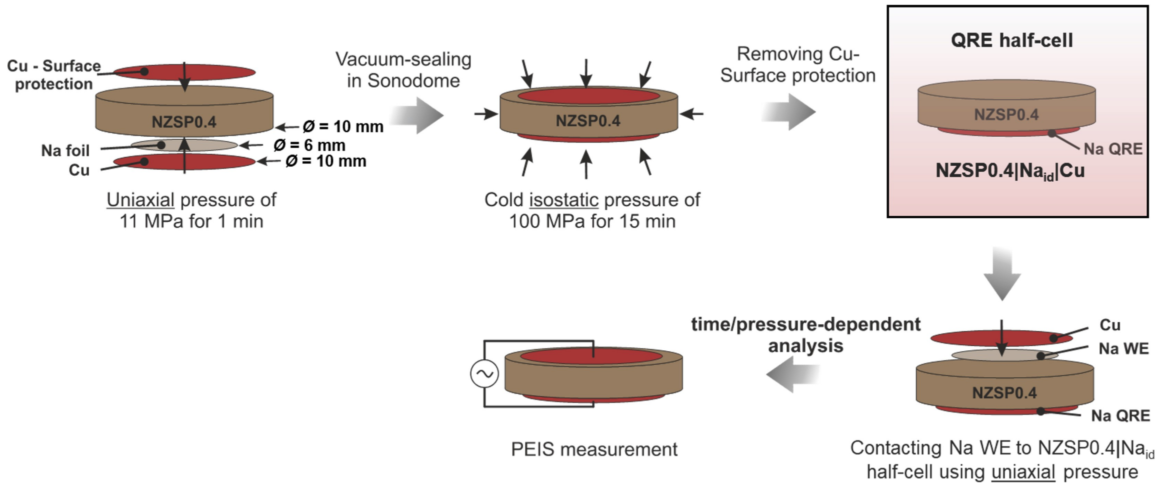

Figure S-13: *Schematic illustration of the preparation process of a quasi-reference (QRE) sodium electrode for a NZSP0.4|Na$_{id}$ half-cell. Na$_{id}$ denotes an ideally reversible sodium electrode. A copper foil is used for easier handling and protection against degradation of the sodium foil inside the glovebox. For time-dependent analysis the NZSP0.4|Na$_{id}$ half-cell is complemented with a working electrode (WE) by pressing a sodium foil at 11 MPa for 1 min uniaxial on the opposite side of the half-cell. For the pressure-dependent analysis the sodium WE is gradually pressed to the SE using uniaxial pressure. For dissolution experiments, symmetrical Na$_{id}$|NZSP0.4|Na$_{id}$ cells were prepared by contacting both sodium electrodes simultaneously to the SE using a uniaxial pressure of 11 MPa for 1 minute or an isostatic pressure of 100 MPa or 15 minutes.*

Table S-1: *List of the obtained binding energies for the measured signals in the Na 1s region for sodium metal under different measurement conditions. A detailed explanation of the measurement conditions can be found in Figure S6. The same color code as in Figure S6 was used. For sodium metal, besides the main signal* Na^0*, the first and second plasma excitation of bulk (*B_{P1} *and* B_{P2}*) and surface (*S_{P1} *and* P_{S2}*) are listed. In addition, the binding energy of the* Na^+ *signal is given, which describes an average BE including signals originating from SE and possible degradation products formed. A detailed description of the fitting model used can be find in section 4 in den supplementary information.*

Measuring condition	**Calib. to**	**Na 1s region**					
		Na^+	**Na^0**	**Na^0 - B_{P1}**	**Na^0 - S_{P1}**	**Na^0 - B_{P2}**	**Na^0 - S_{P2}**
Na on NZSP0.4	C 1s	1070.7	1069.2	1074.9	1073.2	1080.8	1079.0
Na on insulating tape	C 1s	-	1069.5	1075.3	1073.5	1081.1	1079.3
	E_{F}	-	1071.7	1077.5	1075.7	1083.6	1081.6
Na grounded	E_{F}	-	1071.8	1077.6	1075.8	1083.4	1081.6

Table S-2: *List of the determined binding energies (BE) and kinetic energies (KE) for the obtained signals in the O 1s region for sodium metal under different measurement conditions. A detailed explanation of the measurement conditions can be found in Figure S6. The same color code as in Figure S6 was used. For sodium metal, besides the main signal of* Na^0*-*$KL_1L_{2,3}$*, the first plasma excitation of bulk (*B_{Plas}*) and surface (*S_{Plas}*) are listed. In addition, the binding energy of the O1s signal is given, which describes an average BE including signals originating from SE and possible degradation products formed. A detailed description of the fitting model used can be find in section 4 in den supplementary information.*

Measuring condition	**Calib. to**	**O 1s region**						
		O1s	**Na^0-$\mathrm{KL}_1\mathrm{L}_{2,3}$**		**Na^0-$\mathrm{KL}_1\mathrm{L}_{2,3}$ - $\mathrm{B}_{\mathrm{Plas.}}$**		**Na^0-$\mathrm{KL}_1\mathrm{L}_{2,3}$ - $\mathrm{S}_{\mathrm{Plas.}}$**	
		BE	**BE**	**KE**	**BE**	**KE**	**BE**	**KE**
Na on NZSPO	C 1s	530.2	528.9	957.7	534.7	951.9	532.9	953.7
Na on insulating tape	C 1s	-	529.1	957.5	535.0	951.6	533.2	953.4
	E_{F}	-	531.4	955.2	537.2	949.4	535.4	951.2
Na grounded	E_{F}	-	531.4	955.2	537.3	949.3	535.5	951.1

Table S-3*: Absolute signal areas of Na 1s, O 1s, Zr 3d, Si 2p and P 2p of the solid electrolyte and immediately after sodium deposition and after 8 hours of retention time. Plasmons occurring in the Na 1s and O 1s region were not considered for the quantification.*

State of Sample	**Na 1s/cps·eV**	**O 1s/cps·eV**	**Zr 3d/cps·eV**	**Si 2p/cps·eV**	**P 2p /cps·eV**
Pristine	283.6	698.9	138.6	169.9	64.9
60 min	452.0	463.5	68.4	81.0	31.6
8 h	450.5	507.6	66.3	82.7	30.0

Table S-4: *Calculated activation energies of Na ion transport across different symmetrical cells with NZSP0.4 as solid electrolyte in the temperature range between −40 and 40 °C. In addition to bulk and grain boundary, the total activation energy* $E_{a,tot}$ *for all cells was also determined. The abbreviation "id" indicates an ideally reversible electrode whereas "bc" indicates an electrode with low-load bearing contact. Even with small pores at the interface an ideal electrode behavior can be achieved. For the determination of the interfacial activation energy, insufficient contact was achieved by two different methods. For* $E_{a,Int}$ *highlighted in green, insufficient contact was achieved by anodic dissolution, whereas* $E_{a,Int}$ *highlighted in grey was determined by insufficient pressure during assembling.*

Activation energy	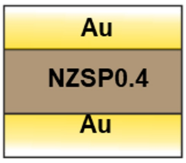		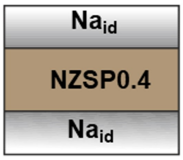	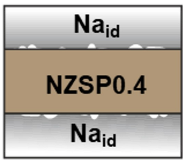		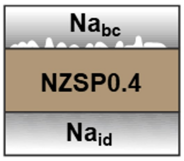	
$E_{a,bulk}$ /eV	0.25(8)	0.25(8)	0.25(7)	0.25(2)	0.24(6)	0.25(7)	0.24(0)
$E_{a,GB}$ /eV	0.36(1)	0.34(0)	0.36(2)	0.37(0)	0.37(1)	0.36(2)	0.37(7)
$E_{a,tot}$ /eV	0.32(1)	0.31(2)	0.32(6)	0.32(4)	0.32(3)	0.32(9)	0.32(6)
$E_{a,Int}$ /eV	-	-	-	-	-	0.37(0)	0.38(1)

References

[1] S. Lunghammer, Q. Ma, D. Rettenwander, I. Hanzu, F. Tietz, H.M.R. Wilkening, *Chemical Physics Letters* **2018**, *701*, 147.

[2] J. T. S. Irvine, D. C. Sinclair, A. R. West, *Adv. Mater.* **1990**, *2*, 132.

[3] Q. Ma, C.-L. Tsai, X.-K. Wei, M. Heggen, F. Tietz, J. T. S. Irvine, *J. Mater. Chem. A* **2019**, *7*, 7766.

[4] S. Naqash, D. Sebold, F. Tietz, O. Guillon, *J. Am. Ceram. Soc.* **2019**, *102*, 1057.

[5] Richard J.D. Tilley, *Understanding Solids. The science of Materials*, John Wiley & Sons Inc., Chichester, **2013**.

[6] A. Barrie, F. J. Street, *Journal of Electron Spectroscopy and Related Phenomena* **1975**, *7*, 1.

[7] J. K. Eckhardt, P. J. Klar, J. Janek, C. Heiliger, *ACS Appl. Mater. & Interfaces* **2022**, *14*, 31, 35545-35554.

7.2.2 Publication 2: Deposition of Sodium Metal at the Copper-NaSICON Interface for Reservoir-Free Solid-State Sodium Batteries

ADVANCED
ENERGY
MATERIALS

Supporting Information

for *Adv. Energy Mater.*, DOI 10.1002/aenm.202302729

Deposition of Sodium Metal at the Copper-NaSICON Interface for Reservoir-Free Solid-State Sodium Batteries

Till Ortmann, Till Fuchs, Janis K. Eckhardt, Ziming Ding, Qianli Ma, Frank Tietz, Christian Kübel, Marcus Rohnke and Jürgen Janek**

Supplementary Information

Deposition of Sodium Metal at the Copper-NaSICON Interface for Reservoir-free Solid-State Sodium Batteries

Till Ortmann, Till Fuchs, Janis K. Eckhardt, Ziming Ding, Qianli Ma, Frank Tietz, Christian Kübel, Marcus Rohnke*, and Jürgen Janek*

Mr. T. Ortmann, Dr. J. K. Eckhardt, Dr. T. Fuchs, Dr. M. Rohnke and Prof. J. Janek
Institute for Physical Chemistry, Justus Liebig University Giessen, 35392 Giessen, Germany.
*E-Mail: juergen.janek@phys.chemie.uni-giessen.de
*E-Mail: marucs.rohnke@phys.chemie.uni-giessen.de

Mr. T. Ortmann, Dr. J. K. Eckhardt, Dr. T. Fuchs, Dr. M. Rohnke and Prof. J. Janek
Center for Materials Research (ZfM), Justus Liebig University Giessen, 35392 Giessen, Germany.

Dr. Q. Ma and Dr. F. Tietz
Forschungszentrum Jülich GmbH, Institute of Energy and Climate Research, Materials Synthesis and Processing (IEK-1), 52425 Jülich, Germany.

Ms. Z. Ding and Prof. C. Kübel
Technische Universität Darmstadt, 64289 Darmstadt, Germany.

Ms. Z. Ding and Prof. C. Kübel
Institute of Nanotechnology (INT) and Helmholtz Institute Ulm (HIU), Karlsruhe Institute of Technology (KIT), 76344 Eggenstein-Leopoldshafen, Germany.

Prof. C. Kübel
Karlsruhe Nano Micro Facility (KNMF), Karlsruhe Institute of Technology (KIT), 76344 Eggenstein-Leopoldshafen, Germany.

1. Illustration of Sample Preparation and Measurement Series

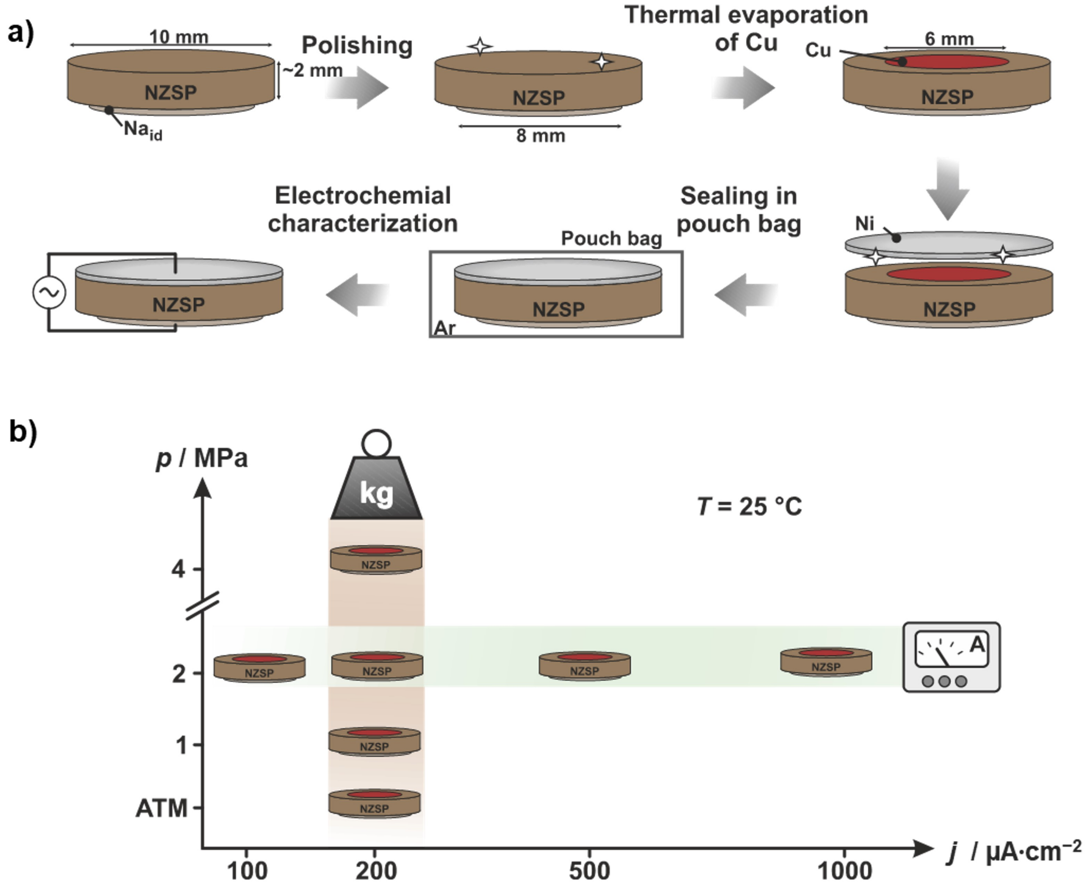

Figure S1: *a) Illustration of sample preparation for analysis of sodium growth at the Cu|NZSP interface. After assembly of an ideal sodium counter electrode* Na_{id} *to an NZSP solid electrolyte pellet, the opposite side was polished using a SiC grinding paper. A 5 µm thick copper electrode was prepared by thermal evaporation on the polished side of the NZSP pellet. Afterwards, the copper film was covered with a Ni disc to ensure homogeneous pressure distribution during electrochemical experiments. The prepared cells were sealed in Ar-filled pouch bags. b) Schematic of the measurement series at different stack pressures and current densities, which have been performed. All measurements were carried out at a constant temperature of 25°C.*

2. Impedance Analysis of Cathodic Sodium Deposition at Various Current Densities

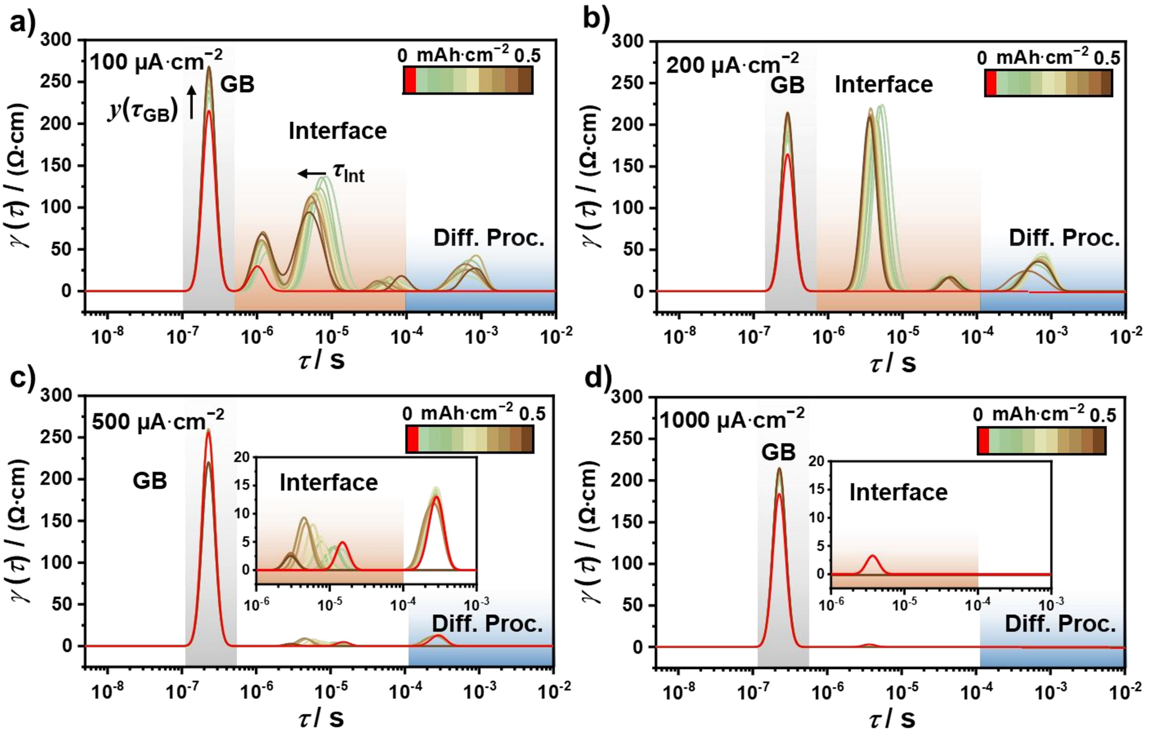

Figure S2: *Distribution of relaxation time analysis for cathodic deposition of sodium at the Cu|NZSP interface at various deposition capacities and current densities. The relaxation time of grain boundary transport process* τ_{GB} *is indicated by the grey background, while the orange background highlights the region where interface-related processes* τ_{Int} *are expected. In addition, signals presumably due to diffusion processes (indicated by blue background) are observed at time constants* $> 10^{-4}$ *s. Independent of the applied current density,* τ_{GB} *remains constant during cathodic deposition. However, a continuous increase in the amplitude of the grain boundary signal* $y(\tau_{GB})$ *is observed as cathodic deposition progresses. Note that this trend becomes less pronounced with increasing current density. As the current density increases, the number and intensity of signals in the region of* τ_{Int} *decreases. At* $j_{app} = 1000\ \mu A{\cdot}cm^{-2}$*, a small signal in the region of* τ_{Int} *is present in the pristine cell, while no signal can be observed during sodium deposition. Irrespective of the current density, a shift of* τ_{Int} *to lower values is observed with increasing deposition capacity* q_{dep} *of sodium.*

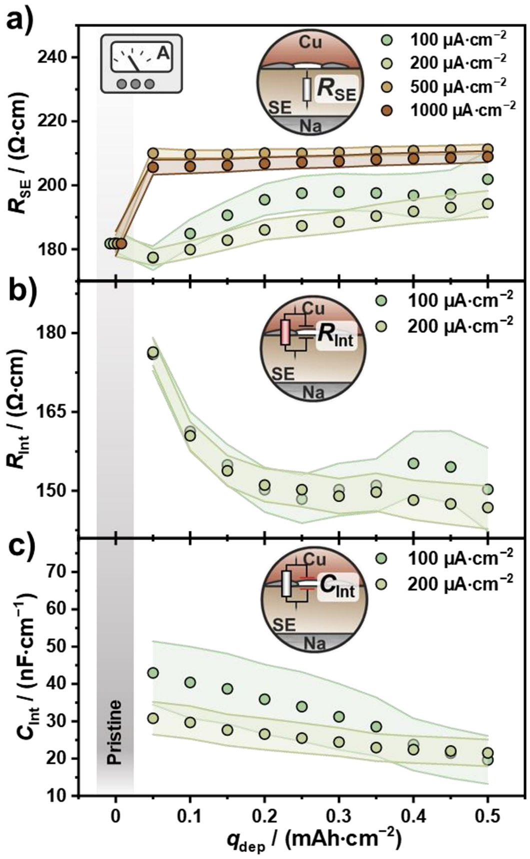

***Figure S3**: Evolution of the solid electrolyte resistance R_{SE} (sum of R_{Bulk} and R_{GB}), during cathodic deposition of sodium at the Cu|NZSP interface for various current densities. Deposition was carried out at $p = 2$ MPa and $T = 25$ °C. Impedance data were fitted using the equivalent circuit models given in Figure 2 and normalized with respect to the cell constant. Due to the normalization to the cell constant, all pristine cells have the same R_{SE}. For a better overview, the R_{SE} of the pristine cells were slightly shifted and highlighted in grey. The error resulting from the fitting of R_{SE}, R_{Int}, and C_{Int} of the respective current density has been highlighted in the corresponding color.*

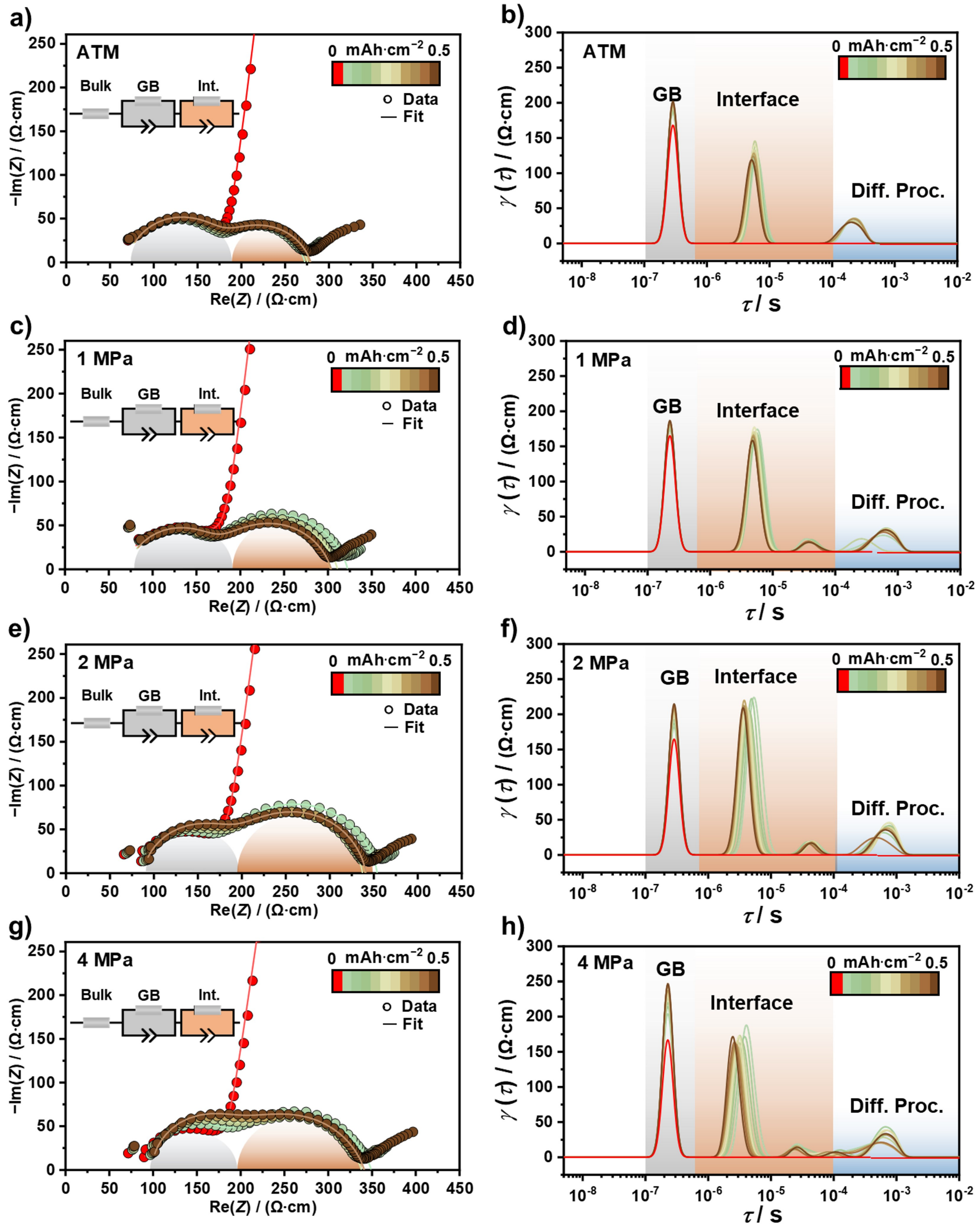

Figure S4: *Impedance spectra (left column) and associated distribution of relaxation times analyses for the measurement series, in which sodium was cathodically deposited at the Cu|NZSP interface at various stack pressures at* $j_{\mathrm{app}} = 200\ \mu\mathrm{A{\cdot}cm^{-2}}$ *and* $T = 25\ °\mathrm{C}$*. In the Nyquist plots and distribution of relaxation times diagrams, the grain boundary transport process is highlighted in grey, while the interface-related process is indicated by an orange background. In addition, diffusion processes in the long relaxation time region are highlighted with a blue background. The impedance data were fitted with the equivalent circuit inserted in the figures and the results are shown in Figure 4. All data* *were normalized by the cell constants. Based on the distribution of relaxation times analysis, the relaxation time of the grain boundary transport process τ_{GB} remains constant during cathodic deposition for all stack pressures. Only an increase of the amplitude $y(\tau_{GB})$ is observed. This is most pronounced at a stack pressure of 4 MPa. For the interface-related relaxation time τ_{Int}, shifts are observed during cathodic deposition to lower values, which is even more pronounced with increasing stack pressure.*

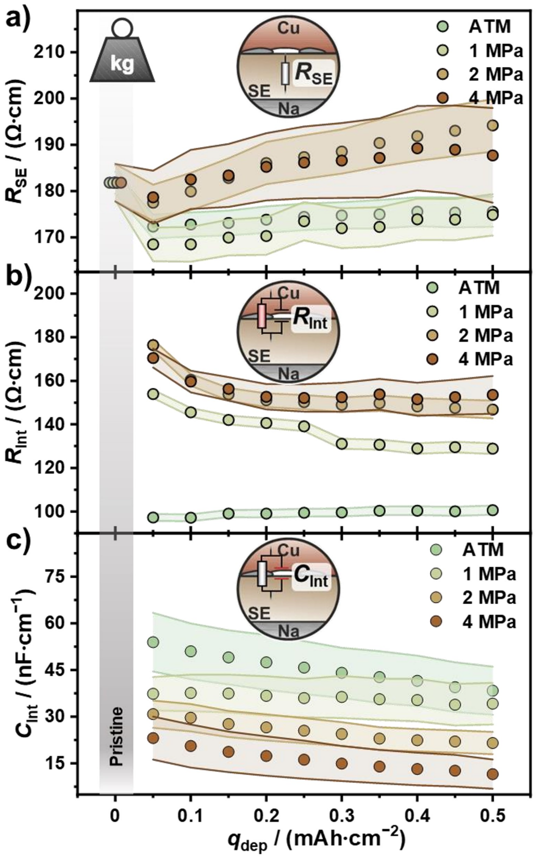

Figure S5: *Evolution of the solid electrolyte resistance R_{SE} (sum of R_{Bulk} and R_{GB}), interface-related resistance R_{Int}, and interface-related capacity C_{Int} at different stack pressures. Deposition was carried out at j_{app} = 200 µA·cm^{-2} and T = 25 °C. Impedance data were fitted using the equivalent circuit models given in Figure S4 and normalized to the cell constants. Due to the normalization to the cell constant, all pristine cells have the same R_{SE}. For a better overview, the R_{SE} of the pristine cells were slightly shifted and highlighted in grey. The error resulting from the fitting of R_{SE}, R_{Int}, and C_{Int} of the respective stack pressure has been highlighted in the corresponding color.*

3. Ex Situ Characterization of Copper Electrodes by Optical and Confocal Microscopy

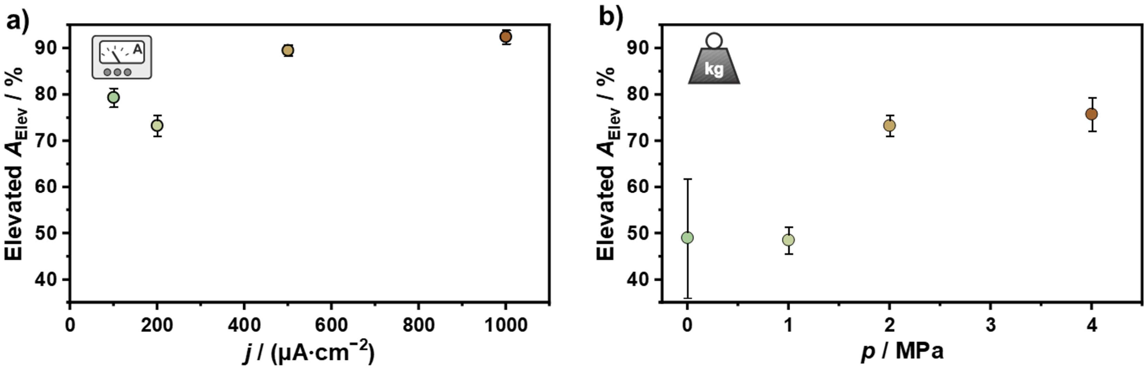

Figure S6: *Elevated area A_{Elev} of the copper electrode after cathodic deposition of 0.5 mAh·cm^{-2} for the a) current density and b) stack pressure series. The elevated area was determined based on the confocal images presented in Figure 5 and Figure S7. For the determination of A_{Elev}, a threshold was determined using the SensoView software package, at which all elevated parts in the 3D confocal microscopy profile were completely captured. The error bars describe the largest deviation when varying the determined threshold by 2% of the total profile height.*

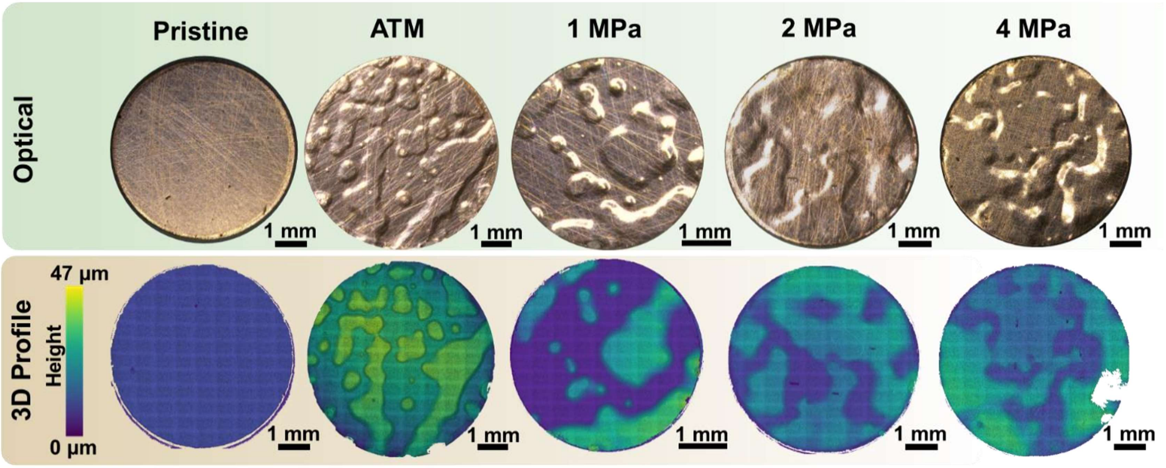

Figure S7: *Optical microcopy images (top row) and corresponding 3D confocal microscopy profiles (bottom row) of a pristine copper electrode and after cathodic deposition of q_{dep} = 0.5 mAh·cm^{-2} at different stack pressures with j_{app} = 200 µA·cm^{-2} and T = 25°C.*

4. Correlation Between FIB-SEM Cross Sections and 3D Profiles of the Copper Electrodes

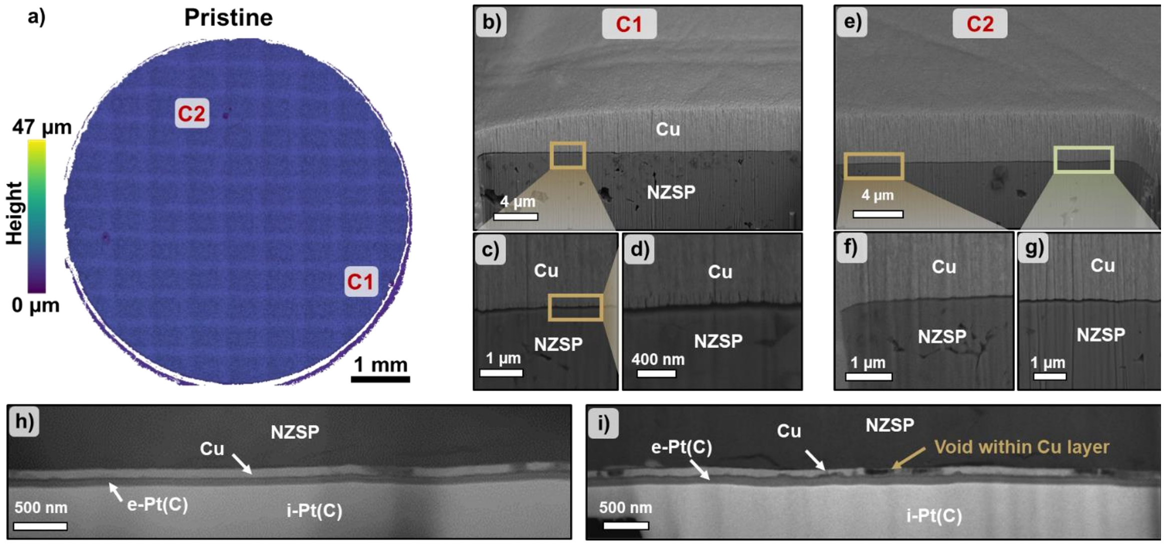

Figure S8: *a) Confocal microscopy image of pristine copper electrode prepared by thermal evaporation on NZSP solid electrolyte. b) Xe$^+$ FIB-SEM cross sections of the edge region of the copper electrode, labeled as C1 in a) with magnified representation of the Cu|NZSP interface in c) and d). Xe$^+$ FIB-SEM cross section of the Cu|NZSP interface with magnified view at the center of the copper electrode, denoted as C2 in (e-g). At the edge as well as in the center of the electrode, a slight gap of roughly 100 nm is present between the copper electrode and NZSP solid electrolyte. h)-i) High angle annular dark field-scanning transmission electron microscopy image of a thermal-deposited copper thin film on NZSP, prepared under cryogenic conditions with Ga$^+$ FIB. For the processing of the lamella, a platinum protective layer was first deposited using an electron beam, named e-Pt(C). Later, a second platinum layer was deposited using an ion beam, known as i-Pt(C). Despite a homogeneous covering of copper (h), small voids are observed locally in the copper layer (i). It is unclear whether these originate from the thermal deposition process or the FIB preparation of the lamella. Thus, it must be assumed that some parts of the copper electrode are not in direct contact with the NZSP.*

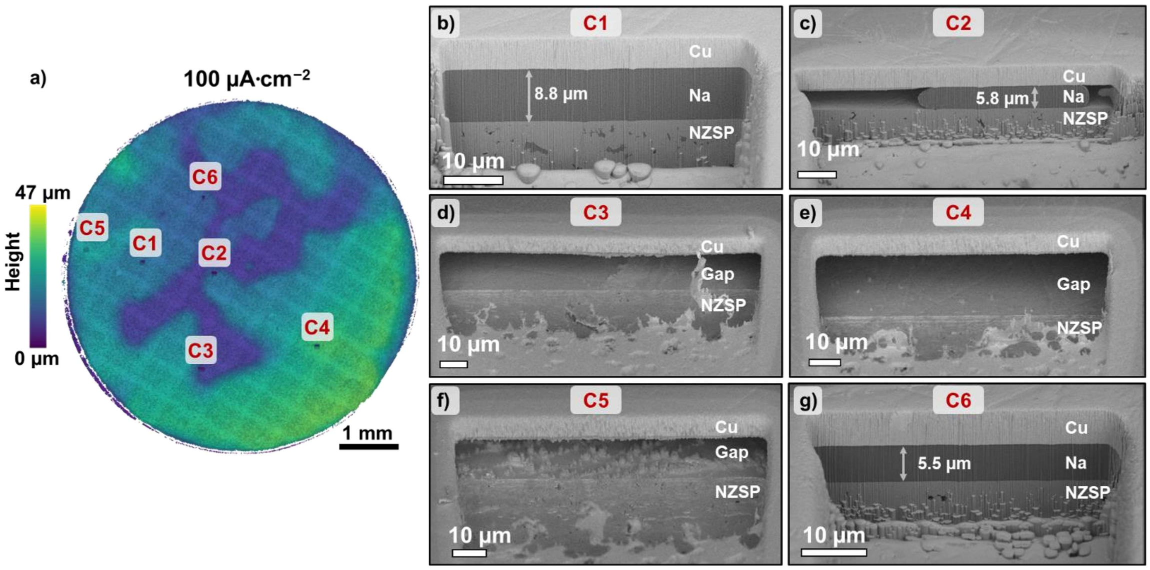

***Figure S9**: a) Confocal microscopy image of the copper electrode after cathodic deposition of q_{dep} = 0.5 mAh·cm^{-2} of sodium at j_{app} = 100 µA·cm^{-2}, p = 2 MPa and T = 25°C. The topography of the electrode is indicated by the color bar. b)-g) FIB-SEM cross-sections of selected spots on the copper electrode labeled as C1 to C6 in (a). Beside the deposition of dense sodium layers (C1, C2 and C6), also regions without sodium and larger gaps between copper and NZSP are observed (C3-C5). Consequently, there is no 1:1 correlation between the elevated copper electrode and the deposited sodium.*

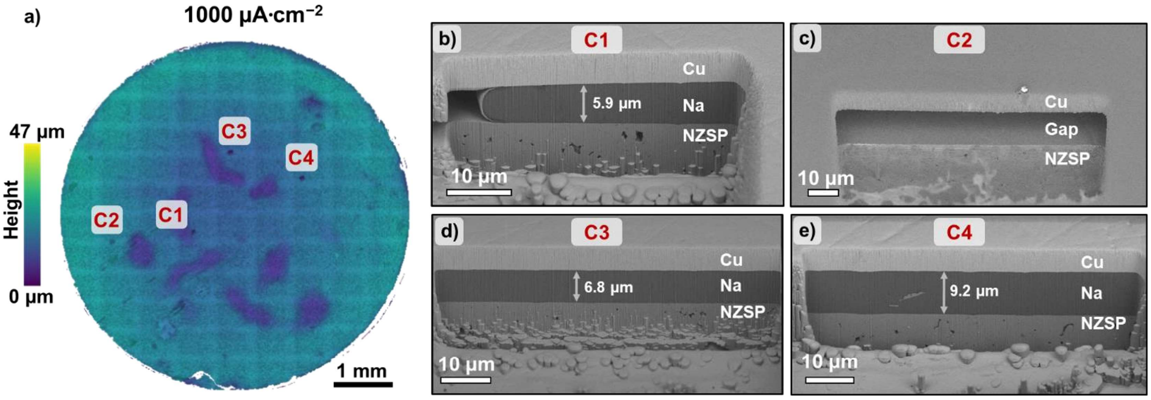

***Figure S10**: a) Confocal microscopy image of the copper electrode after cathodic deposition of q_{dep} = 0.5 mAh·cm^{-2} of sodium at j_{app} = 1000 µA·cm^{-2}, p = 2 MPa and T = 25°C. The topography of the electrode is indicated by the color bar. b)-e) FIB-SEM cross-sections of selected positions on the copper electrode labeled as C1 to C4. Except for position C2, a homogeneous and well distributed sodium layer is found under the copper electrode.*

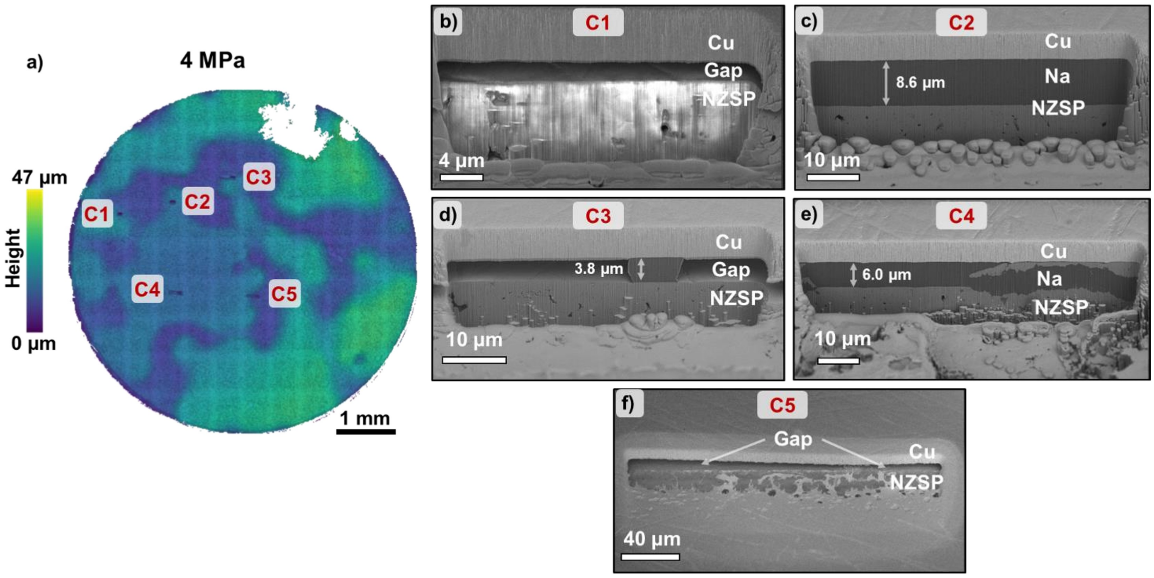

Figure S11: *a) Confocal microscopy image of the copper electrode after cathodic deposition of* q_{dep} *= 0.5 mAh·cm*$^{-2}$ *of sodium at* j_{app} *= 200 µA·cm*$^{-2}$*, p = 4 MPa and T = 25°C. The topography of the electrode is indicated by the color bar. b)-f) FIB-SEM cross-sections of selected positions on the copper electrode labeled as C1 to C5. Beside deposition of homogeneous sodium layers (C2) and gap formation (C1 and C4), growth of a single whisker is observed (C3). In addition, a strong damage of the NZSP near the interface is observed at position C4. Parts of the NZSP broke out of the surface and were pushed onto the copper electrode. It should be mentioned that beside spallation, it did not lead to an inhomogeneous sodium deposition at this spot.*

5. In Situ Scanning Transmission Electron Microscopy Experiments

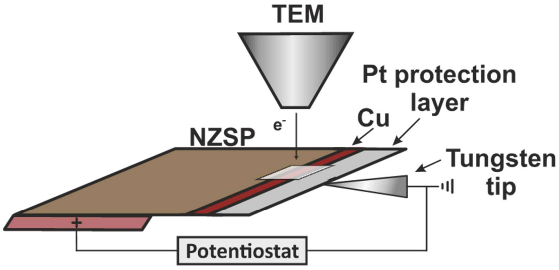

Figure S12: *Illustration of the in situ STEM setup for polarization experiments.*

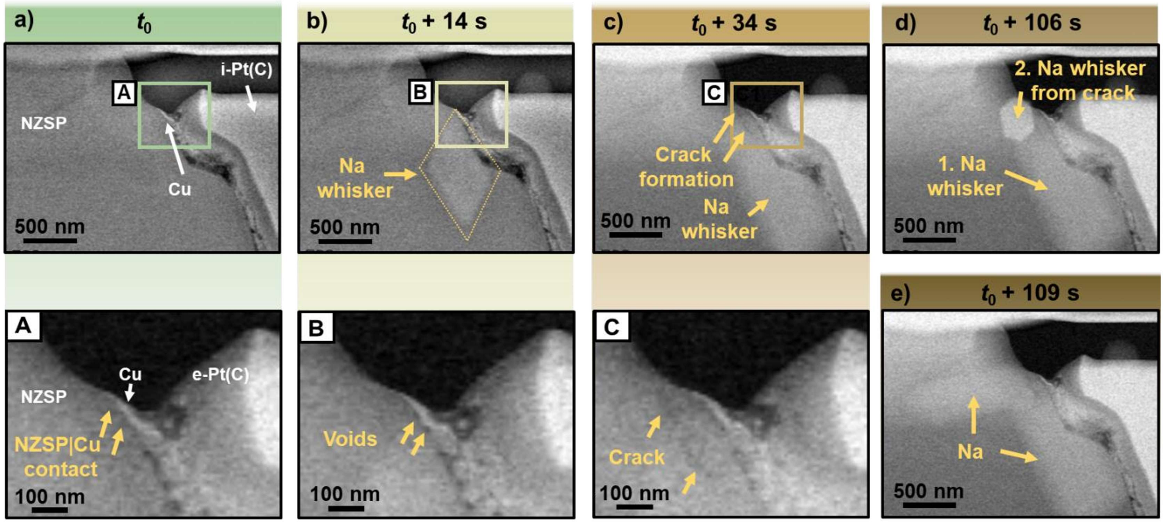

Figure S13: *Time-resolved high angle annular dark field-scanning transmission electron microscopy images of a Cu|NZSP interface during biasing. To initiate sodium deposition, the voltage was gradually increased and image acquisition was started when a voltage of 4 V was reached. This time is referred to as t_0. The pristine lamella is shown in a) with a magnified view of the Cu|NZSP contact spot. For processing of the lamella a platinum protection layer was deposited via electron-beam (denoted as e-Pt(C)) followed by an ion-beam deposition referred to i-Pt(C). After 14 s of polarization, a sodium whisker with rhombohedral shape (yellow dotted line) is observed, as shown in b). Moreover, after the first polarization step small voids at the Cu|NZSP interface are present (B). During further polarization, a crack forms near the Cu|NZSP interface (c). With progressing deposition, a second sodium whisker forms originating from the previously formed crack (d) and grows with further biasing as shown in e).*

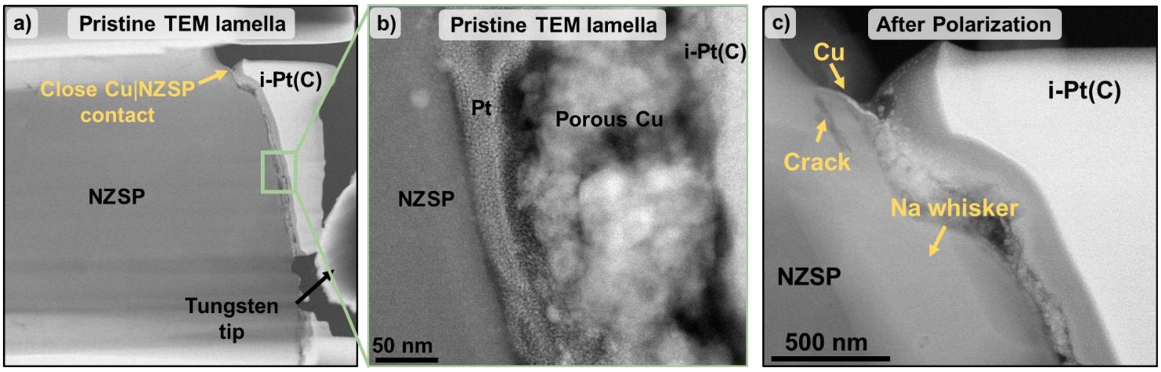

Figure S14: *High angle annular dark field-scanning transmission electron microscopy image of the second prepared TEM lamella for polarization experiments. b) Magnified view of the lamella at the interface. c) TEM lamella after biasing experiment. Clearly a crack near the Cu|NZSP interface can be observed.*

The electron-transparent lamella, shown in **Figure S13**, was fabricated from a NZSP pellet by FIB processing. Before deposition of the copper layer, the NZSP surface under consideration was in contact with a sodium electrode. By anodic dissolution, the physical contact between NZSP and sodium was reduced so that the sodium electrode could be removed very easily without damage, exposing the NZSP surface. A 120 nm thick layer of copper was then deposited on the surface by thermal evaporation. This specimen was used to prepare the lamella for analysis.

As shown in **Figures S13a** and **13b**, in addition to a dense and tight contact on top of the metal|SE interface (highlighted in yellow), a porous copper layer is observed. It might be possible that remaining sodium at the NZSP surface influence the formation and growth of the deposited copper and thus lead to the formation of a porous copper layer. The platinum observed directly at the surface of the NZSP could be due to the porous copper layer that was electron-beam-deposited on the surface of the sample inside the FIB system. A dense copper layer with a close contact to the NZSP (yellow arrow) might be archived at one spot, as all sodium was removed at this spot by anodic dissolution.

The formation of two sodium whiskers in addition to a crack during the biasing experiment was observed which are highlighted in **Figure S14c**.

7.2.3 *Publication 3: Imaging the Microstructure of Lithium and Sodium Metal in "Anode-Free" Solid-State Batteries using EBSD*

nature materials

Supplementary information https://doi.org/10.1038/s41563-024-02006-8

Imaging the microstructure of lithium and sodium metal in anode-free solid-state batteries using electron backscatter diffraction

In the format provided by the
authors and unedited

Table of Contents

1 Kikuchi Pattern of Alkali Metals

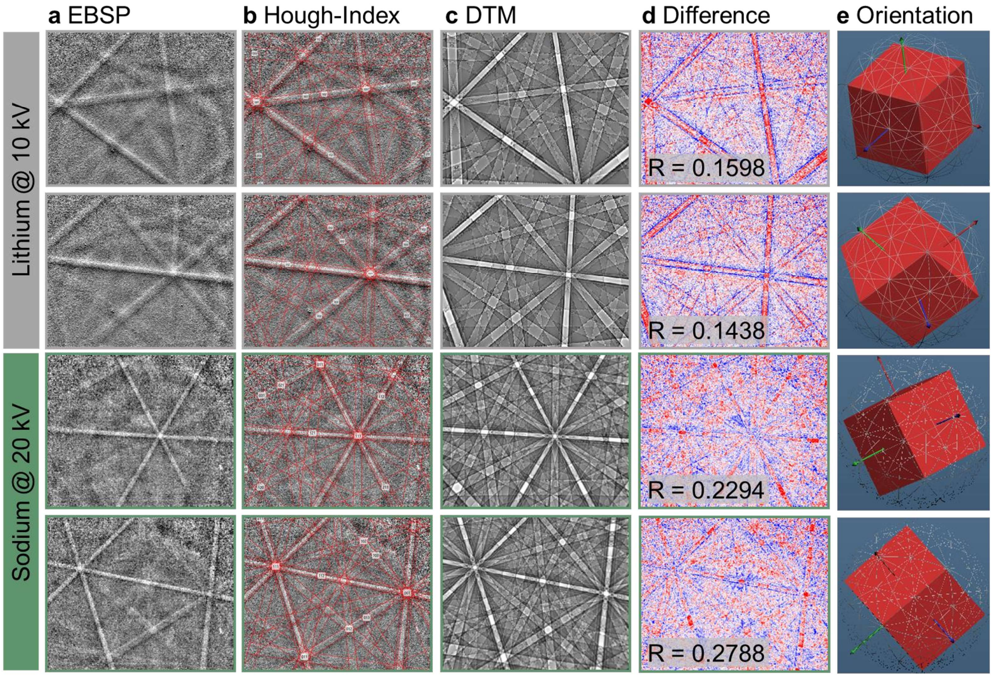

Figure S1. *a) Experimentally obtained representative electron backscatter pattern (EBSP) (Kikuchi pattern) of lithium and sodium metal at two different orientations each. The grain orientation of each pixel is determined by the respective Hough-indexing of the EBSP, as shown in b). To enhance the indexing of less resolved EBSPs and reduce the number of incorrectly indexed pixels, an additional indexing process using a dynamic simulated pattern was conducted. EBSP for different orientations were dynamically simulated based on the crystal structure of each metal and are shown in c). The measured and simulated (EBSPs) were compared until the difference between them was minimized in d). The orientation of the pixel is determined based on the match, as demonstrated in e). Lithium patterns were acquired at 10 kV, whereas sodium patterns were acquired at 20 kV. The pattern quality as well as the R-value obtained by matching the patterns with simulations is superior for sodium due to its higher material density and therefore higher intensity of backscattered electrons.*

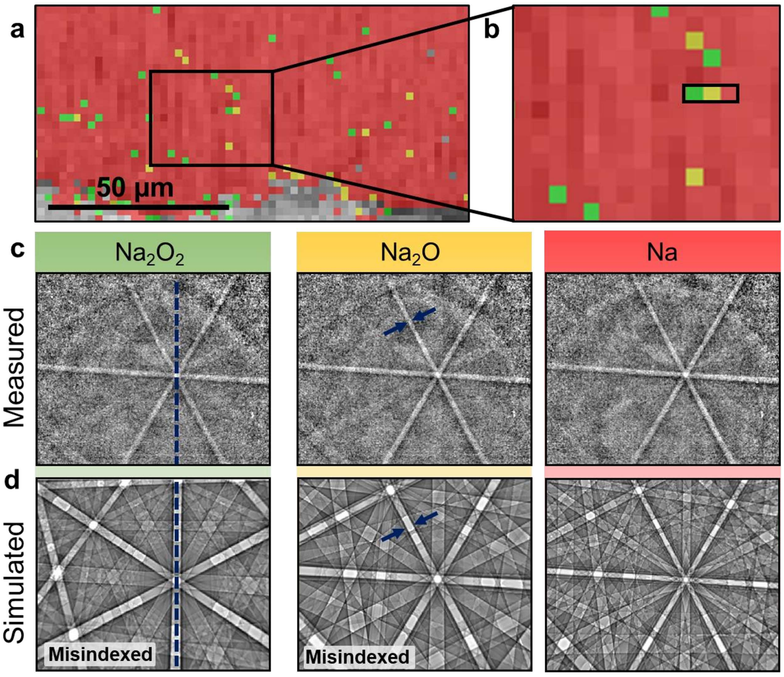

Figure S2. *a) Phase map of a representative sodium cross-section prepared via FIB-SEM without data cleaning. Three different phases were considered during the Hough-indexing algorithm, namely,* Na_2O_2 *(ICSD 26575),* Na_2O *(ICSD 60435), and Na (ICSD 44757) indicated in green, yellow and red, respectively. A magnified region of the phase map is shown in b), where a row of pixel is highlighted by a black frame. According to the phase map all phases are present next to each other although the measured EBSP patterns are the same, as visualized in c). Based on the simulated pattern for the respective phase shown in d), the* Na_2O_2 *and the* Na_2O *phases are clearly indexed incorrectly. For the* Na_2O_2 *phase distinct Kikuchi bands are missing (indicated by the blue dotted line), while for the* Na_2O *phase the band width does not match that of the measured EBSP (blue arrows). The measured EBSP can thus be assigned unequivocally to the sodium metal phase. Furthermore, the formation of oxide-based side phases resulting from residual gases in the SEM chamber can be eliminated. This supports the conclusion that the established workflow is appropriate for characterizing the microstructure of alkali metals.*

2 Inverse Pole Figures of Quenched and Reference Sodium Metal

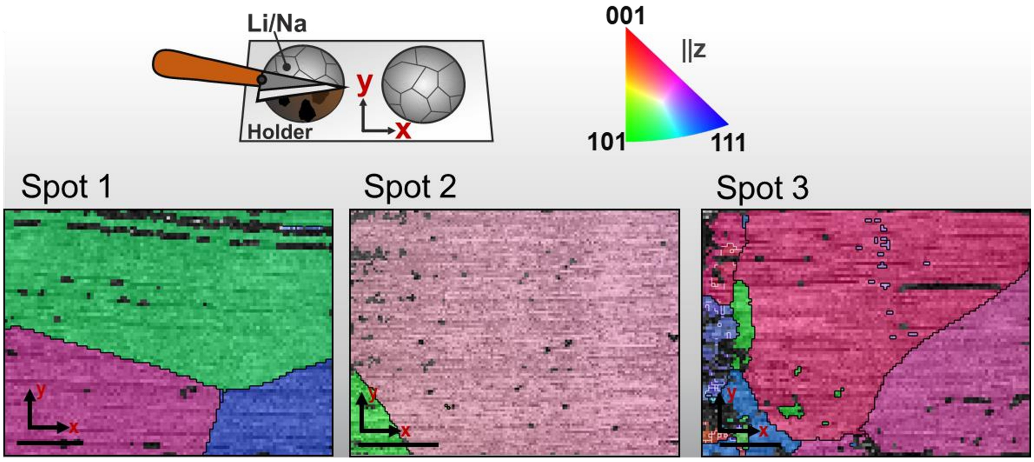

Figure S3. *The inverse pole figure (IPF) map of R-Na was obtained at various spots. The IPF is presented parallel to the z-direction (normal direction, ND), according to the sample coordination system shown in the schemes on the top right. Large angle grain boundaries (>10°) are indicated by black lines. Misorientations between neighboring pixels in the range of 2° - 10° are only observed at spot 3, as marked by white lines. The scale bar in each image equals 200 µm. Grains are observed in the range from a few hundred micrometers to almost one millimeter. Due to the huge grain size and the corresponding small number of grains in the imaged samples, no meaningful grain size distribution can be determined, although several sample spots were analyzed.*

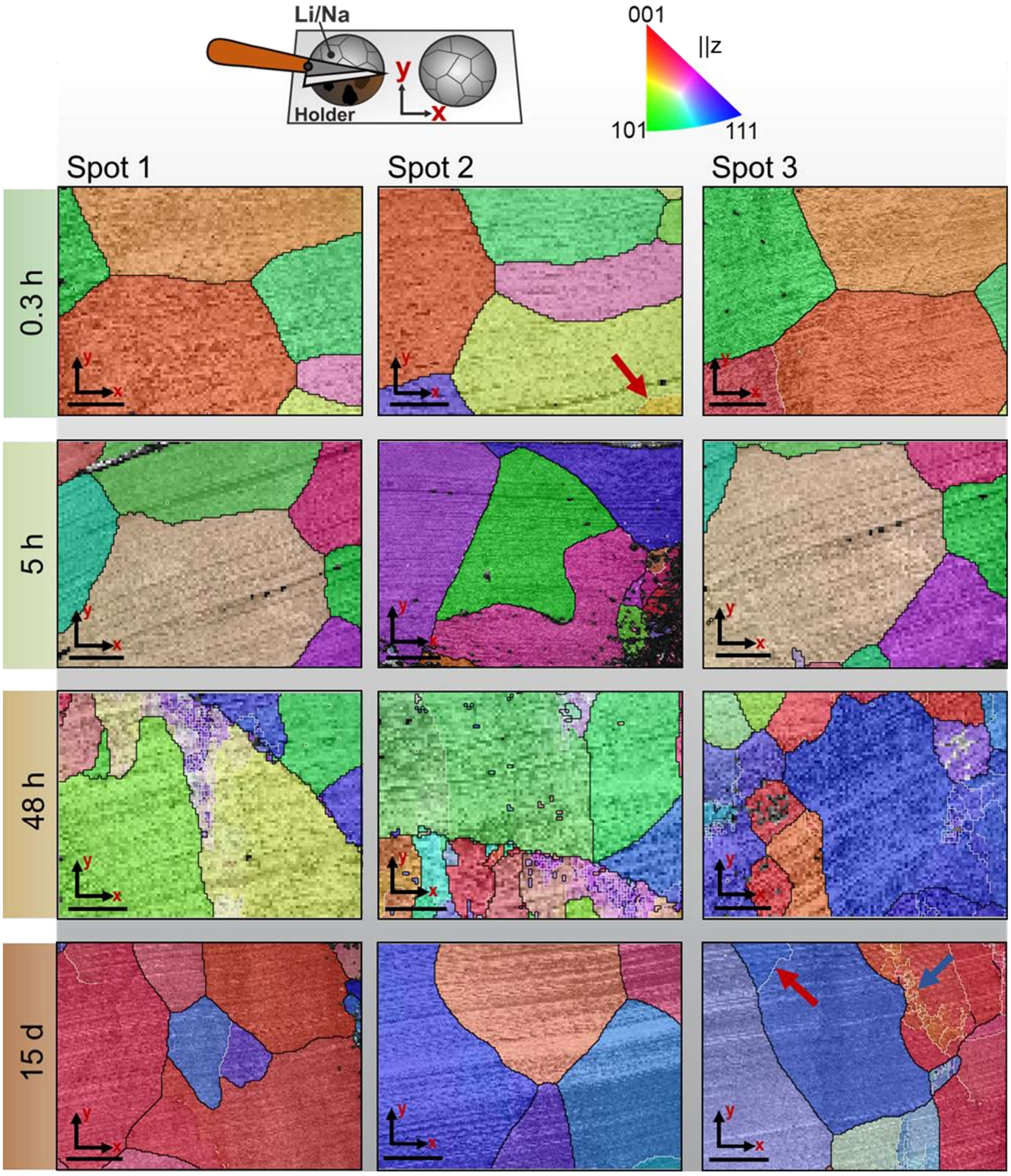

Figure S4. *Time series of inverse pole figures from Q-Na at various spots. The IPF is presented parallel to the z-direction (normal direction), according to the sample coordination system shown in the schemes on the top right. Large angle grain boundaries (>10°) are indicated by black lines. White lines indicate misorientations in between 2° - 10°. It is important to note that this angle range includes both small grain boundaries and material deformations. For instance, in the IPF map in the lower right a small angle grain boundary is indicated by a red arrow and deformed regions marked by a blue arrow. The scale bar in each image denotes 200 µm. The grain size ranges from few to several hundred microns. Although various areas of the Q-Na were captured, a reliable grain size distribution cannot be determined due to the large size and low number of grains. No grain growth is observed over time as a result of annealing.*

3 *Cross-sectional Inverse Pole Figures of Alkali Metal*

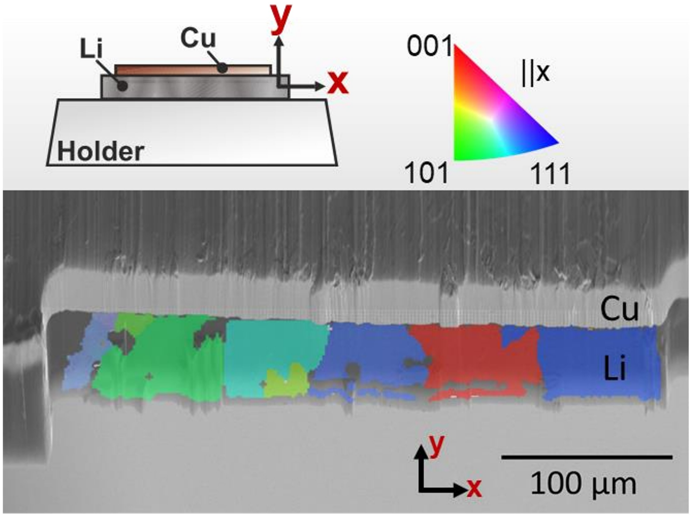

Figure S5. *Magnified IPF map of the sample shown in Figure 2g parallel to the x-direction. Clearly, the large green area assumed to be one grain parallel to the y-direction actually consists of two grains, coincidently oriented the same in y-direction but different in x-direction.*

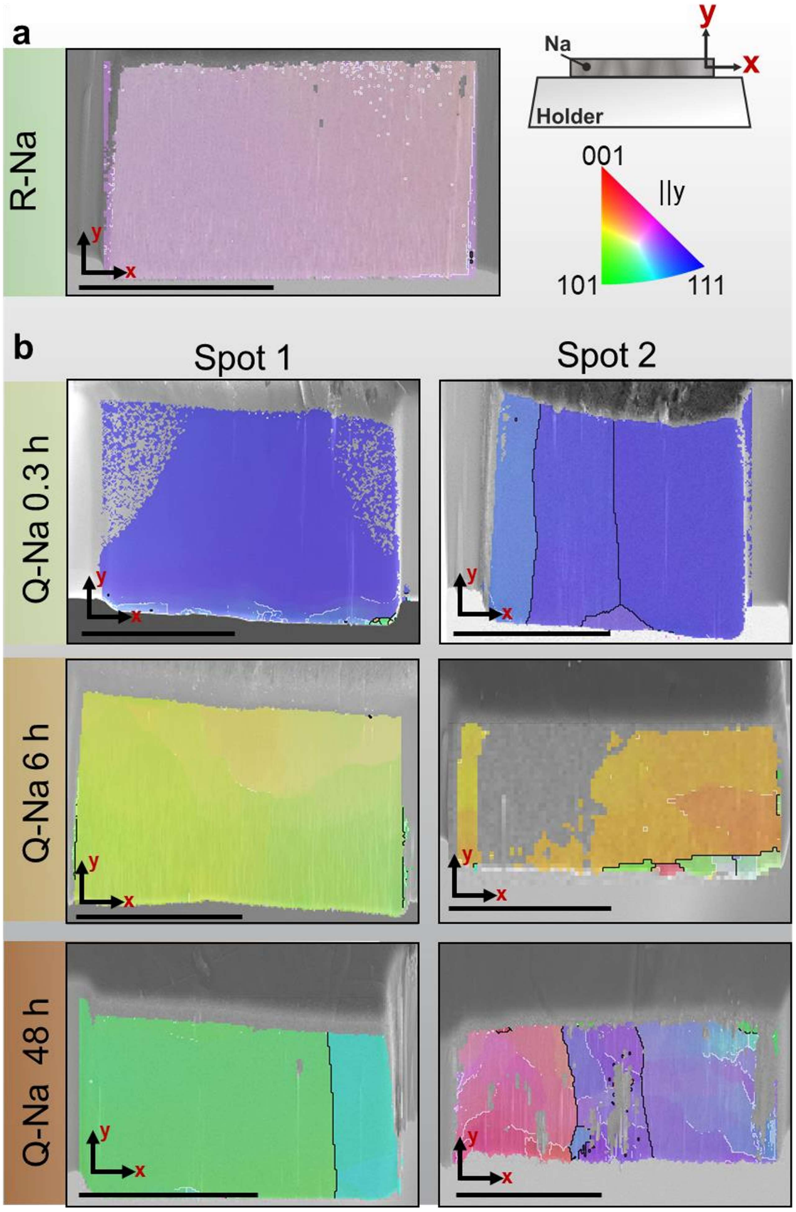

Figure S6. *Compilation of cross-sections of a) R-Na and b) Q-Na foils prepared via focused-ion beam milling. The IPF is presented parallel to the y-direction (milling direction), according to the sample coordination system shown in the schemes on the top right. Large angle grain boundaries (>10°) are indicated by black lines. Misorientation in the angle range between 2° to 10° are highlighted by white lines. The scale bar in each image equals 200 µm. Due to the large size of sodium grains, complete grains cannot be visualized in cross-sections. No opposite trend is seen in the FIB-SEM cross-sections compared to the samples prepared in* ***Figure S4****. The vertical grain boundaries also exhibit a preferred orientation, which can be attributed to the aspect ratio.*

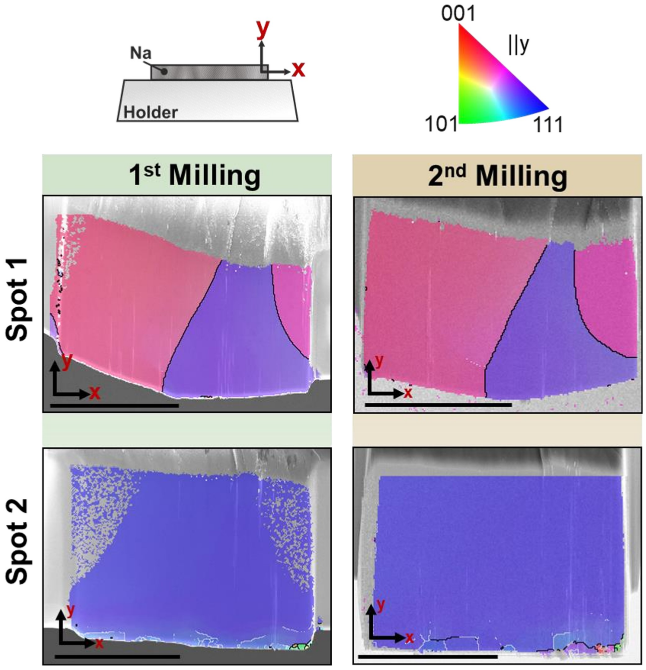

Figure S7. *Inverse pole figure of Q-Na foil after preparation of a cross-section via focused-ion beam and a second milling at two different spots. The IPF are given parallel to the y-direction (milling direction) as indicated in the schemes. Black lines indicate large angle grain boundaries (>10°) while misorientations between 2° and 10° are indicated by white lines. The scale bar equals 200 µm in each image. At both spots, no changes in grain orientation and grain size are observed after a second milling step, demonstrating that the FIB preparation does not affect the microstructure of sodium.*

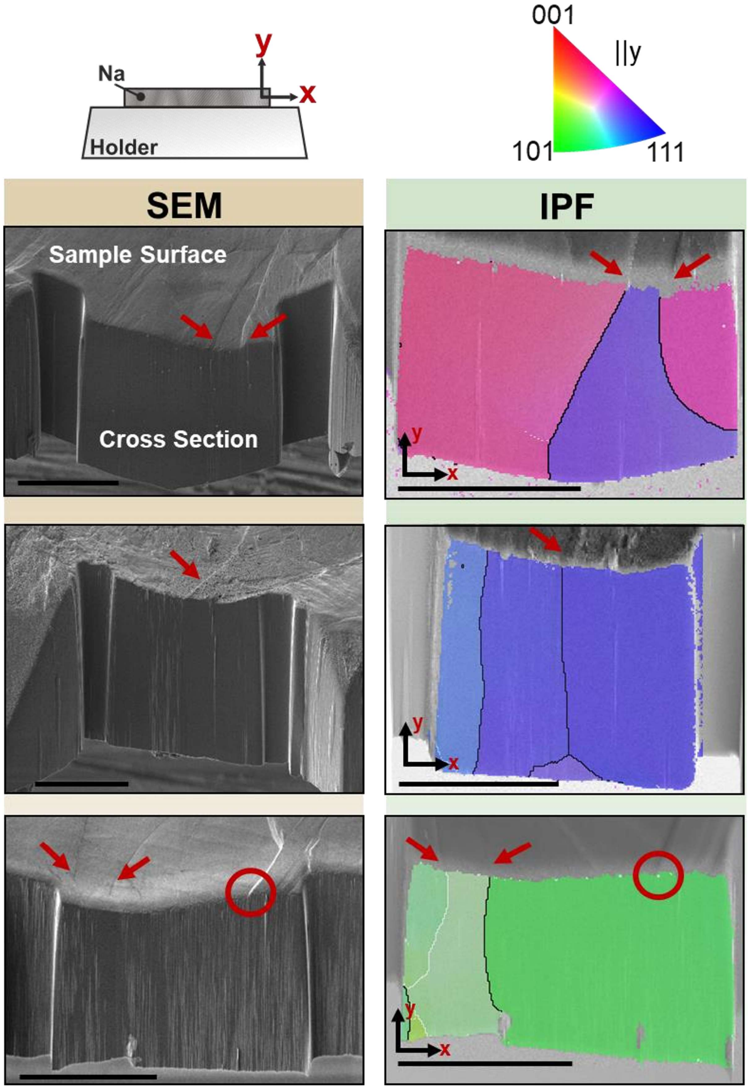

Figure S8. *SEM images of three different cross-sections of sodium foils prepared via focused-ion beam milling (left column) and the corresponding IPF (right column). IPFs are given parallel to the y-direction (milling direction) as illustrated by the schemes in the top of the figure. Large angle boundaries (>10°) are indicated by black lines while misorientations between 2° and 10° are indicated by white lines. In the SEM images (left column), similar lines (highlighted by red arrows) can be seen on the sample surface as already described in Figure 1 (main text). A cross-section perpendicular to the line profile with subsequent microstructure analysis (IPF in the right-hand column) shows grain boundaries along the observed lines in the volume of the sodium film. The identified line on the sodium surface correlates with the presence of a grain boundary. It should be noted that a line on the surface does not necessarily indicate the presence of a grain boundary, as shown in the example circled in red. The evaluation of the line structure on a foil surface is insufficient for an accurate mapping and determination of the grain size.*

4 Impedance Spectra of Electrodeposited Alkali Metals at CC|SE Interface

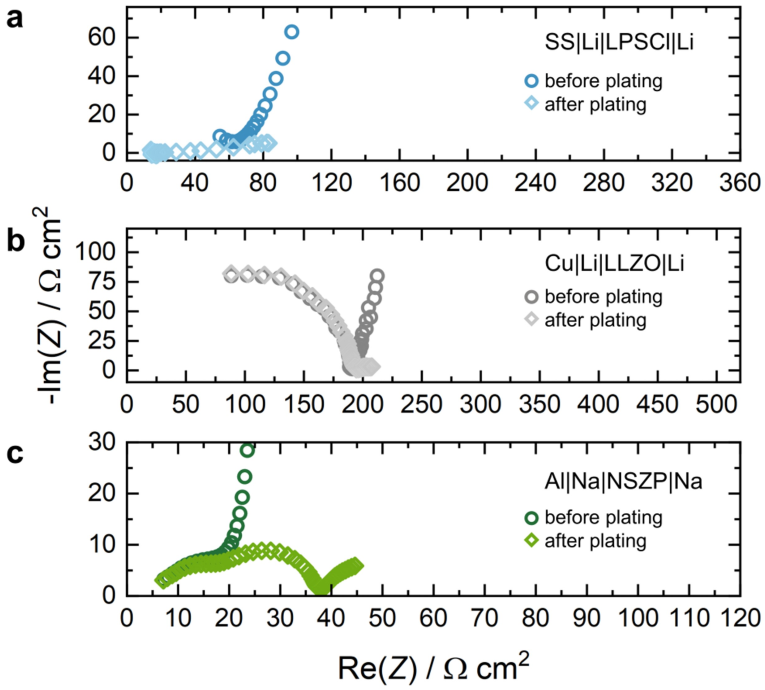

Figure S9. *Impedance spectra before and after electrodeposition of lithium at the SS|LPSCl and Cu|LLZO interface as well as sodium at the Al|NZSP interface. In all cases, a characteristic shift from a blocking electrode impedance to a typical metal electrode impedance can be observed. In the case of SS|LPSCl, a short-circuit occurred, which explains the low resistance and uncommon shape of the impedance spectrum.*

5 Cross-sectional Inverse Pole Figures of Electrodeposited Alkali Metal

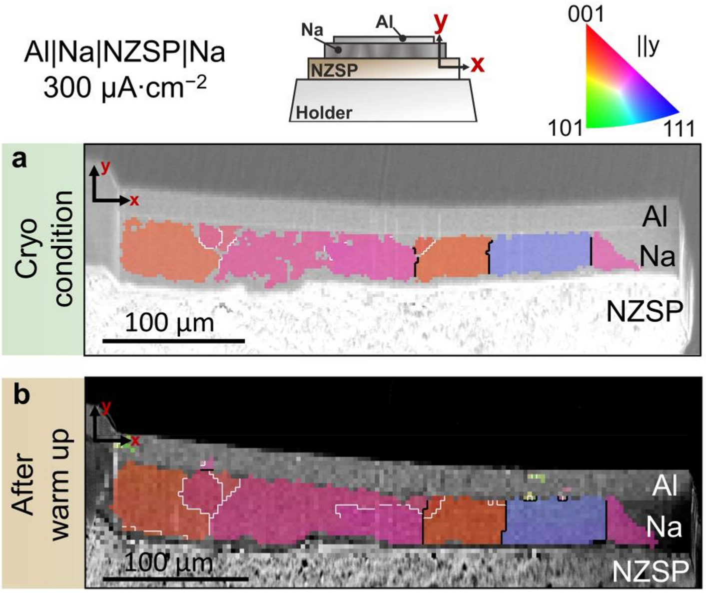

Figure S10. *a) Inverse pole figure of electrodeposited sodium (300 µA cm⁻²) at an interface between a carbon-coated aluminum current collector and NZSP solid electrolyte. The microstructure of the deposited sodium was characterized under cryogenic conditions. b) Inverse pole figure of sodium after warm up of the specimen to room temperature. The IPF of NZSP and aluminum are not shown. The IPF of sodium is presented parallel to the y-direction (growth direction) as visualized by the schemes. Black lines represent large angle grain boundaries (>10°) while misorientations between 2° and 10° are indicated by white lines. The deposited sodium consists of grains on the order of tens of microns. In addition, large grain boundaries are preferentially observed parallel to the deposition direction, i.e., perpendicular to the surface of the NZSP. No changes in grain size or grain boundary orientation were observed after warming the specimen, indicating that no detrimental grain growth by annealing occurred.*

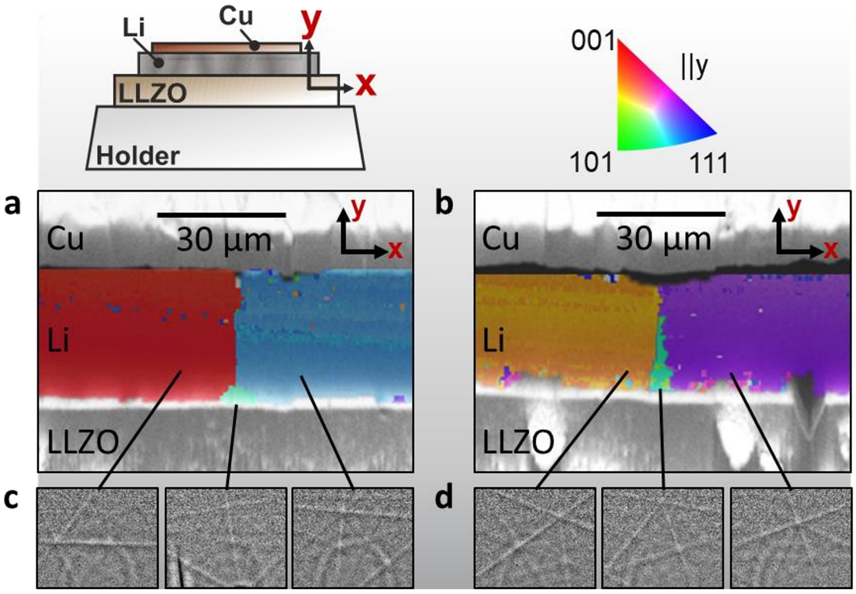

Figure S11. *Magnified IPF maps of different areas of the Cu|Li|LLZO sample shown in Figure 3c are depicted in a) and b). A selected EBSP for each grain is shown in c) and d) confirming the different grain orientations. The small green grains likely exhibit a smaller rate of growth after emergence, which is why the neighboring, faster growing grains constrict the space for the green grains for further growth at higher film thicknesses.*

6 *Influence of SE or CC Microstructure on Electrodeposited Metal Microstructure*

It is not clear what sample property or deposition parameter primarily governs the deposited metal microstructure, such as grain size and microstructure of SE and CC. To check for a relationship between the substrate microstructure with the deposited microstructure, IPF maps of lithium plated on a copper CC with both layers being indexed are shown in **Figure S12a**. Although electrodeposited lithium preferentially deposits on the Cu(111) crystal facet in liquid electrolyte, we found no clear relation between the grain size and orientation of the copper and lithium at the Cu|SE interface.[1] This uncorrelated growth may be due to surface passivation or solid electrolyte interphase (SEI) formation masking the underlying grain structure. A partial masking of preferred deposition sites due to passivation was also reported for lithium growth on copper substrates when different liquid electrolyte with different reactivity were used.[2] In general, it is unlikely for lithium to undergo epitaxial growth on copper due to a mismatch-induced lattice strain (a_{Cu} = 3.6 Å vs. a_{Li} = 3.5 Å).[3,4] The minor effect of the CC microstructure on the resulting grain structure becomes even clearer when lithium is electrodeposited on a Q-Li reservoir foil, as shown by the IPF map in **Figure S12b**. In this case, neither the grain size nor the grain orientation of the electrodeposited grains matches that of the Q-Li reservoir. Furthermore, the size of the solid electrolyte grains (see **Figure S13**) does not appear to have a direct correlation with the microstructure of either electrodeposited alkali metal, as the size difference is quite large. It is therefore likely that the deposit microstructure is dominated by the nucleation process and grain growth itself.

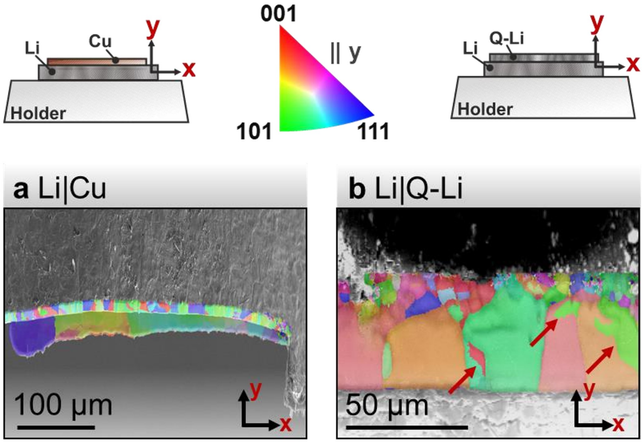

Figure S12. *Alkali metal plated on different current collectors. IPF maps of lithium plated on a copper CC or a Q-Li reservoir are depicted in a) and b), respectively. No correlation between the* *microstructure of the CC or reservoir to the electrodeposited metal is found in any case. Red arrows indicate areas where grains are partly indexed incorrectly due to crystallographic pseudosymmetry.*

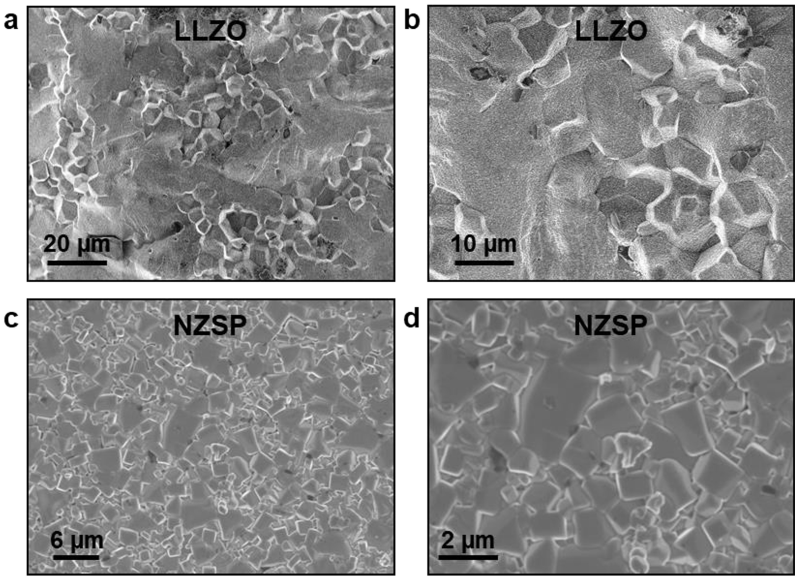

Figure S12. *Scanning electron microscopy images of the surface of LLZO and NZSP. The surface of LLZO is shown in a) and magnified in b) showing a grain size of roughly 5 µm to 20 µm. The grain size of NZSP is in the range of 0.5 µm to 4 µm, as depicted in c) und d).*

7 In situ Lithium Electrodeposition at the Li|LLZO Interface

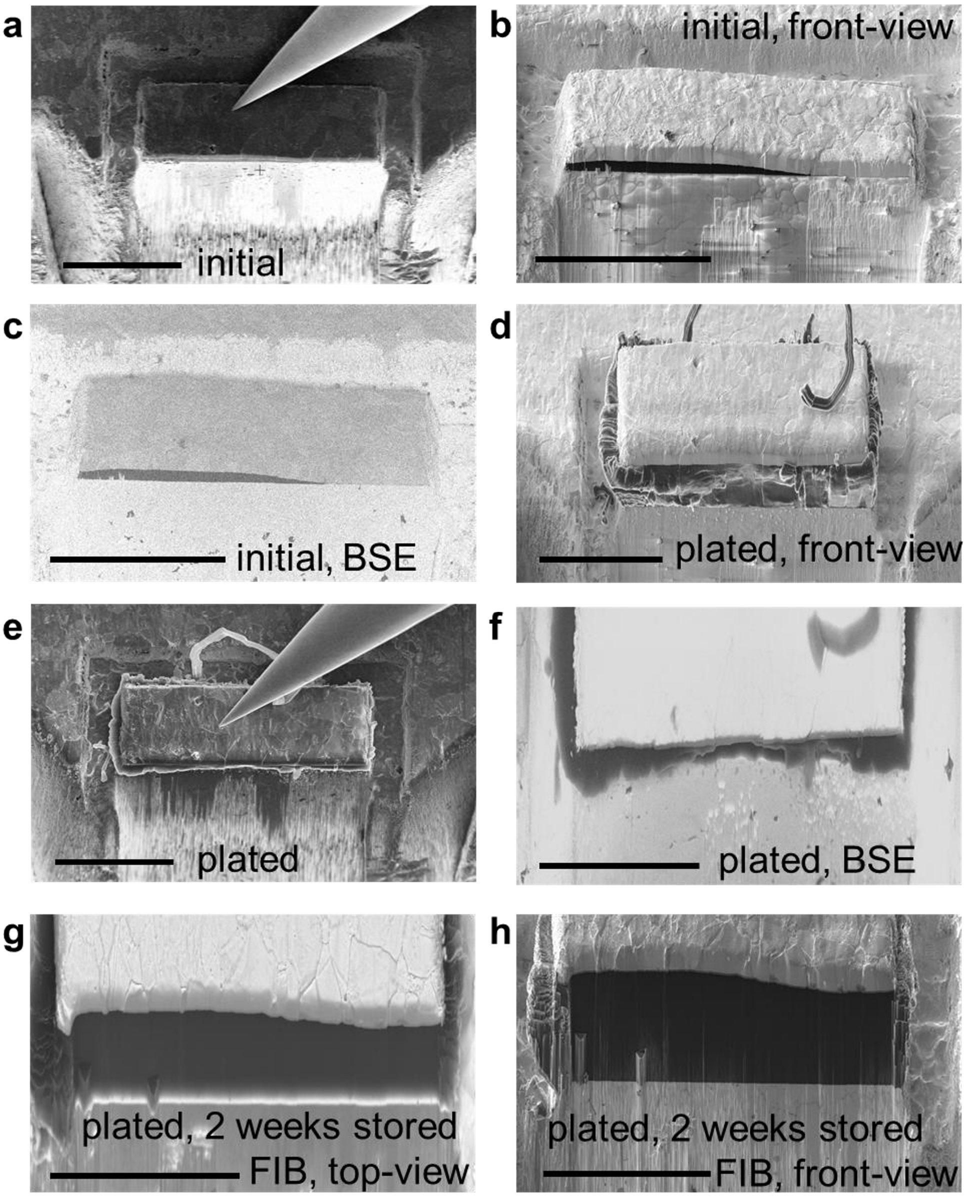

***Figure S14**. Overview SEM images prior and after lithium plating during the in situ EBSD experiment are shown in a) and b). Front-view images after tilting the sample to 55° (including the tilted sample holder) are shown in c) and d). A lithium thickness of around 40-50 µm was achieved dependent on the measurement spot, which fits well to the passed charge. The apparent different aspect ratio of the electrode patch is explained by an uneven film-growth, with higher thicknesses to the back of the patch. BSE images to prove the existence of low-density lithium are shown in e) and f) accordingly. Further, g) and h) show SEM images after two weeks of storage and renewed interface polishing via FIB. All scale bars are equal to 100 µm.*

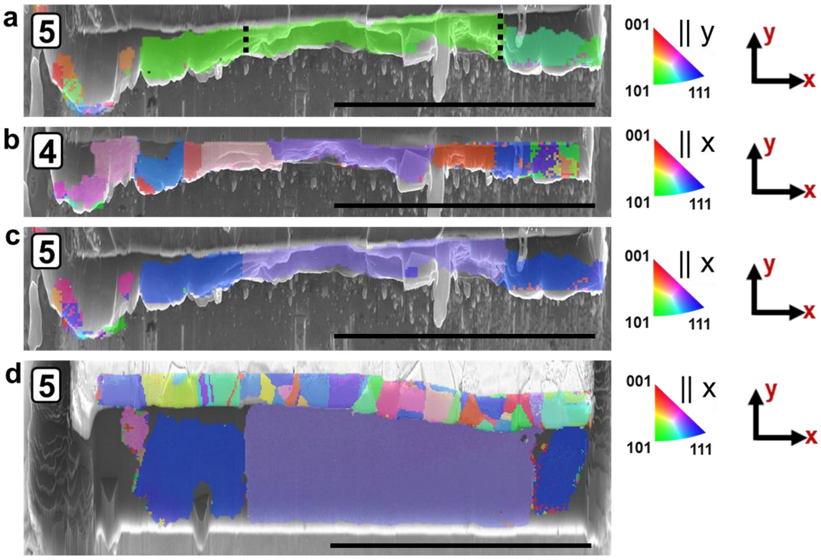

***Figure S15**. Additional IPF maps to **Figure 4c**. a) shows the IPF map in y-direction directly after plating but without additional FIB polishing, confirming the unchanged microstructure during the two-week storage period afterward. Further, b) and c) show the maps of step 4 and 5 also in x-direction to get a better overview of present grain orientations. The map provided in Figure 4c (5) is further shown in x-direction in d). After polishing, the copper grains are also indexed, but do not show a significant influence on the lithium microstructure. All scale bars equal 100 µm.*

8 *In situ Sodium Electrodeposition at the Q-Na|NASICON Interface*

An overview of the electrodeposition of sodium on a pre-existing sodium reservoir is depicted in **Figure S16**. In contrast to lithium, the experiment was conducted using a Q-Na|NZSP|Na cell with an initial electrode thickness of ~50 µm. A smooth and flat voltage plateau is observed during deposition of roughly 1 mAh cm^{-2}. Assuming uniform deposition across the electrode, the deposited capacity corresponds to a sodium layer thickness of approximately 9 µm, which fits to the observed thickness increase at the cross-section shown in **Figure S16b-d**. Prior to deposition, three main grains are observed at the cross-section, while a few small grains are located directly at the interface (**Figure S16e**). Similar to the observation for lithium in **Figure 4c**, the large grain (green) with an orientation close to <101> grows vertically during deposition and consumes the neighboring grains with orientations close to <111>, which results in lateral grain boundary motion. Moreover, the thickness of the smaller grains on the left side of the cross-section directly at the interfaces slightly increases during deposition. The identification of newly formed grains is challenging, as the sodium partly grows out of the image plane leading to shadowing of the interface. However, a new grain appears on the right side of the cross-section as shown by a red arrow in **Figure S16g**. After finishing the deposition experiment, the cross-section was polished via FIB uncovering a second formed grain indicated by red arrows in **Figures S16f** and **S16h**. It should be noted that after polishing, the new cross-section is approximately shifted 10 µm compared to the previous plane, making it difficult to establish an unambiguous correlation. However, upon checking the EBSPs for these grains in **Figures S16i** and **Figure S16j**, it can be concluded that this is the same grain. Similar to the deposition of lithium, the grain width of sodium changes during deposition and grains in the <101> orientation show preferential growth. Although the microstructure of the discussed cross-section has not been characterized after a defined storage time, it is unlikely that the grain width has changed during storage, as shown by the example in **Figure S10**. Thus, the microstructural evolution of sodium likely follows that of lithium.

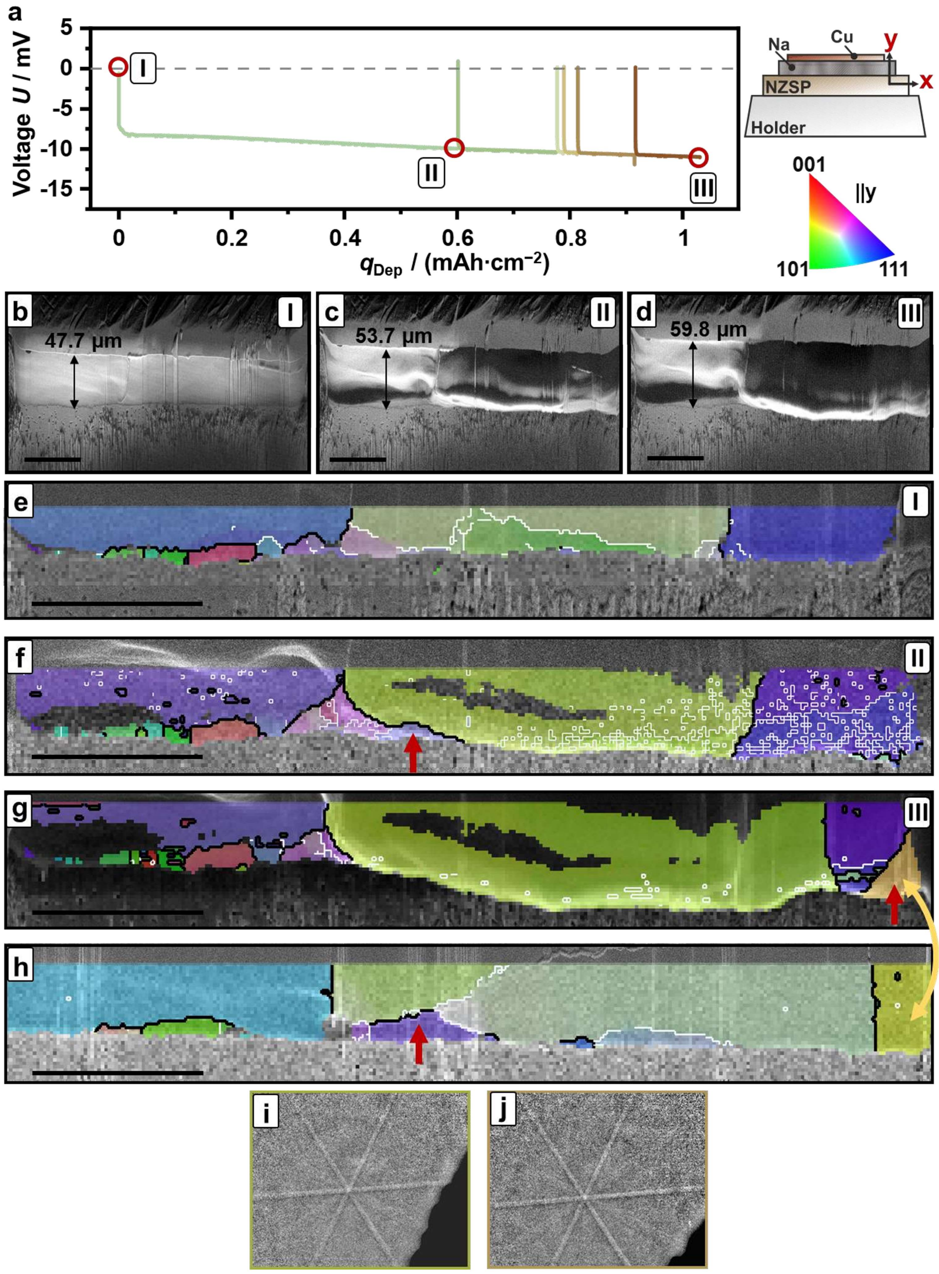

***Figure S16**. In situ EBSD of electrodeposited sodium at a Q-Na/NZSP interface. The deposition was performed inside the SEM using a current density of $300\ \mu A\ cm^{-2}$. The voltage profile of the deposition is shown in a). The voltage spikes indicate the start of each deposition step. EBSD characterization is indicated by a red circle. Forward Scatter Electron images (FSE) of the pristine cross-section and after the two deposition steps are shown in b-d. During each deposition step a layer increase of roughly 5 µm – 6 µm is observed. The corresponding IPF maps of the interface are visualized in e-g. IPF maps are given parallel to the growth direction. Black lines indicate large angle grain boundaries (>10°). White lines visualize misorientations between 2° and 10° of neighbor* *pixels. After the finishing deposition the cross-section was polished via FIB and again characterized by EBSD. The corresponding IPF map is shown in h). Red arrows indicate newly formed grains by electrodeposition. Despite different color in the IPF maps, the highlighted grains by the yellow arrow are similar, as indicated by the pattern in i) and j). The different color originates from pseudosymmetry caused by dynamic pattern simulation. The scale bar indicates 50 µm.*

9 In situ Sodium Electrodissolution at the Q-Na|NASICON Interface

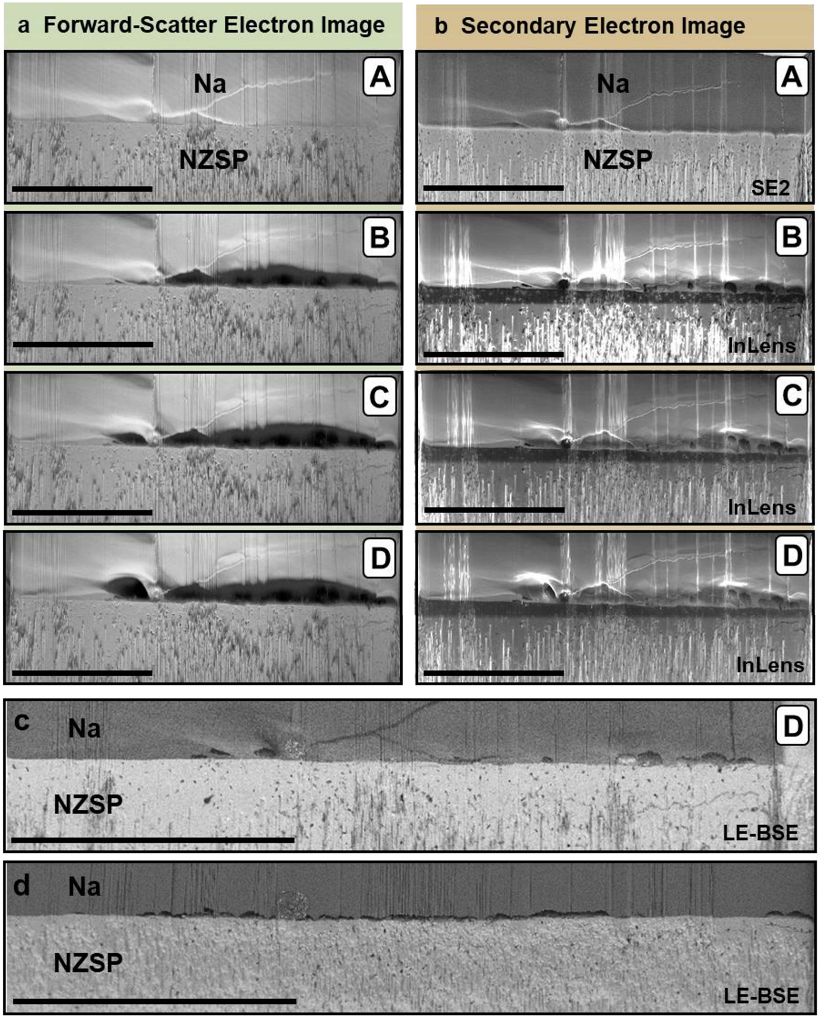

Figure S17*. Compilation of electron images during stripping of sodium at Na/NSZP interface. The given notation (A) to (D) corresponds to the given voltage profile in* ***Figure 4b****. During the in situ experiment the cross-section was imaged at an angle of 70° using a) forward scatter electrons and b) secondary electrons. After the stripping experiment the cross-section was imaged using a low energy-backscatter electron detector (LE-BSE) in an angle of 35°. Based on the different geometries the pore shape and size differ as shown in c). Afterwards the cross-section was again polished revealing unambiguous pores at the Na/NSZP interface. As polishing shifts the cross-section plane roughly 10 µm behind the previous one, no perfect correlation of pores between c) and d) is observed. Scale bars equal 100 µm*

10 References

1. Ishikawa, K., Ito, Y., Harada, S., Tagawa, M. & Ujihara, T. Crystal Orientation Dependence of Precipitate Structure of Electrodeposited Li Metal on Cu Current Collectors. *Cryst. Growth Des.* **17**, 2379–2385 (2017).
2. Kim, Y. J. *et al.* Facet selectivity of Cu current collector for Li electrodeposition. *Energy Storage Mater.* **19**, 154–162 (2019).
3. Nadler, M. R. & Kempter, C. P. Crystallograpic data 186. lithium. *Crystallogr. Data* **31**, 2109 (1959).
4. Davey, W. P. Precision Measurements of the Lattice Constants of Twelve Common Metals. *Phys. Rev.* **25**, 753–761 (1925).

7.3 Scientific Contributions

7.3.1 List of Publications published online as of 11th October 2024

$^{\Delta}$ Indicate equal contribution

2024	T. Fuchs $^{\Delta}$, **T. Ortmann** $^{\Delta}$, J. Becker, C. G. Haslam, M. Ziegler, V. K. Singh, M. Rohnke, B. Mogwitz, K. Peppler, L. F. Nazar, J. Sakamoto, J. Janek, Imaging the microstructure of lithium and sodium metal in anode-free solid-state batteries using electron backscatter diffraction, *Nat. Mater.*, **2024**.
	T. Ortmann, T. Fuchs, J. K. Eckhardt, Z. Ding, Q. Ma, F. Tietz, C. Kübel, M. Rohnke, J. Janek; Deposition of Sodium Metal at the Copper-NaSICON Interface for Reservoir-Free Solid-State Sodium Batteries, *Adv. Energy Mater.* **2024**, *14*, 2302729.
2023	**T. Ortmann**, S. Burkhardt, J. K. Eckhardt, T. Fuchs, Z. Ding, J. Sann, M. Rohnke, Q. Ma, F. Tietz, D. Fattakhova-Rohlfing, C. Kübel, O. Guillon, C. Heiliger, J. Janek, Kinetics and Pore Formation of the Sodium Metal Anode on NASICON-Type $Na_{3.4}Zr_2Si_{2.4}P_{0.6}O_{12}$ for Sodium Solid-State Batteries *Adv. Energy Mater.* **2023**, *13*, 2202712.
	Z. Ding, Y. Tang, **T. Ortmann**, J. K. Eckhardt, Y. Dai, M. Rohnke, G. Melinte, C. Heiliger, J. Janek, C. Kübel; The Impact of Microstructure on Filament Growth at the Sodium Metal Anode in All-Solid-State Sodium Batteries, *Adv. Energy Mater.* **2023**, *13*, 2302322.
2022	Q. Ma, **T. Ortmann**, A. Yang, D. Sebold, S. Burkhardt, M. Rohnke, F. Tietz, D. Fattakhova-Rohlfing, J. Janek, O. Guillon; Enhancing the Dendrite Tolerance of NaSICON Electrolytes by Suppressing Edge Growth of Na Electrode along Ceramic Surface, *Adv. Energy Mater.* **2022**, *12*, 2201680.
2019	T.Weber, **T. Ortmann**, D. Escalera-López, M. J. S. Abb, B. Mogwitz, S. Cherevko, M. Rohnke, H. Over; Visualizing Potential-Induced Pitting Corrosion of Ultrathin Single-Crystalline $IrO_2(110)$ Films on $RuO_2(110)/Ru(0001)$ under Electrochemical Water Splitting Conditions, *ChemCatChem* **2020**, *12*, 855–86.

7.3.2 List of Conference Contributions

$^{\Delta}$ Indicate equal contribution

2024

Poster Presentation: “**SBS-5** – 5th International Sodium Battery Symposium” in Berlin, Germany (9/2024) – “*Characterizing the Microstructure of the Sodium Metal Anode in Solid-State Batteries using EBSD*”

Awarded with best poster award

Poster Presentation: “**Materialforschungstag Mittelhessen**” in Giessen, Germany (6/2024) – “*Imaging the Microstructure of the Sodium Metal Anode in Solid-State Batteries using EBSD*”

2023

Invited symposium talk, online Presentation: University of Waterloo Electrochemical Society Student Chapter (WatECS) – “*Interfaces Matters: The role of impedance spectroscopy for solid state batteries*”, (9/2023) **T. Ortmann** $^{\Delta}$ and Dr. J. K. Eckhardt $^{\Delta}$

Oral Presentation: “**MRS Spring 23** – 50th Materials Research Society Spring Meeting & Exhibit” in San Francisco, United States, (4/2023) – “*Deposition Behaviour of Sodium at the Copper-Solid Electrolyte Phase Boundary for Reservoir-free Solid-State Sodium Batteries”*

2022

Poster Presentation: “**ICNaB 22** – 7th International Conference on Sodium Ion Batteries” in Ulm, Germany (12/2022) – “*Growth Behaviour of Sodium Metal at NaSICON-Type Solid Electrolyte for Reservoir-free Sodium Solid State Batteries*”

Awarded with best poster award

Poster Presentation: “**ICNaB 22** – 7th International Conference on Sodium Ion Batteries” in Ulm, Germany (12/2022) – “*Kinetics and Pore Formation of the Sodium Metal Anode on NASICON-type* $Na_{3.4}Zr_2Si_{2.4}P_{0.6}O_{12}$ *for Sodium Solid-State Batteries*”

Oral Presentation: “**SSI 23** – 23rd International Conference on Solid State Ionics” in Boston, United States (7/2022) – “*Elucidation of the Kinetics at the* $Na|Na_{3.4}Zr_2Si_{2.4}P_{0.6}O_{12}$ *Solid-State Battery Electrode Interface”*

8 Acknowledgements

I would like to express my gratitude to all those who have accompanied and supported me throughout my studies and my time as a doctoral student.

First of all, I would like to sincerely thank my supervisor Prof. Jürgen Janek for the opportunity to work and study in his research group. I'm especially grateful for his trust in my work, the freedom he gave me to explore my ideas, the numerous discussions we had, his always positive attitude, and his unrestrained support in all my projects, which allowed me to develop and grow.

A special thanks goes to Prof. Marcus Rohnke for his continuous support and encouragement throughout my whole time in the research group. I am grateful for his willingness to listen to all kinds of questions and for opening up opportunities and possibilities for me to develop in research.

Furthermore, I like to thank Prof. Bernd Smarsly for being the 2nd reviewer of this dissertation. Moreover, I thank Prof. Matthias Elm and Prof. Anja Henß for being part of the examination committee of my doctoral defense.

I would like to thank Dr. Boris Mogwitz, Dr. Joachim Sann, Dr. Klaus Peppler and Prof. Marcus Rohnke for their support and discussion of experiments on the SEM, XPS and SIMS. Furthermore, I like to thank Dr. Bjoern Luerssen for his open ears on any questions and matter I had.

A special thanks goes to my cooperation partners at the KIT, University of Waterloo and FZJ. I would like thank Prof. Christian Kübel and Dr. Ziming Ding for the great discussions and the numerous experiments performed at the TEM. Furthermore, I would like to thank Dr. Qianli Ma and Dr. Frank Tietz for providing the solid electrolyte material. A special thanks goes to Prof. Linda F. Nazar, for her supervision and the opportunity to stay in her research group. Furthermore I like to thank her for the extended discussion and exchange of scientific ideas. I would also like to thank Vipin Kumar Singh for the warm welcome in Waterloo, his support inside and outside the university, as well as the many wonderful moments together in Waterloo and Gießen!

I thank my colleagues and friends in the research group for the fun and amusement we had during coffee and lunch breaks and the pleasant and friendly working atmosphere. Particularly, I would also like to thank my previous colleagues Dr. Simon Burkhardt, Dr. Dheeraj Kumar Singh and Raika Oppermann. Without their help and support, many things would not have been possible and they promoted the development of my scientific understanding, ethic and carefulness. Especially, I like to thank my colleagues and friends Simon Kunz, Dr. Till Fuchs-Kühn, Dr. Janis K. Eckhardt, Juri Becker, Yuriy Yusim, Thomas Schall, David Schäfer and Maya Ziegler for their support as well as for the wonderful moments in the office (*Zentrale)* and the countless activities beyond the university. Thank you very much!

In particular, I'd like to thank my friends for their endless curiosity about what I'm actually doing at university and for providing a welcome distraction after long days of work at university.

My deepest thanks go to my parents, Heike Ortmann and Thomas Ortmann, and my two brothers, Prof. Jan Ortmann and Mathis Ortmann. Without their help this work would not have been possible. Thank you for always believing in me, for standing by me in difficult situations and for always letting me rely on you!